96 AF

PROBABILITY BASED DESIGN CRITERIA FOR ICE LOADS ON FIXED STRUCTURES IN THE BEAUFORT SEA

FINAL REPORT

Vol.1 - Study Description

Det norkse Veritas (Canada) Ltd.
1110 - 10201 Southport Road SW
Calgary, Alberta

June, 1986

EXECUTIVE SUMMARY

A probabilistic model for the calculation of year-round ice loads on fixed offshore structures in the Beaufort Sea was developed. The model uses probabilistic descriptions of different ice parameters in appropriate ice-structure interaction models to produce probabilistic load descriptions. These are then used in extremal analyses to produce the probability distributions of the extremal forces for any loading scenario or combination of scenarios. Such extremal load distributions are directly applicable to the choice of design criteria against ice. The study considered cylindrical and flat sided vertical structures as well as upward and downward breaking cones.

The year was divided into three distinct seasons, namely summer, winter and break-up. Appropriate criteria for season boundaries were defined and the effect of the uncertainty regarding season boundary dates is considered in the model. An extensive review of data sources was carried out to obtain the best available descriptions of the different ice parameters. The review covered environmental ice parameters such as ice thicknesses, velocities and geometric characteristics, as well as the mechnical behaviour and properties of ice. The data was then analyzed and used to fit probability distributions to each parameter.

Appropriate ice-structure interaction models were used for each combination of loading scenario and structural geometry. New models were developed in cases where the available models were not adequate for the purposes of a probabilistic study. These developments included an overall discrete ice feature interaction model for multi-year floes and ice islands. The model is an energy dissipation model which considers the influence of first-year ice behind the ice feature, and is applicable for both vertical and conical structures by using appropriate local force models. Multi-year ridges are incorporated in this model by changing the local ice geometry to account for the presence of the ridge. Other developments in ice structure interaction included the application of the reference stress method to the calculation of level ice loads on a cylindrical structure fully embedded in the ice, at low velocities.

Different extremal models were used to determine the probability distributions of the annual maximum loads. In most cases, these models lead to closed form solutions which result in significant reductions in the required computation effort. Discrete interactions such as ice island, multi-year floe and first-year ridge impacts were treated as a compound Poisson process. Loads from first-year level ice were treated as continuous random processes for the winter season where a full ice cover exists, and as interrupted processes for the break-up season where patches of open water are present in the ice.

The methodology was combined in a fully interactive computer package (BOREAS). The package is designed such that the user can input the appropriate environmental descriptions and ice mechanical properties for the considered location to obtain site specific results for the structure under consideration. Te package has default values for all parameters but the user can change the distribution type and statistical parameters for any desired ice parameter. The program offers flexibility regarding the input parameter values and distribution types, including the option of describing any parameter by a set of data points without using a mathematical distribution. The program has thorough data checking, and convenient data retrieval options. Besides, producing site specific results, the program can be used to carry out sensitivity analyses to determine the most important ice loading scenarios and parameters.

TABLE OF CONTENTS

Page

NOTATION

a	=	acceleration
B	=	ice feature dimension perpendicular to its direction of motion
C	=	ice concentration
D	=	diameter
E	=	modulus of elasticity
$f_X(x)$	=	probability density function of X
F	=	force
F_H	=	horizontal force
F_V	=	vertical force
$F_X(x)$	=	cumulative distribution function of X
H	=	ride-up height on conical structure
I	=	moment of inertia
ℓ_c	=	characteristic length
m	=	mass
n	=	number of events
$Pr(\bullet)$	=	probability of occurrence of $(\bullet)$
R	=	density of ice features per unit area
T	=	time
V	=	velocity
V_{cr}	=	failure vertical load
w	=	weight
W_s	=	width of structure
X_i	=	peak load during event i
Y	=	extremal load $(\text{Max}\{X_i, i=1,2,\ldots\})$
Z	=	section modulus
α	=	orientation of ice feature
γ	=	specific weight
δ	=	coefficient of variation
ϵ	=	strain

$\dot{\epsilon}$	=	strain rate
λ	=	rate of occurrence
μ	=	mean
ν	=	Poisson's ratio
σ	=	standard deviation

Chapter 1

INTRODUCTION

The present report is the result of a joint industry study carried out for the following participants:

Arco Oil and Gas Company
Conoco Inc.
Elf Aquitaine Petroleum
Gulf Canada Resources Inc.
Ishikawajima-Harima Heavy Industries Ltd.
Kajima Corporation
Minerals Management Service
Mobil Research and Development Corporation
Norwegian Contractors
Sohio Petroleum Company/BP Alaska Exploration Inc.
Taisei Corporation
Tecnomare S.P.A.
Union Oil Company of California

The study was carried out by Det norske Veritas (Canada) Ltd., with the assistance of Mr. D.F. Dickins of D.F. Dickins Associates Ltd., Vancouver, B.C., who provided much of the environmental data used in the study, and Mr. K.R. Croasdale of K.R. Croasdale and Associates Ltd. who advised the project team in the area of ice-structure interaction.

The geographical area of concern is the Beaufort Sea, along the Canadian and Alaskan coast, up to water depths of 60 m (200 ft.) - Figure 1.1. The methodology is, however, general enough to be of use for other areas as well. This study was motivated by the need for ice load models applicable to the selection of design criteria which satisfy reasonable safety requirements at the optimal level of economy for structures in the Beaufort Sea. This objective has been approached by applying probabilistic methods which have been successfully used to achieve optimal designs in numerous areas of structural engineering. A comprehensive probability-based model has therefore been developed for global ice loads resulting from the different ice-structure interaction scenarios encountered in the Beaufort Sea. These include movements of landfast ice, impacts with multi-year floes and combinations of multi-year and first-year ice.

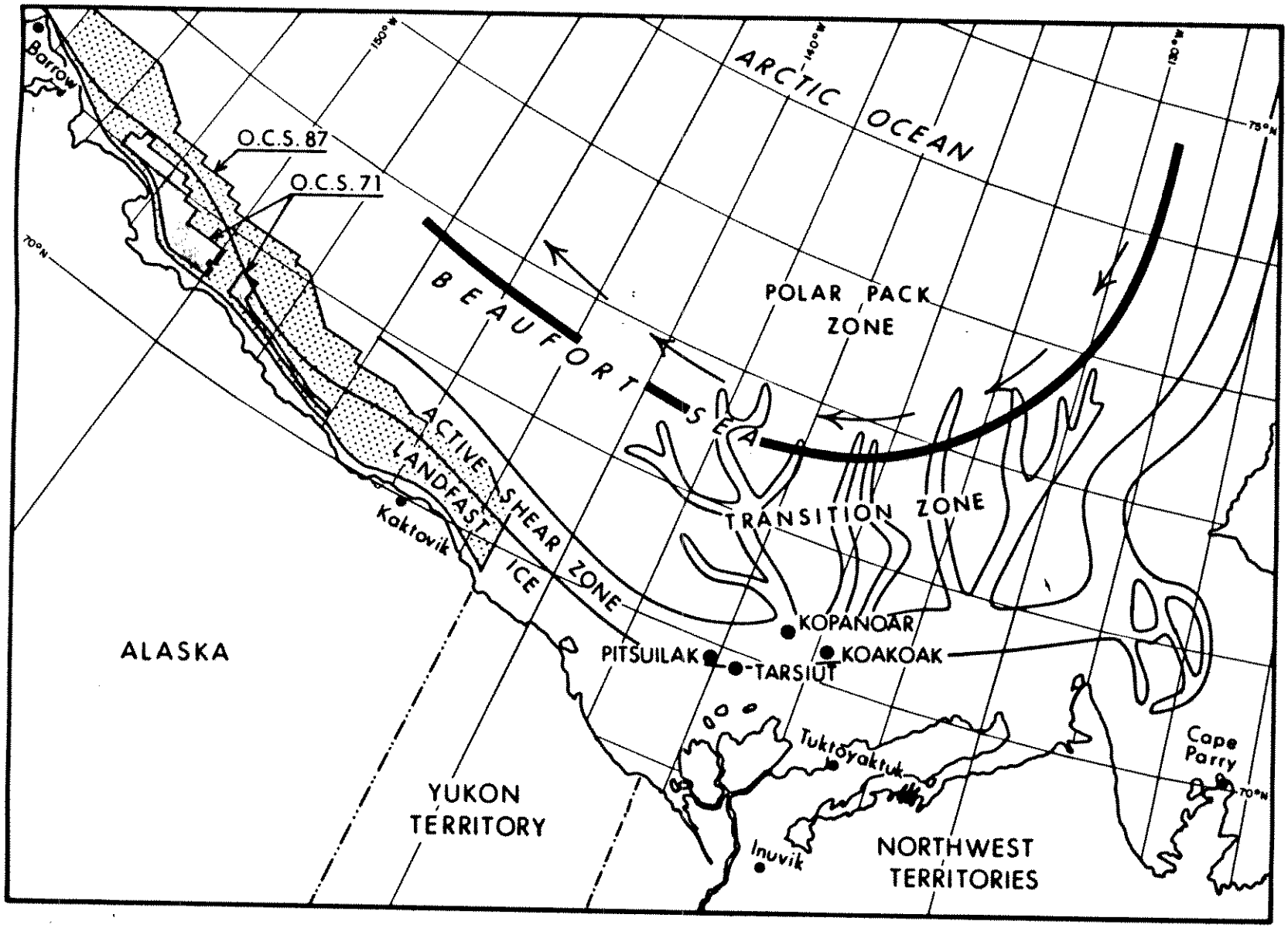

Figure 1.1. Winter Ice Conditions in the Beaufort Sea
(based on EIS for hydrocarbon development in the
Beaufort Sea - Mackenzie Delta region)

A schematic representation of the approach is shown in Figure 1.2. A series of scenarios (as defined in Section 2.3) are considered. These are analyzed separately and later integrated into an extreme load analysis algorithm. An important feature of the developed model is its modular form. The statistical treatment of each load scenario and the ice-structure interaction model for each type of interaction are dealt with in separate modules, which can be amended without affecting other modules at later stages. In fact, the model is designed such that the user can replace a certain module with a relatively minor effort.

The maximum load resulting from a certain ice-structure interaction scenario in a given period of time depends on the environmental parameters relating to this scenario. For multi-year floes, for example, the maximum load depends on the ice concentration, floe diameter, velocity, thickness and mechanical properties. These parameters are all uncertain and are, therefore, modelled probabilistically based on environmental ice data. There is an added uncertainty, due to variations in the length of the season during which a scenario is applicable. This uncertainty affects the extremal analysis, as will be discussed in Sections 3.7 and 3.8, and is taken into account in the model.

The probabilistic modelling of the ice load environmental input parameters is the first step in dealing with each scenario, as illustrated in Figure 1.2. These models are then used with an appropriate ice-structure interaction model, in a Monte Carlo simulation to produce a probabilistic description of the load during an interaction event. The latter is then used in an appropriate extremal model to obtain the probability distribution of the maximum load resulting from the scenario under consideration in the specified time period. As mentioned eralier, the maximum load distributions for different scenarios can be later combined to produce the final extreme load distribution for any combination of scenarios. These extremal distributions can be expressed in different formats, such as the probability of load exceedance or the return period relationship, and used to choose appropriate design loads.

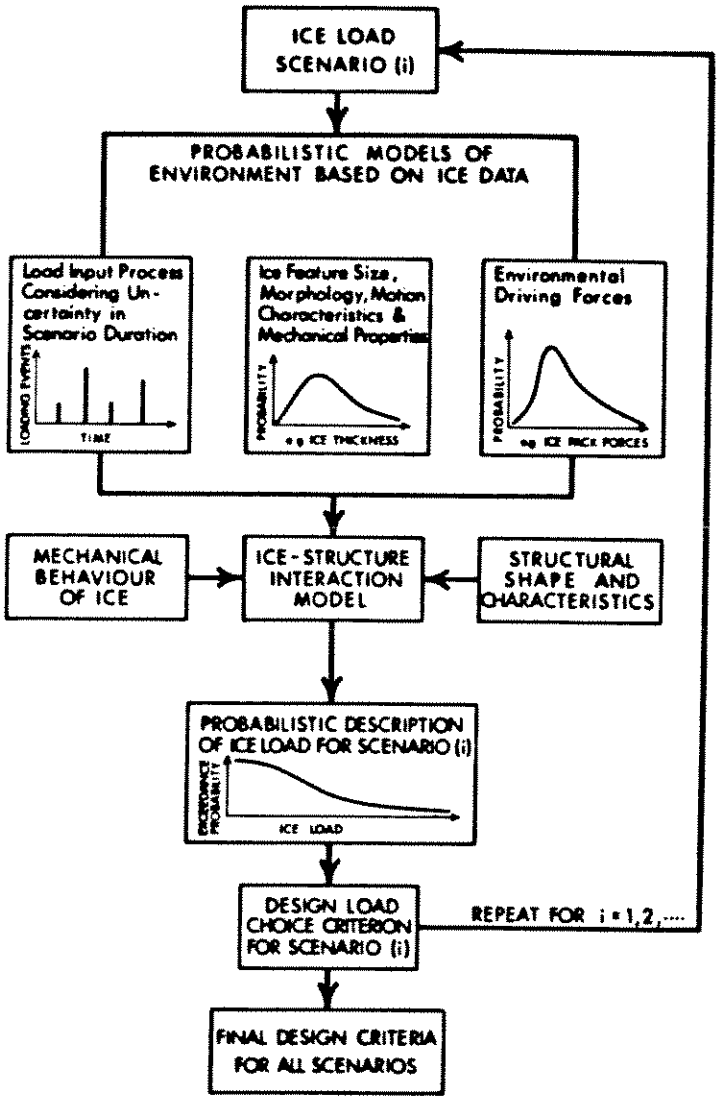

Figure 1.2

Overall Approach

A computer package (BOREAS) was developed to perform the analysis discussed above. The package, for which a user's guide is described in Volume II of this report, consists of three separate programs for pre-processing, computing, and post-processing. The pre-processor is used to create an input file which contains a definition of the seasons and load scenarios to be considered, as well as all the required environmental parameters, ice mechanical properties, and structural parameters. This program is fully interactive and contains default values which can be used or modified by the user. The main program performs the analysis for the user-defined scenarios and creates a database and output files which contain the results. The post-processor, which is also interactive, allows the user to extract the results for any load scenario or combination of scenarios in the desired format. The program is structured with data-retrieval features, such as back-up files and restart options, in order to minimize the cost of running. Safety features such as data checking and parameter bounds are also implemented.

The results of the model are demonstrated by example runs in Chapter 6. Both the model and the computer program give good results, which are directly applicable to the choice of design loads for fixed arctic structures.

Chapter 2

HAZARD IDENTIFICATION

2.1 Ice Conditions

The study area for this project covers both the U.S. and Canadian parts of the Beaufort Sea, as shown in Figure 1.1. Ice conditions within this area vary spatially and temporally, as detailed in Chapter 4 of this report. A general description of ice conditions is given in this section as background information for the characterization of the problem. The polar pack rotates continually in a clockwise direction in the Beaufort Gyral, carrying old ice from east to west through the Beaufort Sea. Multi-year ice in nearshore waters, say less than 90 m depth, originates from the polar pack, the boundary of which is normally north of 72 degrees latitude.

The rate of movement of ice is at its maximum during the summer (open water) season, at which time floes can move at speeds up to about 1 meter per second. After freeze-up, which usually occurs in October, the rate of movement decreases to an average of less than a third of the open water average. There is also first-year ice coverage, increasing in thickness during the winter and decreasing at later dates as the break-up season approaches.

As a result of the distinctive seasonal characterics of the ice within the Beaufort Sea, the ice conditions were described according to the season and location in the Beaufort Sea. These seasonas and scenarios within each season are described in detail in Sections 2.2 and 2.3. The ice parameters are characterized in Chapter 4 of the report.

2.2 Seasons and Season Boundaries

In order to estimate the length of each season, it is necessary to define suitable criteria to describe the boundaries between each of the three seasons. The situation is illustrated in Figure 2.1. The boundaries between different seasons should be defined,

SEASONAL VARIATIONS

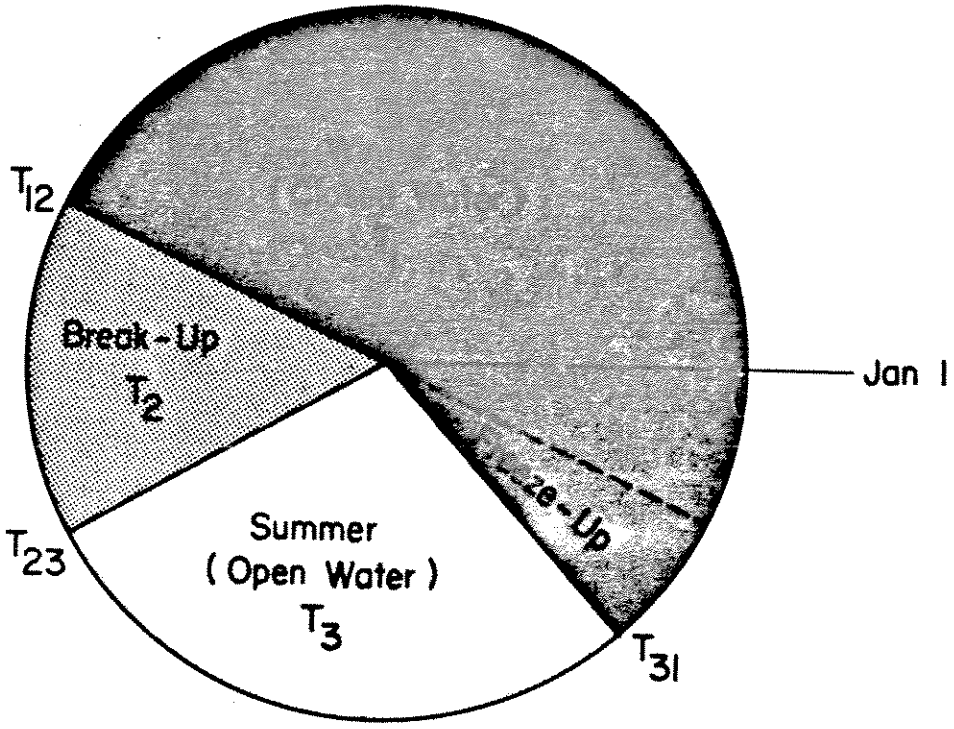

$$T_1 = T_{12} - T_{31}$$

$$T_2 = T_{23} - T_{12}$$

$$T_3 = T_{31} - T_{23}$$

Figure 2.1. Illustration of the Season Length and Season Boundary Models

such that the ice conditions within each season are similar from the point-of-view of ice-structure interaction. The criteria for the beginning of each season were defined as shown in Table 2.1.

TABLE 2.1

Definitions of season boundaries

SEASON	BEGINNING
Summer	$\leq$ 30% of first-year ice remaining.
Winter	80% of first-year ice is white ($\geq$ 30 cm thick).
Break-up	$\leq$ 80% of first-year ice remaining.

It is noted that the dates at which the season transition criteria are satisfied will vary from year to year. This is illustrated in Figure 2.2 for the Canadian Beaufort Sea, with an illustration of the possible load scenarios in each case. Season boundary dates are modelled probabilistically (see Section 4.2.1), and these models are used to derive probability distributions of the season lengths, as will be discussed in Chapter 6.

2.3 Ice Load Scenarios

One of the most important steps in the present analysis is the identification of the scenarios to be considered. The scenarios are defined so that the ice=structure interaction calculation methods are common to each scenario.

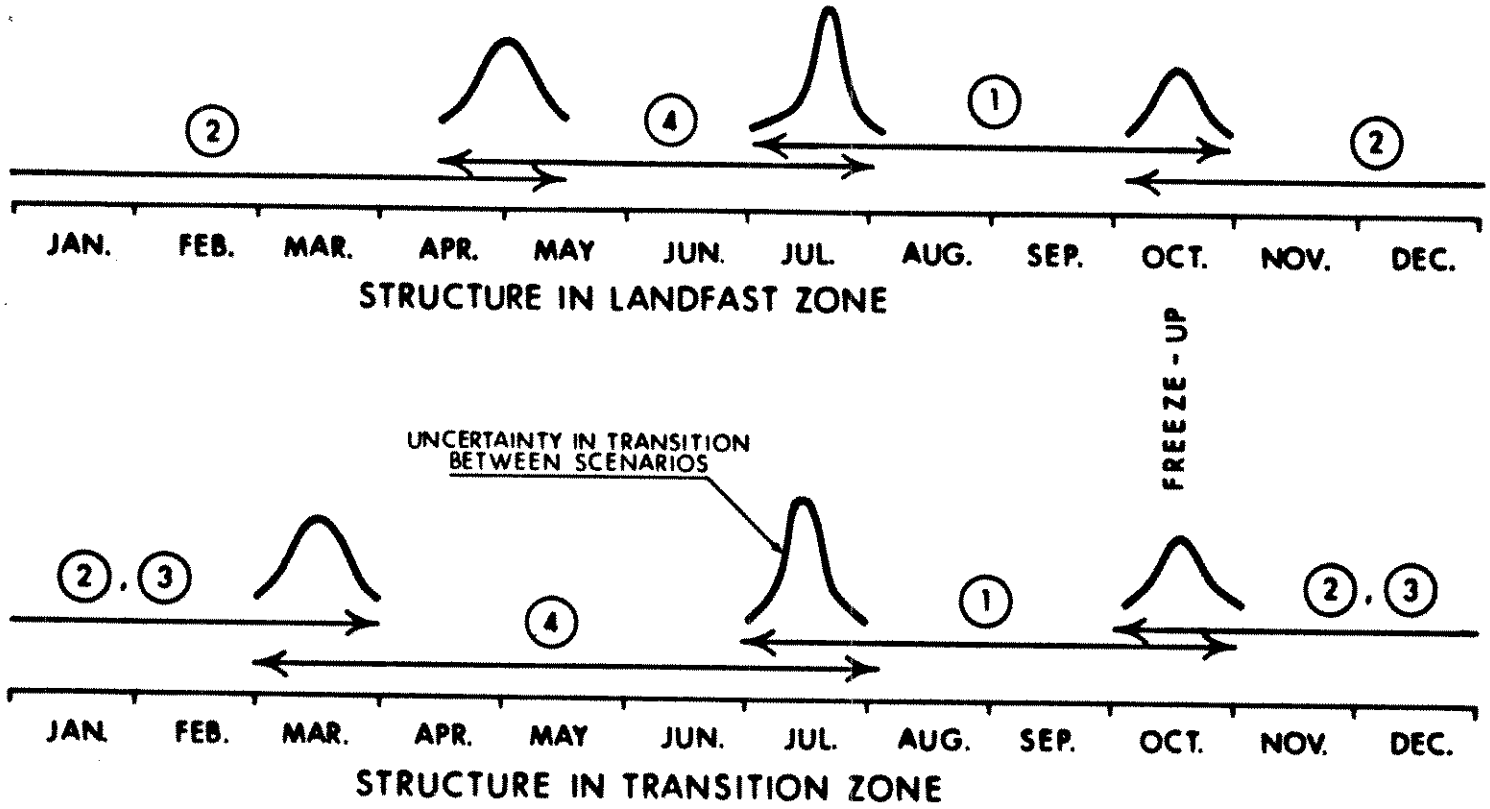

(1) OPEN WATER COLLISIONS.

(2) MOVEMENT OF FULL FIRST-YEAR ICE COVER (INCLUDING FIRST-YEAR RIDGES).

(3) MULTI-YEAR FEATURES EMBEDDED IN FIRST-YEAR ICE

(4) PARTIAL ICE COVER.

Figure 2.2. Illustration of the Uncertainty Regarding Season Boundaries and Season Lengths

The identification of appropriate load scenarios is related to the ice conditons which may occur during different seasons at the locaton of interest. In order to forecast the loads resulting from any scenario, a set of input parameters which determine the frequency and severity of the scenario should be estimated. Table 2.2 shows the agreed categorization of load scenarios according to the season and the water depth. The table includes a list of the environmental parameters required for the statistical and ice-structure interaction models selected for each scenario (see Chapter 5). The basic scenarios are illustrated in Figure 2.3.

It is noted that interactions with discrete features such as first-year ridges and multi-year floes are not considered in the landfast zone in the winter. This was based on a study of the patterns of movement of landfast ice, as is detailed in Appendix A. It was found that the net movement of the landfast ice cover is typically very small (in the order of a few meters per season), and therefore the probability of encountering a discrete feature is very small. On the other hand, even if an interaction occurs, the penetration of the structure into the feature will be small, and high loads will not develop. The results of the calculations substantiating this conclusion are given in Appendix A.

The manner in which the different scenarios are dealt with in the model is shown in Figure 2.4. The ice-structure interaction scenarios grouped on a seasonal basis in Table 2.2 (the top of Figure 2.4), can be regrouped into three major categories on the basis of similarities in the interaction process, as shown in the bottom of the Figure. These models are:

1. Areal feature interaction, covering ice islands in the summer, and multi-year floes during all seasons. Multi-year ridges are considered as part of the multi-year floe in this model. This is based on the random floe model, which was developed to investigate the probability of ridge encounters during a floe interaction. Details of this model are given in Appendix B, and are discussed further in Section 5.3.1.

TABLE 2.2

Load scenarios and required parameters

SEASON	WATER DEPTH	SCENARIOS	PARAMETERS
Winter	Less than 30 metres	(1) Landfast Ice Movement	
		- FY level ice (full cover) Figure 2.3-2	- Frequency of movement events (including the frequency and duration of a break-off event*) - Average duration of break-off events - Ice thickness - Peak movement speed - Creep law constants - Ice pressure
	Greater than 15 metres	(2) Pack Ice Movement	
		- FY level ice Figure 2.3-2	- Ice thickness - Creep law constants - Ice pressure - Ice flexural resistance - Ice elastic modulus - Ice Poissons's ratio - Creep-crushing transition
		- FY ridges in level ice Figure 2.3-2	- FY ridge concentration - FY ridge length - Ice velocity - FY ridge height - FY ridge cross section geometry - Rubble cohesion - Rubble friction angle - Creep-crushing transition strain rate

Table 2.2 (continued)

SEASON	WATER DEPTH	SCENARIOS	PARAMETERS
		- MY ice in FY level ice Figure 2.3-3	- MY floe density - Ice velocity - Ice movement direction - MY floe diameter - MY floe thickness - MY floe shape - MY ridge height - MY ridge orientation - MY ridge length - MY ridge cross section geometry - FY ice thickness - Eccentricity - Added mass - MY ice pressure - FY ice pressure - Ice flexural resistance - Ice elastic modulus - Ice Poisson's ratio
(Break-up)	All depths	(3) Movement of Partial Ice Cover	
		- FY level ice (partial cover) Figure 2.3-1 - FY ridges in level ice Figure 2.3-4 - MY ice in FY level ice	- As for pack ice movement - FY ice concentration

Table 2.2 (continued)

SEASON	WATER DEPTH	SCENARIOS	PARAMETERS
Summer	All depths	(4) Multi-year Floe Impact Figure 2.3-1	- Ice density - MY floe velocity - MY floe size (mass) - MY floe thickness (mass) - MY floe shape - MY ridge height - MY ridge orientation - MY ridge length - MY ridge geometry - Eccentricity - Added mass - Ice pressure - Ice flexural resistance - Ice elastic modulus - Ice Poisson's ratio
	Greater than 30 metres	(5) Ice Island Impact Figure 2.3-1	- As above for ice islands

* Break-off of a portion of the landfast ice from the rest of the ice cover. This portion may subsequently move at higher rates than those characteristic of landfast ice.

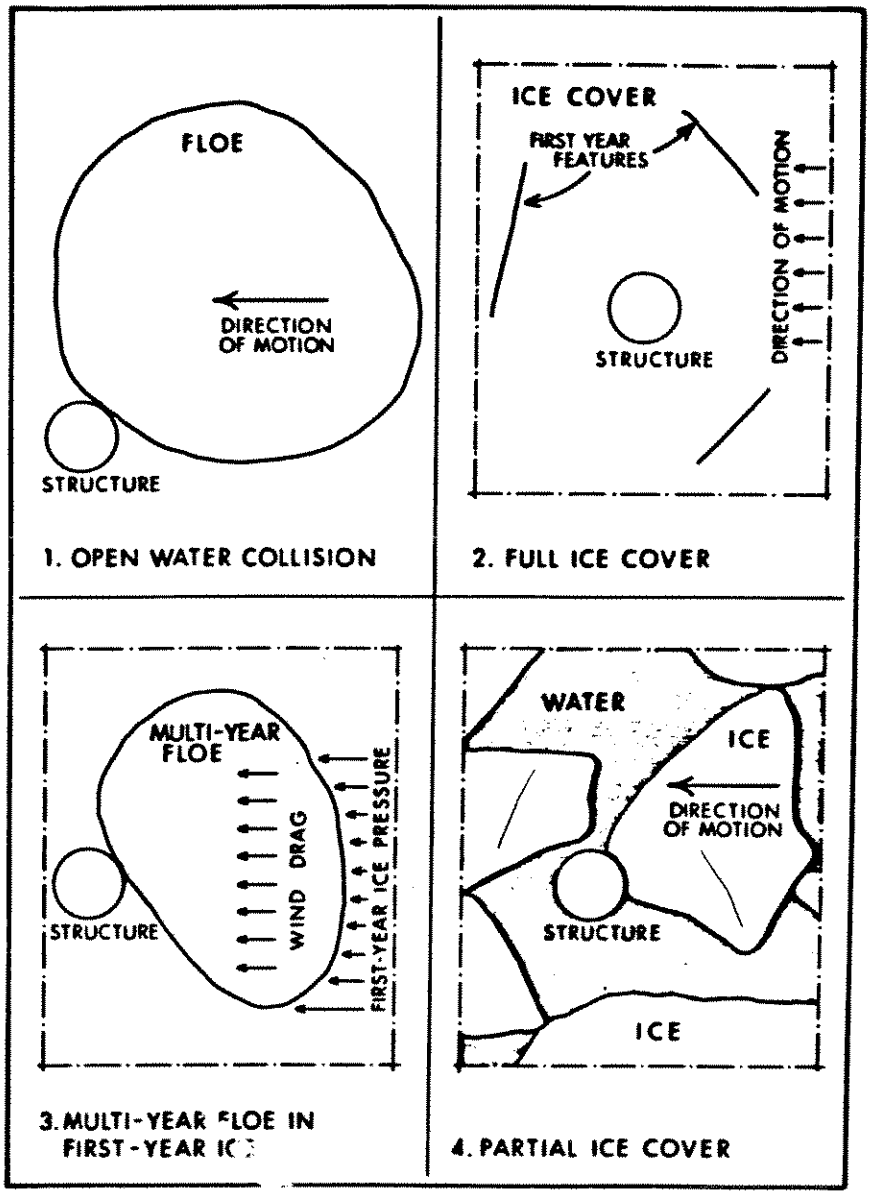

Figure 2.3. Schematic Representation of Main Ice Load Scenarios

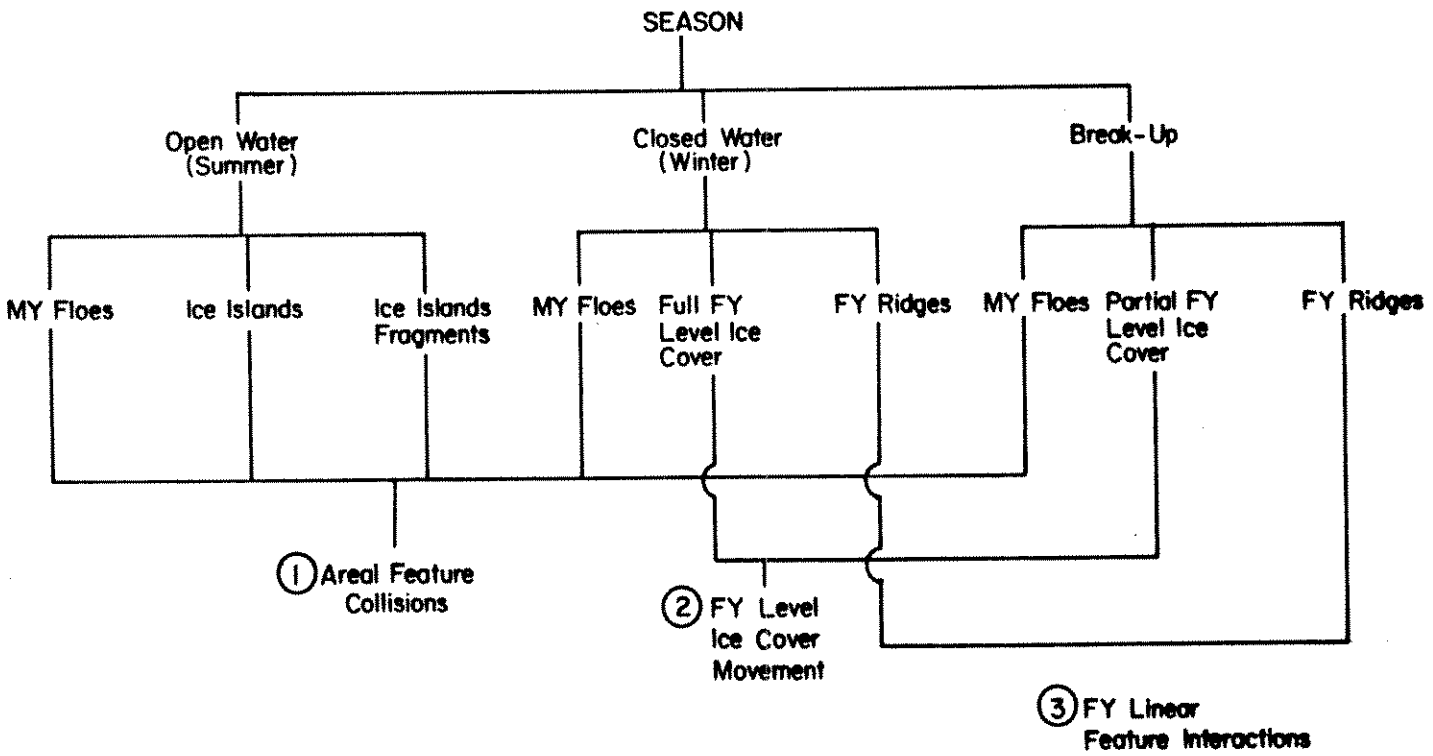

Figure 2.4. Categorization of Ice Load Scenarios With Respect to Ice-Structure Interaction Models

2. Movement of first-year level ice, which covers both the landfast and the active ice zones in the winter closed-water and break-up seasons.

3. First-year linear feature interactions which during the winter closed-water season in the active ice zones, and the break-up season in all zones.

2.4 Structural Geometries

The structural geometries considered in the study are as follows:

(i) Vertical-sided structures with cylindrical sides (i.e. circular in plane) or flat sides (i.e. polygonal in plan). The polygon can have up to 20 sides, and can be defined by the coordinates of its apexes with respect to an arbitrary set of axes through its centre. The polygon must be concave with respect to its centre.

(ii) Upward and downward breaking cones.

Chapter 3

PHILOSOPHY AND APPROACH

3.1 Decision-making Under Uncertainty

Information on the appropriate probabilistic models in the structural design process can be used in a wide range of contexts. These could consist of general design questions, such as choice of structural system, or for formulating design loads. The overall approach is shown on the decision trees of Figure 3.1. The focus of the present report is to develop the relevant probabilistic information pertaining to global ice loads for fixed offshore structures in the Beaufort Sea. This information can be obtained in several forms, and is therefore useful for a variety of purposes. The end use will not be discussed further here, since this is beyond the scope of the present report.

One of the consequences to be considered in structural design is safety, and design generally involves the trade-off between safety and economy. This might include strategies such as evacuation in the presence of an ice island (for example) - and again consideration of such aspects can flow from the results of the present work.

It is generally acknowledged that absolute safety is not a realistic objective. Rather, the question of risk to a structural system should be considered, and this involves two aspects:

- probability of the undesirable event, failure in the present cases; and
- consequences of the undesirable event.

For the purposes of the present work, attention is focussed on the first of these aspects, and specifically on the determination of the probability distribution for load - curve A in Figure 3.2. It is considered useful to outline the methods for the calculation of failure probability.

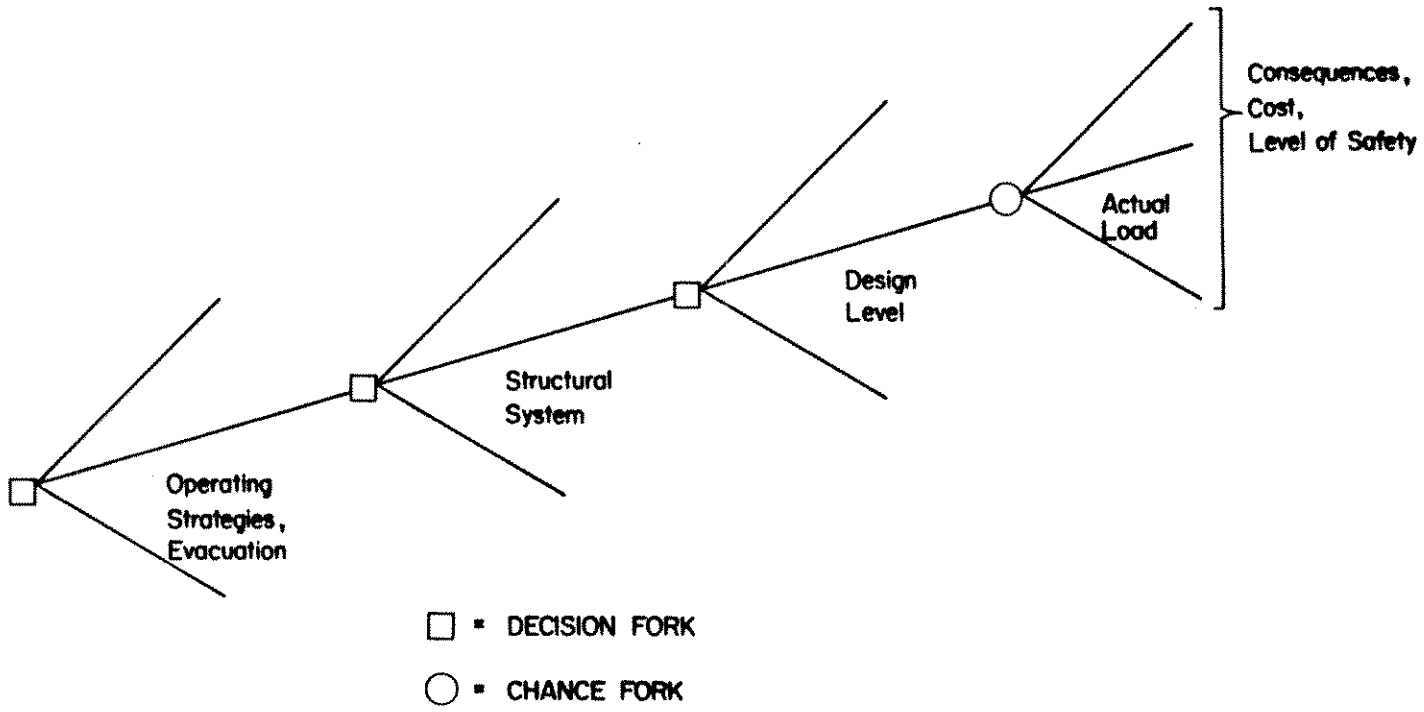

Figure 3.1. Illustration of the Use of Decision Theory to Make Design and Operation Decisions

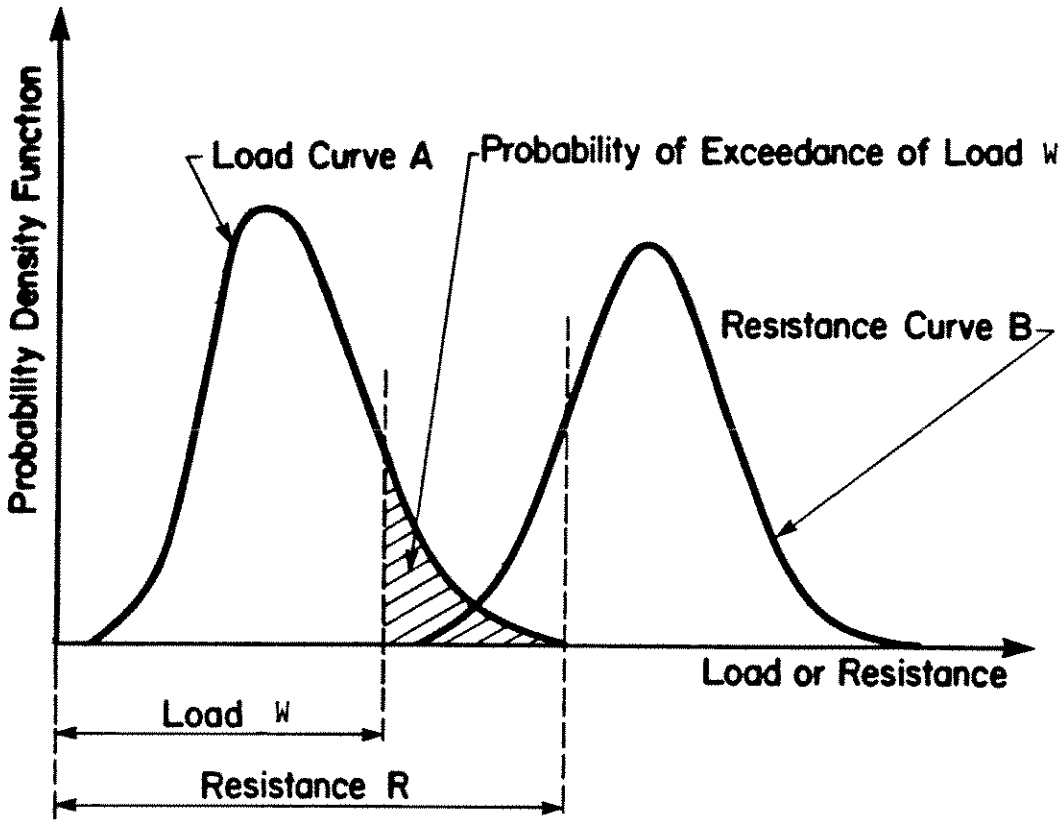

Figure 3.2. Illustration of the Calculation of the Probability of Failure

3.2 Probability of Failure and Reliability

The reliability of a structure, component or system, is generally defined as $(1 - p_f)$, where p_f is the probability of failure. We shall therefore concentrate on the evaluation of p_f. In Figure 3.2, let W represent load and R resistance. These could be the lateral ice loads on a Beaufort Sea structure, and the lateral resistance to sliding, respectively. The probability density functions (pdf) for W and R are denoted $f_W(w)$ and $f_R(r)$, respectively. To evaluate the failure probability, consider the random quantity

$$Z = R - W \tag{3.1}$$

with probability density function $f_Z(z)$.

Failure occurs if Z is negative, i.e. $R < W$. Therefore,

$$p_f = \int_{-\infty}^{0} f_Z(z)\, dz. \tag{3.2}$$

Now $f_Z(z)$ can be obtained from $f_W(w)$ and $f_R(r)$ by the following convolution integral:

$$f_Z(z) = \int_{-\infty}^{\infty} f_R(x)\, f_W(x-z)\, dx \tag{3.3}$$

where x is a common (dummy) variable measuring load or resistance. The derivation of (3.3) is standard, and is based on the assumption of independence of load and resistance.

Therefore,

$$p_f = \int_{-\infty}^{0} \int_{-\infty}^{\infty} f_R(x)\, f_W(x-z)\, dx dz \tag{3.4}$$

This integral is not readily evaluated in closed form, except in special cases which are not of practical importance. However, numerical integration can always be seen as an alternative provided this level of detail is required.

Cases in which the failure probability can be evaluated using standard normal tables include the case of two normal, and two lognormal distributions. In the former case, let the means and variances be (μ_W, σ_W^2) and (μ_R, σ_R^2) for W and R respectively. Then $Z = R - W$ is also normal $(\mu_R - \mu_W, \sigma_R^2 + \sigma_W^2)$ based on our assumption of independence, and p_f is the value of the cumulative distribution function (CDF) corresponding to the value $Z = 0$.

For lognormal random quantities, it is easier to consider:

$$Z = R/W. \tag{3.5}$$

Let the means and coefficients of variation ($\delta_W = \sigma_W/\mu_W$ and $\delta_R = \sigma_R/\mu_R$) be (μ_W, δ_W) and (μ_R, δ_R) for W and R respectively. Then the logarithm of Z is normal with mean and variance equal to:

$$\mu_{\ell nZ} = \ell n\left(\frac{\mu_R\ (1 + \delta_W^2)^{1/2}}{\mu_W\ (1 + \delta_R^2)^{1/2}}\right), \tag{3.6}$$

$$\sigma_{\ell nZ}^2 = \ell n\left((1 + \delta_R^2)(1 + \delta_W^2)\right). \tag{3.7}$$

Consequently, the probability of failure is equal to:

$$p_f = Pr\ \left(\frac{R}{W} < 1\right) = Pr\ (\ell nZ < 0), \tag{3.8}$$

which is the value of the normal CDF at $\ell nZ = 0$.

Numerical techniques to determine the reliability of a component or structure are widely used. Level II reliability methods are extremely powerful in the case of multi-dimensional failure spaces: instead of just two random quantities (load and resistance), there are many more, for example, scantlings, material properties, loadfactors, and model uncertainties. For complex systems, Level II methods are superior to Level III methods, based on an "exact", but lengthy, probabilistic analysis,

using a full-distributional approach. Among the important Level II algorithms, is the popular first-order second-moment methods (Cornell, 1969). In the DnV program, PROBAN, for example, on an adequate value of p_f, is found by linear approximation of the normal transformation of a user-defined limit-state function.

Level III methods are limited to relatively simple systems and are based on numerical integration and Monte Carlo algorithms. When only two random quantities are in play, the Level III method boils down to a numerical solution of equation (3.4), as performed by the DnV program PROF for four arbitrary probability distributions.

The result of the calculation of p_f can be quite sensitive to the distributions used. Figure 3.3 (Lind and Davenport, 1972) shows the wide variation of p_f at different values of nominal safety factor (mean resistance $\div$ mean load) for various distributions of R and W. Therefore, it is important to study the underlying process - one of the motivations for the present study.

3.3 Statistical Analysis of Ice Loads

3.3.1 General

In most cases of Arctic environment, the loads imposed by floating ice can be considered to be a series of discrete events, e.g. arrivals of ice floes or ice islands. Even in the case of landfast ice movement, these can be taken to be the result of a series of discrete events such as storms or sudden changes in temperature.

Before proceeding to a detailed analysis of ice loads, it is useful first to review the approach to the study of extremes for waves. Here, the practice is to consider short-term sea states, in which certain parameters (H_s, significant wave height; $\bar{T}$, the average wave period) are considered as constant. The maximum wave height during the duration of such a stationary sea state is then calculated. Subsequently, long-term sea states vary in time. The result of this could, for example, be represented in a joint probability distribution of H_s and $\bar{T}$. These results are then used to compound the

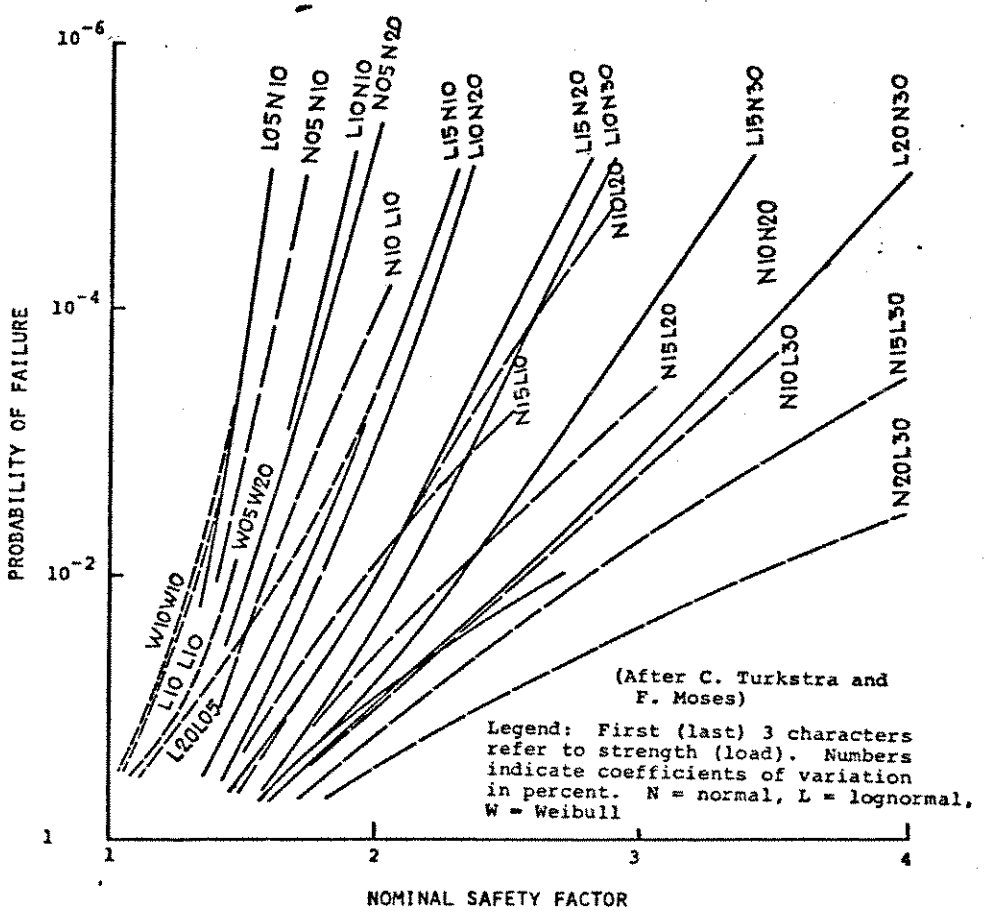

Figure 3.3. Probability of Failure as a Function of Distribution and Nominal Safety Factor

results for short-term sea states to obtain distributions of maximum wave heights over the long-term. An extremal distribution, i.e. of the maximum wave height, can also be derived.

The approach to ice loads is similar in several respects. For example, the numbers of arrivals of multi-year ice floes at a structure is proportional to the multi-year ice concentration, C. Now C will vary significantly from one season to another, so that for a long-term statistical assessment, the results for a given C = c must be compounded by the probability distribution of C.

The similarities between ice loads and other environmental loads should not be over-emphasized. The approach has been followed of modelling the ice-load scenarios from first principles.

3.3.2 Discrete arrival process

Generally, a quantity that varies randomly in time can be modelled by means of a stochastic process. This can be either a continuous parameter process, or a discrete parameter process. In the former, the continuous time axis is used as a time parameter, whereas in the latter, the value of a random quantity is specified at fixed points in time, e.g. the end of each month. As was pointed out in Section 3.3.1, many events such as arrivals of multi-year floes or ice islands, can be modelled as arrivals in time of load-events, as illustrated in Figure 3.4. After each arrival, there will be a random fluctuation in load, as illustrated in the figure. The first requirement of the present study is seen as the modelling of the main arrival process. Let the peak load within each arrival be X_1, X_2, X_3, ..., occurring at times t_1, t_2, t_3 ..., as shown in Figure 3.4. Then these arrivals can be modelled realistically by means of a Poisson process, with each of the arrival events E_1, E_2, E_3, ..., say, corresponding to a subsequent peak load, X_1, X_2, X_3, ...

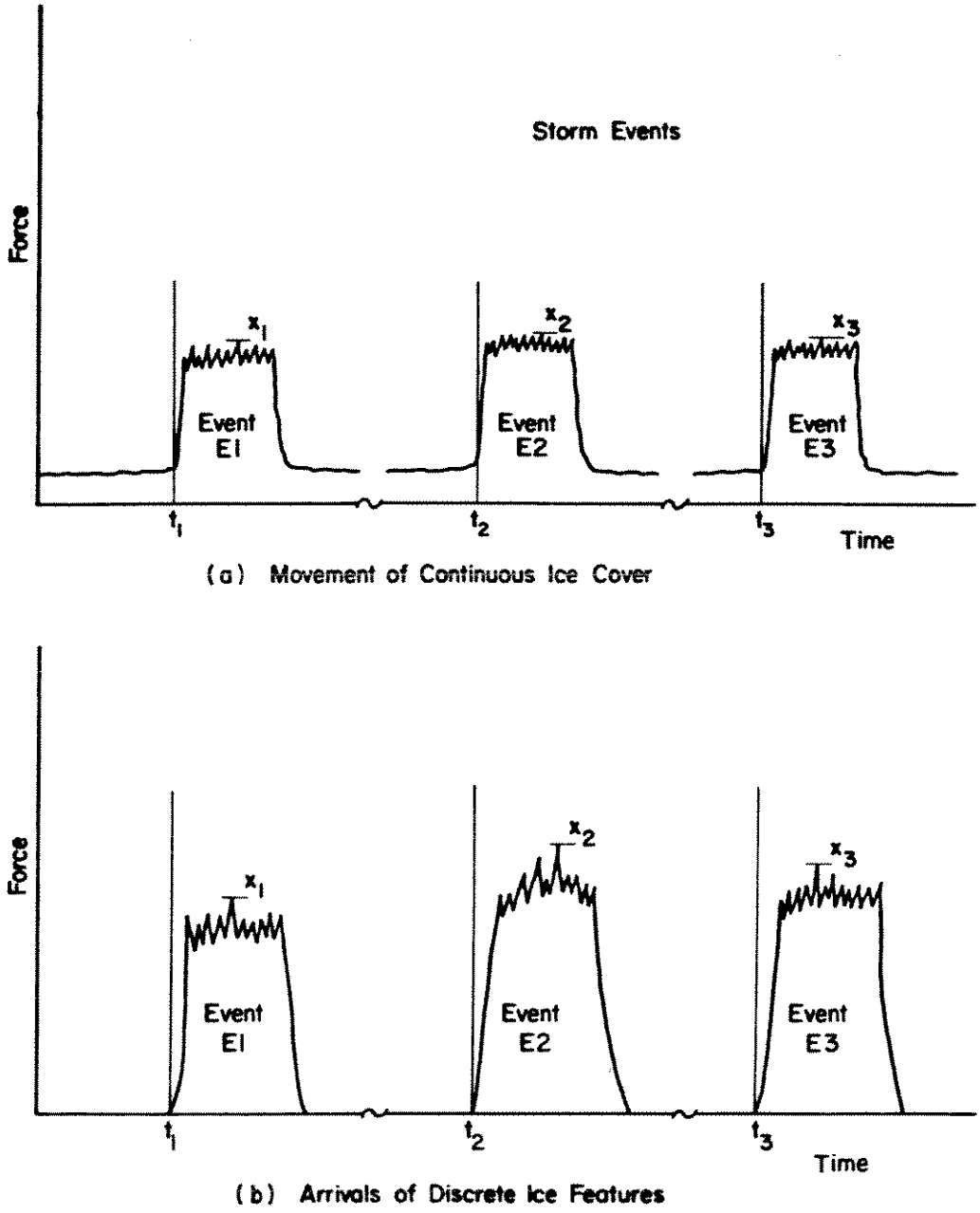

Figure 3.4. Schematic Representation of Discrete Arrival Processes

The Poisson process deals with a continuous time parameter, yet the individual arrivals are discrete. The use of this model can be justified on the basis of several arguments. The Poisson process is the limiting case for a binomial distribution, in which one considers a series of trials with probability of success at constant value p. Imagine each floe originating in the Arctic gyre as being a "trial". Then the binomial distribution gives the probability of n successes in m trials: $Pr(N=n) = b(n|m,p) = \binom{m}{n} p^n(1-p)^{m-n}$. In this and the Poisson distribution, the number of successes is random. In the limit, as $p \to 0$, but keeping the expected value $\nu = (mp)$ constant, we obtain the Poisson distribution:

$$Pr(N=n) = p(n|\nu) = \frac{e^{-\nu}\nu^n}{n!}, \quad n = 0,1,2,\ldots. \tag{3.9}$$

The process to the limit in this case appears to represent a reasonable model of the arrival at a fixed point (or small area) in the Arctic of various features (floes, ridges, ...).

The Poisson process is technically a random point process. This provides a mathematical model for a physical situation characterized by highly localized events occurring at random points in a continuum. In its usual form, it is a counting process in which the value $N_t = \sum_{\text{all } i} E_i$ is obtained for a given time, t, using the notation $E_i = 1$ for a "success" or occurrence and $E_i = 0$ for "failure". The summation is over possible (countable) points n. This is illustrated in Figure 3.5.

The rate of the Poisson process, λ, is illustrated in Figure 3.5. Although λ is often introduced as a constant, this is not a necessary assumption for the use of the Poisson process model. This fact is of great importance in the present study, because the arrival rate is proportional to concentration and velocity (for example), both of which vary continuously in time. The evaluation of the expected value, ν, or equivalently, the mean arrival rate $\bar{\lambda}$ will be dealt with in subsequent sections.

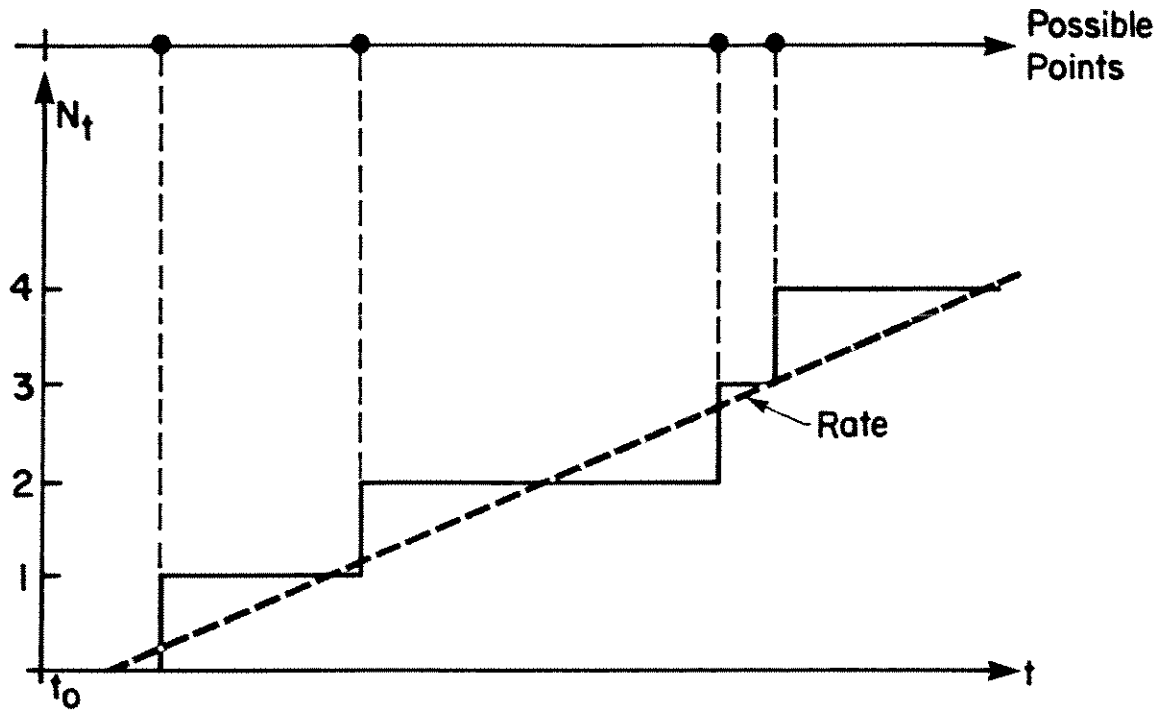

Figure 3.5. Illustration of the Poisson Counting Process

The formal assumptions underlying the Poisson distributions are as follows (Snyder, 1975):

(i) $\Pr(N_{t_o} = 0) = 1$

(ii) For times t in the interval $t_o \leq s < t$, the increment $N_{s,t} = N_t - N_s$ is Poisson distributed with parameter $\nu_t - \nu_s$:

$$\Pr(N_{s,t} = n) = \frac{(\nu_t - \nu_s)^n \, e^{-(\nu_t - \nu_s)}}{n!}$$

(iii) The increments in $\{N_t; t \geq 0\}$ are independent.

The function ν_t is a non-negative, non-decreasing function of t. The third condition above implies that the number of points in intervals that do not overlap are statistically independent, for any size or position of two intervals.

The Poisson distribution can be derived on the basis of general concepts (conditional orderliness, evolution without after effects), as in Snyder (1975). For our purposes, we need to recognize the nature of the process: independence and that the rate need not be constant. On the latter point, we can illustrate this property by considering a pseudotime, t', as follows. If the rate does vary with time, say $\lambda = \lambda(t)$, then we can transform $\lambda(t)dt \rightarrow \lambda dt'$, such that λ is constant in t'. The same Poisson distribution results in the two cases.

It should be noted that the Poisson distribution and process is appropriate even for a variable rate, but special attention has to be paid to the distribution of the time to the next event, or to the kth event, and so on. The formulae based on a constant rate (e.g. the Erlang distribution) will no longer apply.

The progression from a Poisson counting process to a compound Poisson process is relatively straightforward. We continue with the inhomogeneous Poisson process, but to each point where an increment occurs, we associate an auxiliary random quantity. This would, in our case, be the quantity of interest associated with the ice load-event (load, mass, velocity, kinetic energy). In the compound Poisson process, this will be sampled from a family of mutually independent, identically distributed (iid) random quantities. It is usual in this process to accumulate (add) the values of the auxiliary random quantity. Let the values be denoted $\{X_1, X_2, X_3, ..., X_i, ...\}$. Rather than the total $\sum_{\text{All } N=n} X_n$, we are interested in the maximum, i.e.

$$\text{Max } \{X_1, X_2, \ldots\ldots, X_i, \ldots\ldots, X_n\}. \tag{3.10}$$

It should be emphasized that the number of the entries X_n can be random, with a Poisson distribution of the random quantity N. The extremal problem associated will obtain the maximum value given by (3.10), and will be addressed in Section 3.7, Extremal Analysis.

3.4 Calculation of Expected Numbers of Arrivals

The analysis of the Poisson process described in Section 3.3 requires an estimate of the expected number of arrivals, ν or alternatively, the mean arrival rate, $\bar{\lambda}$, given by:

$$\nu = \int_0^t \lambda(s)\, ds = \bar{\lambda} t \tag{3.11}$$

where $\lambda(s)$ is the arrival rate (intensity), at time s, and t = total time under consideration.

3.4.1 Areal ice features

This subsection will be concerned with features such as floes or ice islands, as against lineal features (e.g. ridges). The ice feature is modelled as follows (see Figure 3.6):

B is the lateral dimension of ice feature, at right angles to velocity. B is random with probability density function (pdf), $f_B(b)$;

A is the area of ice feature, with pdf $f_A(a)$;

V is the velocity of the ice featre, with pdf $f_V(v)$;

C is the ice concentration (proportion of surface covered by ice category under consideration), with pdf $f_C(c)$;

Velocity and concentration can be correlated, with joint pdf $f_{C,V}(c,v)$;

R is the density of ice features, i.e. the number per unit area, with pdf $f_R(r)$; and

W_s is the width of the structure.

It should be noted initially that:

$$c = r \int a \, f_A(a) \, da = r\bar{a} \tag{3.12}$$

where $\bar{a}$ = mean area.

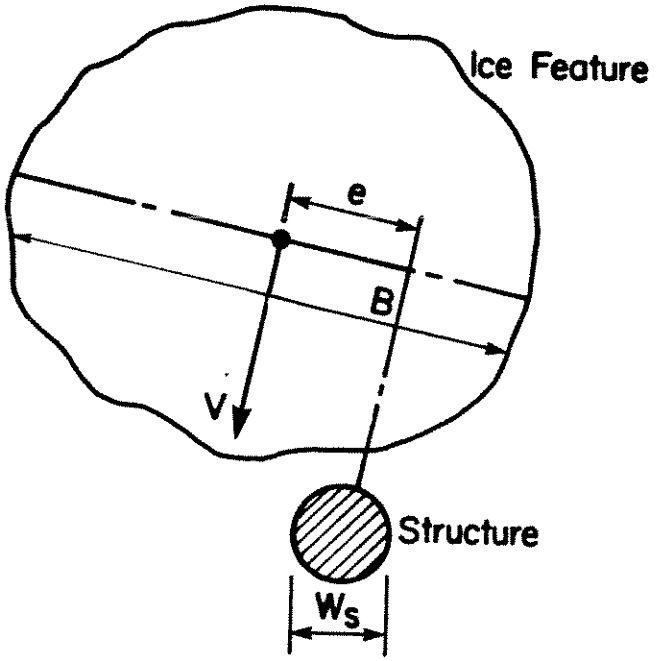

Figure 3.6. Areal Ice Feature Interaction Scenario

Then, for a short period of time, Δt:

$$Pr(collision) = \lambda(t)\Delta t = r(b + W_s)\, v\Delta t \tag{3.13}$$

If the probability distributions, $f_{C,V}(c,v)$ and $f_B(b)$ reflect the changing conditions during the total interval of time considered (e.g. concentration changes with time), then:

$$\bar{\lambda} = \iiint \frac{c}{a} (b + W_s)\, v\, f_{C,V}(c,v)\, f_B(b)\, dc\, db\, dv \tag{3.14}$$

in which we have assumed stochastic independence of B with respect to C and V (this assumption could be avoided if necessary).

Then:

$$\bar{\lambda} = \frac{\bar{b} + W_s}{a} \iint cv\, f_{C,V}(c,v)\, dcdv \tag{3.15}$$

or

$$\bar{\lambda} = \frac{\bar{b} + W_s}{a} (\bar{c}\,\bar{v} + \sigma_{CV}), \tag{3.16}$$

where the bars denote mean values and σ_{CV} = covariance between C and V. Note that $\sigma_{CV} = \sigma_C \sigma_V \rho_{CV}$, where ρ_{CV} is the correlation coefficient.

3.4.2 Linear ice feature

The methodology described in Section 3.4.1 for areal ice features is also applicable with slight modifications to linear ice features such as ridgs. It is noted that the development of the result in Eq.(3.16) does not require making any assumptions regarding the direction of ice movement. The methodology is therefore

equally applicable to summer ice load scenarios, where separate features move independently, and to winter cases, where the ice features all move in the same direction with the first-year ice cover. For a linear feature (i.e. a ridge), the width in a direction perpendicular to the direction of motion is given by (see Figure 3.7):

$$b = \ell \cos\alpha + w \sin\alpha, \tag{3.17}$$

where ℓ is the feature length, with pdf $f_L(\ell)$, w is its width with $f_W(w)$, and α is its orientation measured from the direction of motion. The average width $\bar{b}$ is therefore given by:

$$\bar{b} = \iiint (\ell \cos\alpha + w \sin\alpha)\, f_L(\ell)\, f_W(w)\, f_\Gamma(\alpha)\, d\ell\, dw\, d\alpha \tag{3.18}$$

Under the assumption of independence between L, W and α, and assuming that the angle α is uniformly distributed between 0 and π, Eq. (3.18) simplifies to:

$$\bar{b} = \frac{2}{\pi} (\bar{\ell} + \bar{w}) \tag{3.19}$$

An ice ridge is usually embedded in the surrounding level ice. The rate of interaction is therefore conditional on the presence of level ice. In other words, one is interested in the rate of interaction with a multi-year ridge during (i.e. given) interaction with a multi-year floe. The concentration C in this case represents the percentage of the area of level ice covered with ridges. Consequently, the correlation between C and V discussed in Section 3.4 for free-floating areal features is not applicable in this case. The average rate can be calculated by substituting $\bar{b}$ from Eq.(3.19) into (3.16), setting $\sigma_{CV} = 0$ in the latter and substituting $\bar{\ell}\,\bar{w}$ for $\bar{a}$. This leads to:

$$\bar{\lambda} = \frac{2\,\bar{c}\,\bar{v}}{\pi\,\bar{\ell}\,\bar{w}} (\bar{\ell} + \bar{w} + w_s) \tag{3.20}$$

Poisson Process ⟶ Rate λ

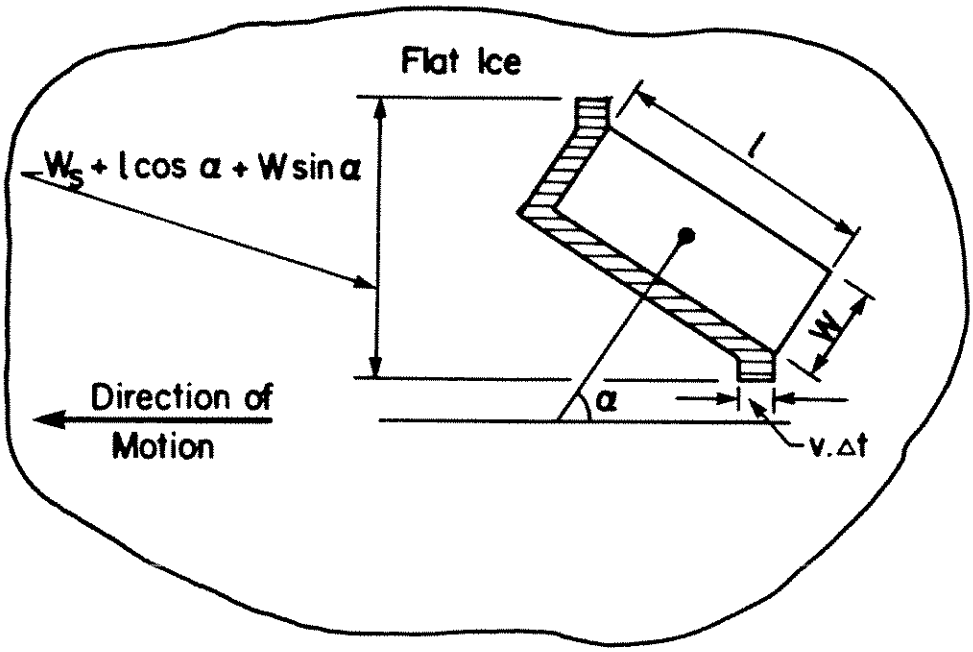

Assumtions :

- Features Randomly Positioned
- Features Randomly Oriented

$$\lambda = \frac{2}{\pi} d_r \bar{v} \left[\bar{l} + \bar{W} + W_s\right]$$

d_r = Number of Ridges Per Unit Area
$\bar{v}$ = Average Velocity
$\bar{l}$ = Average Ridge Length
$\bar{W}$ = Average Ridge Width
W_s = Width of Structure

Figure 3.7. Illustration of the calculation of the average interaction between a linear feature and the structure

3.4.3 High concentration of multi-year ice - congestion effects

This subject was investigated from two points of view: (1) the effect of correlation between concentration and velocity on arrival rates (as illustrated in the minutes of 3rd project meeting); and (2) queuing theory. The result of the first analysis showed that even a small (negative) correlation could have a marked effect on the arrival rates. The second is described in this section.

With regard to queuing theory, consider a queuing system where the structure represents the server. The ice floes (or features generally) arrive at the server. These wait if there is already a floe (cusomter) there. The server mechanism deals with the arrivals which eventually depart. We are interested in such aspects, as the number of floes (customers) in the waiting line (queue-length problem), for appropriate **arrival** and **service** processes. The rate of the arrival process λ was addressed in Sections 3.4.1 and 3.4.2. The serving time t in the present application is the interaction time before the clearing of the floe.

For a Poisson arrival process with rate λ, and an exponentially distributed serving time with mean μ_t, it can be shown that the probability distribution of the number of floes in the queue N, can be given by (Clarke and Disney, 1970):

$$P_N(n) = (1 - \frac{\lambda}{\mu_t})(\frac{\lambda}{\mu_t})^n, \qquad n = 0, 1, 2, \ldots \tag{3.21}$$

This equation was used with a range of reasonable values for λ and μ_t to assess the probability of having more than one floe in the queue at any given time. For an arrival rate of one floe every 30 minutes, for example, the probabilities of having more than one floe in the queue are .001 and .009 for average interaction times of 1 and 3 minutes, respectively. For a rate of one floe every two hours (which is more representative if very small floes are not considered), these probabilities are .0007, .0006, and .006 for average interaction times of 1, 3 and 10 minutes, respectively. This illustrates that multiple collisions are unlikely to be an important factor for multi-year floe interactions.

3.5 Generic and Updated (Collision-Conditional) Data

Environmental data that affects the collision probability must be specially treated in calculating the situation at the instant of collision. Examples of this are:

- diameter of an ice floe, since $Pr(I \mid B = b) \propto (b+w_s)$, and
- velocity of a floe or other feature, since $Pr(I \mid V = v) \propto v$,

in which I denotes the event "impact". To appreciate this kind of parameter, consider the "area swept out" by the ice feature per unit time. The diameter, or velocity, as in the examples above, lead to an enhanced probability, since this is an increasing function of the "area swept out", which in turn is directly proportional to diameter or velocity as noted above.

Now to the point: since larger or faster floes (or features generally) are more likely to collide, then floes that collide are more likely to be larger and faster. To illustrate this, consider the probability distribution of velocity for a floe chosen at random in the Beaufort Sea. Let this distribution be $f_V(v)$.

The distribution $f_V(v)$ will be termed **generic.** The **updated (collision-conditional)** distribution is denoted $f_{V|I}(v|I)$ and is deduced using Bayes' theorem as follows:

$$f_{V|I}(v|I) = \frac{f_{I|v}(I|v)\ f_V(v)}{N}$$

where N is a normalizing constant equal to :

$$\int_{all\ v} f_{I|v}\ f_V(v)\ dv. \tag{3.22}$$

Now $f_{I|v}(I|v) \propto v$, as noted above. Therefore,

$$f_{V|I}(v|I) = \frac{v\ f_V(v)}{\int v\ f_V(v)\ dv} = \frac{v\ f_V(v)}{N} \tag{3.23}$$

While we have used floe velocity V in the above example, the same methodology is applicable to other parameters such as floe diameter, circular floes, or more generally the dimension presented to structure (at right angles to velocity vector - Figure 3.6), as will be discussed later in this section.

A typical example of the above procedure is illustrated in Figure 3.8.

A case of particular usefulness is that of the gamma distribution; we take this to be as follows:

$$\gamma(v|\alpha, \beta) = f_V(v) = \frac{1}{\beta^{\alpha}\Gamma(\alpha)} v^{\alpha-1} e^{-v/\beta}, \qquad v \geq 0. \tag{3.24}$$

This distribution has been found to provide reasonable fits for velocity and diameter data. Now in this case, the updated distribution becomes:

$$f_{V|I}(v|I) = \frac{1}{\beta^{\alpha}\Gamma(\alpha)} v^{\alpha} e^{-v/\beta}, \qquad v \geq 0. \tag{3.26}$$

Now, the form $v^{\alpha}e^{-v/\beta}$ indicates a gamma distribution with parameters $\alpha + 1$ and β:

$$f_{V|I}(v|I) = \frac{1}{\beta^{\alpha+1}\Gamma(\alpha+1)} v^{\alpha} e^{-v/\beta}, \quad v \geq 0. \tag{3.27}$$

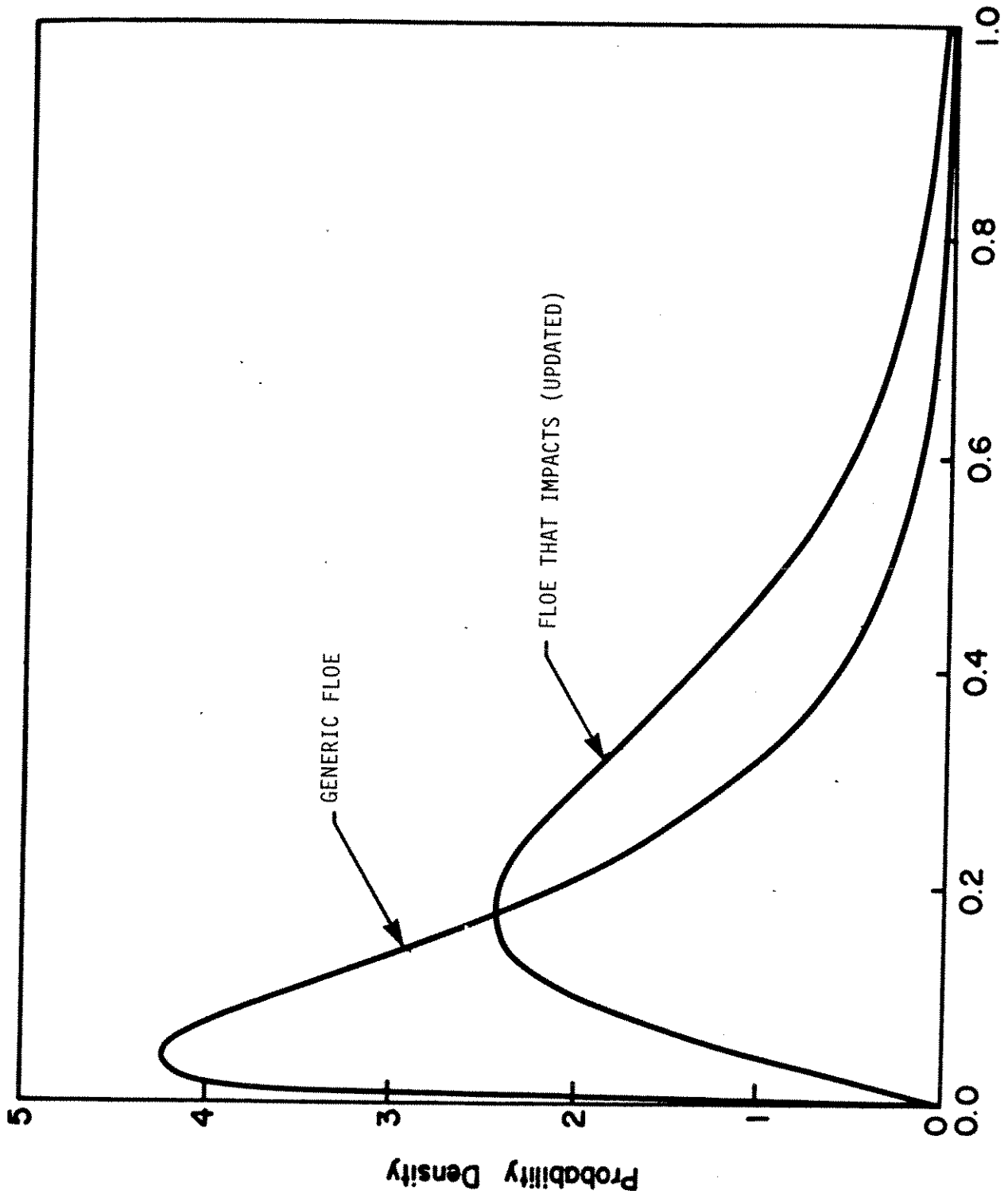

Figure 3.8. Illustration of the Results of Updating the Velocity pdf for Impacting Floes

We arrive in this case at the interesting and useful result: if the generic distribution is $\gamma(v|\alpha,\beta)$ with mean = $\alpha\beta$ and variance = $\alpha\beta^2$, then the updated distribution is also gamma, $\gamma(v|\alpha+1,\beta)$, with mean $(\alpha+1)\beta$, and variance = $(\alpha+1)\beta^2$.

The result of updating the pdf of the floe width B is slightly different because the probability of impact is proportional to $(b + W_s)$, where W_s is the width of the structure. Taking this into account in the same procedure used for the velocity, the updated pdf is given by:

$$f_{B|I}(b|I) = \frac{(b + W_s)\ f_B(b)}{\int (b + W_s)\ f_B(b)\ d\ b} \tag{3.28}$$

For a gamma distribution of B, $\gamma(b|\alpha,\beta)$ the final result is given by:

$$f_{B|I}(b|I) = \frac{W_s}{\bar{B}+W_s} \cdot \gamma(b|\alpha,\beta) + \frac{\bar{B}}{\bar{B}+W_s} \cdot \gamma(b|\alpha+1,\beta),\ b\geq 0 \tag{3.29}$$

which is a mixture of the generic gamma pdf and a modified gamma pdf which is obtained by increasing the value of α by unity.

3.6 Area-Diameter Relationship for Discrete Ice Features

Normally we have the relationship $a = \pi b^2/4$, and the equivalent diameter b for an irregularly-shaped ice floe or feature should be calculated using this relationship, from the measured area.

If we are considering a set of floes with equivalent diameters b and areas a varying from floe to floe, we can treat the value of these parameters as random (B or A). (This was done in Section 3.4.) In order to calculate the mean floe diameter, taking into account the variation from floe to floe, we note that:

$$\bar{a} = \int a \, f_A(a) \, da; \tag{3.30}$$

this was used in Eq.(3.12) in calculating concentration c from $c = r\bar{a}$, where r = density of ice features.

Now we can write Eq.(3.30) as:

$$\bar{a} = \int \frac{\pi b^2}{4} \, f_B(b) \, db, \tag{3.31}$$

and it should be noted that:

$$f_B(b) = f_A(\frac{\pi b^2}{4}) \cdot \frac{\pi b}{2}, \tag{3.32}$$

by the usual rule for the transformation of random quantities. The expression (3.31) can be written as:

$$\bar{a} = \frac{\pi}{4} \int b^2 \, f_B(b) \, db, \tag{3.33}$$

$$\text{i.e. } \bar{a} = \frac{\pi}{4} (\bar{b}^2 + \sigma_B^2) \tag{3.34}$$

where σ_B^2 = variance of B. This follows from the definition of σ_B.

Eq.(3.34) should be used when one is considering collections of ice floes or ice features, for instance, in concentration-density relationships.

Strictly speaking, the calculation of average diameter from area ($\bar{b} = 2\,a/\pi$ for an irregularly shaped ice feature is correct for coverage calculations. Yet the appropriate calculation for mean projected length (or diameter) for use in calculation of collision probabilities gives a different value. The two are identical in the case of circular features, but differ in the case of linear features. Therefore the collision rate calculations have been formulated on a different basis (Section 3.4).

3.7 Extremal Analysis

3.7.1 General introduction

Very often we are considering a series of random quantities $\{X_1, X_2, \ldots, X_n\}$. These might be a series of global impact loads on structures, and for design purposes, we are interested in the maximum of these, i.e. in

$$Y = \max(X_1, X_2, \ldots, X_n). \tag{3.35}$$

In general, n can be random (in which case it is denoted by upper case N), and the variety of situations is illustrated in Figure 3.9 (Maes, 1986).

The probability distribution for a given (single) interaction is termed the parent distribution, $f_X(x)$. The extreme distributions for any integer n are easily generated by considering the cumulative distributions provided, a further assumption is made. The most convenient and usual assumption is that the repeated "sampling" of the parent distribution is on the basis of independent and identically-distributed random quantities, i.e. that the same distribution $f_X(x)$ applies each time the uncertainty regarding successive loads are considered.

Let the cumulative distribution function of X be $\Pr(X \leq x) = F_X(x)$. Then for n values of load, with n fixed (not random), let

$$Y = \max(X_1, X_2, \ldots, X_n). \tag{3.36}$$

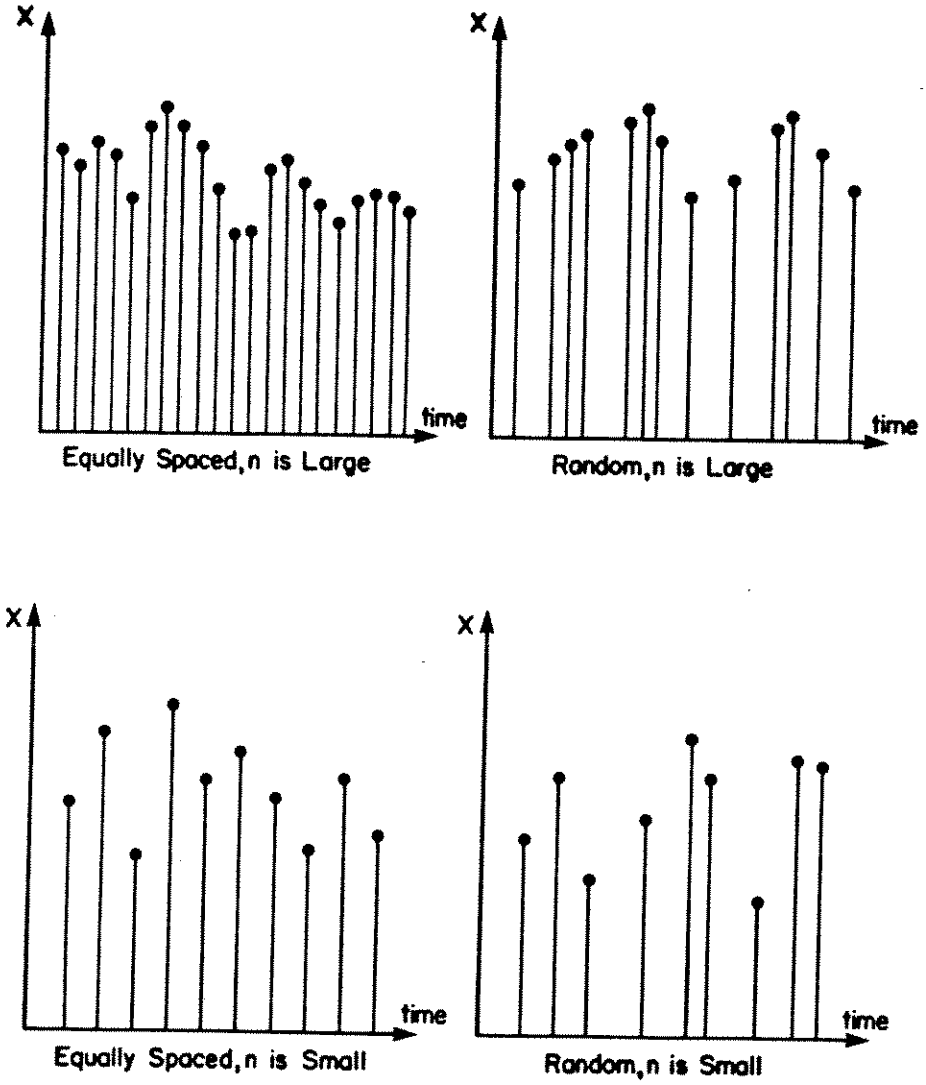

Figure 3.9. Various Types of Random Processes

Then:

$$F_Y(y) = Pr(Y < y)$$

$$= Pr(All\ X_i < y), \tag{3.37}$$

i.e.

$$F_Y(y) = F_X^n(y) \tag{3.38}$$

The effect of this is to "shift" the probability distributions to the right, as n increases. The question of random N will be addressed in the next sub-section (3.7.2).

3.7.2 Random N: Poisson process

It was shown in Section 3.3 that the Poisson model is quite widely applicable to the succession of load events in Arctic engineering. We will assume in this section that the random number of load events N is Poisson-distributed, with expected value $\nu = \bar{\lambda} t$, to be computed as outlined in Section 3.4. Then:

$$P_N(n) = \frac{e^{-\nu} \nu^n}{n!}, \tag{3.39}$$

and

$$F_Y(y \mid N=n) = F_X^n(y). \tag{3.40}$$

Combining these two equations, we have:

$$F_Y(y) = \sum_{all\ n} \frac{e^{-\nu}\nu^n}{n!} F_X^n(y) \tag{3.41}$$

$$= \sum_{all\ n} \frac{e^{-\nu F} \cdot e^{-\nu(1-F)} \cdot (\nu F)^n}{n!}, \tag{3.42}$$

in which the shorthand $F \equiv F_X(y)$ has been used.

Now Eq.(3.42) can be written as:

$$F_Y(y) = e^{-\nu(1-F)} \sum_{all\ n} \frac{e^{-\nu F}(\nu F)^n}{n!},$$

and noting that the summation is over an entire probability distribution (i.e. to unity), we have (in full):

$$F_Y(y) = \exp\left(-\nu(1 - F_X(y))\right) \tag{3.45}$$

This is also the probability of non-exceedance, i.e. Pr(N = 0), for a Poisson process with rate $\nu(1 - F)$ - as also described in Maes (1986), see also Figure 3.10. Typical results are illustrated in Figure 3.11, showing the density function $f_X(x)$ for a single encounter and the extreme load density function $f_Y(y)$ for different values of ν. The spike at y = 0 corresponds to no events in the Poisson process.

3.7.3 Combining different scenarios

It is reasonable to assume that the extreme loads for successive seasons will be independent of each other, given the ice conditions for the period (e.g. year) in question. It is suggested that such factors as persistence of heavy ice conditions be handled by means of treating concentration, for instance, as correlated from one season to another. Then knowledge of the ice loads in one season will not lead us to amend our distribution for the next season - the basic condition for independence.

If the successive seasons are denoted 1,2,3 ..., and if the associated extremal distributions are denoted $F_{Y_1}(y_1)$, $F_{Y_2}(y_2)$, $F_{Y_3}(y_3)$, ..., then the final extremal distribution for n successive seasons is:

$$F_Y(y) = \prod_{i=1}^{n} F_{Y_i}(y_i). \tag{3.46}$$

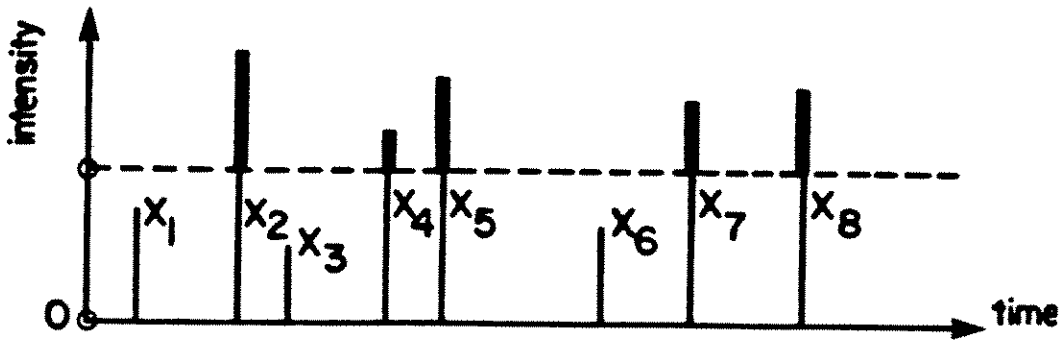

Figure 3.10. Exceedances of the intensity y

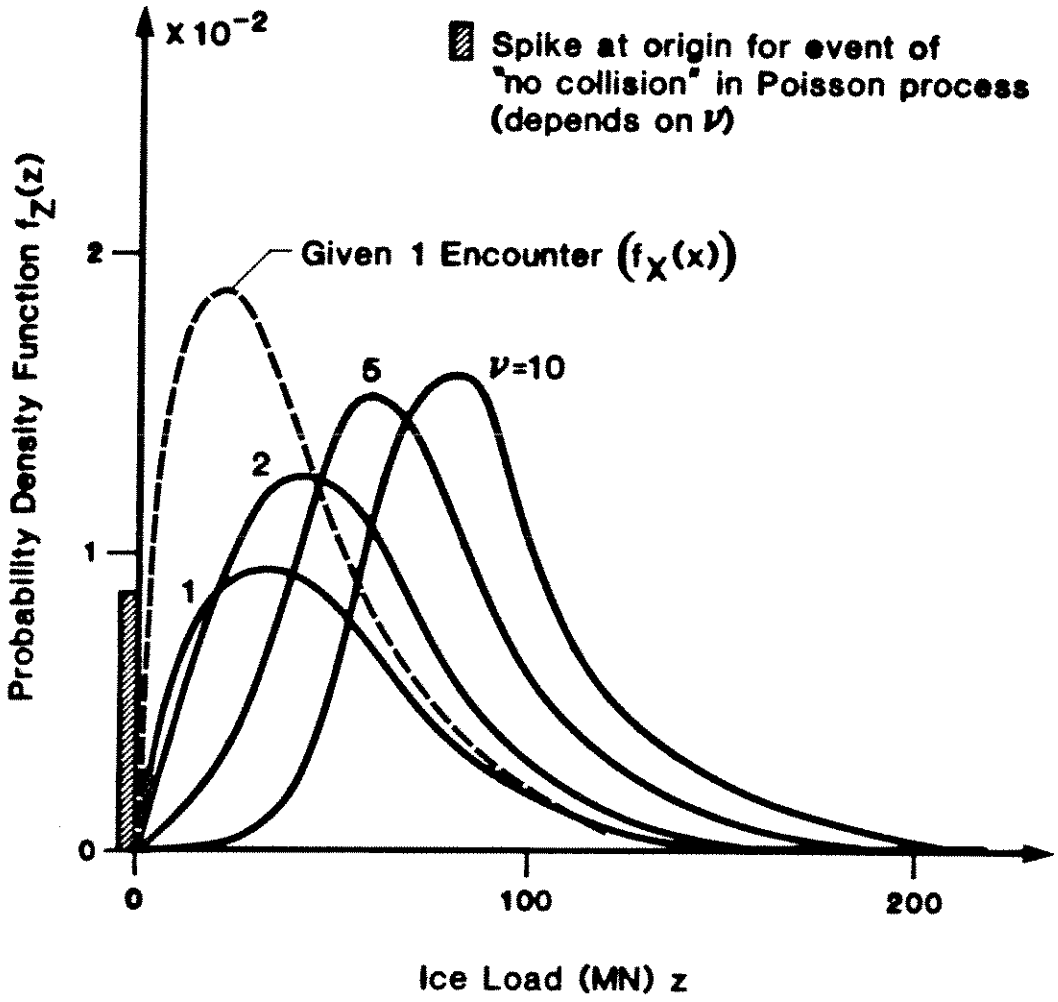

Figure 3.11. Illustration of the Parent and Extremal Probability Density Functions (the Spike at Origin Represents the Event of "no impacts" in the Poisson Process)

3.8 Asymptotic Distributions of Extremes

If one considers the maximum of n independent and identically distributed random quantities (with n being deterministic):

$$Y = \max(X_1, X_2, \ldots, X_n), \tag{3.46}$$

one obtains a rather striking result. Under wide conditions, the probability distribution of Y tends to a nondegenerate limiting distribution, as $n \to \infty$. The limiting distribution is:

$$F_Y(y) = \exp(-e^{-y'}), \tag{3.47}$$

where $y' = (y-a)/b$, where a and b are normalizing constants. It should be noted that the double exponential distribution (3.47) is arrived at if one starts with virtually any of the common distributions for the "parent" random quantity X (e.g. exponential, normal, lognormal, ...). The principal exceptions are the pathological distributions of the Cauchy and the Pareto type.

It is also worth noting that if there are enough occurrences of X in a period of time to justify the use of the extreme distribution (3.47), then if we have m repetitions of the period of time, the new extremal is derived from Eq.(3.47) on the basis of the following:

$$F'_{Y(y)} = \left(\exp(-e^{-\left(\frac{y-a}{b}\right)})\right)^m = \exp\left(-e^{-\left(\frac{y-a-b\ \ell n(m)}{b}\right)}\right), \tag{3.48}$$

where F' is the "new" extremal, which has the same form as (3.47), but with a "new" value of a:

$$a \to a + b\ \ell n\ (m). \tag{3.49}$$

Chapter 4

DATA ANALYSIS AND PROBABILISTIC MODELLING OF ICE CONDITIONS

4.1 Software

Software was developed to assist in the analysis of the raw data which was compiled during the course of the study. Figure 4.1 is a flow chart for the program. The data is entered in a histogram form (i.e. number of data points in different intervals of the parameter values). Once the data has been entered, the program allows for a choice of distribution types, depending on the data type. If the parameter is discrete, the options are Binomial and Poisson distributions. For continuous parameters, the program allows for a Gamma, Beta, Exponential, Normal, Lognormal, or Uniform distribution. In each instance the distribution parameters can be calculated from the data, or entered by the user. This option allows for varying the mean and standard deviation of the data, to determine its sensitivity.

To determine whether the data set fits the distribution type chosen, the Chi-square goodness of fit test is applied. The test is based on comparing the data histogram to the assumed distribution. The deviation of the data from the distribution is quantified by the Chi-square statistic (χ^2), which is calculated from:

$$\chi^2 = \sum_{i=1}^{k} \frac{(O_i - E_i)^2}{E_i}, \qquad (4.1)$$

where O_i is the observed number of points in bin i (from data);
E_i is the estimated number of points in bin i (from distribution); and
k is the number of bins.

It can be shown that the deviation χ^2 itself (given by Eq. (4.1)) has a Chi-square probability distribution which depends on the number of bins k, hence the name of the test. The level of significance is defined as the probability that the calculated deviation χ^2 is to be exceeded. A level of significance of .05, for example, means that one is willing to accept the hypothesized distribution as a good model for the data if

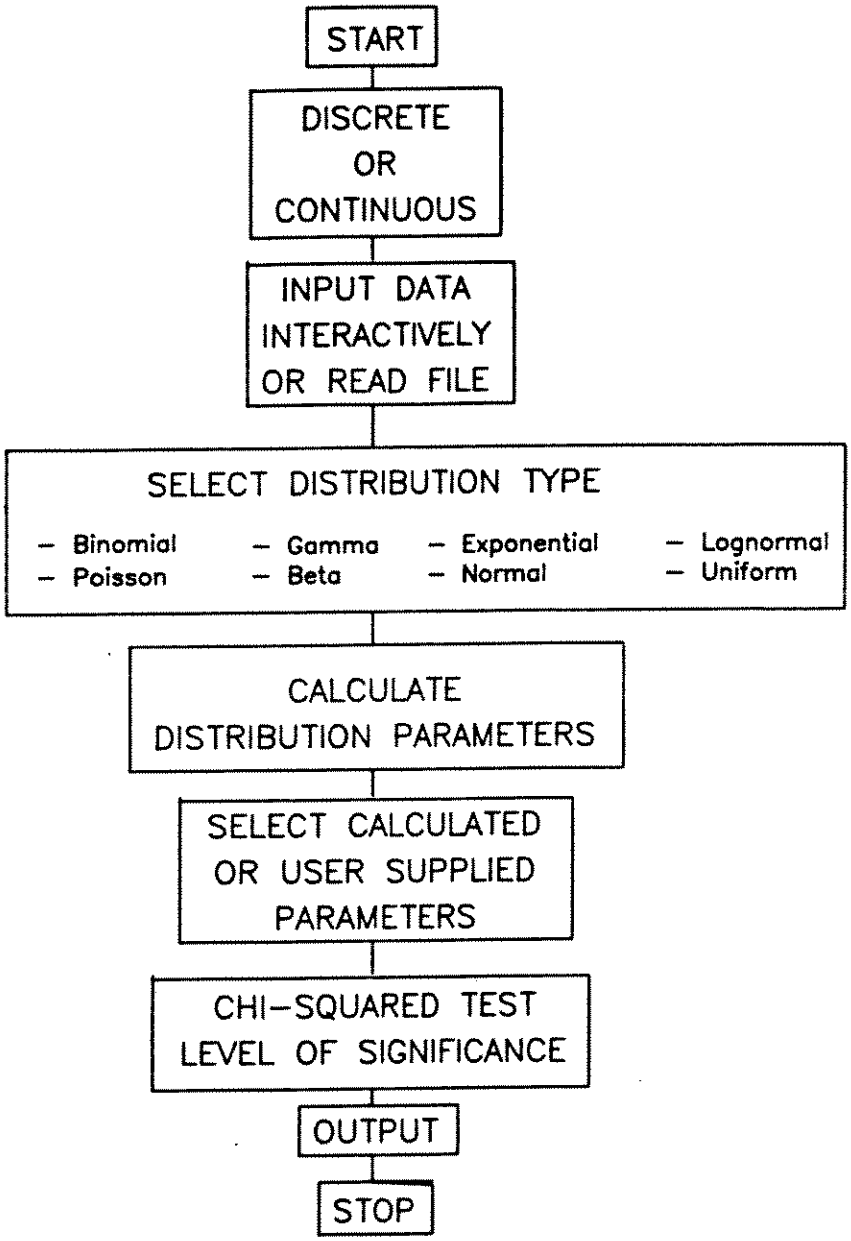

Figure 4.1. Flow Chart of Software for Testing the Goodness of Fit

the resulting deviation is less than the deviation associated with a probability of exceedance of .05 ($\chi^2_{.05}$).

Following the performance of the test, the program prints the data and distribution parameters, as well as the results of the Chi-Square test. Plots of the data histogram and the fitted distribution can also be obtained.

4.2 Selection of Parameter Distribution

This section reviews each of the different environmental and mechanical ice parameters individually, identifying the sources of data and the selection procedure to arrive at a single distribution type for each parameter. Contained in Appendix C are tables with the original data, which was used to arrive at a distribution to represent each variable.

The Chi-Square goodness of fit test was performed using different distributions for each parameter. The choice of mathematical distributions to be attempted was based on their consistency with the parameter bounds and histogram shape. In general, the distribution with the highest level of significance above .05 (i.e. lowest Chi-Square value) was chosen. In some cases, the data was only available in histogram form where a large number of data points are grouped in a small number of bins. This is known to result in low levels of significance, thus making the Chi-Square test overly restrictive (Cochran, 1952). In such cases, the choice of distribution was based on visual comparison with the data histogram using the graphic output of the program.

It is important to note that the mathematical distributions which are chosen for each parameter are defined over the whole range of the parameter. In certain cases, as will be highlighted later in this section, the data set does not cover the whole parameter range. For example, there is a lower bound of 0.76 m on ridge height data. In such cases, the distribution must be inferred over the range of data that does not exist, before it is used as input to the program. This aspect will be discussed further in Volume II of this report.

Research into each of these parameters was conducted by Det norske Veritas, and via subcontract by D.F. Dickins and Associates of Vancouver, British Columbia. In the instances where data was not publicly available in sufficient quantity, an estimate was made based on prior experience of the researchers. Those parameters which were described based on the experience of the researchers are highlighted in the table of default values (Table 4.1). It should be emphasized at this point that the model developed in this study allows the user complete freedom in selecting a distribution type and parameters of a given input parameter. The results of the data analysis carried out in the study are used as default values in the computer model.

4.2.1 Season boundaries

In the following, season boundaries are defined by the time lapse in days referred to January 1. Standard deviations are also given in days.

4.2.1.1 Start of break-up Canadian Beaufort

The Atmospheric Environment Service (1953 - 1984) recorded ice concentrations, primarily during the non-winter months. By analyzing these records, the start of break-up was determined.

For this study, the start of break-up was defined as the date when first-year ice concentrations were reduced by at least 20% from their mid-winter levels (usually to 8/10 first-year ice or less). Table 4.1 displays the results of the data analysis for the start of break-up in the Canadian Beaufort for various distances from the shore (see Figure 4.2). Based on the results in Table 4.1, it was decided to use the Normal distribution to describe the start of break-up in the Canadian Beaufort Sea.

NORMAL

μ = 173 days = June 22

σ = 18.095 days

The original data is summarized in Table C.1 in Appendix C.

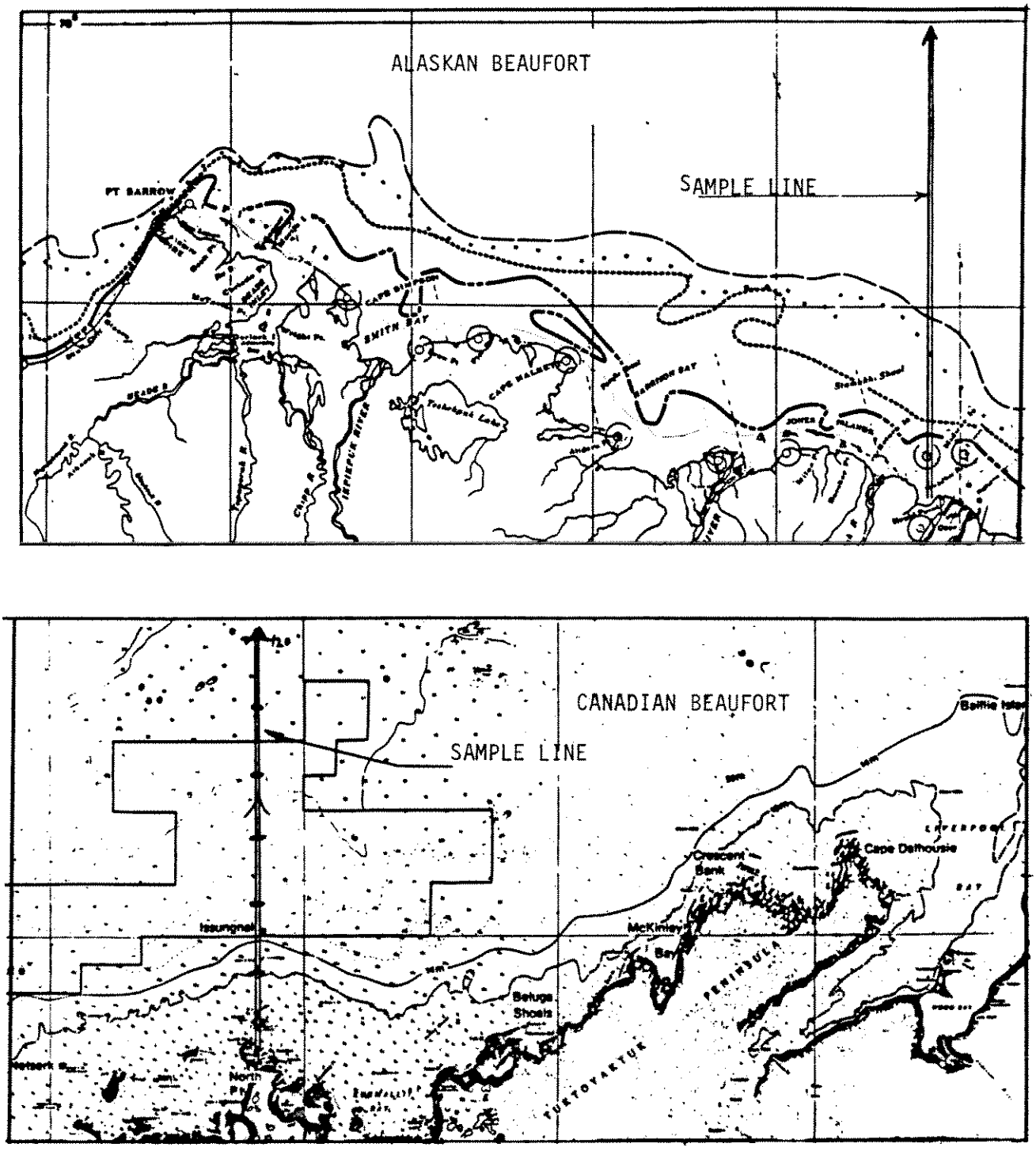

Figure 4.2. Canadian and Alaskan Sides of Beaufort Sea -
Sample Lines Running North of North Pt. and Prudhoe Bay

TABLE 4.1

Start of break-up Canadian Beaufort

LOCATION	DISTRIBUTION	μ_{DATA} (DAYS)	σ_{DATA} (DAYS)	x^2	LOS
20 - 40 km	Gamma	177	15.5	0.856	0.652
	Beta	177	15.5	2.230	0.328
	Lognormal	177	15.5	0.603	0.740
	Normal	177	15.5	0.643	0.423
60 - 80 km	Normal	165	17.4	4.395	0.04
	Beta	165	17.4	7.316	0.068
	Lognormal	165	17.4	6.483	0.011
	Gamma	165	17.4	5.981	0.050
80 - 100 km	Normal	173	15.5	3.441	0.064
	Beta	173	15.5	5.526	0.019
	Gamma	173	15.5	3.463	0.063
	Lognormal	--	--	--	No fit possible

TABLE 4.1 (continued)

Start of Break-Up Canadian Beaufort

LOCATION	DISTRIBUTION	μ DATA (DAYS)	σ DATA (DAYS)	χ^2	LOS
100 - 120 km	Beta	175	19.3	4.755	0.093
	Gamma	175	19.3	3.063	0.216
	Normal	175	19.3	3.756	0.153
	Lognormal	175	19.3	3.238	0.072
120 - 140 km	Beta	175	19.9	5.112	0.164
	Normal	175	19.9	3.923	0.141
	Gamma	175	19.9	3.093	0.079
	Lognormal	175	19.9	4.234	0.120
All Sections	Normal	173	18.1	20.861	0.004
0 - 140 km	Beta	173	18.1	24.163	0.001
	Gamma	173	18.1	20.449	0.002
	Lognormal	173	18.1	33.609	0.000

4.2.1.2 End of break-up Canadian Beaufort

The ice charts compiled by Atmospheric Environment Service (1953-1984) were used to determine a date for the end of break-up. Final break-up was defined as the date when first year ice concentrations were reduced by at least 70% from their mid-winter levels (i.e. to 3/10 first-year ice or less). Table 4.2 summarizes the results of the data analysis. The normal distribution was selected to describe the end of break-up in the Canadian Beaufort.

NORMAL

μ = 187 $\equiv$ July 6

σ = 22.9 days.

The original data set is in Table C.2 in Appendix C.

4.2.1.3 Freeze-Up Canadian Beaufort

Data was compiled from Atmospheric Environment Services (1953 - 1984) and Table 4.3 below summarizes the results of the data analysis.

The data provided was not adequate to analyze for individual sections; therefore, the entire data set (0 to 140 km) was studied. None of these distributions meet the Chi-Square test requirements at the .05 level of significance, however, the Normal distribution had the highest level of significance and was therefore selected as the most representative.

NORMAL

μ = 309 days $\equiv$ Nov. 5

σ = 22.8 days

The original data set is in Table C.3, Appendix C.

TABLE 4.2

End of Break-Up Canadian Beaufort

LOCATION	DISTRIBUTION	μDATA (DAYS)	σDATA (DAYS)	χ^2	LOS
20 - 40 km	Lognormal	187	19.0	1.085	0.581
	Beta	187	19.0	3.305	0.347
	Normal	187	19.0	0.666	0.415
	Gamma	187	19.0	0.209	0.648
60 - 80 km	Lognormal	179	26.0	3.856	0.145
	Normal	179	26.0	3.645	0.302
	Beta	179	26.0	4.778	0.311
	Gamma	179	26.0	2.608	0.271
80 - 100 km	Lognormal	186	20.5	3.457	0.178
	Normal	186	20.5	2.437	0.296
	Beta	186	20.5	3.864	0.277
	Gamma	186	20.5	2.032	0.362

TABLE 4.2 (continued)

End of break-up Canadian Beaufort

LOCATION	DISTRIBUTION	μDATA (DAYS)	σDATA (DAYS)	X^2	LOS
100-120 km	Lognormal	192	23.4	4.715	0.194
	Normal	192	23.4	3.991	0.262
	Beta	192	23.4	4.485	0.214
	Gamma	192	23.4	3.026	0.220
120-140 km	Lognormal	194	22.9	2.369	0.306
	Normal	194	22.9	3.959	0.266
	Beta	194	22.9	4.223	0.238
	Gamma	194	22.9	1.106	0.576
All Sections	Lognormal	187	22.9	23.078	0.006
	Normal	187	22.9	12.811	0.171
	Beta	187	22.9	14.278	0.113
	Gamma	187	22.9	16.738	0.033

TABLE 4.3

Freeze-Up Canadian Beaufort

LOCATION	DISTRIBUTION	μDATA (DAYS)	σDATA (DAYS)	χ^2	LOS
All Ranges	Lognormal	309	22.8	27.541	0.00
	Normal	309	22.8	16.857	0.005
	Beta	309	22.8	30.624	0.00
	Gamma	309	22.8	25.772	0.00

4.2.1.4 Start of break-up Prudhoe Bay

The source of the limited database was the Atmospheric Environment Service (1953-1984). The ice charts were not as comprehensive for the Prudhoe Bay area, as in the Canadian Beaufort. There was, however, sufficient data to analyze for the entire Prudhoe Bay area. The results of the analysis are shown in Table 4.4.

TABLE 4.4

Start of break-up Prudhoe Bay

LOCATION	DISTRIBUTION	μDATA (DAYS)	σDATA (DAYS)	χ^2	LOS
All Sections	Lognormal	199	20.6	39.671	0.000
	Normal	199	20.6	7.224	0.204
	Beta	199	20.6	8.721	0.121
	Gamma	199	20.6	5.838	0.212

The normal distribution was chosen as being most representative of the data set.

NORMAL

μ = 199 days $\equiv$ July 18

σ = 20.6 days

The original data is contained in Table C.4 in Appendix C.

4.2.1.5 End of break-up Prudhoe Bay

Once again, because of the relatively small database compiled from Atmospheric Environment Service (1953-1984), all sections were combined to represent the entire Prudhoe Bay region. Table 4.5 summarizes the results.

TABLE 4.5

End of break-up Prudhoe Bay

LOCATION	DISTRIBUTION	μDATA (DAYS)	σDATA (DAYS)	χ^2	LOS
All Sections	Lognormal	219	24.3	6.629	0.157
	Exponential	219	24.3	11.939	0.063
	Beta	219	24.3	10.029	0.123
	Normal	219	24.3	8.213	0.145
	Gamma	219	24.3	6.821	0.234

The Normal distribution was selected to represent the data.

NORMAL

μ = 219 days $\equiv$ August 1
σ = 24.3 days

The original data is provided in Table C.5 in Appendix C.

4.2.1.6 Freeze-Up Prudhoe Bay

Atmospheric Environment Service (1953-1984) ice charts provided the database for determining the freeze-up date in Prudhoe Bay. The data was treated as one section, as opposed to individual ranges because of the limited size of the database. Table 4.6 summarizes the results of the analysis.

TABLE 4.6

Freeze-Up Prudhoe Bay

LOCATION	DISTRIBUTION	μDATA (DAYS)	σDATA (DAYS)	χ^2	LOS
All Sections	Lognormal	310	21.8	72.611	0.000
	Normal	310	21.8	16.498	0.002
	Beta	310	21.8	22.664	0.000
	Gamma	310	21.8	16.337	0.003

The Normal distribution was selected to represent the data.

NORMAL

μ = 310 day $\equiv$ Nov. 6
σ = 21.8 days

The original data is in Table C.6 in Appendix C.

4.2.2 Summer Season

4.2.2.1 Summer multi-year floe speeds

Marcellus and Morrison (1982), Danielewicz and Pilkington (1980), and Marcellus (1985) were identified as sources of data for determining the multi-year floe speed during the summer. The results of the data analysis are stated in Table 4.7. No fit

TABLE 4.7
Summer multi-year floe speed

DISTRIBUTION TYPE	μ_{DATA} (cm/s)	σ_{DATA} (cm/s)	χ^2	LOS	COMMENTS
Gamma	15.63	11.891	171.843	0.00	1980 data
Exponential	15.63	11.891	338.939	0.00	
Lognormal	15.63	11.891	430.586	0.00	
Gamma	18.618	14.247	336.450	0.00	1979 data
Exponential	18.618	14.247	371.318	0.00	
Lognormal	18.618	14.247	652.064	0.00	
Gamma	17.131	13.213	445.295	0.00	
Lognormal	17.131	13.213	1,059.207	0.00	Combined
Exponential	17.131	13.213	682.196	0.00	Data

was found to satisfy the Chi-Square test with the data provided, because of the very large number of data points, and the relatively few bins (i.e. the speed intervals were too large).

It was decided that the Gamma distribution best described the data, based on the results of the analysis for the combined data set. The mean also agreed quite closely to that of other data sources (Marcellus, Morrison (1982)). A discussion of the analysis used to reach this conclusion despite the fact that the data is grouped too coarsely, is presented in Section 4.2.7.

GAMMA

μ = 17.131 cm/s

σ = 13.213 cm/s

The data provided by Morrison (1985) is listed in Table C.7.

4.2.2.2 Multi-year floe thickness

Three sources of publicly available data were identified, namely Marcellus and Morrison (1982), C-CORE (1980), and AIDJEX (1976). The latter was selected as the most suitable data set and analyzed with the results given in Table 4.8. These results are in agreement with the experience of the researchers.

TABLE 4.8

Multi-year floe thickness

DISTRIBUTION TYPE	μDATA (m)	σDATA (m)	χ^2	LOS	COMMENTS
Gamma	3.89	1.584	1.549	0.671	
Normal	3.89	1.584	3.198	0.362	
Lognormal	3.89	1.584	4.150	0.245	

The gamma distribution was selected based on the results in Table 4.8.

GAMMA

μ = 3.89 m
σ = 1.584 m

The original data set is in Table C.8.

4.2.2.3 Multi-year ice concentration - Canadian Beaufort

Multi-year summer ice concentrations were obtained from the Atmospheric Environment Service (1953-1984). The concentrations were found for various sections along a line running north from North Point (see Figure 4.2).

No distinction was made between second year and multi-year ice floes. The results of the data analysis are summarized in Table 4.9. It should be noted that for ice concentration, only the average value and standard deviation are required for the model, and not the distribution type. The original data set is contained in Table C.9, of Appendix C.

4.2.2.4 Multi-year ice concentration - U.S. Beaufort

Multi-year ice concentrations were compiled from the Atmospheric Environment Service (1953-1984) for a representative line running north from Prudhoe Bay (see Figure 4.2).

No distinction was made between second year and multi-year ice floes. The results of the data analysis are summarized in Table 4.10. As mentioned in Section 4.2.2.3, only the average value and standard deviation are required, and not the distribution type. The original data set is contained in Table C.10, Appendix C.

TABLE 4.9
Summer Ice Concentration - Canadian Beaufort

Section (km)	Average Concentration (Ratio)	Standard Deviation (Ratio)
0 - 20	.2/10	.7/10
20 - 40	.3/10	1.0/10
40 - 60	.4/10	1.2/10
60 - 80	.6/10	1.6/10
80 - 100	.7/10	1.8/10
100 - 120	.9/10	2.0/10
120 - 140	.9/10	2.1/10
140 - 160	1.3/10	2.4/10

TABLE 4.10

Summer Ice Concentration - U.S. Beaufort Sea

Section (km)	Average Concentration	Standard Deviation
0 - 20	1.1/10	1.3/10
20 - 40	1.1/10	2.1/10
40 - 60	1.5/10	2.5/10
60 - 80	1.7/10	2.8/10

4.2.2.5 Ice island fragment diameter

Reports by Spedding (1974), Spedding (1975), and Barton et al. (1972) were used to obtain data for this parameter. A summary of the data analysis is provided in Table 4.11.

TABLE 4.11

Ice island fragment diameter

DISTRIBUTION TYPE	μ_{DATA} (m)	σ_{DATA} (m)	χ^2	LOS	COMMENTS
Gamma	69.987	43.134	28.937	0.00	No fits to data.
Exponential	69.987	43.134	162.912	0.00	Numerical distri-
Lognormal	69.987	43.134	6.082	0.014	bution selected.

The data analysis did not yield a "good fit" for ice island fragment diameter. Therefore, a numerical distribution was chosen with the following parameters.

NUMERICAL

μ = 70.0 m

σ = 43.1 m

The original data is recorded in Table C.11 of Appendix C.

4.2.2.6 Ice island diameter

Data for this parameter is very sparse. In a paper by Dunwoody (1983), a mean ice island diameter of 12 km was estimated. This compares very well with the results from a report by De Paoli et al. (1982), who studied the major ice shelves which calve ice islands and identified cracks in the shelves. This lead to estimates of the area which would calve from the ice shelf producing an ice island. The ice shelves studied and the equivalent diameter of the potential ice islands (assuming a circular shape), are listed in Table C.12 of Appendix C.

A numerical distribution was chosen to represent ice island diameter with the following properties:

NUMERICAL

μ = 12.5 km
σ = 7.07 km

4.2.2.7 Ice island/fragment thickness

In the paper by Dunwoody (1983), the assumption was made that the thicknesses of both ice islands and fragments were similar to that of the ice shelves which calved them. Based on this assumption, a mean thickness of 40 m was calculated. This value compared very well with the results from the study by De Paoli et al. (1982). Table C.13 contains the thicknesses of the major ice shelves responsible for ice islands and fragments.

A numerical distribution was generated using this data with the following parametres.

NUMERICAL

μ = 39.75 m
σ = 14.5 m

4.2.2.8 Ice island / fragment speed

It was assumed that the same forces which acted on a multi-year floe would also act on an ice island or fragment (Dunwoody, 1983). Therefore, the velocity distribution for ice islands and fragments was approximated by the speed of a multi-year floe in the summer (see Section 4.2.2.1). This is as follows:

GAMMA

μ = 17.131 cm/s

σ = 13.213 cm/s

4.2.2.9 Ice island density

In the paper by Dunwoody (1983), the following assumptions were made with respect to calculating the ice island density:

i) on average, there are two ice islands in the Beaufort Gyre at any one time;

ii) the Beaufort Gyre is approximately 2,000,000 km^2 in total area. Therefore, there is one ice island per 1,000,000 km^2; and

iii) the concentration of ice islands in the Canadian Beaufort Sea should be directly proportional to the multi-year ice floe concentration. Therefore, given that the average concentration of multi-year floes, in summer, is .66/10, the density of ice islands is equal to .066 ice islands per 1,000,000 km^2, for the Canadian Beaufort. Using the same logic, and given that the average summer multi-year floe concentration is 1.35 tenths in the U.S. Beaufort, the density of ice islands is .135 islands per 1,000,000 km^2 in the U.S. Beaufort.

For the purpose of this study, this parameter was taken as deterministic, and equal to .066 and .135 islands per 1,000,000 km^2 in the Canadian and U.S. Beaufort respectively.

4.2.2.10 Ice island fragment density

Ice island fragments result from the break-up of ice islands when they ground near the shore line. Because the total combined area of ice island fragments should be equal to the total area of ice islands, the rough assumption can be made that the

density of ice island fragments is equal to the density of ice islands multiplied by the average number of fragments per ice island. This value has been chosen as 100 fragments per ice island, therefore resulting in a density of 6.6 fragments /1,000,000 km^2 for the Canadian Beaufort and 13.5 fragments per 1,000,000 km^2 in the U.S. Beaufort.

4.2.2.11 Multi-year floe average ice pressure

Data summarized by Nessim (1984), was generated using small scale tests. No publicly available data was identified for multi-year ice crushing strength from large-scale tests. Based on experience, the following density function was chosen for the effective average ice pressure.

EXPONENTIAL

μ = 0.5 MPa
σ = 0.5 MPa

Further study is required in this area, to arrive at a better defined estimate of this parameter.

4.2.2.12 Multi-year flexural strength

Results from large-scale tests, typically in-site cantilever beam tests, were recorded by Schwarz and Weeks (1977) and Takekuma (1983). Figure 4.3 illustrates results from several studies, with a range of ice flexural strength from 0.1 Mpa to 0.5 MPa. It was concluded, based on the references cited, that the following distribution be used to describe multi-year ice flexural strength.

NORMAL

μ = 0.25 MPa
σ = 0.15 MPa

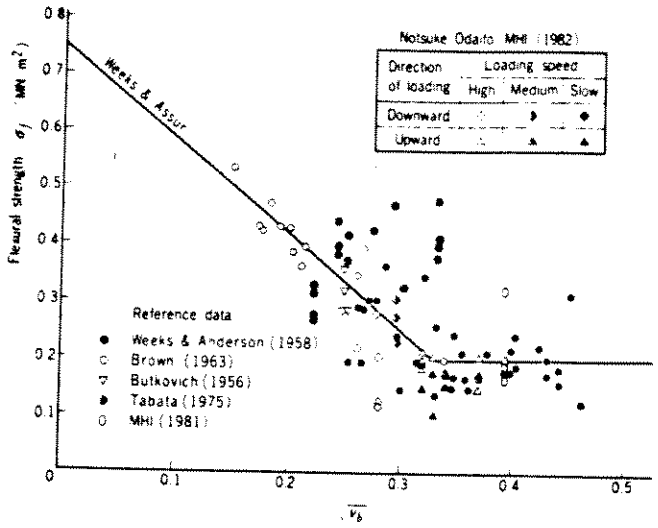

Figure 4.3. Results of In-Situ Cantilever Beam Test (Takekuma, 1983)

4.2.2.13 Multi-year ridge length

Publicly available data could not be located, therefore the past experience of the researchers was used, and the average multi-year ridge length was estimated to be 150 m. Only the average value of this parameter is needed for the model and therefore it is treated as deterministic.

4.2.2.14 Multi-year ridge height

Data was not publicly available for this parameter, however, by analyzing first-year ridge heights (Section 4.2.3.3), and utilizing past experience, the following distribution was selected:

EXPONENTIAL

μ = 0.9 m

σ = 0.9 m

The average ridge height appears to be rather low in comparison with familiar values of data averages. This is because available data sets only contain ridges above a given cut-off value, whereas the distribution used is adjusted to cover all ridge heights starting at zero.

4.2.2.15 Multi-year ridge coverage

Using a paper by Weeks, et al. as guidance, combined with past experience, the available value of this parameter was estimated. It was concluded that, on average, 30% of a multi-year floe would be covered by multi-year ridges. Further study and documentation is required to quantify this parameter more accurately.

4.2.2.16 Multi-year floe diameter

The two sources of data identified were Spedding (1979) and Weeks, et.al. (1977). The data compiled by Spedding was selected because it contained a large number of data points and included floes of all sizes. Weeks' data, as will be illustrated, served to verify the conclusions derived from Spedding.

The data by Weeks (see Table C.14 of Appendix C) was collected for locations near Pt. Barrow and Cape Simpson as shown in Figure 4.4. The results of the data analysis are summarized in Table 4.12. It is noted that the chosen fit was based on visual agreement, since the data was too coarsely grouped to allow a successful Chi-Square test.

GAMMA

μ = 100.3 m
σ = 150.7 m

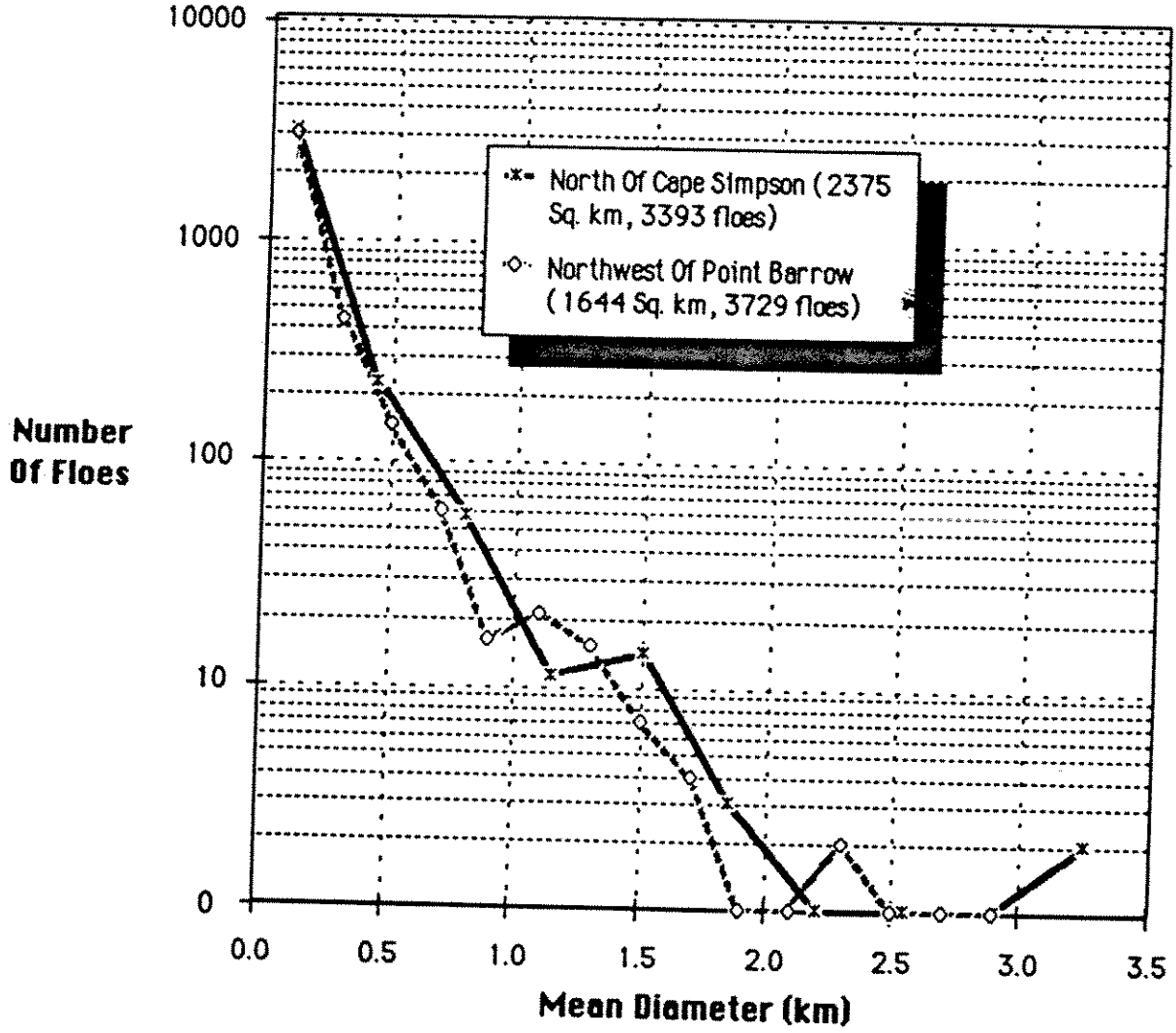

Figure 4.4. Floe Diameter Data - Alaskan Beaufort

TABLE 4.12

Summer multi-year floe diameter - Alaskan Beaufort

DISTRIBUTION TYPE	μ_{DATA} (m)	σ_{DATA} (m)	χ^2	LOS	COMMENTS
Lognormal	321.1	172.6	-	-	Cape Simpson
Exponential	321.1	172.6	313.1	0.00	
Gamma	321.1	172.6	330.7	0.00	
Lognormal	269.6	198.5	865.0	0.00	Pt. Barrow
Exponential	269.6	198.5	451.7	0.00	
Gamma	269.6	198.5	270.9	0.00	

It should be noted that for both the Cape Simpson and Pt. Barrow data sets, there was a lower bound of 100 m diameter, below which floes were not recorded. To verify the choice made using Spedding's data, assume that one is only interested in floes larger than a certain cutoff value d*. The probability distribution of the diameter of these floes can be obtained by truncating the distribution for all floes at d* and normalizing for values of d > d* such that the area under the curve is 1. Choosing d* = 100 m, the new distribution created, after truncating and normalizing the original gamma distribution, has a mean of 265.79 m (see Figure 4.5). This compares very well with the mean values calculated using the data by Weeks (see Table 4.12), and therefore supports the decision to use the data compiled by Spedding.

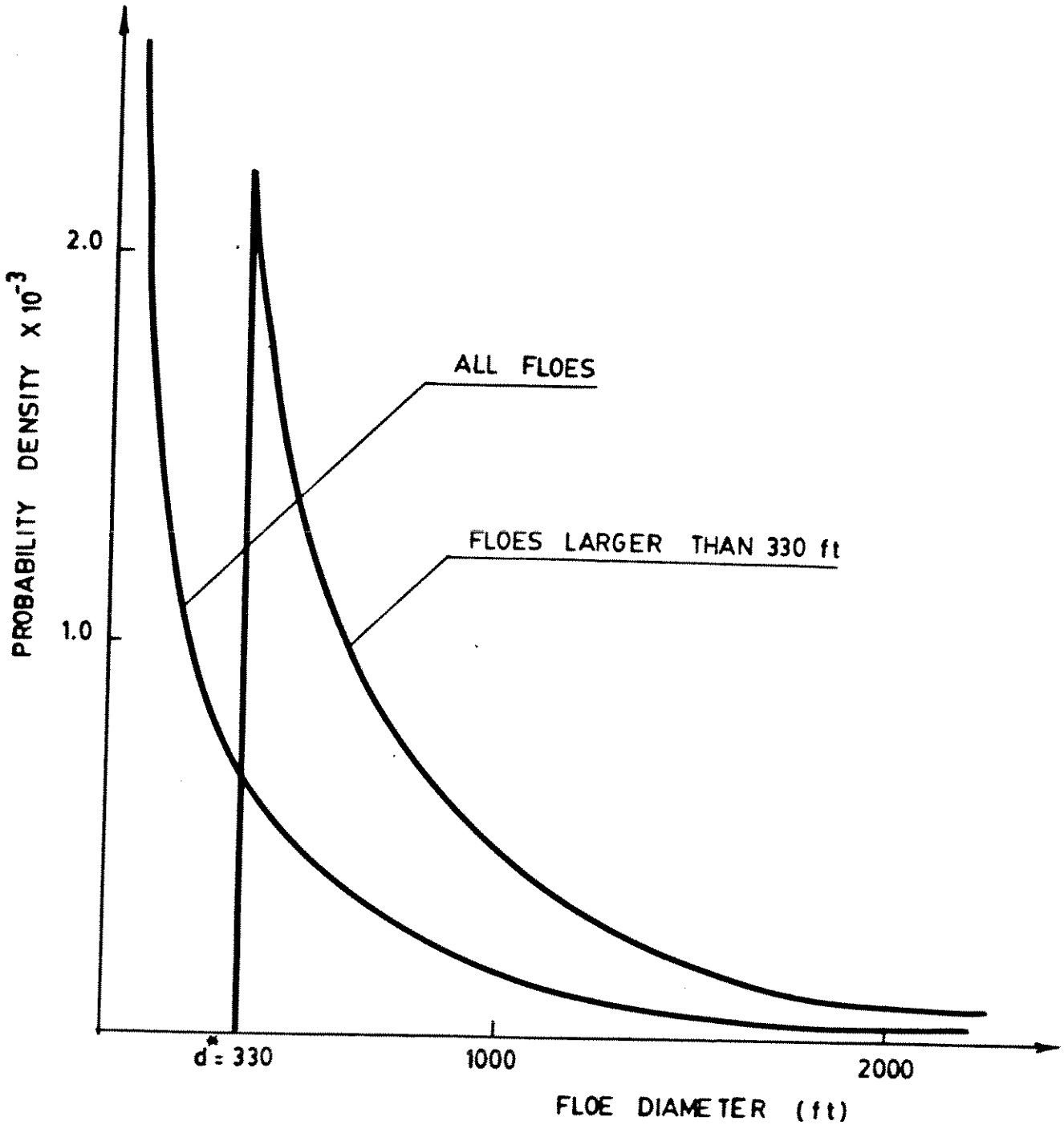

Figure 4.5. Distribution of Multi-Year Floe Diameters

4.2.2.17 Ice island/fragment average ice pressure

The average ice pressure for ice islands and fragments was assumed to be equal to the average pressure of multi-year ice (see Section 4.2.2.11).

EXPONENTIAL

μ = 0.5 MPa
σ = 0.5 MPa

4.2.3 Winter season

4.2.3.1 First-year level ice thickness

Data was obtained from Richardson and Burns (1975). In this report, ice thickness measurements were monitored north of Cape Parry, North West Territories, over a period of several years. From this data, an ice growth curve was constructed, and is shown in Figure 4.6. This figure represents the growth of landfast ice, approximately .0085 m/day, over the course of a winter in the Beaufort Sea. It was assumed that this data was representative of both the Canadian and U.S. Beaufort Sea.

The original data set is summarized in Table C.16 of Appendix C.

4.2.3.2 Peak landfast ice speed

This parameter is defined as the speed at a local peak on the velocity time trace as shown in Figure 4.7. Several sources of data were identified and included; Spedding (1973, 1975, 1975, 1977) and Croasdale and Spedding (1972). Displacement data of the landfast ice was measured using telemetry and tape extensions. From this data, which was obtained on an hourly basis, a computer generated the speed traces, which are shown in Figure 4.6. The resolution of the data, according to Spedding, was limited to speeds above 0.5 ft/hr (4.23×10^{-5} m/s). All speed peaks above this lower limit were recorded and are summarized in Table C.17 of Appendix C.

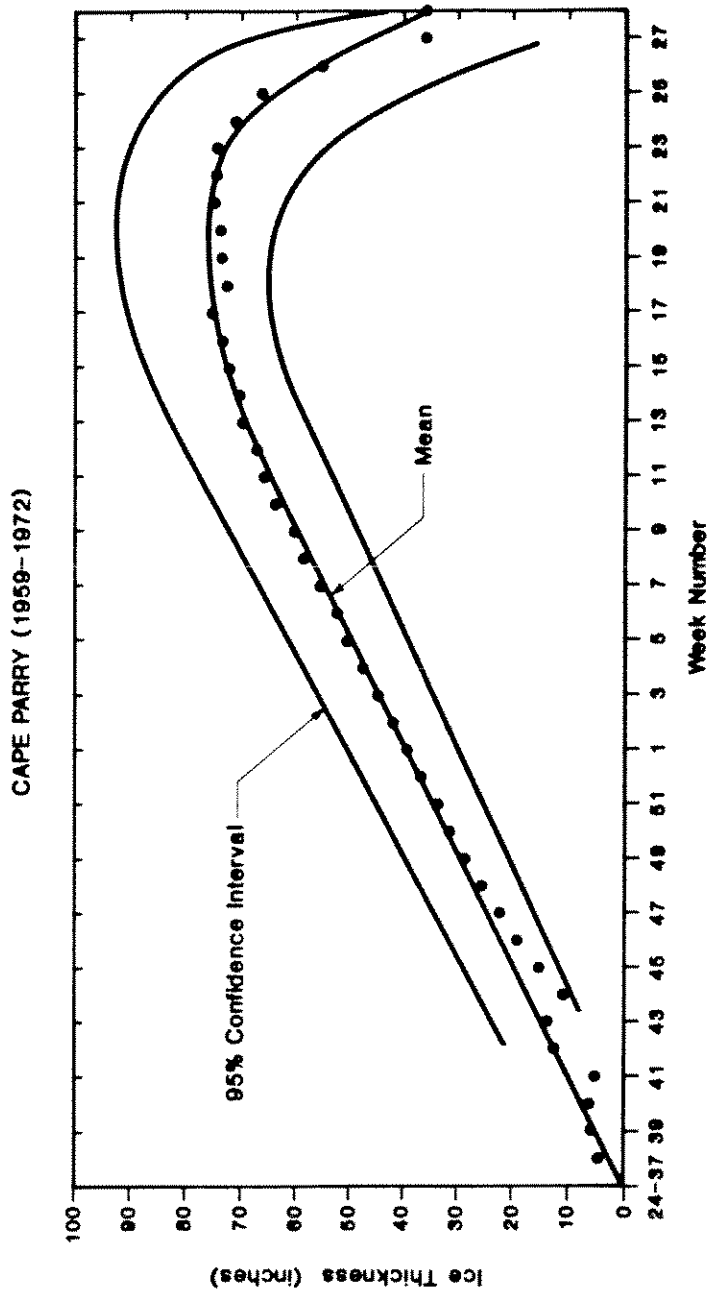

Figure 4.6. Landfast Ice Growth Pattern

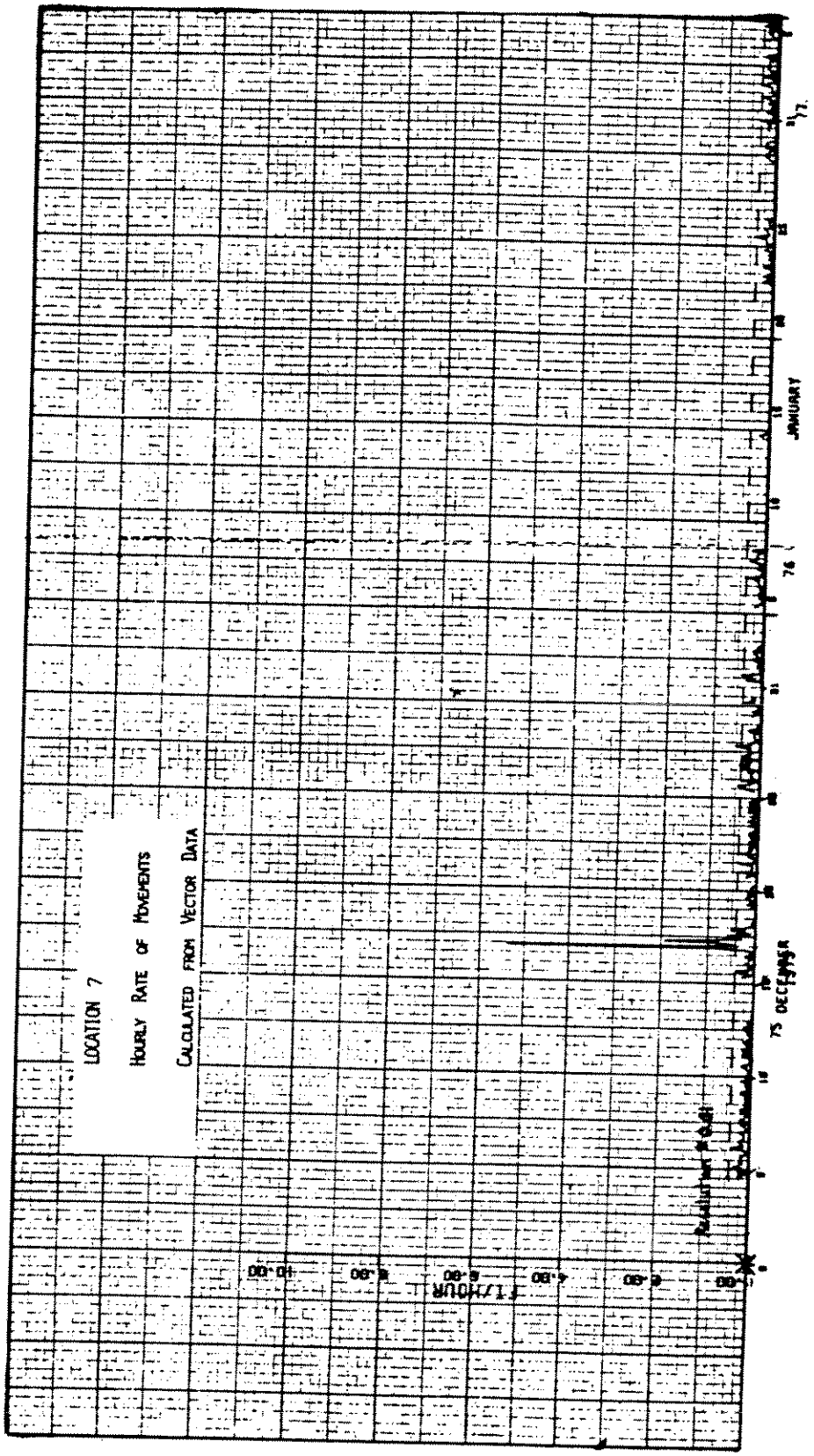

Figure 4.7. Computer Generated Speed Traces

This data was analyzed, and the results summarized in Table 4.13. For each water depth interval, the digitized data was used as a numerical distribution to model ice speed because no mathematical distribution had an acceptable level of significance.

To permit an extremal analysis, the average number of events (peak speeds) per month had to be estimated from the data. This calculation is detailed in Table C.18 of Appendix C, and is summarized in Table 4.14. This information was extracted from the same references used to calculate the average landfast ice speed.

4.2.3.3 First-year ridge height

The sources of data identified for this parameter were Wright and Schwab (1979), and Wright, Gupta and Lusssenburg (1982). A summary of the data analysis is provided in Table 4.15 From the data analysis, the distributions selected to represent first-year ridge height in the shear zone were as follows:

EXPONENTIAL

μ = 0.9 m
σ = 0.9 m

For the pack ice zone, the following was selected:

EXPONENTIAL

μ = 0.69 m
σ = 0.69 m

The distribution average is lower than the data average by 0.76 m in both cases. This is due to the fact that the data is given only for ridges higher than 0.76 while the distribution was inferred for the whole range of ridge heights starting at zero.

TABLE 4.13

Landfast peak speed distribution

Zone	Distribution Type	μDATA (m/hr)	σDATA (m/hr)	χ^2	LOS
> 60'	Gamma	.548	.848	22.33	0.034
(> 18.3 m)	Lognormal	.548	.848	52.22	0.00
	Exponential	.548	.848	136.304	0.00
40'-60'	Gamma	.336	.247	85.943	0.00
(12.195-	Exponential	.336	.247	32.142	0.00
	Lognormal	.336	.247	14.085	0.00
20'-40'	Gamma	.314	.295	13.157	0.022
(6.098 -	Exponential	.314	.295	42.166	0.00
	Lognormal	.314	.295	44.603	0.00
0'-20'	Gamma	0.3	.197	22.545	0.00
(0-6.098 m)	Exponential	0.3	.197	47.829	0.00
	Lognormal	0.3	.197	65.189	0.00
All Depths Combined	Gamma	.392	.302	942.106	0.00
	Exponential	.392	.302	707.574	0.00

TABLE 4.14

Landfast ice speed peak distribution

WATER DEPTH	TOTAL HOURS	NUMBER OF PEAKS		
		TOTAL	AVERAGE PER HOUR	AVERAGE PER MONTH*
0 - 20 ft (0 - 6.098 m)	25,910	380	1.467×10^{-2}	10.560
20 - 40 ft (6.098-12.195 m)	8,952	276	3.083×10^{-2}	22.198
40 - 60 ft (12.195-18.293 m)	5,952	921	1.547×10^{-1}	111.410
> 60 ft (> 18.293 m)	1,128	158	1.401×10^{-1}	100.850
ALL DEPTHS	40,083	1,735	4.392×10^{-2}	31.165

* Average/month calculated as:

(Average/hour) x (24 hrs/day) x (30 days/mo.)

TABLE 4.15

First-year ridge height

ICE ZONE	DISTRIBUTION TYPE	μ_{DATA} (m)	σ_{DATA} (m)	χ^2	LOS	COMMENTS
SHEAR	Exponential	1.66	0.99	14.558	0.104	1980-81 data.
	Gamma	1.66	0.99	14.842	0.095	
PACK	Exponential	1.45	0.68	16.799	0.052	

4.2.3.4 First-year ridge orientation

Data for this parameter was recorded by Wright and Schwab (1979). A summary of the data analysis is provided in Table 4.16 below.

TABLE 4.16

First-year ridge orientation

ICE ZONE	DISTRIBUTION TYPE	μ_{DATA} (deg.)	σ_{DATA} (deg.)	χ^2	LOS	COMMENTS
SHEAR	Beta	90.45	43.70	1.474	0.225	Beta distribution fits all data sets.
PACK	Beta	92.25	46.84	2.409	0.121	

The results of the data analysis indicate that the Beta distribution is appropriate for first-year ridge orientation with the parameters given in Table 4.16 for each ice zone. The method for measurement of the ridge angle is shown in Appendix C along with Table C.20, which lists the data set. It is noted that this parameter was not required for the final model and is included here for reference.

4.2.3.5 First-year ridge frequency

Two references were studied for this parameter, namely Wright and Schwab (1979), and Spedding (1979). A summary of the data analysis for the first reference is given in Table 4.17.

TABLE 4.17
First-year ridge frequency

ICE ZONE	DISTRIBUTION TYPE	μ_{DATA} (/km)	σ_{DATA} (/km)	χ^2	LOS	COMMENTS
SHEAR	Beta	14.21	8.25	9.868	0.130	
	Gamma	14.21	8.25	18.417	0.002	
PACK	Gamma	14.93	7.95	10.719	0.097	

This parameter was not required in the final model where ridge frequency of occurrence was estimated from areal coverage information (see Section 4.3.2). The data analysis is presented here for reference. The original data from Wright et al. (1979) is provided in Table C.21.

4.2.3.6 First-year ridge cohesion

First-year ridges are mostly composed of unconsolidated rubble, and as a result, are usually studied using soil models. Prodanovic (1981) used a value of 0.035 MPa as the cohesion pressure in first-year ridges, and was used as a deterministic value in this study.

4.2.3.7 First-year ridge friction angle

The internal friction angle was estimated by Prodanovic (1981) to be 25^{o}, and this was used as a deterministic value in this study.

4.2.3.8 First-year ridge coverage

Using the same sources as for estimating the multi-year ridge coverage (see Section 4.2.2.14), the coverage was estimated to have an average value of 30% of the floe area.

4.2.3.9 First-year ice pressure

Ice pressure was treated as a random process for which the pressure at a local peak is the sum of two components, namely the process mean and a random component (see Sec. 6.4.2). Results from large-scale tests to determine the pressure of first-year ice in the crushing mode were not found in the public domain. A process average value of 0.3 MPa was selected based upon judgemental adjustment of the average ice pressure for multi-year ice. The extremal pressure component was assumed to have a mean value of 0.2 MPa, and a standard deviation of 0.15 MPa. These were used in a double exponential extremal density function (see Section 3.8). Further field data are required to better quantify this parameter.

4.2.3.10 First-year ice flexural strength

This parameter is treated in a similar manner to the average pressure (Section 4.2.3.9), as the sum of a process average and a random component. Several sources of data were reviewed to arrive at an average value for the flexural strength of first-year ice. These sources included Frederking (1978), Schwarz and Weeks (1977), and Takekuma (1983). The results shown earlier in Figure 4.3 combined with data from Frederking (1978), led to the conclusion that the average flexural strength of first-year ice was approximately 0.20 MPa.

No data could be found to estimate the extremal component of flexural strength and this was based on judgement. The selected mean value for the flexural strength extremal component is 0.1 MPa, with a standard deviation of 0.05 MPa. The double exponential distribution was used (see Section 3.8).

4.2.3.11 First-year ridge speed

First-year floes containing first-year ridges would move with the whole ice cover during the winter. As a result, the speed of these ridges can be modelled using winter ice speeds (see Section 4.2.3.15). The chosen distribution is:

GAMMA

μ = 0.062 m/s
σ = 0.073 m/s

4.2.3.12 First-year ridge length

An average value of 130 m is used. This is based on the value used for multi-year ridge length since it is believed that the two types of ridges are similar in length.

4.2.3.13 Winter ice speed - shear zone and pack zone

A USCG study by Murphy et al. (1983), analyzed the tracks of buoys from the Canadian to U.S. Beaufort during the winter season. This study was considered more suitable than the results obtained from McGonigal and Wright (1977), and was therefore used in the data analysis. Figure 4.8 is a sketch showing the position of the buoy during the course of the study.

The data consisted of net daily drift speeds, which were calculated based on displacements measured every 24 hours. To verify that the fit obtained was applicable to both the U.S. and Canadian Beaufort Sea, the data set was divided geographically into Canadian and U.S. measurements, as recorded in Table C.22 in Appendix C. The results of the data analysis are summarized in Table 4.18.

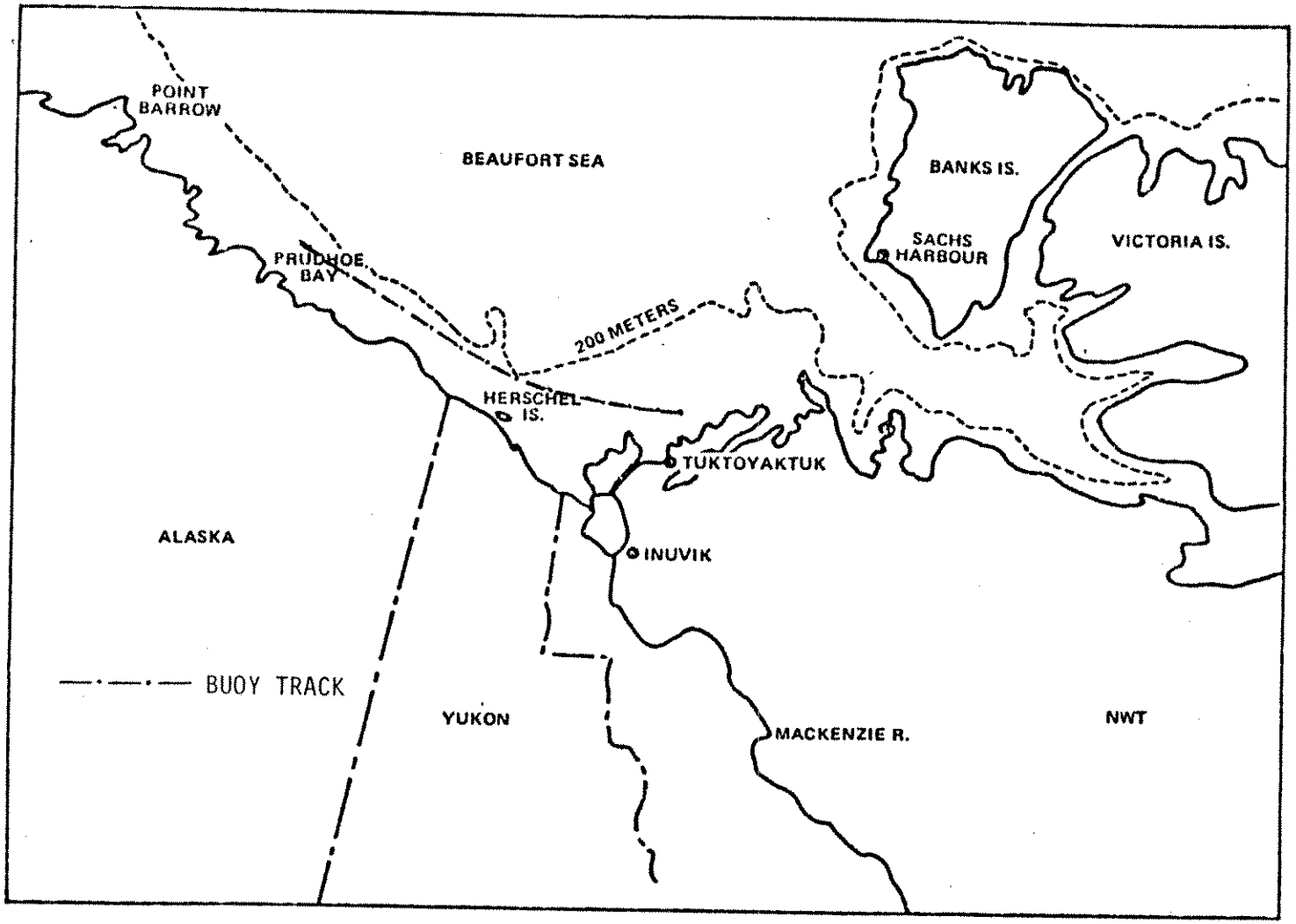

Figure 4.8. Track of Buoy Used in Estimating Winter Ice Speeds

The Gamma distribution, fitted to combined data set, was selected as representative of winter ice velocities in the shear and pack ice zones.

GAMMA

μ = 0.062 m/s
σ = 0.073 m/s

4.2.3.14 Multi-year ice concentration

The ice charts provided by the Atmospheric Environment Service (1953-84) do not provide detailed information for the winter season. Using the limited data available, the mean concentration was determined to be 0.2 tenths, with a standard deviation of 0.4 tenths. This value was used for both the U.S. and Canadian Beaufort Sea.

4.2.3.15 Pack ice pressure

Based on a paper by Jordaan, I.J., et. al. (1985), which reviewed several sources of data (Figure 4.10), the following was used for pack ice forces:

NORMAL

μ = 0.05 MPa
σ = 0.05 MPa

4.2.3.16 Other winter parameters

Several other winter parameters were found to be equal to the values for the summer season, and these are listed below in Table 4.19

TABLE 4.18
Winter ice speed

LOCATION	DISTRIBUTION TYPE	μDATA (m/s)	σDATA (m/s)	χ^2	LOS	COMMENTS
Canadian Beaufort	Exponential	0.060	0.53	0.281	0.596	Murphy et al. (1983)
	Gamma	0.060	0.053	-	-	No fit possible
	Lognormal	-	-	-	-	Murphy et al. (1983)
U.S. Beaufort	Exponential	0.065	0.092	17.621	0.000	
	Gamma	0.065	0.092	9.214	0.002	
	Lognormal	-	-	-	-	No fit possible
Both U.S. & Canadian Beaufort	Exponential	0.062	0.073	10.425	0.005	
	Gamma	0.062	0.073	4.735	0.094	

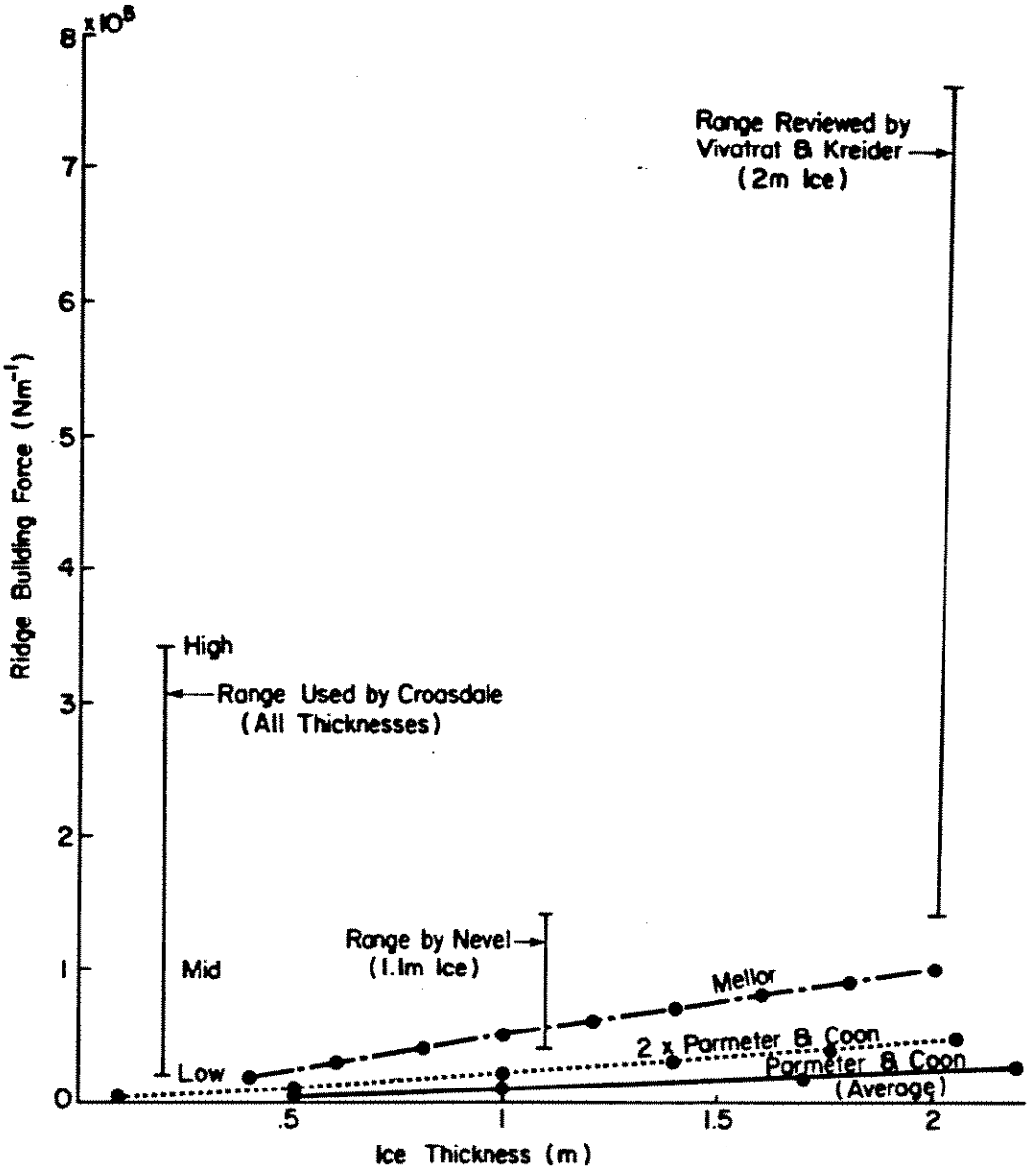

Figure 4.10. Summary of Pack Ice Pressure Data

TABLE 4.19

Winter parameters

Parameter	Report Section Referenced
Multi-year floe thickness	4.2.2.2
Multi-year floe diameter	4.2.2.15
Multi-year average ice pressure	4.2.2.11
Multi-year ice flexural strength	4.2.2.12
Multi-year ridge coverage	4.2.2.14
Multi-year ridge height	4.2.2.14
Multi-year ridge length	4.3.2.12

4.2.4 Break-Up Season

4.2.4.1 First-year ice thickness

The ice thickness was considered to be a maximum at the time of break-up, due to the continuous growth during the winter season. For this parameter, a deterministic value of 1.5 m was chosen.

4.2.4.2 Break-up speeds Prudhoe Bay

Data for break-up speeds in Prudhoe Bay were based on a study by Oceanographic Services, Inc. (1980). Table 4.20 summarizes the results of the data analysis.

TABLE 4.20

Break-up speed Prudhoe Bay

STATION NO.	DISTRIBUTION TYPE	μ_{DATA} (cm/s)	σ_{DATA} (cm/s)	χ^2	LOS	COMMENTS
1	Lognormal	4.140	3.08	17.198	0.004	5 Minute
	Exponential	4.140	3.08	54.633	0.000	Movements
	Gamma	4.140	3.08	8.985	0.110	
	Lognormal	2.291	1.934	4.132	0.127	1 Hour
	Exponential	2.291	1.934	1.384	0.709	Movements
	Gamma	2.291	1.934	2.772	0.250	
3	Lognormal	7.534	7.800	110.411	0.000	5 Minute
	Exponential	7.534	7.800	138.105	0.000	Movements
	Gamma	7.534	7.800	142.222	0.000	
	Lognormal	5.055	6.005	5.471	0.361	1 Hour
	Exponential	5.055	6.005	5.246	0.513	Movements
	Gamma	5.055	6.005	7.599	0.180	

TABLE 4.20 (continued)

STATION NO.	DISTRIBUTION TYPE	μ_{DATA} (cm/s)	σ_{DATA} (cm/s)	χ^2	LOS	COMMENTS
4	Lognormal	12.429	9.768	61.392	0.000	5 Minute
	Exponential	12.429	9.768	75.505	0.000	Movements
	Gamma	12.429	9.768	67.659	0.000	
	Lognormal	4.549	5.552	6.155	0.188	1 Hour
	Exponential	4.549	5.552	7.066	0.315	Movements
	Gamma	4.549	5.552	8.558	0.128	
All Stations	Lognormal	8.018	8.157	99.894	0.000	5 Minute
	Exponential	8.018	8.157	146.903	0.000	Movements
	Gamma	8.108	8.157	151.361	0.000	
	Lognormal	4.177	5.225	4.325	0.633	1 Hour
	Exponential	4.177	5.225	5.148	0.642	Movements
	Gamma	4.177	5.225	9.287	0.158	

Figure 4.11 shows the area where the stations were located. There is a large difference between the means of the 5-minute movements and the 1-hour movements. The difference can be attributed to the fact that 1-hour measurements are averaged over a longer period of time (1 hour) than 5-minute speeds.

The distribution selected to represent the break-up speeds in the Prudhoe Bay area is the Exponential distribution, based on the 1-hour measurements from all stations.

EXPONENTIAL

μ = 4.177 cm/s

σ = 4.177 cm/s

The original data is listed in Table C.23 found in Appendix C.

4.2.4.3 Other break-up parameters

Table 4.21 summarizes the break-up parameters which have been defined in previous sections of this report.

4.2.5 Ice Behaviour

4.2.5.1 Elastic modulus of ice

Values of the elastic modulus of ice vary in a wide range depending on the type of ice and loading direction (Lainey and Tinawi, 1984). A deterministic value of 5 GPa was selected for this study.

4.2.5.2 Poisson's ratio of ice

This parameter was assigned a deterministic value of 0.3 (Hutter, 1975).

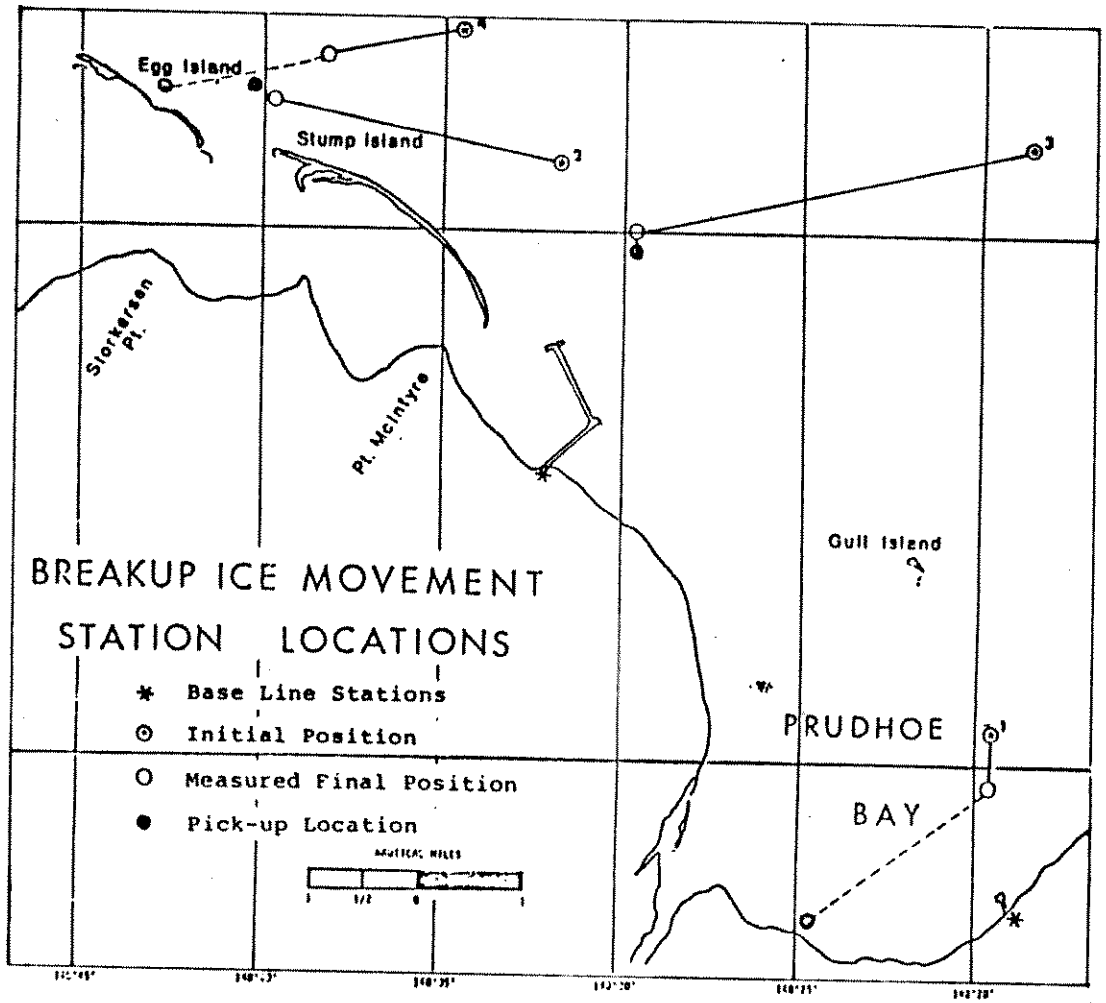

Figure 4.11. Location of Break-up Speed Measurement Stations
(Oceanographic Services, Inc., 1980)

TABLE 4.21

Break-up parameters

Parameter	Report Section Referenced
First-year ridge coverage	4.2.3.8
First-year ridge height	4.2.3.3
First-year ridge length	4.2.3.14
First-year ridge friction angle	4.2.3.7
First-year ridge cohesion	4.2.3.6
Level ice crushing strength	4.2.3.9
Mean of extremal pressure component	4.2.3.12
S.D. of extremal pressure component	4.2.3.12
Multi-year floe concentration	4.2.3.17
Multi-year floe speed	4.2.2.2
Multi-year ice crushing strength	4.2.2.11
Multi-year ridge coverage	4.2.2.14
Multi-year ridge height	4.2.2.13
Multi-year ridge length	4.2.2.12
Environmental driving force	4.2.3.19

4.2.5.3 Creep constants

The reference stress method was used to calculate the forces exerted by the ice on the structure, as will be discussed in Section 5.4.1.2. The basic creep law for ice is as follows:

$$\dot{\varepsilon} = A\sigma^{n}$$

where A is the creep multiplier

n is the creep exponent

Both n and A are treated as deterministic values. The creep exponent is taken as n = 3, Sinha (1981). The creep multiplier A was determined from the slope of strain rate-maximum stress curve for in situ tests on specimens stressed in a direction perpendicular to the c-axis (Wang, 1979). This lead to a value of $A = 10^{-5}(MPa)^{-3}.s^{-1}$.

4.2.6 Default values

The default values are listed in Table 4.22. In many cases, these values were based Chi-Square fits to actual data. Those parameters highlighted by a single asterisk (*) indicate the use of limited data along with experience and judgment. Those with double asterisks (**) were based solely on the researchers' estimates.

Table 4.22 contains only those parameters which were used in the final model. Some environmental parameters were analyzed in the initial stages of the study, but were later found to be unnecessary for the selected models (e.g. linear ridge frequency). These parameters were included in the previous sections of this chapter for completeness, but do not appear in Section 4.22.

TABLE 4.22

Parameter Default values

PARAMETER	DISTRIBUTION TYPE	DISTRIBUTION PARAMETERS	COMMENTS
Start of break-up Canadian Beaufort	Normal	μ = 173 days ≡ June 22 σ = 18.1 days	
End of break-up Canadian Beaufort	Normal	μ = 187 days ≡ July 6 σ = 22.9 days	
Freeze-Up Canadian Beaufort	Normal	μ = 309 days ≡ Nov. 5 σ = 22.8 days	
Start of break-up Prudhoe Bay	Normal	μ = 199 days ≡ July 18 σ = 20.6 days	

TABLE 4.22 (continued)

Parameter Default values

PARAMETER	DISTRIBUTION TYPE	DISTRIBUTION PARAMETERS	COMMENTS
End of break-up Prudhoe Bay	Normal	μ = 219 days ≡ Aug. 7 σ = 24.3 days	
Freeze-Up Frudhoe Bay	Normal	μ = 310 days ≡ Nov. 6 σ = 21.8 days	
Summer multi-year floe speeds	Gamma	μ = .171 m/s σ = .132 m/s	
Multi-Year floe thickness-Winter and Summer*	Gamma	μ = 3.89 m σ = 1.584 m	
Multi-year ice concentration Summer - Canadian Beaufort	Beta	μ(0-20)=.2/10 σ(0-20)=.7/10 μ(20-40)=.3/10 σ(20-40)=1./10 μ(40-60)=.4/10 σ(40-60)=1.2/10 μ(60-80)=.6/10 σ(60-80)=1.6/10 μ(80-100)=.7/10 σ(80-100)=1.8/10 μ(100-120)=.9/10 σ(100-120)=2.0/10 μ(120-140)=.9/10 σ(120-140)=2.1/10 μ(140-160)=1.3/10 σ(140-160)=2.4/10	(.-.) represents the range of distance offshore north of North Point.
Multi-year ice concentration Summer - U.S. Beaufort	Beta	μ(0-20)=1.1/10 σ(0-20)=1.3/10 μ(20-40)=1.1/10 σ(20-40)=2.1/10 μ(40-60)=1.5/10 σ(40-60)=2.5/10 μ(60-80)=1.7/10 σ(60-80)=2.8/10	(.-) represents the range of distance offshore north of Prudhoe Bay

TABLE 4.22 (continued)

Parameter Default values

PARAMETER	DISTRIBUTION TYPE	DISTRIBUTION PARAMETERS	COMMENTS
Ice island fragment diameter	Numerical	μ=70.0 m σ=43.1 m	
Ice island diameter*	Numerical	μ=12.5 km σ=7.07 km	Inferred from cracks in ice shelves
Ice island/ fragment thickness*	Numerical	μ=39.75 m σ=14.5 m	Inferred from the thickness of ice shelves
Ice island/fragment summer speed*	Gamma	μ=.171 m/s σ=.132 m/s	Assumed to be the same as multi-year floe speed
Ice island density Canadian Beaufort*	Deterministic	μ=.066 islands per 1 million km^2	
Ice island density U.S. Beaufort*	Deterministic	μ=.135 islands per 1 million km^2	
Ice island fragment density Canadian and U.S. Beaufort*	Deterministic	μ=6.6 fragments per 1 million km^2	
Multi-year ice average pressure**	Exponential	μ=0.5 MPa σ=0.5 MPa	
Multi-year ice flexural strength*	Normal	μ=0.25 MPa σ=0.15 MPa	
Multi-year ridge length**	Deterministic	μ=136.8 m	
Multi-year ridge height*	Exponential	μ=0.9 m σ=0.9 m	

TABLE 4.22 (continued)

Parameter Default values

PARAMETER	DISTRIBUTION TYPE	DISTRIBUTION PARAMETERS	COMMENTS
Multi-year ridge coverage*	Deterministic	30%	
Multi-year floe diameter	Gamma	μ=100.3 m σ=150.7 m	
Ice island/fragment average ice pressure*			Same as multi-year ice
First-year level ice growth rate	Deterministic	.0085	Monthly mean ice thicknesses are calculated from growth rate
Peak landfast ice speed			
water depth			
0-6.1 m	Numerical	$\mu=8.2\times10^{-5}$ m/s $\sigma=5.4\times10^{-5}$ m/s	
6.1-12.2 m	Numerical	$\mu=8.7\times10^{-5}$ m/s $\sigma=8.2\times10^{-5}$ m/s	
12.2-18.3 m	Numerical	$\mu=9.3\times10^{-5}$ m/s $\sigma=6.9\times10^{-5}$ m/s	
> 18.3 m	Numerical	$\mu=1.5\times10^{-4}$ m/s $\sigma=2.4\times10^{-4}$ m/s	
First-year ridge height			
Shear Zone	Exponential	μ=0.9 m σ=0.9 m	
Pack Zone	Exponential	μ=0.69 m σ=0.69 m	
First-year ridge cohesion	Deterministic	μ=0.035 MPa	

TABLE 4.22 (continued)

Parameter Default values

PARAMETER	DISTRIBUTION TYPE	DISTRIBUTION PARAMETERS	COMMENTS
First-year ridge friction angle	Deterministic	$\mu=25^{o}$	
First-year ridge coverage	Deterministic	$\mu=30\%$	
First-year ice average pressure**	Deterministic	$\mu=0.3$ MPa	
Extremal component first-year ice average pressure**	Double Exponential	$\mu=0.2$ MPa $\sigma=0.15$ MPa	
First-year ice flexural strength*	Deterministic	$\mu=0.20$ MPa	
Extremal component first-year ice flexural strength**	Double Exponential	$\mu=0.1$ MPa $\sigma=0.05$ MPa	
First-year ridge length**	Deterministic	$\mu=150$ m	
Winter ice speed shear and pack zone	Gamma	$\mu=0.062$ m/a $\sigma=0.073$ m/s	
Multi-year ice concentration winter U.S. and Canadian Beaufort*	Beta	$\mu=0.2$ tenths $\sigma=0.4$ tenths	
Pack ice pressure*	Normal	$\mu=0.05$ MPa $\sigma=0.05$ MPa	

TABLE 4.22 (continued)

Parameter Default values

PARAMETER	DISTRIBUTION TYPE	DISTRIBUTION PARAMETERS	COMMENTS
Break-up speed Prudhoe Bay	Exponential	μ=0.042 m/s σ=0.042 m/s	Same for Canadian Beaufort
Break-up thickness first-year ice	Deterministic	μ=1.5 m	
Elastic modulus of ice	Deterministic	5 GPa	
Poisson's Ratio	Deterministic	0.3	
Creep Constants			
Exponenent	-	3	
Multiplier	-	$10^{-5}(MPa)^{-3}s^{-1}$	

* Based on limited data combined with judgment
** Based on judgment

4.2.7 Discussion of results

For the most part, the data analysis led to satisfactory results regarding input parameter distribution types and parameters. The criterion which was selected in order for a distribution to be considered a "good fit" for a given set of data was a level of significance greater than or equal to 0.05. In some instances, however, the data set was too coarsely defined (i.e. too few bins for the number of data points) to meet the 0.05 level of significance criterion. To overcome this problem, several strategies can be used. They are as follows:

i) sensitivity analysis;
ii) using the original histogram; and
iii) performing the Chi-squared test on the tail portion of the data.

It was felt that sensitivity analysis to the distribution type could be left to the discretion of the user. Using the final model the distribution types for any parameter can be varied to determine their influence on the final outcome.

Using the original histogram, or describing the data as a numerical distribution, is a very appropriate solution to the problem. The program allows the user to define the cumulative density function for a given parameter, with a maximum of 20 points. The model then uses this numerical distribution as a description of the parameter concerned.

Finally, a Chi-squared test can be performed on the tail portion of the data. The justification for this action is that it is the latter portion of the data which is of primary interest in the current model.

As an example of how this method is applied, the summer multi-year floe speeds were examined. Table C.7 in Appendix C lists the raw data, which have too many data points for the number of bins, consequently no fit is possible based on the Chi-squared goodness of fit test. When the data is analyzed more closely, a trend towards obtaining a "better fit" for the gamma density functions was evident, as the Chi-squared test is applied to the tail portion of the data. This finding supports the use of the gamma density function despite the low value of the level of significance over the whole data range.

Chapter 5

ICE-STRUCTURE INTERACTION MODELS

5.1 General

In order to estimate ice-structure interaction loads, the ice is usually idealized in two respects, namely geometry and constitutive behaviour. Geometric idealizations are needed to allow the use of structural analysis theories which are developed for man-made structural elements with regular geometries. Examples are the idealization of an ice sheet as an homogeneous plate with uniform thickness, or the idealization of a ridge as a beam with uniform cross-section. Combined with appropriate models of the stress-strain relationship of ice, the interaction process can be analyzed and the force between the ice and the structure calculated.

In a global sense, ice acts as a medium to transmit such environmental forces as winds and currents to the structure. Consider, for example, an ice floe moving at a constant velocity (i.e. in equilibrium) under the effects of wind/current drag, and forces from surrounding ice. If the floe motion is obstructed by a rigid structure, forces develop in the contact zone which introduce accelerations to the floe motion. The maximum force on the structure will be governed by one of the two folllowing conditions (Croasdale, 1980):

a) The interaction may end if the forces exerted by the structure introduce sufficient inertial forces to stop the floe or change its direction of motion such that it loses contact with the structure. This is a global consideration which requires modelling the ice movement under the environmental driving forces and the forces exerted on the ice by the structure.

b) If the driving forces are sufficiently high, the condition described in a) above may not be reached before the structure is fully enveloped in the ice feature, as shown in Figure 5.1 b. In this case the contact width is at its maximum value and the local indentation problem reaches its steady-state maximum load. Any further energy dissipation will occur at the same load level, and the maximum load can therefore be calculated from a local model.

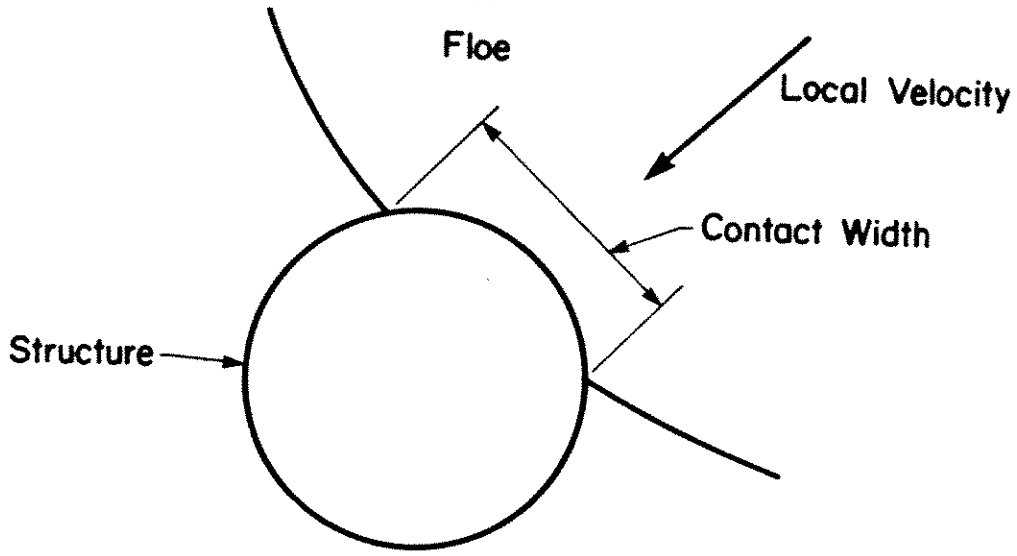

(a) Transitional Case of Increasing Contact Width

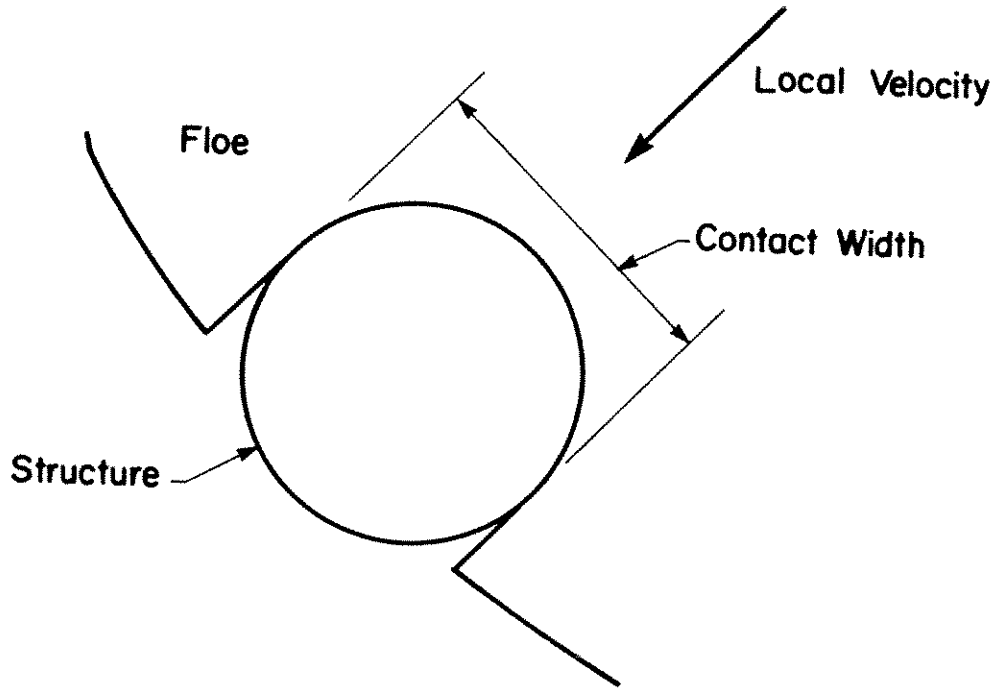

(b) Steady State Case of Maximum Constant Contact Width

Figure 5.1. Illustration of the transitional and steady state cases

The applicability of either of the conditions a) and b) mentioned above depends on the interaction scenario and the magnitude of the driving forces in comparison to the potential local forces between the ice and the structure. If the driving forces transferrable to the structure are large, condition b) is likely to apply and a local model based on the deformation of the ice in the interaction zone is appropriate. An example of this case is the movement of a first-year ice cover against the stucture. The ice cover is usually large enough so that its movement will not be affected by the structure. The structure is fully embedded in the ice, and the force can be calculated from the failure or creep stresses of the ice along the width of the structure, depending on the rate of movement.

On the other hand, if the driving forces transferrable to the structure are small in comparison to the potential local forces, the maximum local forces will not be reached. The use of a local model would lead to an overestimation of the load and thus a global model as described in a) above is necessary. It is essential in a probabilistic analysis of the present type that these aspects be adequately accounted for to eliminate a systematic overestimation of the load values. The main scenarios for which this consideration applies are those associated with multi-year floes and ice islands. Impacts with such features are generally eccentric, and a portion of the original kinetic energy of the feature will be dissipated in rotation. This is true even for cases where the multi-year floe is surrounded by first-year ice. The first-year ice will exert stresses on the multi-year floe which are of the same order of magnitude as the ridge building stresses. Once the local ice structure interaction force reaches a value which equilibrates this force (considering other inertial forces), the multi-year floe starts to move relative to the surrounding first-year ice and the floe can rotate and clear around the structure. A multi-year ridge is a locally thickened part of a multi-year floe, which can exert higher local forces on the structure. These forces, however, contribute to the overall floe movement and this factor should be taken into account.

As shown in Table 5.1, the different loading types corresponding to different features in the three seasons considered can be categorized in three major interaction cases. These cases along with the approach used for each are summarized in Table 5.1. After a brief discussion of the constitutive behaviour of ice, the models developed and used for each of the cases in Table 5.1 will be discussed.

TABLE 5.1

Approaches used for different ice-structure interaction models

Case	Scenarios	Force Calculation Approach
Areal Feature Interaction	- MY Floes in all seasons (with MY ridges) - Ice islands	Global ice feature load model
Level Ice	- Winter full FY ice cover (all zones) - Break-up partial ice cover (all zones)	Local force model
Linear Ice Rubble	- FY ridges in the active ice zone (winter and break-up)	Local force model

5.2 The Mechanical Behaviour of Ice

The estimation of ice-strucure interaction forces is highly dependent on the postulated material behaviour of ice. This is true for both local models, which are based entirely on stress analyses of the ice, and global models, which require the definition of a force-penetration curve for the ice. In this section, the key aspects to the behaviour of ice and the chosen material models for the different types of interaction are discussed. Two types of ice will be considered, namely intact ice and rubble. The properties of rubble are needed for the evaluation of forces from first year ridges, whereas the properties of the intact ice are needed for all other loading scenarioes.

5.2.1 The mechanical behaviour of intact ice

For the present study, the material behaviour of ice is modelled according to the mode of ice deformation in each type of interaction as follows:

a) **Indentation:**

This covers the movement of first-year or multi-year ice against a vertical-sided structure. In this mode, the dominant type of ice behaviour depends on the deformation rate. In the landfast ice zone, average ice speed during the winter season is approximately 0.5 m/hr. For a 100-m wide structure, this corresponds to a nominal strain rate of about 1.4×10^{-6} (see Secton 5.5 for details of calculating the strain rate), which is well below the creep-crushing transition strain rate of about 10^{-3}. Under these conditions creep dominates the interaction. The ice flows around the structure and does not fail. The secondary creep law for ice is given by (Sinha, 1981):

$$\dot{\varepsilon} = A\sigma^{n} \qquad (5.1)$$

where $\dot{\varepsilon}$ is the strain rate;

σ is the stress; and

A,n are the creep constants of ice.

Experimental evidence (Sinha, 1981, and Lainey and Tinawi, 1984) indicates that $n = 3$ and that $A = 10^{-5}(MPa)^{-3}\ sec.^{-1}$.

The creep law in Eq. (5.1) is for uniaxial loading under a constant stress σ. The use of this law to derive a solution for the indentation problem under a constant velocity is the subject of Section 5.5.

For other load scenarios, such as summer impacts, and high rate winter and break-up interactions with first-year ice, ice velocities are high enough to result in local crushing of the ice. Three different types of behaviour will take place, depending on the distance from the indenter, as shown in Figure 5.2. The intact ice in Zone I will behave as a visco-elastic material as discussed earlier. Zone II contains a progressively damaged material which provides the transition between the intact ice in zone I and the completely crushed ice in Zone III. Such failure patterns have been observed in small-scale and large-scale indentation tests (Kurdyumov and Kheisin, 1976, and Timco, 1986), and have been recognized as the key aspects to proper modelling of the indentation problem. In fact, some analytical work has been carried out (Tomin, et.al., 1986) in this area, but this is still in the early stages of development.

The most common presently available approach to model the ice response in indentation is based on deducing the crushing strength of ice from its uniaxial strength by multiplying the latter by several factors (Korzhavin, 1962). These factors represent the effects of multi-axial confinement, incomplete contact, loading rate, and shape of the structure, and are usually determined using semi-empirical approaches. For example, the indentation factor which quantifies the multi-axial stress effects can be determined as a function of the aspect ratio

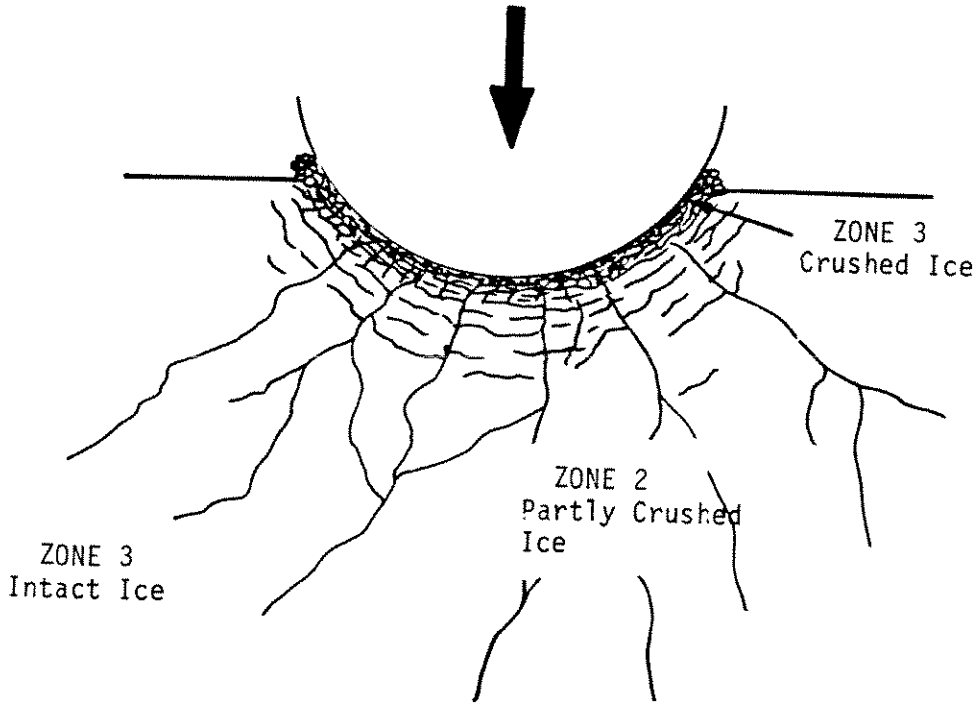

Figure 5.2. Illustration of the ice response for high speed indentation

(ratio between contact width and ice thickness) based on the theory of plasticity (Michel and Toussaint, 1977). Also the contact area reduction factor can be quantified on the basis of a statistical approach which assumes that crushing occurs independently at different small zones within the contact area (Kry, 1977).

In the present study, a constant average indentation pressure is used for each interaction event. This value is randomly selected from the probability distributions given in Chapter 4 for this parameter. The ice is assumed to be a rigid-crushing material, and the deformation of ice beyond the crushing zone is not accounted for. The rationale behind this choice is summarized as follows:

i) At high loading rates, the deformations of ice beyond the crushing zone are small and the interaction will be governed by the flow of the crushed ice.

ii) Experimental evidence from large-scale tests indicates that the use of empirical indentation constants to extrapolate from small-scale test results gives unrealistically high loads. This is due to the imperfections and weaknesses in natural ice which do not exist in laboratory ice. Also, the assumptions used in the determination of the indentation factors do not model the actual phenomena which have been observed in recent indentation tests, as discussed earlier.

iii) For global load evaluation it is sufficient to estimate the average pressure, and details of the pressure distribution are not needed.

iv) The dependence of the average pressure on the aspect ratio (ratio between the contact width and the ice thickness) is very weak for high aspect ratios, which are characteristic of Beaufort Sea structures. This can be seen in Figure 5.3 (Marcellus and Morrison, 1982), where the slope of the average pressure versus aspect ratio curve is very flat for aspect ratios higher than 10.

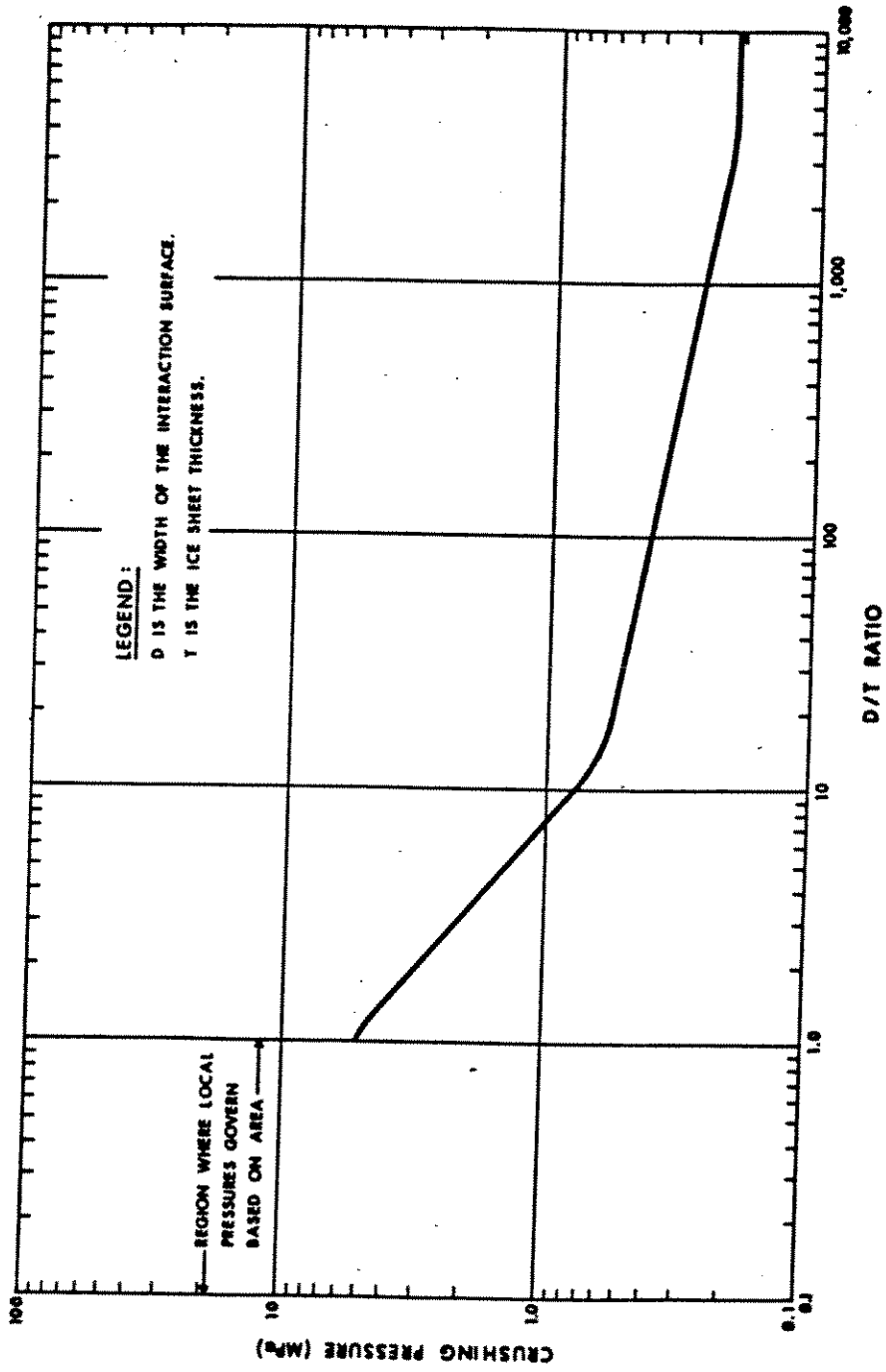

Figure 5.3. Pressure–Aspect Ratio Relationship (Marcellus and Morrison, 1982)

The average ice pressure should be based on the best large-scale experimental evidence available.

b) Bending

Ice fails in bending against sloping structures. The bending resistance of ice is not a basic property, but is a manifestation of its tensile resistance. Ice is an extremely brittle material with low tensile resistance. Since conical structures in the landfast ice zone are not considered in this study, loading in bending will always be at relatively high rates. Elasticity dominates the ice behaviour at high rates and, therefore, elastic behaviour is used throughout the study for ice deformations in bending.

5.2.2 The behaviour of ice rubble

Ice rubble behaves like a granular material (Prodanovic, 1981). The shear strength (τ) of ice rubble can be expressed as a function of its cohesion c and angle of friction ϕ as follows:

$$\tau = c + \sigma \tan\phi \qquad (5.2)$$

where σ is the normal stress on the shear plane.

This granular material model is used in the study for calculating loads from first-year ridges.

5.3 Areal Feature Interactions

This case covers interactions with areal features, such as ice islands and multi-year ice floes. It covers both open-water summer collisions, and closed-water interactions where the feature is surrounded by first-year ice. Multi-year ridges within a multi-year floe are also considered as part of this model. For this case, a detailed ice-structure interaction model, which accounts for the global considerations of the feature motion, was developed. Such a model was deemed appropriate for the following reasons:

1. Multi-year ice is believed to be the most serious hazard which would govern the design load in most cases.

2. Maximum forces calculated from local failure stresses are seldom reached in this case. This is due to the fact that an ice feature collision with a structure is generally eccentric, causing some of the initial kinetic energy to be transformed into rotation. In most cases, the initial kinetic energy of the ice feature will be completely dissipated (i.e. the ice feature stops) and/or the ice feature will clear around the structure before there is enough local penetration to expose the full width of the structure to the ice. The maximum force in such cases will be lower than that based on maximum local forces. This effect was accounted for to avoid force over estimation.

3. Some of the proposed force models for multi-year ice featues give upper bound forces based on assumptions which are not consistent with a probabilistic analysis. The treatment of multi-year ridges as beams, for example, assumes that they move perpendicular to their longitudinal axis and that they are loaded up to failure by a point load in the middle. Considering that ridges are randomly oriented and that they are usually embedded in multi-year floes in which the structure penetrates only a limited distance, the above-mentioned beam assumptions can be seen to have a small probability of occurrence. Moreover,

the average length of multi-year ridges is about 150 m. For structures in the order of 100-m wide, the point load assumption is unrealistic. A random floe model was developed to assess the probability of encountering a ridge during interaction with a multi-year floe. The height and orientation of the ridge were modelled probabilistically, and the probability of encountering a ridge in a given penetration distance was calculated. Details of this model are given in Appendix B. Based on this analysis, it was decided that multi-year ridges should be incorporated in the overall multi-year floe crushing model. This allows probabilistic modelling of their orientation and point of contact, and allows for the consideration of the effect of load increases due to the local thickening of the ice on the overall floe motion.

The overall model is depicted in Figure 5.4. The ice feature can be embedded in first-year level ice as shown in the figure, or it can be free-floating. The problem can be divided into two distinct parts as follows:

1. The overall interaction problem, which deals with the motion of the feature under the forces acting on it.

2. The local problem, which is concerned with the calculation of the local forces between the feature and the structure.

Even with simple assumptions regarding the constitutive behaviour of ice (as discussed in Section 5.2.1), the problem is non-linear. There is a geometric non-linearity which results from the interdependence between the local force and the movement of the ice feature. It is noted that energy models have been used before for open-water, free-floating features (e.g. Fidjestoel, 1983). This methodology is extended here to include the effects of forces from surrounding ice and to account for local variations in thickness due to the encounter of ridges.

The overall interaction problem and the local interaction problem will be discussed separately in the following sections.

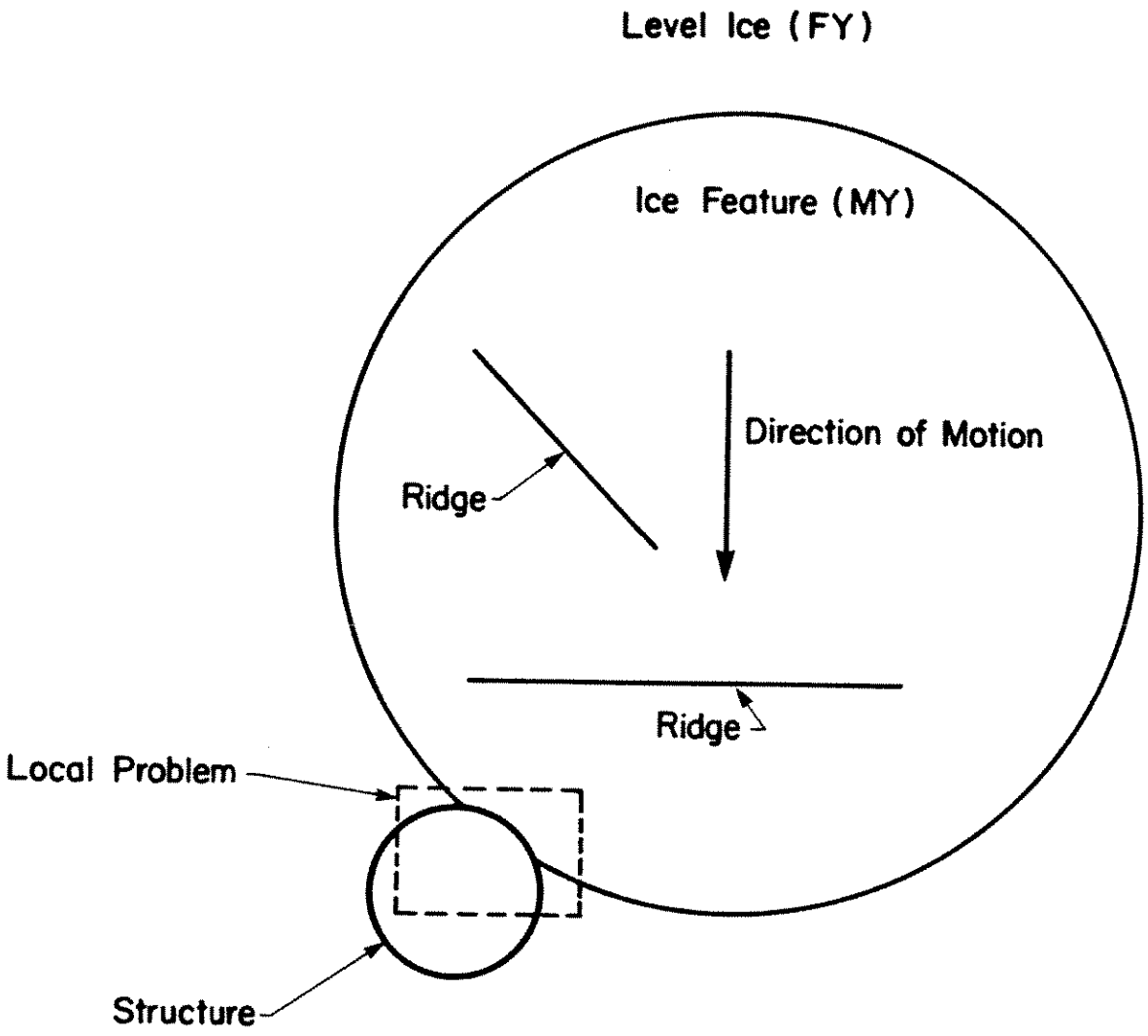

Figure 5.4. Overall areal feature collision model

5.3.1 Overall areal feature model

The forces acting on an ice feature as it interacts with a structure are depicted in Figure 5.5. The assumptions made are as follows:

i. The ice feature is circular with radius R_f and uniform average thickness t_f.

ii. There is no friction between the multi-year floe and the surrounding ice.

iii. There is no relative translation between the ice feature and the surrounding ice in the initial stages of interaction. Relative translation starts when the force exerted on the floe by the structure reaches the maximum force which can be sustained by the first-year ice along its contact with the floe, causing the floe to "break-out" from the surrounding ice. This break-out force is equal to the ridge-building force.

iv. After the break-out event disccused in (iii.) above, the pressure on the ice feature from the surrounding ice is uniformly distributed along a line perpendicular to the direction of the relative velocity between the ice feature and the surrounding ice.

v. The velocity of the surrounding ice remains constant throughout the interaction.

The equations governing the motion of the feature are as follows:

$$\{F(t)\} = (m)\{a(t)\} \tag{5.3}$$

$$\{V_G(t)\}_{3x1} = \{V_{G0}\}_{3x1} + \int_0^t \{a(t)\}_{3x1}\,dt \tag{5.4}$$

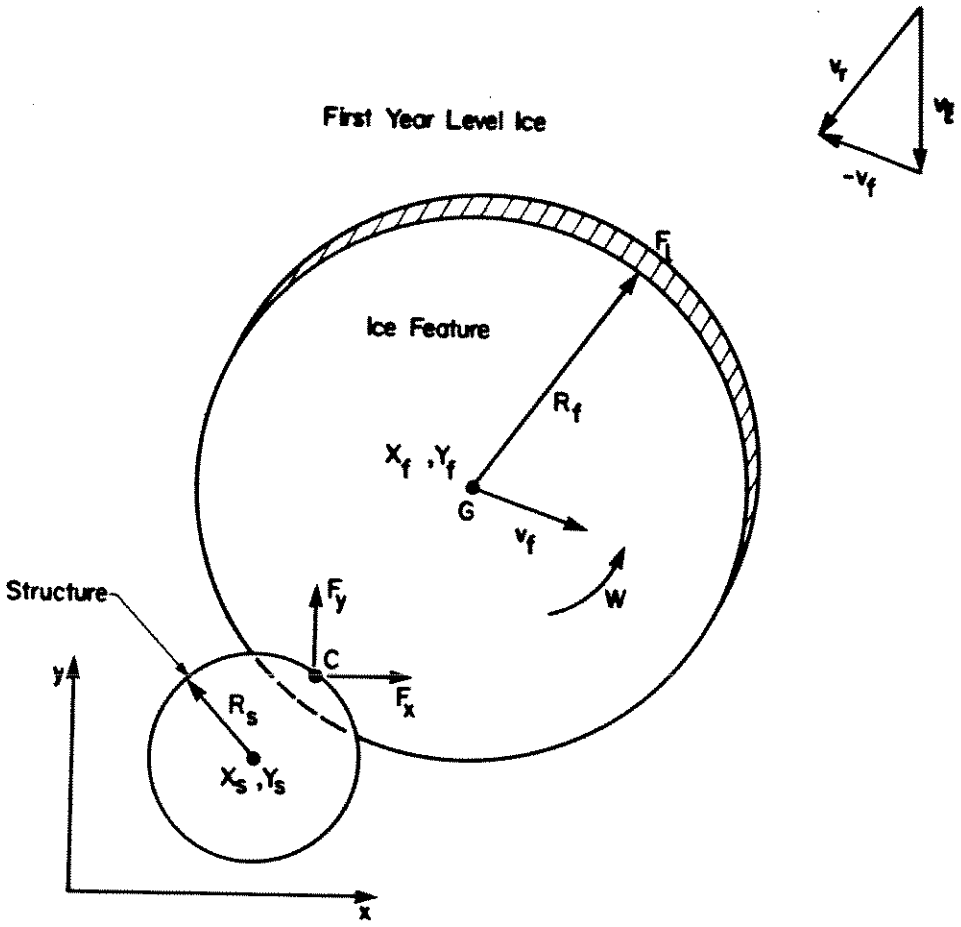

v_l = First Year Level Ice Velocity

v_f = Ice Feature Velocity

v_r = Relative Velocity Between Multiyear Floe and First Year Ice

F_l = First Year Level Ice Force or Multiyear Floe

F_x , F_y = Forces Exerted by Structure on Multiyear Floe

Figure 5.5. Closed water interaction model

$$\{X_G(t)\}_{2x1} = \{X_{G0}\}_{2x1} + \int_0^t \{V_G(t)\}_{2x1} dt \tag{5.5}$$

$$\{V_C(t)\}_{2x1} = (T(t))_{2x3}\{V_G(t)\}_{3x1} \tag{5.6}$$

where F is the resultant of the forces acting on the feature, m is the mass, a is the acceleration, V is the velocity, X is the centroid location, T is a transformation matrix from global to local velocity, and t is the time. Subscripts G and C refer to points G and C on Figure 5.5, and denote global and local motion parameters, respectively. Subscript 0 denotes the value of a parameter at t = 0. The parameters in Equations 5.3 to 5.6 are all in vector and matrix form, with the dimensions given as subscripts to the vector or matrix in each case. These matrices contain the standard parameters of planar motion.

The vector $\{F(t)\}$ can be given as:

$$\{F(t)\}_{3x1} = \{F_C(t)\}_{3x1} + \{F_\ell(t)\}_{3x1} \tag{5.7}$$

where $F_c(t)$ is the force from the structure on the ice feature, and $F_\ell(t)$ is the force from the surrounding level ice. Based on assumption (iv) above, $F_\ell(t)$ can be expressed as:

$$\{F_\ell(t)\}_{3x1} = (c)_{3x3}\{V_\ell - V_G(t)\}_{3x1} \tag{5.8}$$

where

$$(c) = \frac{2\sigma_s t_s R_f}{V_r} \begin{matrix} 1 & 0 & 0 \\ 0 & 1 & 0 \\ 0 & 0 & 0 \end{matrix}$$

and σ_s = stress from surrounding ice;
t_s = thickness of surrounding ice;
R_f = radius of ice feature; and
V_r = magnitude of the velocity of the surrounding ice relative to the ice feature.

The local contact force can be expressed as a function of the feature position and local velocity as:

$$\{F_C(t)\}_{3x1} = \{F_C(X_G,\ V_C,\ t)\}_{3x1} \tag{5.9}$$

Details of equation (5.9) constitute the local force model which will be discussed in Section 5.3.2 for different structural geometries.

Using Equations (8) and (9) in equation (7) leads to:

$$\{F(t)\}_{3x1} = \{F_C(X_G,\ V_C,\ t)\}_{3x1} + [c]_{3x3}\ \{V_\ell - V_g(t)\} \tag{5.10}$$

Equations (5.3) to (5.6) and (5.10) can be solved in a time-stepping algorithm to obtain a time history of any of the time-dependent parameters. The problem is non-linear due to the interdependence between the forces and the motion of the ice feature. Newmark's Beta method (Bathe and Wilson, 1976) is used in an iterative solution to reduce the error at the end of each time step to an acceptable tolerance.

The solution of the problem begins by determining the position of the floe upon initial contact, and the initial contact point. This can be obtained from the geometry of the problem as shown in Figure 5.6. For the axisymmetric circular structure in Figure 5.6(a), the eccentricity, e, between the floe centre and the centre of the

structure is given. This can be used to write the equations of the floe perimeter at an arbitrary position along the y axis and the perimeter of the structure in a set of x-y axes, which have the centre of the structure as an origin, and are parallel and perpendicular to the approach velocity direction. The point of contact is the point on the structure which is closest to the floe perimeter along the y axis (i.e. point which minimizes the distance y in Figure 5.6(a)). For a polygonal structure (see Figure 5.6(b)), the problem is not axisymmetric and the approach angle α is also required as input. Since the structure is originally defined in a fixed set of axes (x_o-y_o), a transformation must be applied first to rotate these axes through an angle α. The equations of the sides of the structure can then be defined in the x-y axes and the point of contact can be obtained by minimizing the distance along the y-axis between the structure and the floe as before. The coordinates of the floe centre at initial contact can then be found from simple geometry.

The interaction continues until one of the following conditions is satisfied:

i. The kinetic energy of the ice feature is reduced to zero (i.e. the feature stops);

ii. The centroid of the ice feature starts to move away from the centroid of the structure. This signifies the clearing of the ice feature; or

iii. The ice feature begins to move away from the structure in the local contact area. This condition is illustrated in Figure 5.7 and signifies loss of contact between the ice feature and the structure.

The maximum allowable interaction time is two hours. Although test runs show that this limit is not expected to be reached, it is imposed as a programming safety feature.

5.3.2 Local force models

The objective of local force models is to determine the force between the ice feature and the structure as a function of the position of the ice feature (the penetration), and the local feature velocity at the contact point (i.e. to define the

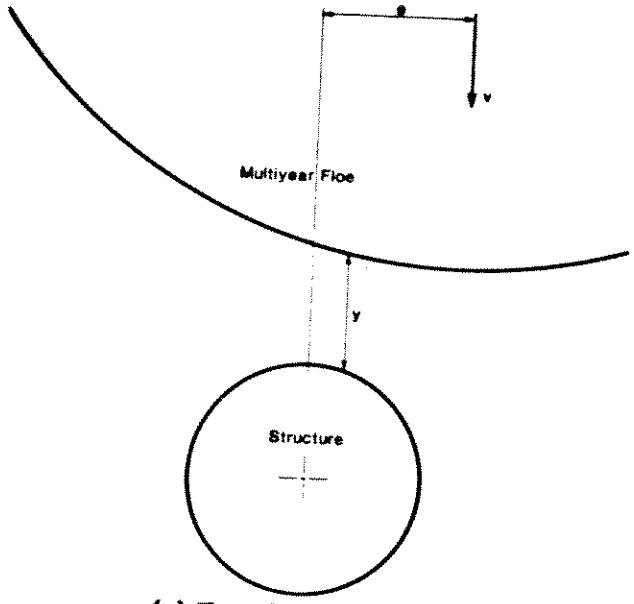

(a) For circular structure

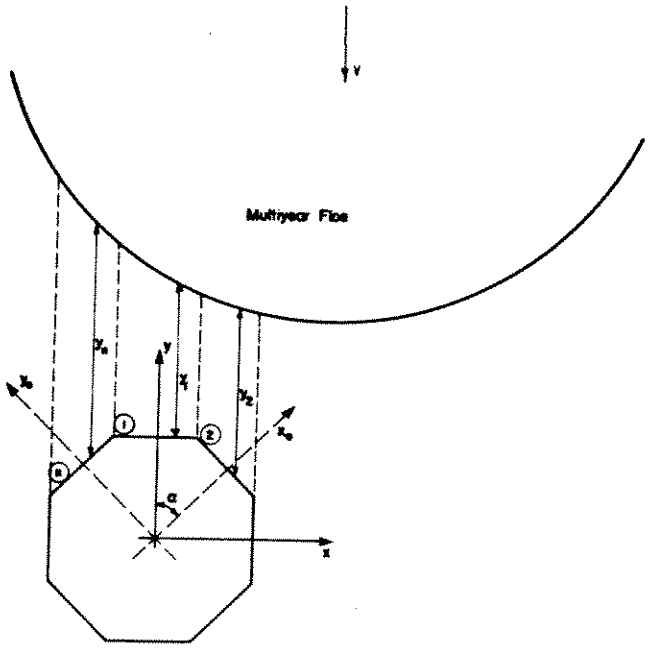

(b) For polygonal structure

Figure 5.6 Illustration of the location of the initial ice feature contact position

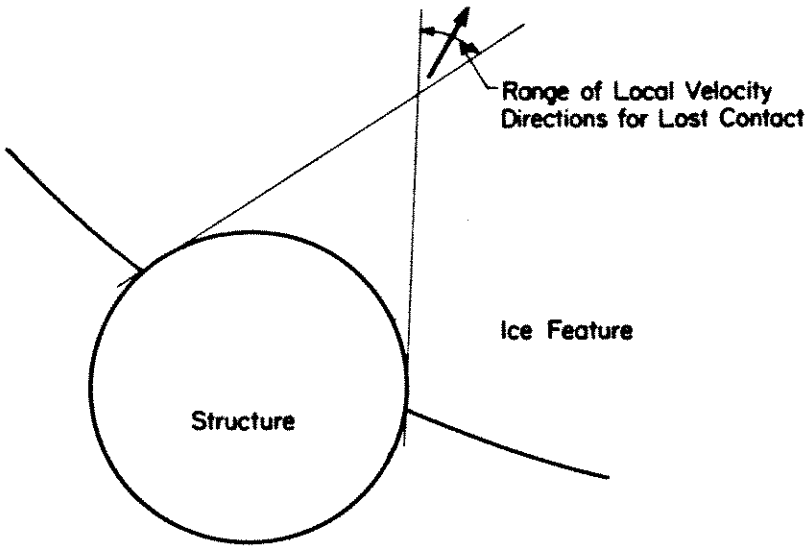

(a) Circular structure

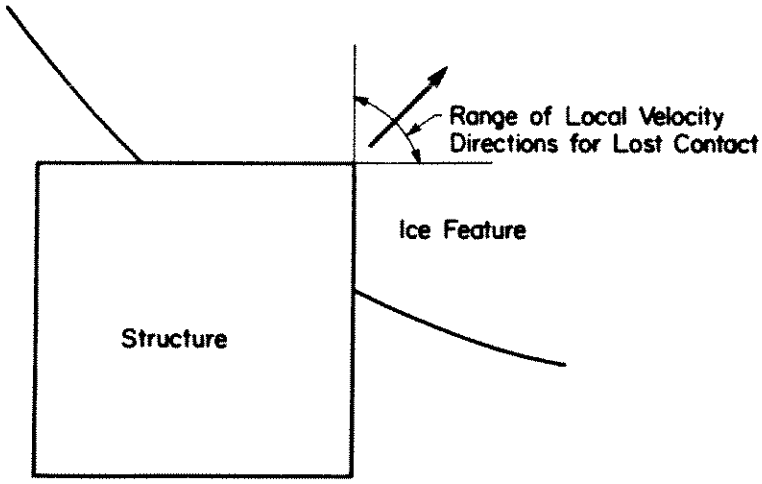

(b) Polygonal structure

Figure 5.7 Illustration of local velocity directions signifying loss of contact between the ice feature and the structure

relationship in Equation 5.9). The main assumption regarding the ice response is that the direction of the resultant local force in the horizontal plane is opposite to the direction of the local velocity. The magnitude of the force depends on the structural geometry. Models used for vertical structures and conical structures will be discussed separately in the following.

5.3.2.1 Vertical-sided structures

The local force on a vertical structure is obtained by multiplying the average ice pressure by the projection of the contact area on a plane perpendicular to the direction of the local velocity. For penetration in flat ice, the projected contact area is obtained by multiplying the ice thickness by the projected width shown in Figure 5.8. The projected width is defined as the distance in a direction perpendicular to the local velocity between the extreme points of the part of the structure embedded in the ice feature. This width is obtained by rotating the axes through the angle of the local velocity direction (new axes are denoted x_l-y_l in Figure 5.8), and locating the points on the structure which are inside the floe and have extreme y_l-coordinates. The contact width is the difference between $y_{l\,max}$ and $y_{l\,min}$ as shown in Figure 5.8.

If a ridge is encountered within the floe, the force is calculated in the same manner as for flat ice, using the actal shape of the contact area. The Kovacs idealized multi-year ridge cross-section (Wright et.al., 1978) is used (see Figure 5.9). Given the ridge orientation upon coming in contact with the structure, the initial point of contact can be found in a similar manner as discussed in Section 5.3.1 for the initial contact of the ice feature. Due to the variation of thickness in the ice, the contact area has an irregular shape, as shown in Figure 5.10, and must, therefore, be calculated by integration. The integration limits are the points on the structure with maximum and minimum y_l coordinates (as discussed earlier in this section for flat ice and shown in Figure 5.8). For the case shown in Figure 5.10, these points are points A and B in the figure. The projected area is calculated by subdividing it into smaller areas. The cross-section of the ridge is divided into sections corresponding to portions of the

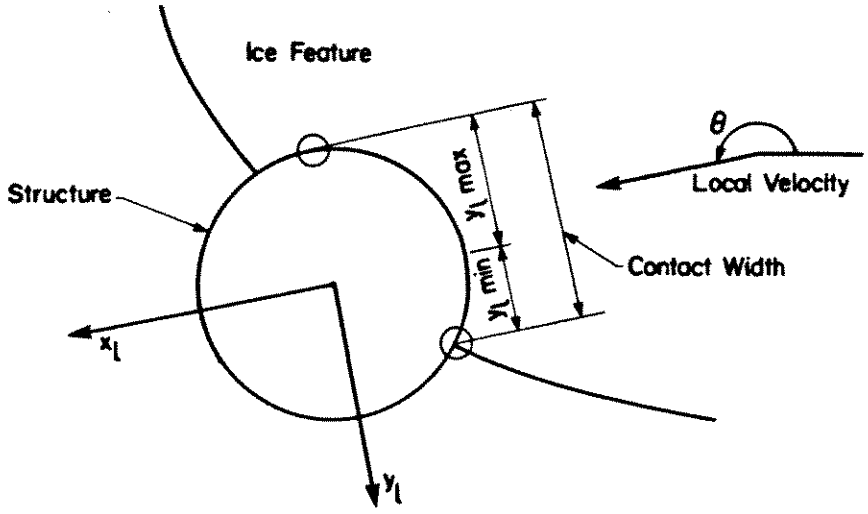

(a) Circular structure

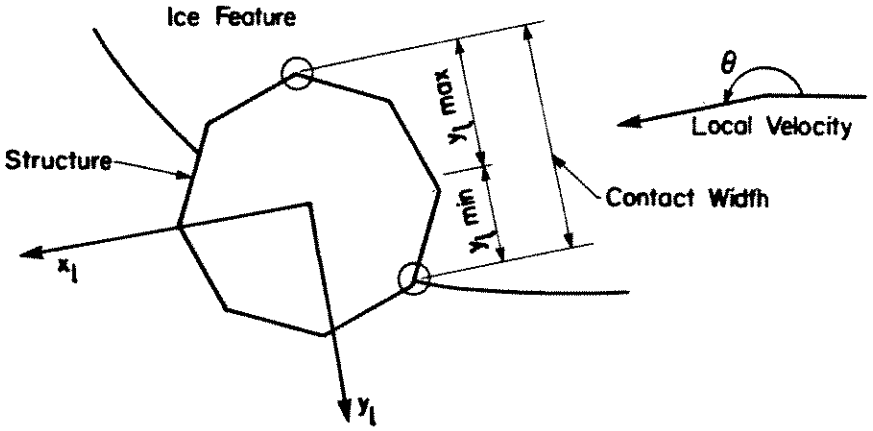

(b) Polygonal structure

Figure 5.8. The contact width between the structure and an ice feature

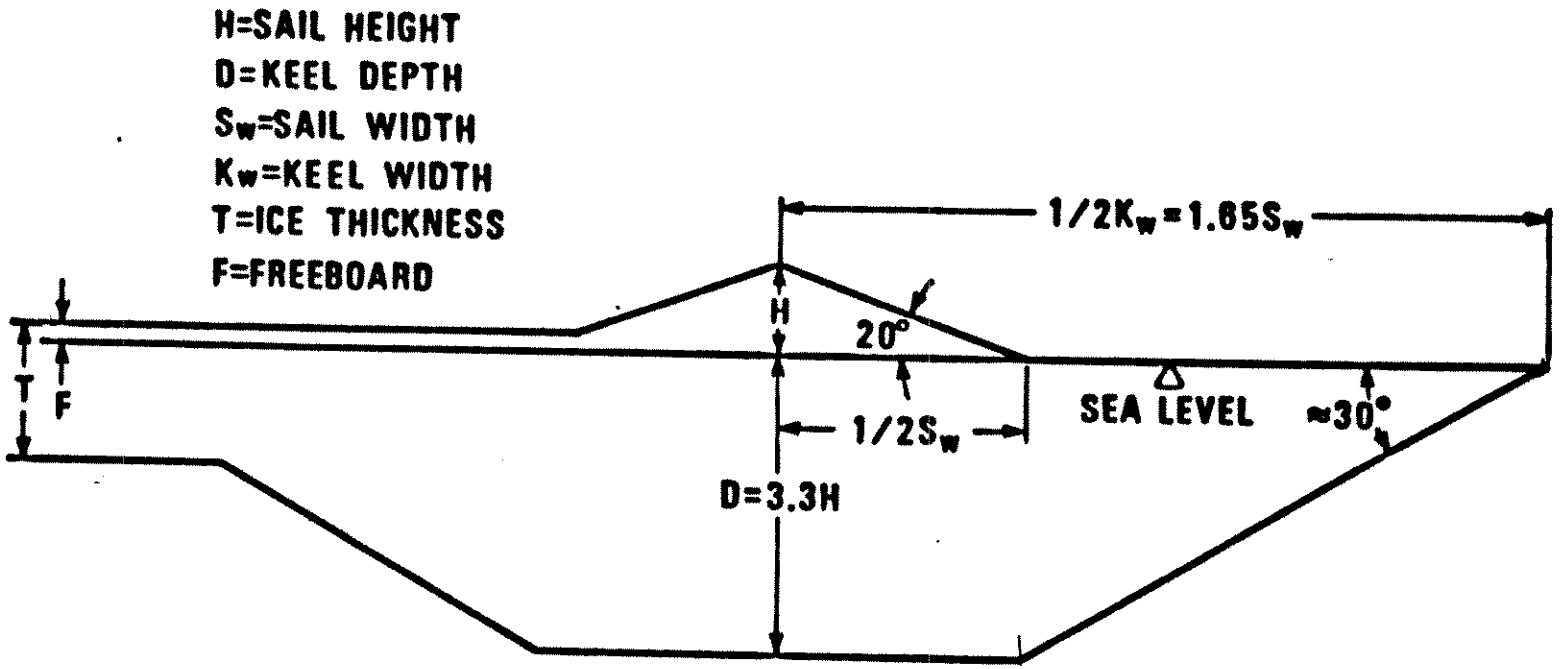

Figure 5.9. The Kovacs Idealized Multiyear Ridge Cross Section

cross-section with a given slope (see Figure 5.10). The total area is calculated as the sum of the contact areas between the surface of the structure and each of the ridge sections. This reduces the problem to carrying out the integration for one section with a given slope angle. The same methodology is used for polygonal structure by carrying out the integration in segments corresponding to the polygon sides.

5.3.2.2 Conical structures

For conical structures, two different local processes take place during different phases of the interaction, namely crushing and ride-up. When an ice feature comes into inital contact with a cone, local crushing of the ice occurs (see Figure 5.11) in the contact zone. This crushing results in increasing vertical and horizontal forces between the structure and the cone. The horizontal force in this case represents the required local force input to the overall global interaction model described in Section 5.3.1. The vertical force, which does not affect the in-plane equilibrium of the ice feature, increases up to the value which fails the ice in bending. When this takes place, the broken ice pieces begin to ride up the cone (or ride down in the case of a downward breaking cone). The local forces associated with this process are those forces needed to lift (or submerge) the broken ice pieces on the cone surface. When all the broken ice pieces have ridden up the cone, the feature comes in contact with the structure once more and crushing begins. In this case, the ice crushes against the cone and sustains the ice pieces riding-up at the same time. A second bending failure occurs when the net vertical force at the contact area reaches the bending failure force of the ice feature. Ride-up then begins again, and this alternation between ride-up and crushing continues until the interaction terminates. As the riding ice pieces reach the top of the cone (or bottom of a down-breaking cone), they clear around the structure and thus cease to contribute to the ride-up force.

It is assumed that the edge of the ice feature is always perpendicular to the local ice movement. This is a reasonable simplifying assumption for conical stsructures, because in most cases, the penetration of the cone into the ice feature is large enough to make the shape of the ice edge irrelevant to the analysis.

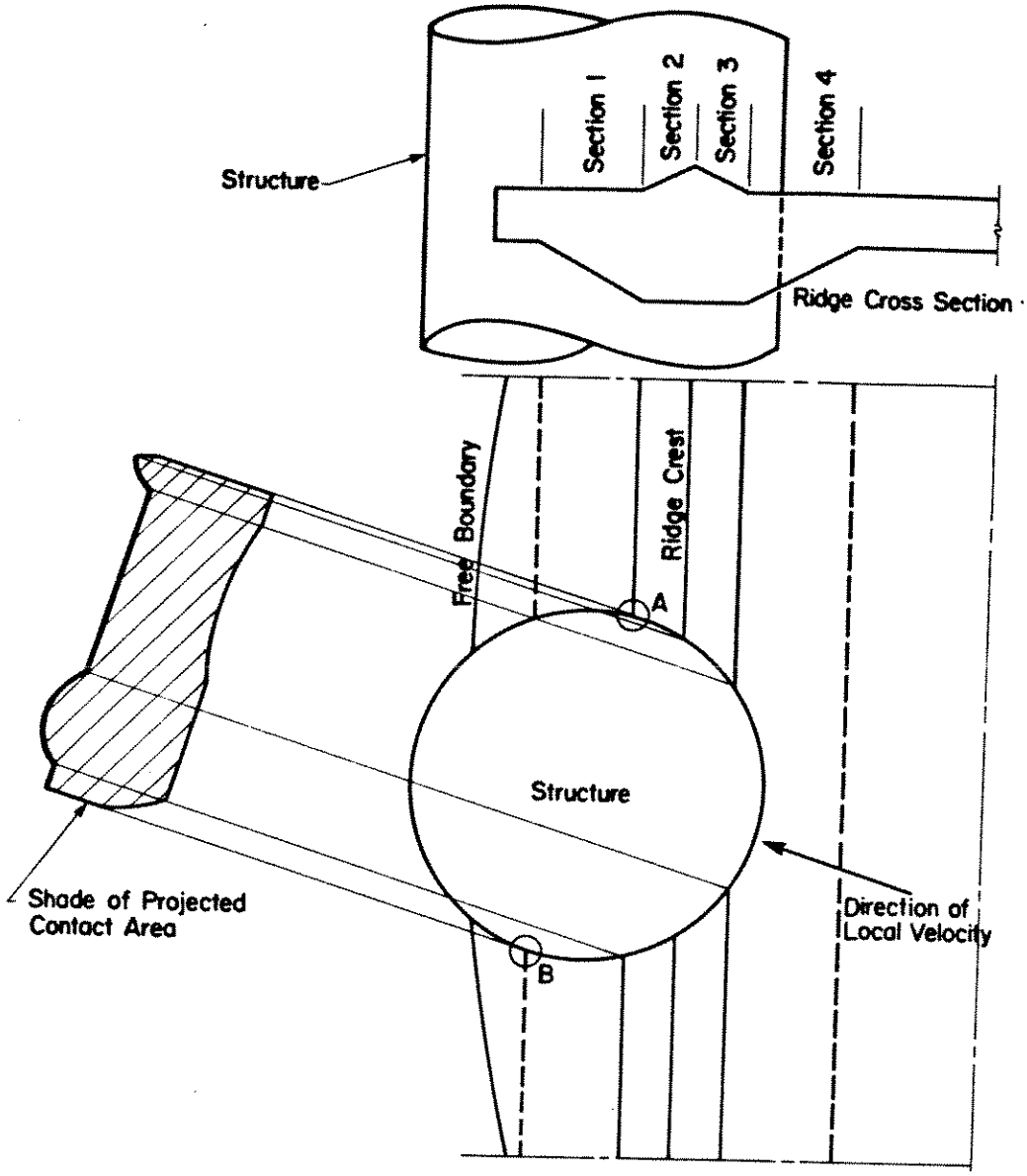

Figure 5.10. The contact area between a MY ridge and a circular structure

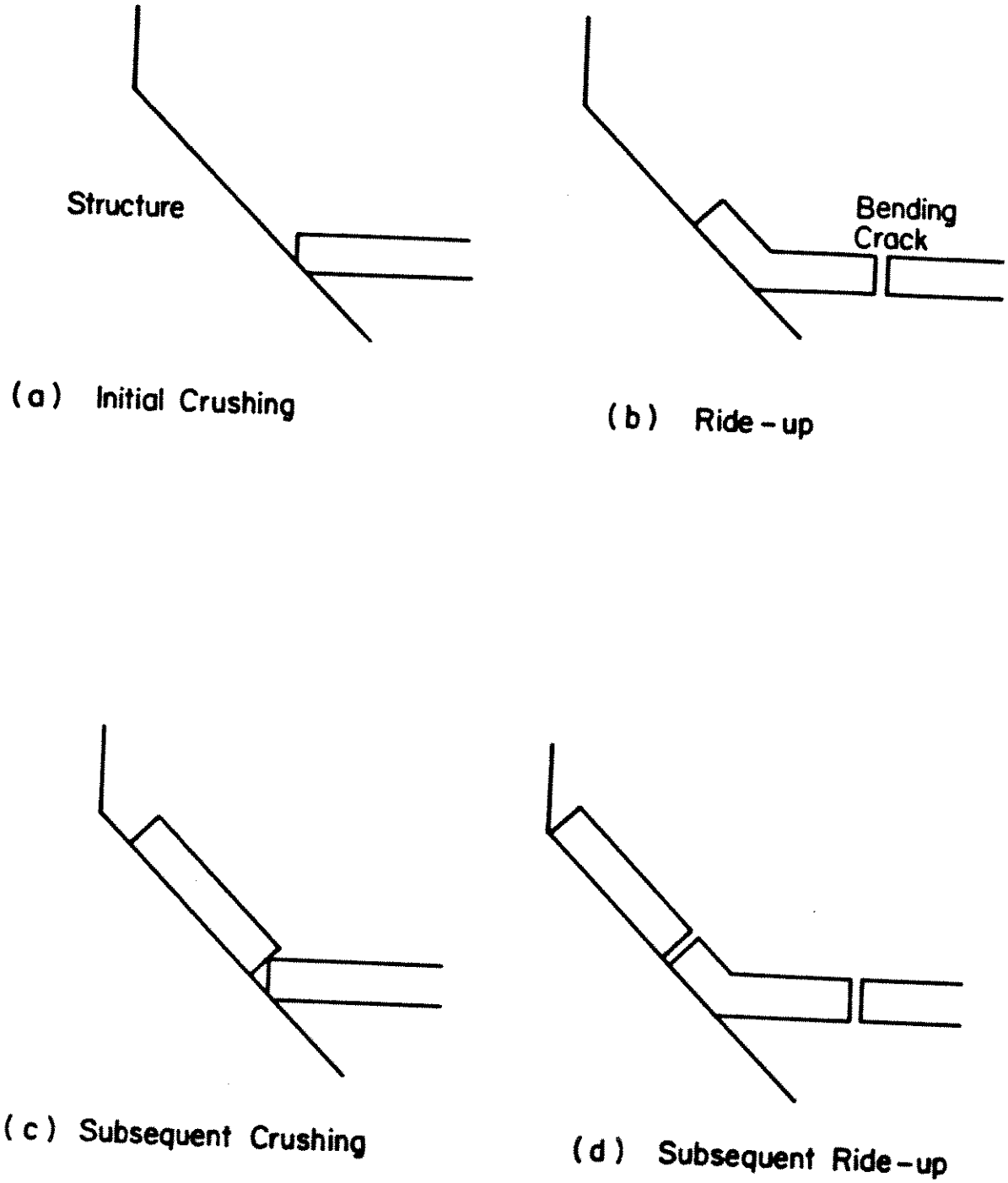

Figure 5.11. Local interaction process between an ice feature and an upward-breaking conical structure

(a) The Crushing Phase

It is assumed that the crushing force, F, is perpendicular to the cone surface (i.e. no friction condition), and is equal to the contact area projected on a plane perpendicular to the force direction multiplied by the average ice pressure. The horizontal and vertical components of the crushing force (F_H, F_V) can be obtained by multiplying the average pressure by the projection of the contact area on the vertical and horizontal planes respectively (see Figure 5.12). The total horizontal and vertical forces on the floe are given by:

$$F_{H_f} = F_H + P \cos\alpha \tag{5.11}$$

$$F_{V_f} = F_V - P \sin\alpha \tag{5.12}$$

where P is the force from the ride-up ice (see Figure 5.12), and α is the cone slope angle. P is given by:

$$P = w (\sin\alpha + \mu \cos\alpha) \tag{5.13}$$

where w is the ride-up weight and μ is the friction coefficient between the ice and the structure.

The total horizontal and vertical forces on the structure are given by:

$$F_{H_s} = F_H + w \cos \alpha (\sin \alpha + \mu \cos \alpha) \tag{5.14}$$

$$F_{V_s} = F_V + w \cos \alpha (\cos \alpha - \mu \sin \alpha) \tag{5.15}$$

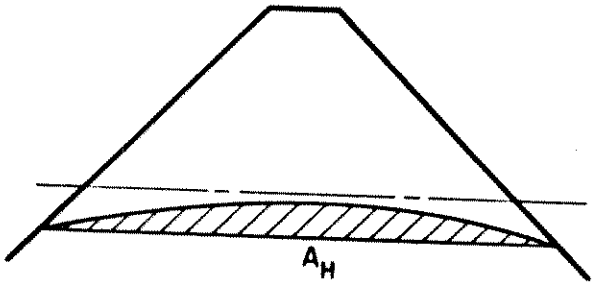

(a)

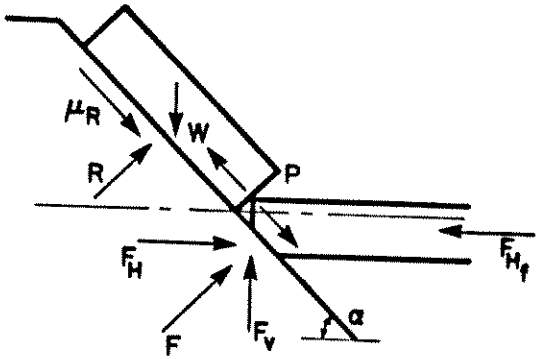

(b)

$F_H = A_{H\sigma}$

$F_v = A_{v\sigma}$

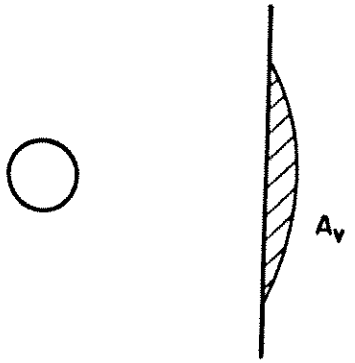

(c)

Figure 5.12. The Calculation of Local Forces on a Conical Structure During the Crushing Phase

For downward breaking cones, the weight, w, in Eqs. (5.13) to (5.15) is replaced by the difference between the buoyancy and the weight.

The crushing process continues until the net vertical force on the floe, F_{V_f}, reaches a critical value corresponding to the bending failure of the ice. The latter is calculated using Croasdale's approach, in which the ice is treated as an elastic plate on elastic foundation (reference). Croasdale used a 2-dimensional model based on a flat, sloping surface and then adjusted the resulting force by multiplying it by the ratio of the breaking length to the contact length (see Figure 5.13). The critical breaking force can be expressed as (reference):

$$V_{cr} = 0.68\ \sigma_f\ \left(\frac{\gamma_w t^5}{E}\right)^{1/4}\ \ell_b \tag{5.16}$$

where σ_f is the flexural strength of ice, γ_w is the specific weight of water, E is the modulus of elasticity for ice, t is the ice thickness, and ℓ_b is the breaking length of ice. The length, ℓ_b, can be expressed as (Figure 5.13):

$$\ell_b = \pi\ \left(\frac{b}{2} + \frac{\pi}{4}\ \ell_c\right) \tag{5.17}$$

where b is the contact width and ℓ_c is the characteristic length given by:

$$\ell_c = \left(\frac{Et^3}{12\gamma_w\ (1-\nu)^2}\right)^{1/4} \tag{5.18}$$

and ν is Poisson's ratio for ice.

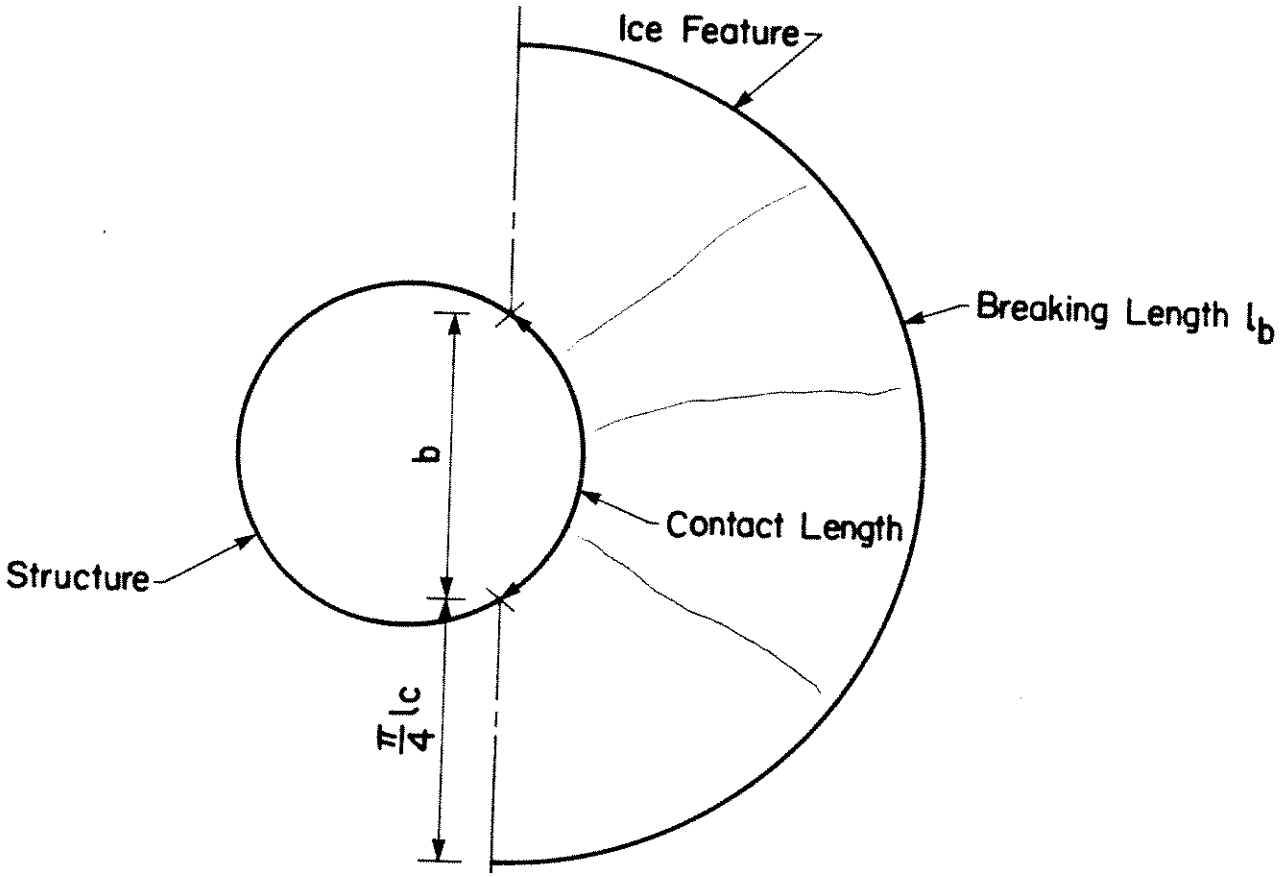

Figure 5.13 Croasdale's 2-dimensional corrected model for bending failure load of ice on conical structures

(b) The ride-up phase

Ride-up forces are the forces necessary to lift the broken ice pieces out of the water in the case of an upward breaking cone, or to submerge them on the underside of a downward breaking cone. Ride-up forces are calculated from the model in Figure 5.14 (a). It is understood that the ice will not bend in the fashion shown in Figure 5.14(a), but will ride-up in small discrete pieces, as shown in Figure 5.14 (b). The idealization in Figure 5.14(a) allows for the calculation of the ride-up force for any given penetration using one simple approach. The approximation involved is very small, because the forces needed to turn the ice pieces from the horizontal position to the cone-slope position (see piece 2 in Figure 5.14(b)) are much smaller than the forces needed to lift the ice pieces out of the water. It is worth noting that this model assumes that the ice pieces will ride-up and clear around the structure. If the cone is not designed properly, the ice pieces may be trapped under the oncoming ice and proper clearing will not take place.

The forces on the floe and the structure can be calculated from Equations 5.11 to 5.15 by substituting zero for F_H and F_V, and including the above water weight of the ice piece currently riding up in the calculation of w. The ride-up process continues until the ice feature comes into contat with the structure once more. It is noted that the height of ice on the cone from which the ride-up weight is calculated cannot exceed the cone freeboard.

If a ridge is encountered during the interaction, the above mentioned crushing force, failure force and ride-up force will be increased. The crushing force of the ridge is calculated on the basis of its average thickness using the same methodology described in (a) above. The limiting vertical force is that necessary to cause out of plane failure of the ice including the ridge. To consider the different possible positions, angles and possible failure modes of multi-year ridges would be an extremely complex task. Therefore it was decided that the increase in out of plane failure load can be accounted for by increasing the bending resistance of the ice in Equations 5.16. This increase could be made probabilistic and based upon the randomness in ridge dimensions location and orientation, and can be quantified on the basis of some

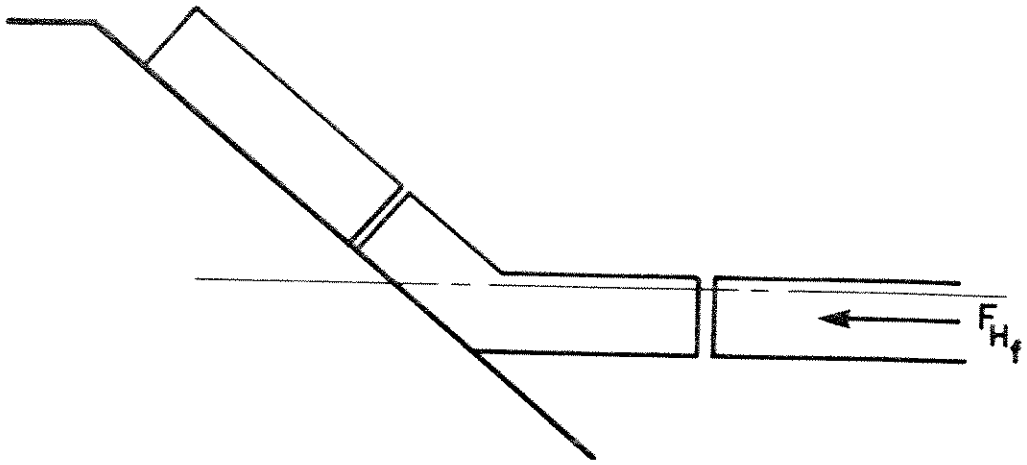

(a) Idealized Model

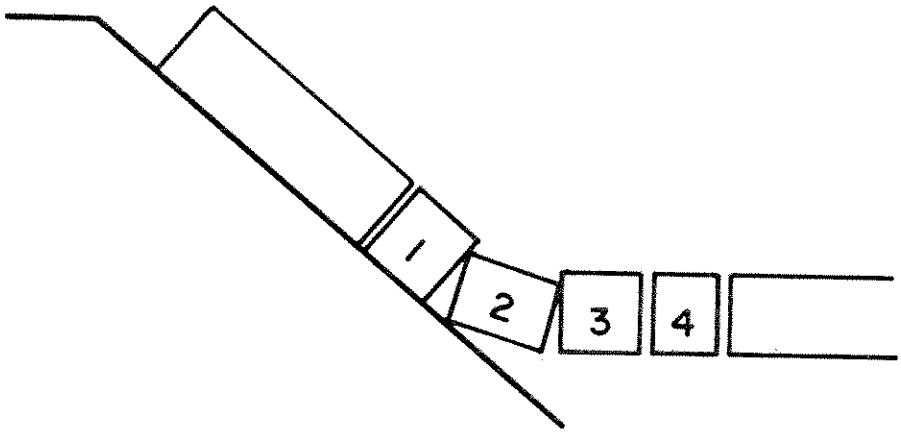

(b) Expected Actual Behaviour

Figure 5.14. Illustration of the model used for calculating ride-up forces

calibration work of individual ridge interaction cases. For the present version, the increase in out of plane failure force was based on the force necessary to fail the ridge (causing two hinge cracks) as an inifinite beam on elastic foundation. This force is given by (Hetenyi, 1946):

$$V_r = \frac{6.2\ Z_x}{\ell_c} \cdot \sigma_f \qquad (5.19)$$

where Z_x is the section modulus about a horizontal axis (bottom for upward breaking cones and top for downward breaking cone), and ℓ_c is the characteristic length of the beam given by:

$$\ell_c = \left(\frac{4E\ I_x}{\gamma_w\ b}\right)^{0.25} \qquad (5.20)$$

where I_x is the ridge moment of inertia about a horizontal axis and b is the ridge width. The parameters Z_x, I_x and b are calculated from the Kovacs idealized ridge cross section (Figure 5.9). The Force V_r is added to the force necessary to fail the floe (see (a) above) along the circumference of the failure zone after subtracting the part of this circumference which lies on the ridge and is accounted for by Eq. (5.19). This method is expected to lead to conservative results and further research should be carried out to refine this methodology.

The ridge ride-up force is calculated using the same method in (b) above, after distributing the additional wight due to the ridge over the failed area of the ice (see Figure 5.13).

5.3.3 Examples

Force histories for some ice structure interaction events, calculated using the global and local models described in Section 5.1 and 5.2, are given in this section. These examples serve as illustrations of the application of the model and as verification of its results.

The first set of examples are given in Figure 5.15 for a summer multi-year floe collision. The floe is 4 m thick and has a diameter of 1 km. The initial floe velocity is 0.25 m/s, and the eccentricity of the collision is 200 m. The average ice pressure is 1 MPa. The example illustrates the effect of the shape of the structure on the energy dissipation process, and consequently, on the maximum force value. Three cases are considered as follows:

a) a square structure (100 m x 100 m), with the initial direction of motion perpendicular on one of the flat sides of the structure;

b) a circular structure of 100 m diameter; and

c) a square structure (100 m x 100 m), with the initial velocity direction parallel to one of the structure diagonals.

It can be seen that the maximum force can vary substantially depending on the development of the contact between the ice and the structure. If the ice contacts the structure at a flat side (case A), the contact area is initially large and the force rises quickly. On the other hand, if the ice contacts an edge (case C), the contact develops slowly and the resulting maximum force is much lower. The circular structure (case B) is an intermediate case between cases A and B.

Figure 5.16 shows a force history for a multi-year floe interaction with a 100 m diameter circular structure in the winter. As shown in the figure, the floe is 1 km in diameter, 5 m thick and was initially moving with the surrounding 1.5 m thick first-year ice at 0.2 m/s. The eccentricity of the interaction is 200 m. The average multi-year ice pressure is 1 MPa, and the pressure from the surrounding ice on the floe is 0.1 MPa. The total force is plotted along with the x and y force components (perpendicular and parallel to the initial direction of ice movement, respectively). The peak load occurs when the multi-year floe breaks out of the surrounding ice. The total force drops after this event takes place, and remains at an almost stable level. After the peak load occurs, F_y decreases gradually, while F_x increases as the floe rotates around the structure.

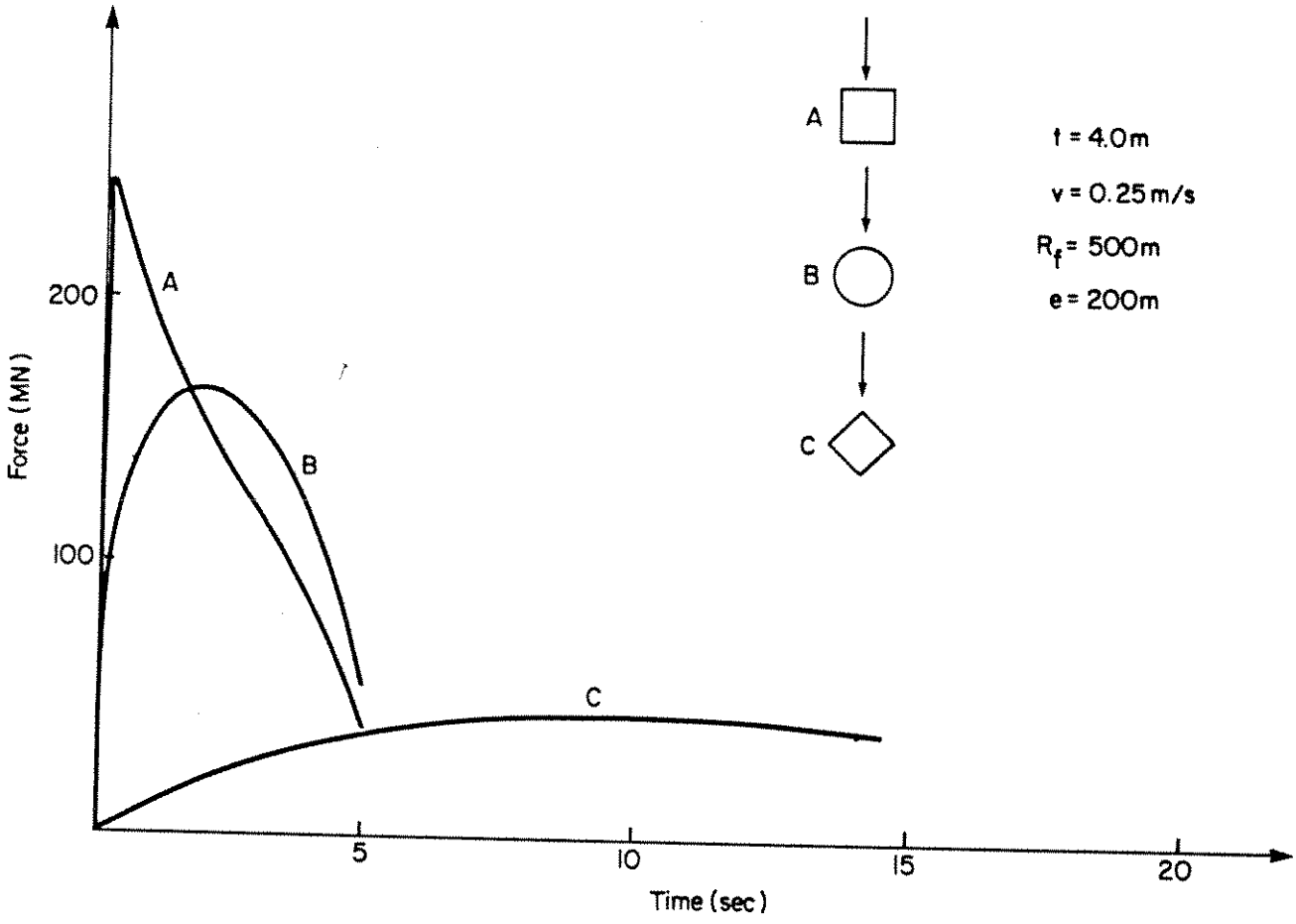

Figure 5.15. Sample force history results for summer multi-year floe collisions

v_f = 0.2 m/s t_f = 1.5m (FY Ice Thickness)

R_s = 50m

R_m = 500m t_m = 5m (MY Floe Thickness)

Eccentricity = 200m

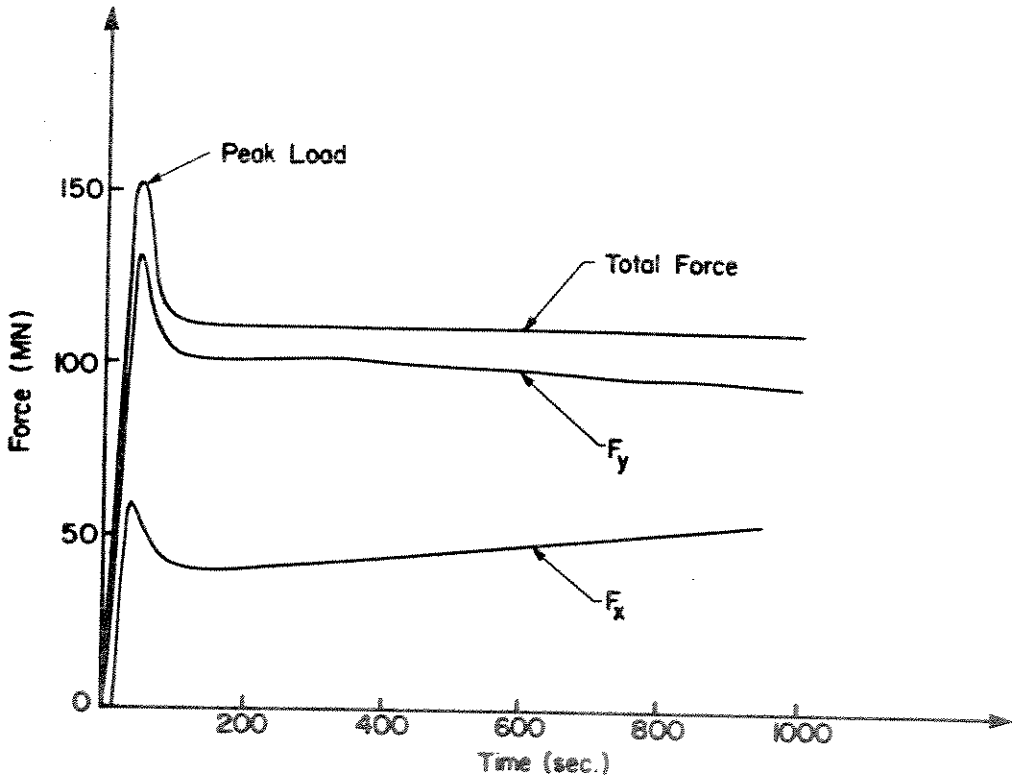

Figure 5.16. Sample force history results for a winter multi-year floe interaction

The force histories for three multi-year floe interactions involving multi-year ridges are given in Figures 5-17(a) to 5-17(c). The parameters used in each case are shown on the figures. It can be seen that a sudden rise in the rate of force increase occurs when the ridge is encountered due to the increase in thickness. It is also worth noting that the interaction stops shortly after the ridge is encountered in each case. This is a reflection of the effect of the increased local force on the overall deceleration and clearing of the multi-year floe.

Figures 5.18 and 5.19 show the force histories for multi-year floe interaction with upward and downward breaking cones respectively. The crushing strength of ice used is 0.5 MPa, the flexural strength is 0.2 MPa, the modulus of elasticity is 5 GPa, and the friction coefficient is 0.15. Comparison between the two figures shows that the maximum force occurs during ride-up for the upward breaking cone and during crushing for the downward breaking cone. This is a reflection of the buoyancy effect, which reduces the load in the case of the downward breaking cone. In general, loads on downward breaking cones are smaller than those on upward breaking cones, because less force is required to submerge the ice, and then to lift it out of the water. It is noted that multi-year ridges are not included in the results of Figures 5.18 and 5.19.

5.4 First-Year Level Ice Interactions

This scenario is depicted in Figure 5.20. The movement of first-year ice covers is generally not significantly affected by the presence of a structure. This is due to the fact that the magnitude of the driving forces under which such a large ice surface moves are much higher than the forces exerted on the ice by the structure. As discussed in Section 5.1, the forces on the structure under these conditions are governed by local considerations regarding the maximum stresses, which can be sustained by the ice in the vicinity of the structure. The models presented in this section for the forces resulting from the movement of first-year ice against the structure are, therefore, based on local force models (see Table 5.1).

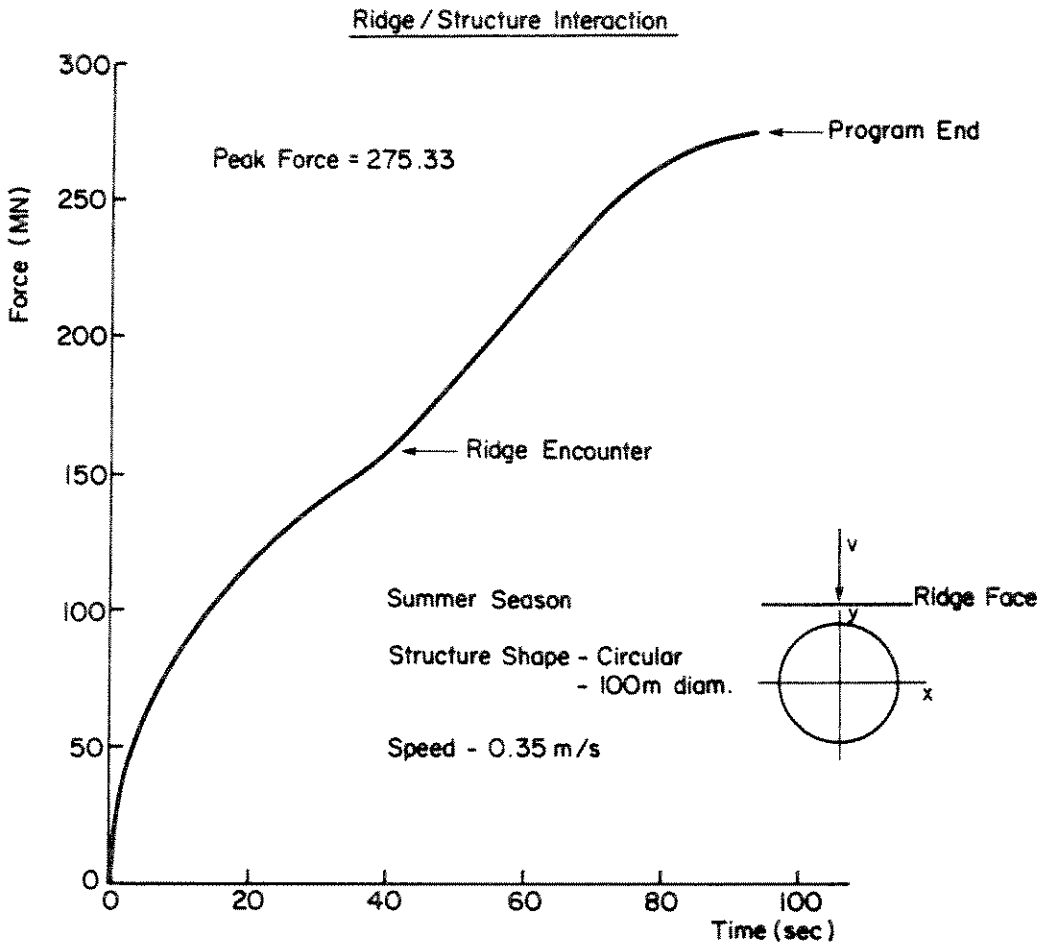

Figure 5.17(a). Force history for structure interaction with multi-year floe floe with an embedded multi-year ridge

Example 1

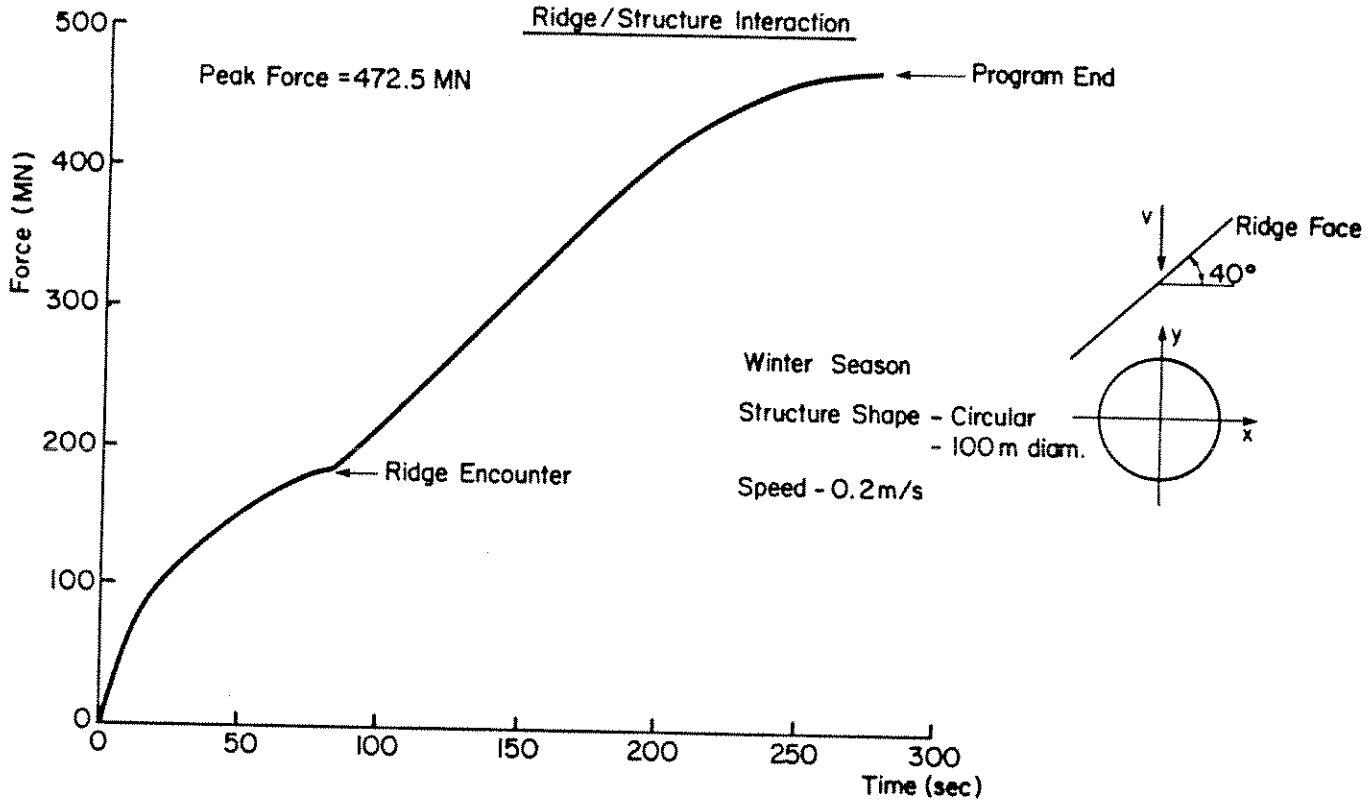

Figure 5.17(b). Force history for structure interaction with multi-year floe floe with an embedded multi-year ridge

Example 2

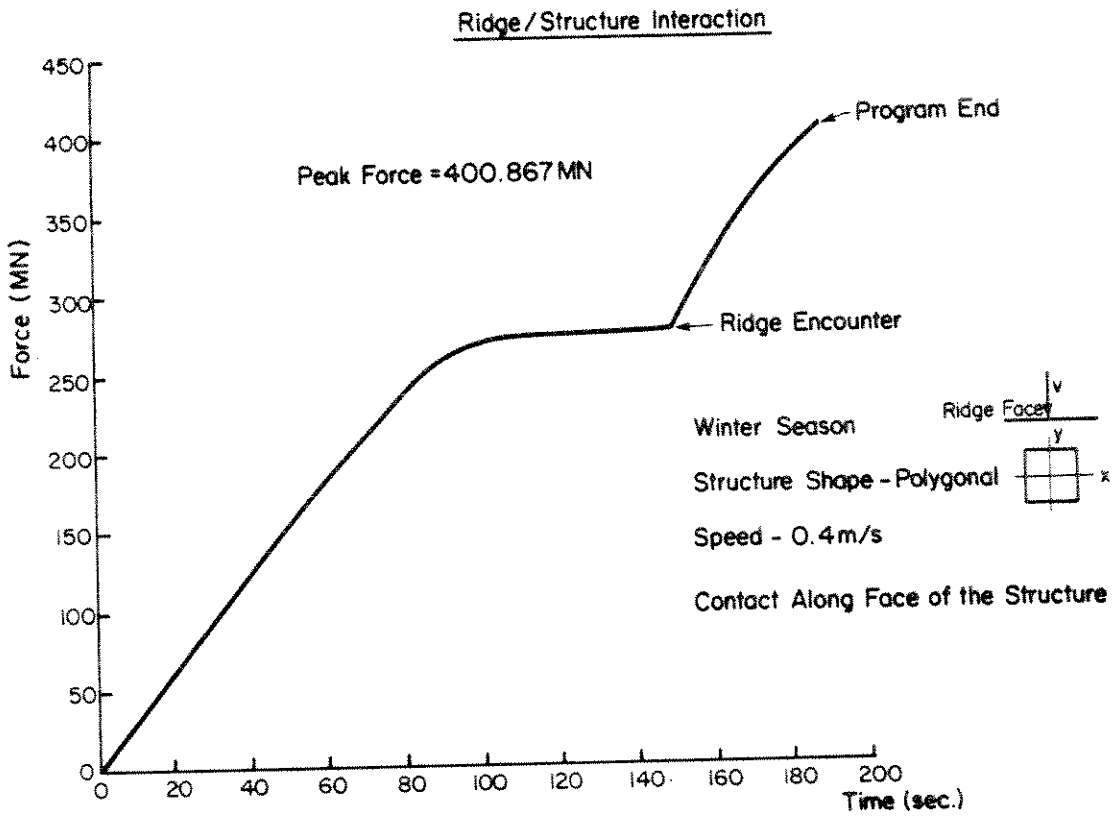

Figure 5.17(c). Force history for structure interaction with multi-year floe floe with an embedded multi-year ridge

Example 3

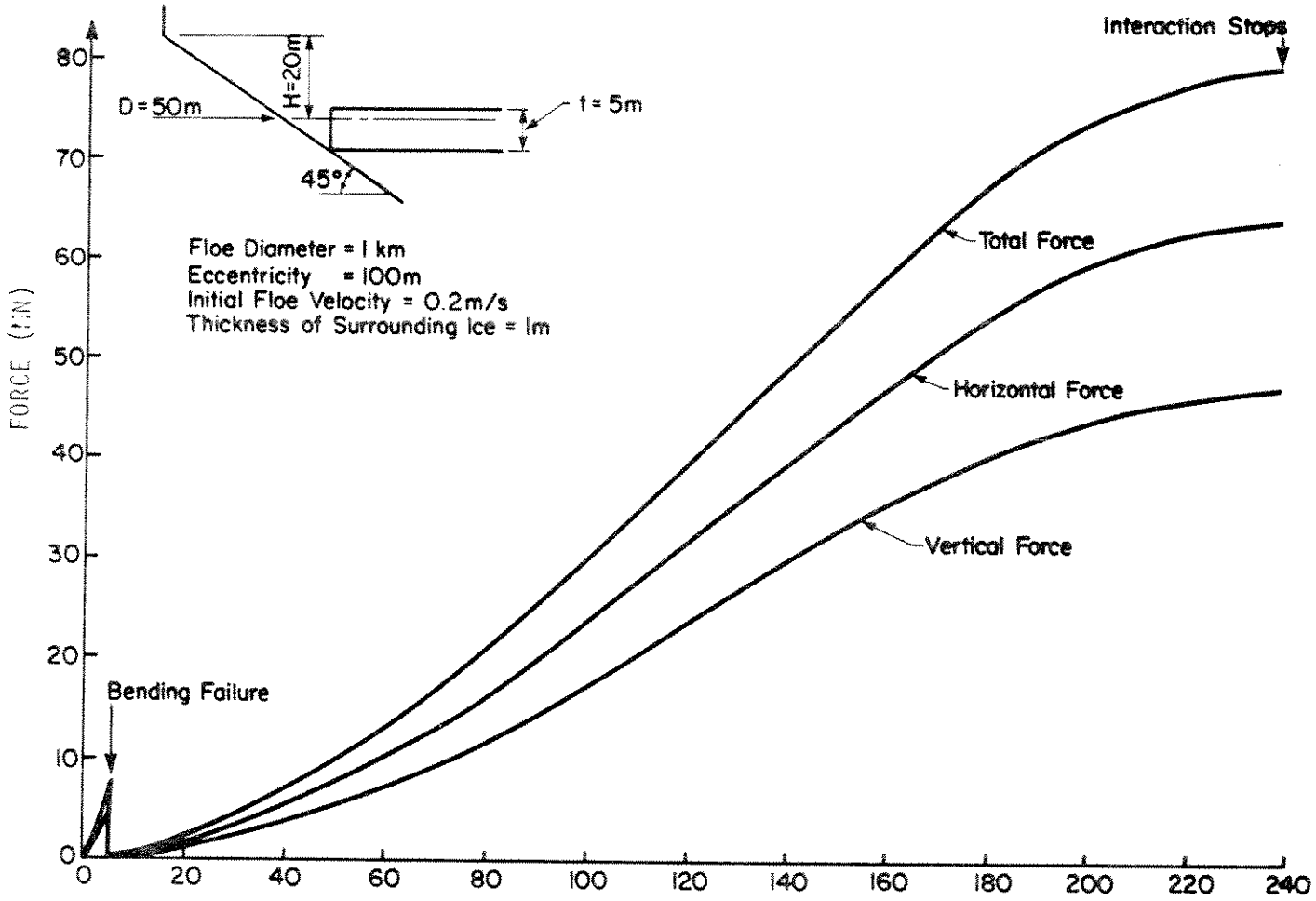

Figure 5.18. Force History for the Interaction With an Upward Breaking Cone

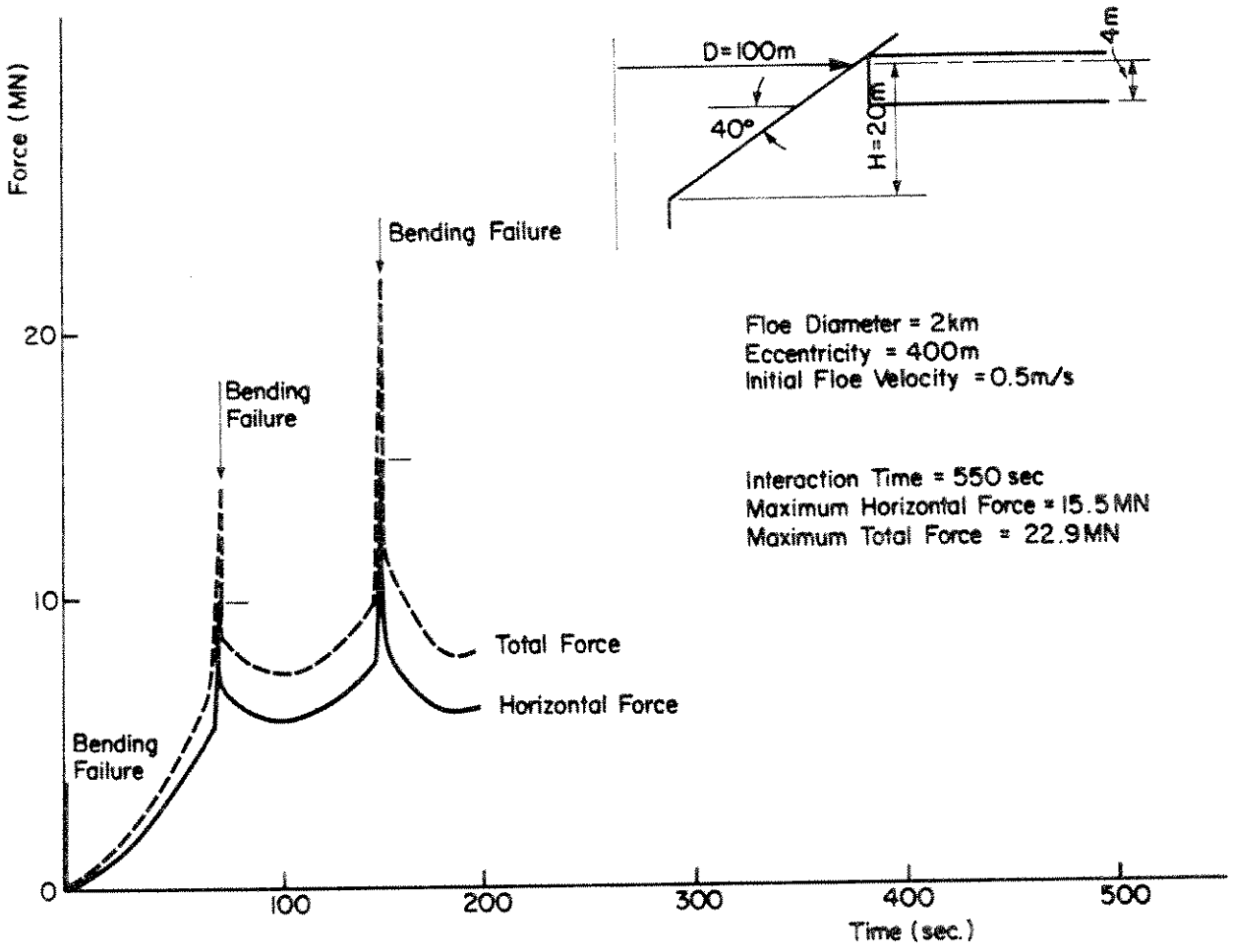

Figure 5.19. Force History for Multi-year Floe Interaction with a Downward Breaking Cone

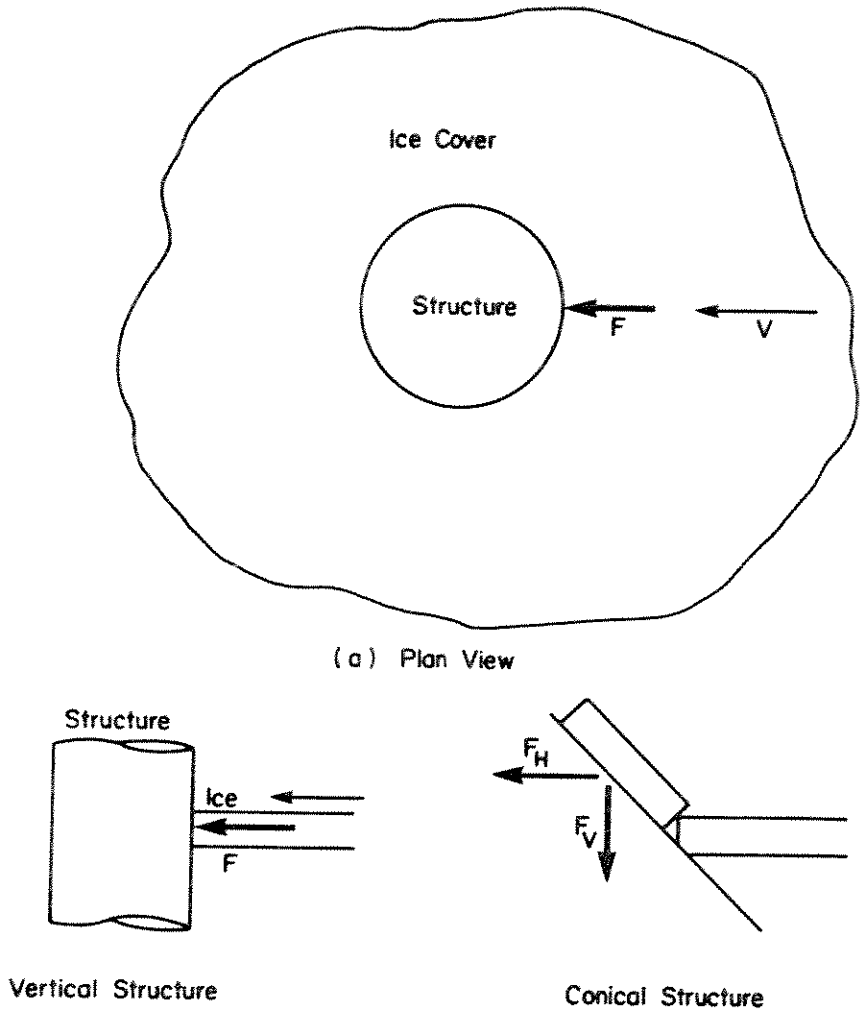

Figure 5.20. Representation of the movement of a first-year ice cone against a structure

5.4.1 Vertical structures

5.4.1.1 The brittle mode

As discussed in Section 5.2, ice responds in a brittle manner at high loading rates, and the ice behaviour is dominated by crushing. Velocities which lead to this behaviour are dominant in the active ice zones (pack zone in the U.S. Beaufort and shear zone in the Canadian Beaufort) during all seasons, and in the landfast ice zone during the break-up season. Given the average ice pressure (σ) during an interaction event, the force (F) can be calculated from:

$$F = \sigma D t \tag{5.21}$$

where D is the width of the structure perpendicular to the direction of ice movement, and t is the ice thickness.

5.4.1.2 The creep mode

In the landfast ice zone, ice movement speeds are usually in the range which results in strain rates well below the creep-crushing transition. Only under special circumstances, such as the event of the "breaking off" of a large area of the landfast ice cover during a storm, are the ice velocities likely to reach the threshold of brittle behaviour. Under these conditions, the crushing model discussed in Section 5.4.1 is used. For normal landfast ice movements, the forces are calculated from a creep solution. The model is also used for the low velocities (i.e. below creep-crushing transition) in the active ice zones.

A simple and accurate creep solution can be obtained using the reference stress method (Ponter et.al., 1983). In general, the force F on the structure at a given ice movement speed v can be calculated from the equilibrium condition given as:

$$Fv = \int_V \sigma_{ij} \dot{\varepsilon}_{ij} \, dV \tag{5.22}$$

where σ_{ij} is the stress tensor;
$\dot{\varepsilon}_{ij}$ is the strain rate tensor;
V is the volume; and
the relationship between σ_{ij} and $\dot{\varepsilon}$ is given by the creep law in Eq. (5.1) (Section 5.2).

Clearly, the difficulty in calculating the force from Eq.(5.22) is in finding the stress distribution required to evaluate the integral on the right hand side of the equation for any values of the constants A and n in the creep law (see Eq.(5), Section 5.2). The essence of the reference stress method is to evaluate this integral using an approximate method which is based on the solutions of two problems with the same geometry as the problem considered, but with two different constitutive laws of the creeping material. These constitutive laws need not include the actual constitutive law for ice. Equation (5.22) can be rewritten in the approximate form:

$$Fv = \sigma_R \, \dot{\varepsilon} \, (\sigma_R) \, V_R \tag{5.23}$$

where σ_R is defined as the reference stress, V_R is defined as the reference volume, and $\dot{\varepsilon}(\sigma_R)$ is the actual creep law of the material considered.

The reference stress is defined such that its ratio to the plastic yield stress is equal to the ratio between the force F for the actual constitutive law of the material, and the yield force, Y, obtained from a plastic solution. Thus:

$$\sigma_R = \frac{F}{Y} \, \sigma_y \tag{5.24}$$

The evaluation of σ_R as a function of F from Eq.(5.24) requires a plastic solution to evaluate Y for a given σ_y. It is noted that the use of a plastic solution does not imply that the ice behaves in a plastic manner.

The only unknown quantity in Eq.(5.23) (besides F, which is to be calculated from the equation), is V_R. This is where a second solution of the problem is required. This should be a creep solution for any value of the creep exponent (n in the creep law of Eq.5.1). An elastic solution can be used, along with the viscous-elastic analogy (reference), to produce a creep solution for a purely viscous material (i.e. n = 1). Once this solution is obtained, it can be used in Eq. (5.23) with σ_R, as previously defined in Eq.(5.24), to obtain V_R. Equation (5.23) can then be used to evaluate the load F for any speed, v, and any constitutive law, $\dot{\varepsilon}(\sigma_R)$.

Equation (5.23) can be rewritten, by expressing σ_R and V_R in terms of non-dimensional constants ϕ and ψ as follows (reference):

$$F = \phi \, Dt \, \sigma \, \left(\frac{v/D}{\phi\psi}\right) \tag{5.25}$$

where D is the width of the structure, and t is the ice thickness.

As mentioned earlier, ϕ and ψ are specific to a given geometry of the problem and are, therefore, dependent on the aspect ratio, D/t. For the plane stress case, the shape of the in-plane stress distribution is independent of D and t. This is a useful property, because it allows the same values of ϕ and ψ to be used for different values of D and t, for which plane stress conditions can be expected to prevail.

In order to evaluate the constants ϕ and ψ for the problem in Figure 5.29(a), a 100 m diameter circular indenter embedded in a 1-m thick ice sheet was considered. The problem was idealized, as shown in Figure 5.21. There are no standard plastic and

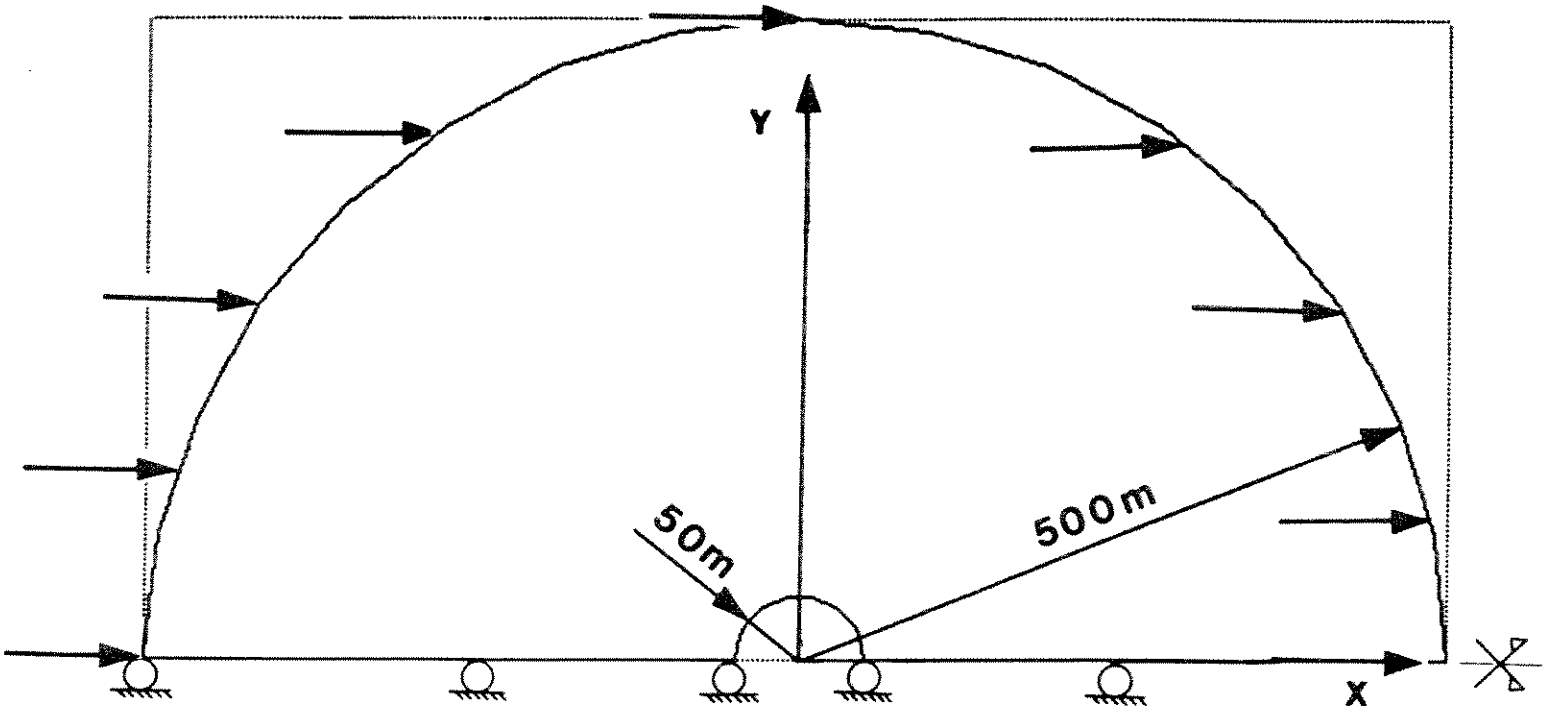

Figure 5.21 Geometry and boundary conditions for the problem of circular indenter in an ice sheet

creep solutions for this problem, and therefore, finite element solutions were used. The finite element mesh is shown in Figure 5.22. The c-axis of columnar sea-ice is most commonly randomly oriented in the horizontal plane. This type of ice has axially symmetric mechanical properties about the vertical axis. Since we are dealing with a plane stress problem, where the properties along the vertical axis to not affect the in-plane stresses, the results of isotropic solutions are applicable. For the finite element analysis, the eight-node isoparametric plane stress element shown in Figure 5.23 was used. The contact problem was modelled using 3-node interface elements, as shown in Figure 5.24. The FE package ABAQUS (reference) was used for the analysis.

A plastic solution gives a value of $\phi = 1.174$. The other parameter ψ, was calculated from a creep solution with a creep exponent $n = 3$ and a creep multiplier $A = 10^{-5}\ (MPa^3\ s)^{-1}$ (references). An ice velocity of 10^{-4} m/s was used. The stress distribution and the load history for this solution are given in Figure 5.25. This solution gives a ψ value of 0.419. In order to verify this result, ψ was calculated again using a solution for a purely viscous material (i.e. $n = 1$). All other parameters had the same values as for the creep solution. The stress distribution and load history for this solution are given in Figure 5.26. This solution yielded a value of .424 for ψ.

The conclusion of this analysis is that for the creep mode, Eq. (5.25) is used in calculating loads on vertical structures, fully embedded in an ice sheet with $\phi = 1.174$ and $\psi = 0.42$. Although this result is based on a circular structure, it is generalized for a polygonal structure by using a value of D equal to the width of the structure, in a direction perpendicular to the direction of motion.

5.4.2 Conical structures

The material and structural models used for the movement of level ice against a conical structure are the same as was used for calculating the local forces for an areal ice feature interaction (Section 5.3.2.2). Ice is assumed to fail in bending, and to ride-up (or down) the structure until it clears. The maximum force will occur when half the

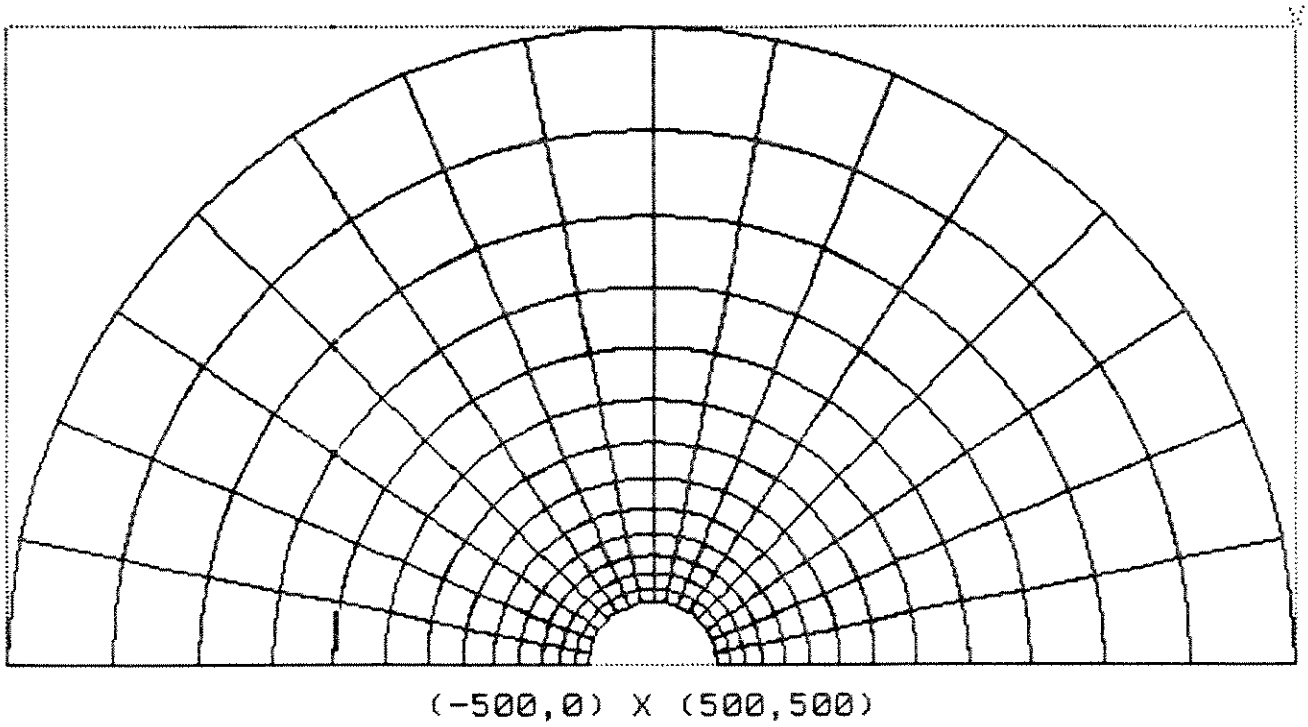

Figure 5.22. Finite element mesh used for the problem of a circular indenter in an ice sheet

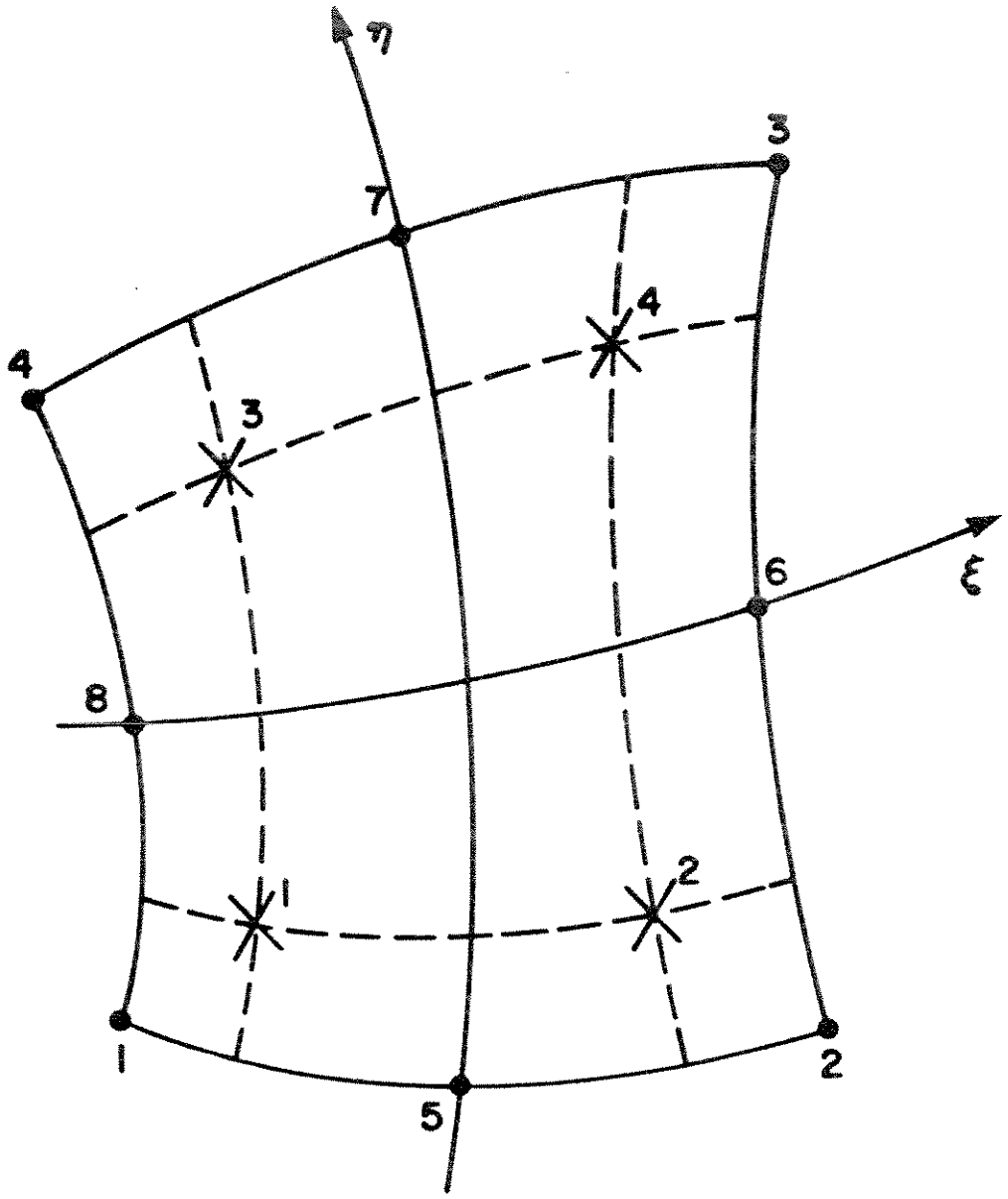

Figure 5.23 Eight-node isoparametric plane stress element used for the problem of a circular indenter in an ice sheet

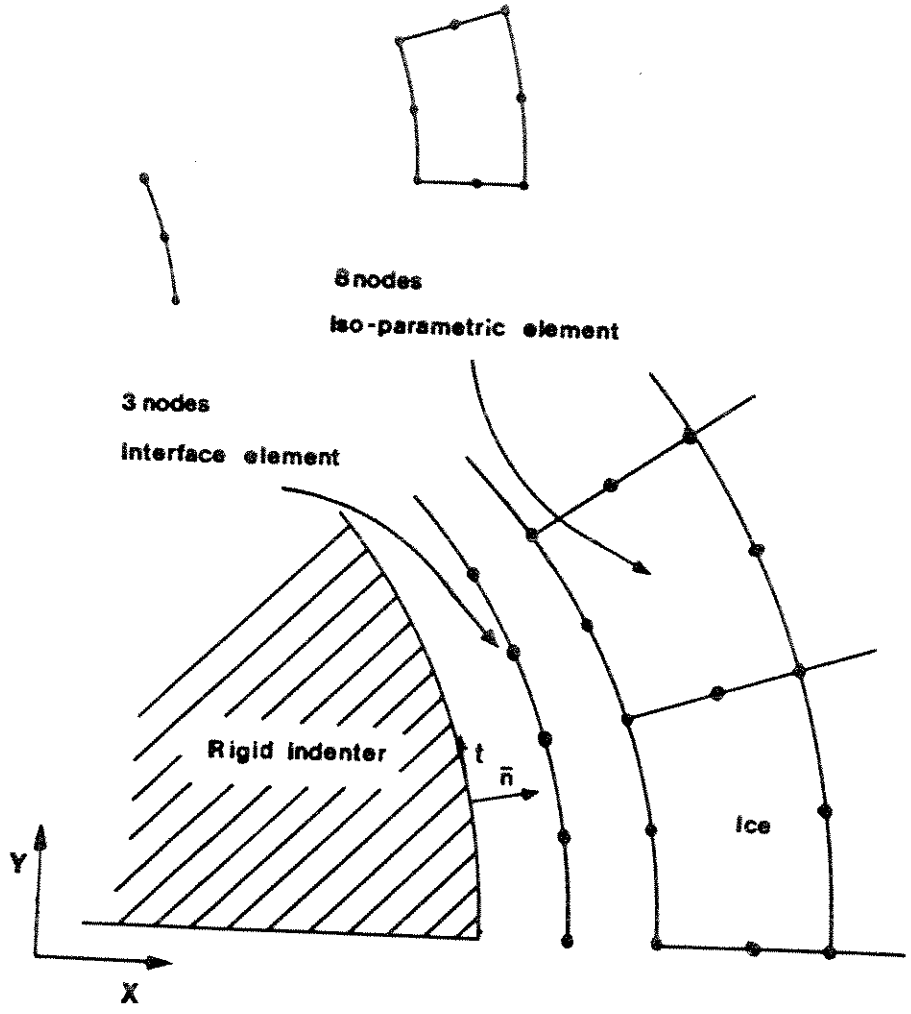

Figure 5.24. Description of the interface elements used for the problem of a circular indenter in an ice sheet

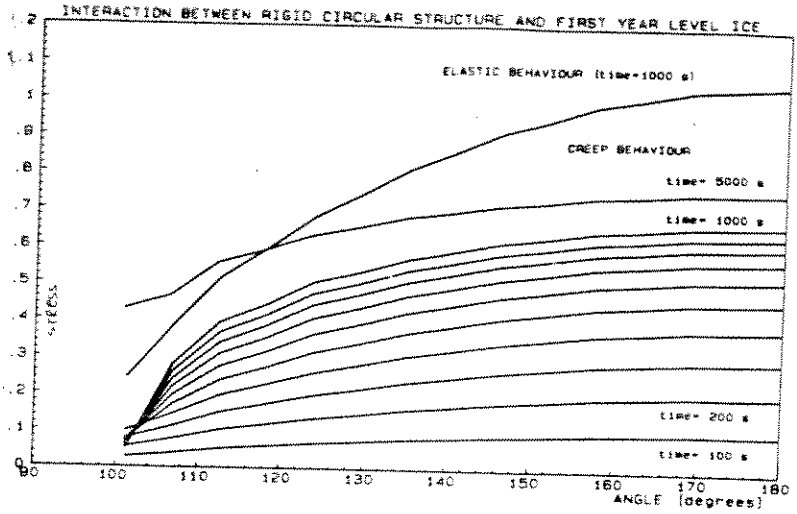

(a) Stress distribution

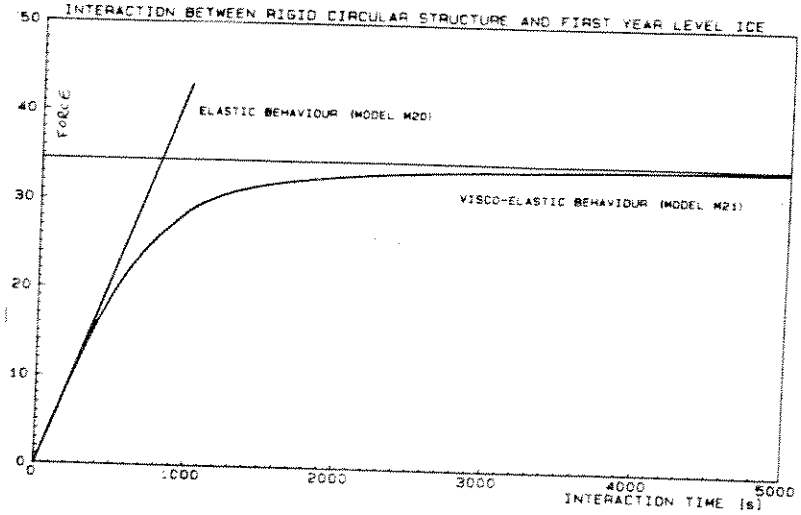

(b) Force history

Figure 5.25. Results of creep solution for the problem of a circular indenter in an ice sheet ($n = 3$, $A = 10^{-}$ $(MPa^3\ s)^{-1}$

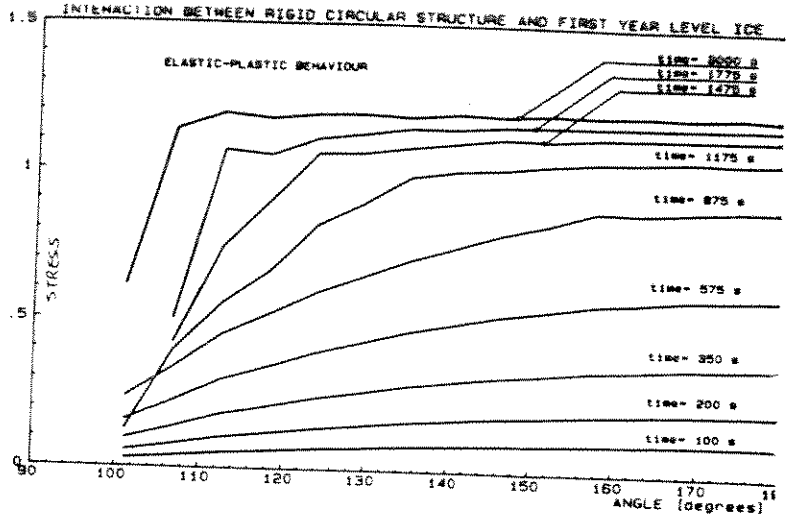

(a) Stress distribution

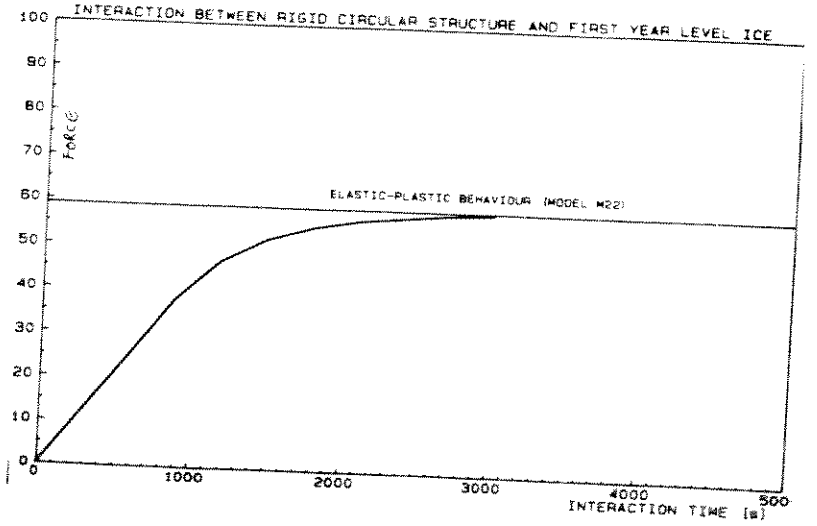

(b) Force history

Figure 5.26. Results of linear viscous solution for the problem of a circular indenter in an ice sheet (n = 1, A = 10^{-5} (MPa s)$^{-1}$

cone is covered with ice, and the vertical encroaching ice sheet (F_V in Figure 5.12) has reached the bending failure force of the ice. At this instant, the ice sheet starts to slide up (or down) the cone, and the horizontal force between the ice sheet and the structure (F_H in Figure 5.12) can be calculated using the relationship between the normal reaction to the cone and the friction force at sliding. Forces on the structure can be calculated by substituting the appropriate values of w, F_H, and F_V, which correspond to the present assumption, into Eqs. (5.14) and (5.15) (refer also to Figure 5.12(b)). For an upward breaking cone, w is the weight of a volume of ice equal to surface area of half the cone multiplied by the ice thickness. This is given by:

$$w = \frac{t}{\cos \alpha} \left(2R_w H/\tan \alpha - (H/\tan \alpha)^2 \right) \gamma_i \tag{5.26}$$

where t is the ice thickness, R_w is the water line radius of the cone, H is the cone freeboard, α is the cone slope to the horizontal, and γ_i is the weight of ice per unit volume. For a downward breaking cone, γ_i is to be replaced by $\gamma_w - \gamma_i$, where γ_w is the weight of water per unit volume.

The vertical force, F_V, is equal to the sum of ice bending failure load, and the vertical component of the force between the riding ice and this ice sheet. This leads to

$$F_V = V_{cr} + w(\sin \alpha + \mu \cos \alpha) \sin \alpha \tag{5.27}$$

where V_{cr} is given by Eq. (5.16), and μ is the coefficient of friction between the ice and the structure. The horizontal force, F_H, is then given by:

$$F_H = F_V \frac{\sin\alpha + \mu \cos\alpha}{\cos\alpha - \mu \sin\alpha} \tag{5.28}$$

The vertical and horizontal forces on the structure F_{V_s} and F_{H_s} can be obtained by substituting Eqs.(5.26), (5.27), and (5.28) into Eqs. (5.14) and (5.15).

5.5 First-Year Ridges

First-year ridges exist in the first-year ice, and move with the ice cover. As discussed in Section 5.4, this movement is driven by sufficient environmental forces to cause the structure to penetrate through the entire first-year ridge, and a local force model based on the maximum force sustained by the ridge is appropriate in this case.

5.5.1 Vertical structures

An idealized first-year ridge cross section is shown in Figure 2.57 (a) (Prodanovic, 1979). As a Columb-Mohr material (see Section 5.2.2), the rubble can fail in one of the two modes shown in Figure 5.27 (b) and (c), namely crushing or shear. An upper bound force on the structure due to rubble crushing can be calculated by postulating a clearing mechanism such as the one shown in Figure 5.27 (b) and finding the force necessary to shear the ice along the boundary of the clearing ice. For the shearing failure shown in Figure 5.27 (b), the force on the structure is simply equal to the integral of the shearing stresses along the two shear planes.

The shear strength of a Columb-Mohr material can be expressed in terms of its cohesion, friction, and normal stress, as given in Eq. (5.2). The normal stress σ is equal to the passive resistance of the material (Gregory and Tschekotarrioff, 1973) given by:

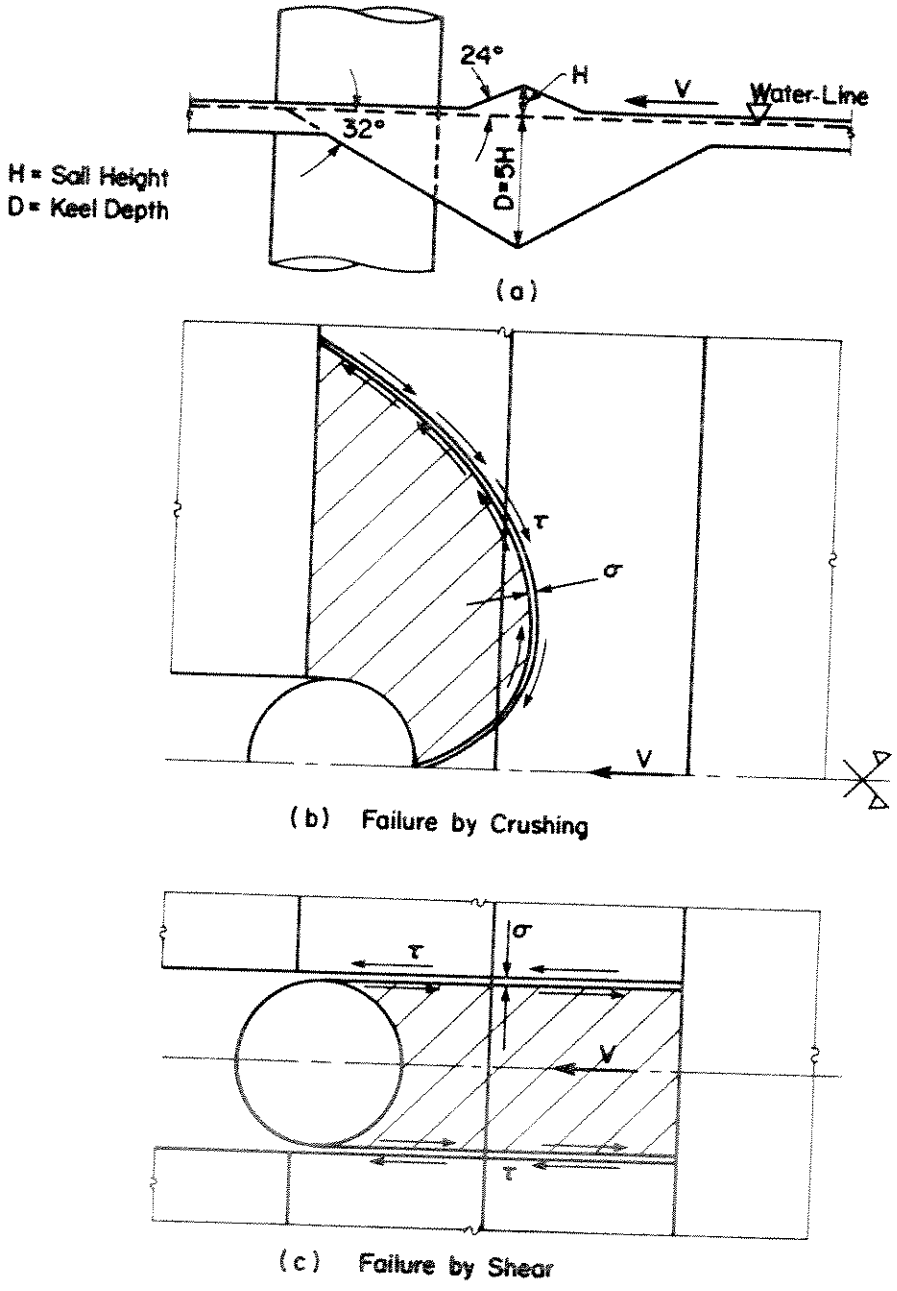

Figure 5.27 Idealized first-year ridge cross section and failure mechanisms

$$\sigma = p \tan^2(45^\circ + \frac{\phi}{2}) + 2C \tan (45^\circ + \frac{\phi}{2}) \tag{5.29}$$

where p is the vertical "overburden" pressure, ϕ is the material friction angle, and c is the cohesion. For the ridge sail, the vertical pressure at any point is equal to the weight of the ice $\gamma_i h$, where γ_i is the weight per unit volume for ice and h is the depth from the top ice surface. For the keel, the vertical pressure is due to the difference between the buoyancy and the weight, and is equal to $(\gamma_w - \gamma_i)d$, where γ_w is the weight of water per unit volume, and d is the height from the bottom surface of the ice.

For the rubble-crushing mechanism in Figure 5.27(b), Prodanovic (1981) suggested defining the discontinuity surface by logarithmic spirals. For simplicity, this shape is replaced here by the shape in Figure 5.28. The sail area of the idealized ridge cross-section in Figure 5.27(a) is very small compared to the keel area (about 5.3% of total area). The major force contribution will, therefore, come from the keel, and the sail is neglected in the analysis. The force on the structure can be calculated from the equilibrium of the hatched zone in Figure 5.28. This leads to:

$$F = 2(N_2 + (N_1 + N_3) \sin 45^\circ + (T_1 - T_3) \cos 45^\circ) \tag{5.30}$$

The normal forces N_1, N_2, and N_3 are calculated by integrating the normal stress given by Eq. (5.29) over the corresponding area in each case. In evaluating these integrals, different cases, depending on whether the structure and/or the discontinuity surface have penetrated past the lowest point on the ridge keel. These cases are all taken into consideration in the calculations. The tangential forces T_1, T_2, and T_3 can be calculated by integrating the shear stresses as follows:

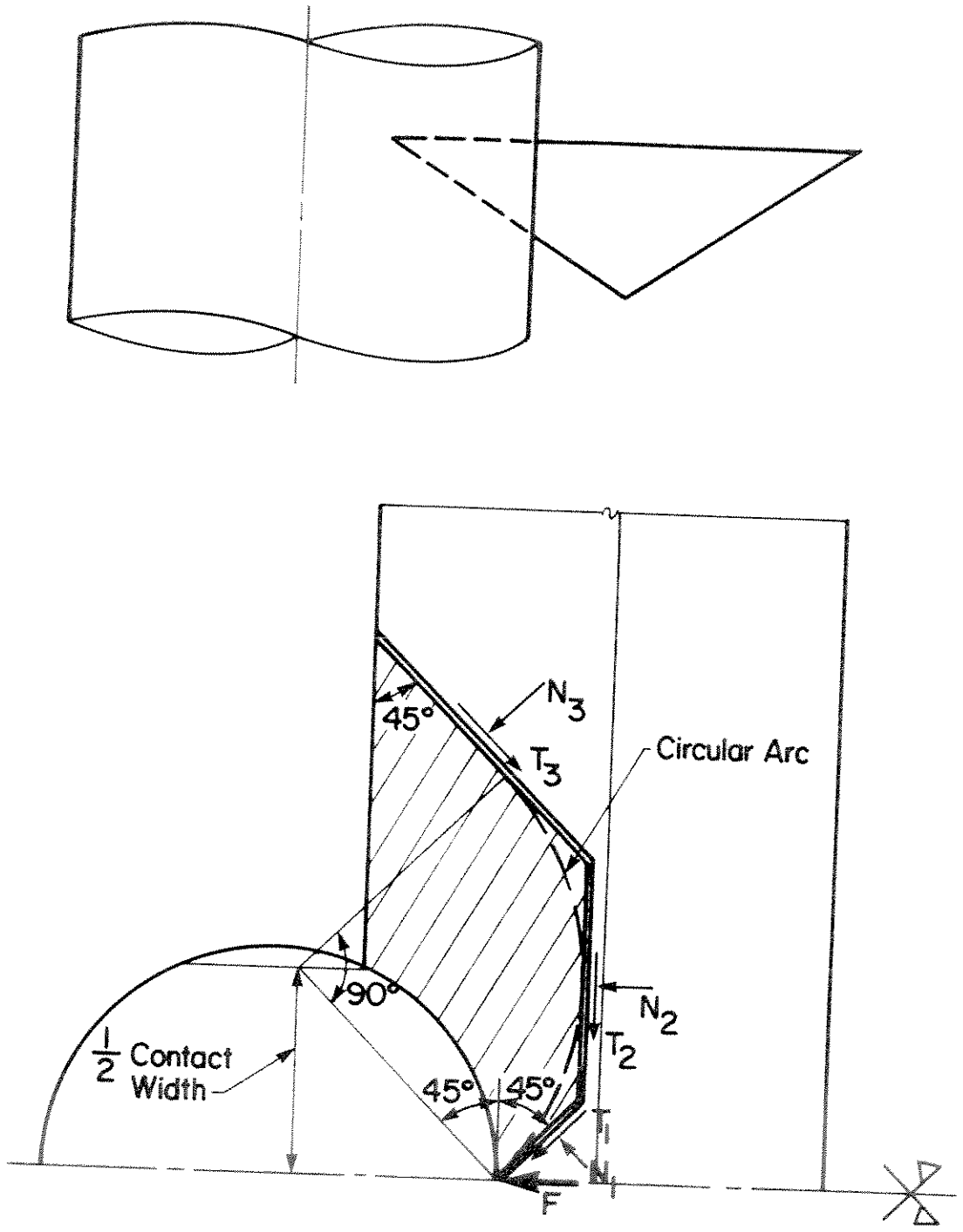

Figure 5.28 Simplified shape of rubble discontinuity surface

$$T = \int_A \tau \, da \tag{5.31}$$

where a denotes area, and A is the total area over which T is calculated. Substituting Eq.(5.29) into Eq.(5.2), and using the result in (5.31) leads to:

$$T = cA + N \tan \phi \tag{5.32}$$

This procedure can be used to calculate a force-penetration curve for the process of ridge-structure interaction by using the appropriate contact width (see Figure 5.28) for each value of the penetration. Polygonal structures are treated in the same manner by using the actual contact width between the ridge and the structure.

For the shear failure depicted in Figure 5.27 (c), the force on the structure is given by:

$$F = 2T \tag{5.33}$$

where the shear force T on the failure plane is calculated as before. The maximum force on the structure is obtained as the lowest of the maximum ridge crushing force and the ridge shearing force.

5.5.2 Conical structures

The loose rubble constituting a first-year ridge is not expected to ride-up a conical structure, and the envisaged failure mechanisms for the ridge are the same as those for vertical structures. Therefore, the horizontal force on the structure is

calculated in the same manner as for vertical structures. It is noted that the intersection surface between the ridge and the conical structure will be variable in width, as shown in Figure 5.29, where R_t and R_b denote the radii of the structure at the top and bottom of the intersection surface. For the purpose of this analysis, the contact width corresponding to the average contact radius R_a is used. If friction forces between the rubble and the structure are ignored, the vertical force F_{V_s} is calculated from the horizontal force F_{H_s} using:

$$F_{V_s} = F_{H_s} \tan \alpha \tag{5.34}$$

where α is the cone slope angle.

5.5.3 Examples

The results of the model used to calculate forces from first-year ridges on the structure are illustrated in Figure 5.30. The figure shows the force penetration curves for the interaction of a ridge which has a 2-m high sail with the two structures shown. The rubble cohesion used is .035 MPa (Prodanovic, 1981), and the friction angle of the rubble is 25°. It can be seen that the rubble-crushing force rises faster, and reaches a higher value in the case of the circular structure than for the case of the square structure. This is due to the high rate of increase of contact width with the penetration for the circular structure. The drop of the force value in each case starts once the discontinuity surface passes the thickest point on the ridge (see Figure 5.28). It can also be seen that the shear failure force is less than the maximum rubble-crushing force for both structures and thus, shear is the governing mechanism in these two examples.

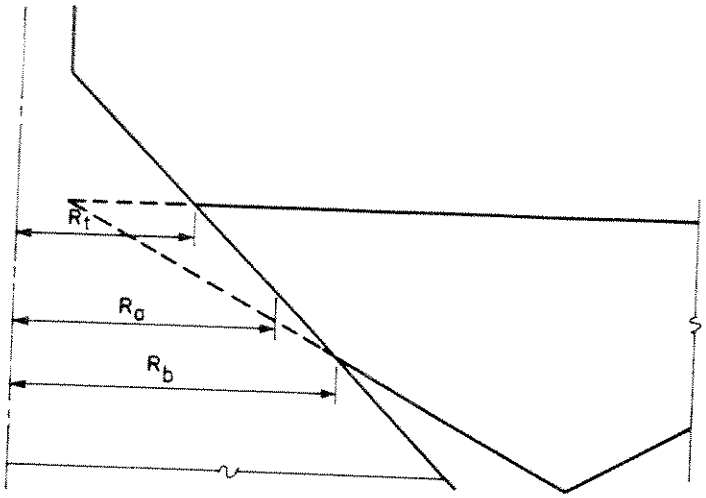

(a) Upward Breaking Cone

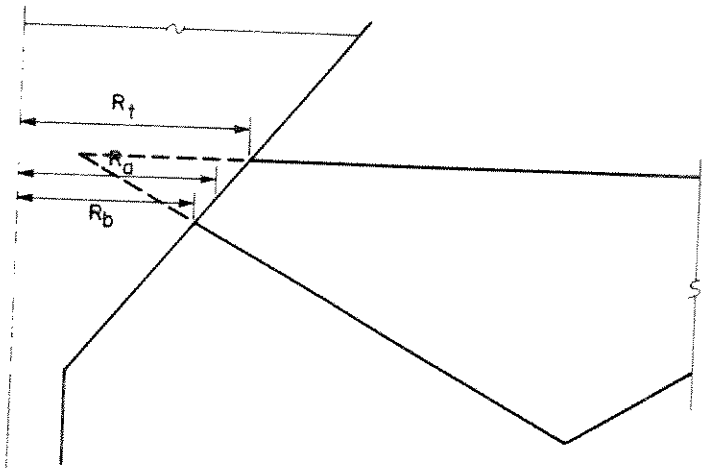

(b) Downward Breaking Cone

Figure 5.29 The intersection between a first-year ridge and a conical structure

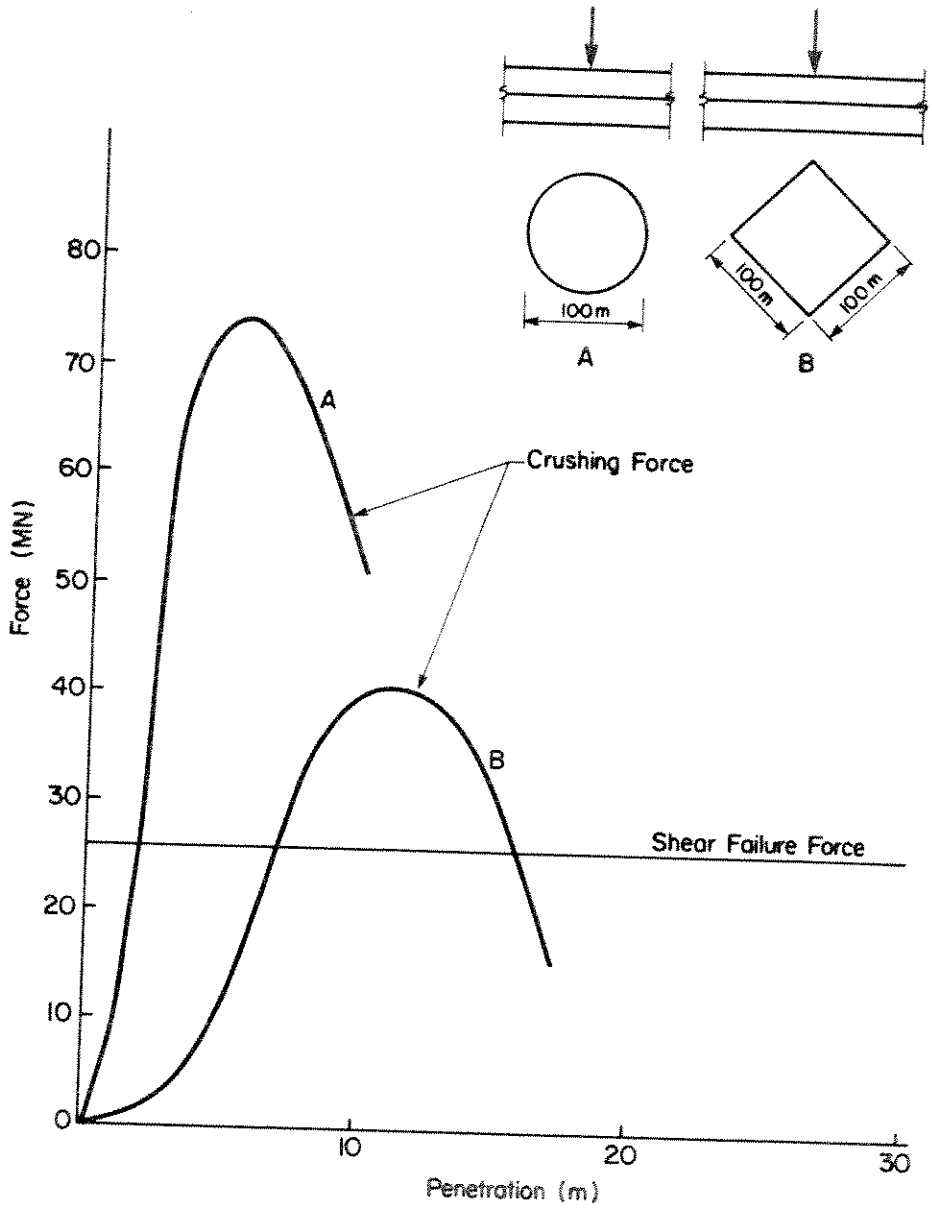

Figure 5.30 Sample result of first-year ridge forces on vertical structures

Chapter 6

DEVELOPMENT OF PROBABILISTIC LOAD MODELS

6.1 General

The probability density function of the extremal load for any load scenario depends on the period of time during which the scenario is applicable, and the severity of the ice conditions during loading. There are two distinct types of stochastic time processes which apply to different ice loading scenarios, namely discrete processes and continuous processes (see Chapter 3). The former is applicable to all loading scenarios which relate to discrete ice features, such as multi-year floes, ice islands and first-year ridges. On the other hand, continuous processes are appropriate for first-year level ice which is constantly moving against the structure. The basic principles relating the calculation of extremal distributions for each of the above-mentioned processes was discussed in Chapter 3. The present chapter addresses the application of this methodology to each specific ice load scenario and the development of the required inputs. The basic probability distribution, which is calculated throughout this analysis, is the cumulative probability distribution of the maximum annual load. This distribution is used to derive an extremal load probabilistic description for any time period and in any desired format (i.e. return periods, probability density or probability of exceedance).

6.2 Season Length Model

This section deals with the derivation of the probability density function of the length of each season from the pdf's of the season boundaries as discussed in Section 2.2. As illustrated in Figure 6.1, the following equations can be written:

$$T_1 = 365 - (T_{31} - T_{12}) \tag{6.1}$$

$$T_2 = T_{23} - T_{12} \tag{6.2}$$

$$T_3 = T_{31} - T_{23} \tag{6.3}$$

where T_1, T_2, and T_3 are the lengths of the winter, break-up, and summer seasons respectively, and T_{12}, T_{23}, and T_{31} are the season boundary dates in days from the beginning of the year, as shown in Figure 6.1

It was concluded in Section 4.2.1 that the season boundary dates follow a normal pdf. It can be shown that a quantity which is the difference between two normally-distribued random quantities is also normally distributed with a mean equal to the difference between the means of the two original quantities, and a variance equal to the sum of their variances. T_2, for example, is normally distributed with a mean μ_{T_2} given by:

$$\mu_{T_2} = \mu_{T_{23}} - \mu_{T_{12}} \tag{6.4}$$

and a standard deviation σ_{T_2} given by:

$$\sigma^2_{T_2} = \sigma^2_{T_{23}} + \sigma^2_{T_{12}} \tag{6.5}$$

Similar results are applicable to T_1 and T_3, with the average value of T_1 equal to $365 - (\mu_{T_{31}} - \mu_{T_{12}})$.

A normally-distributed parameter varies between $-\infty$ and ∞. In the case of season lengths, some physical bounds apply. The length of any season, for example, cannot be smaller than zero or greater than 365. Season lengths are also bounded by the difference between the extreme values of the season boundary dates. For the break-up season, for example $(T_{23_{min}} - T_{12_{max}}) < T_2 < (T_{23_{max}} - T_{12_{min}})$. These bounds are applied to the pdf of each season length by truncating the density function at the limiting values, and adding a concentrated probability mass at each end of the function equal to the truncated area. In the computer model, the maximum and minimum season boundary values are taken at three standard deviations on either side of the mean.

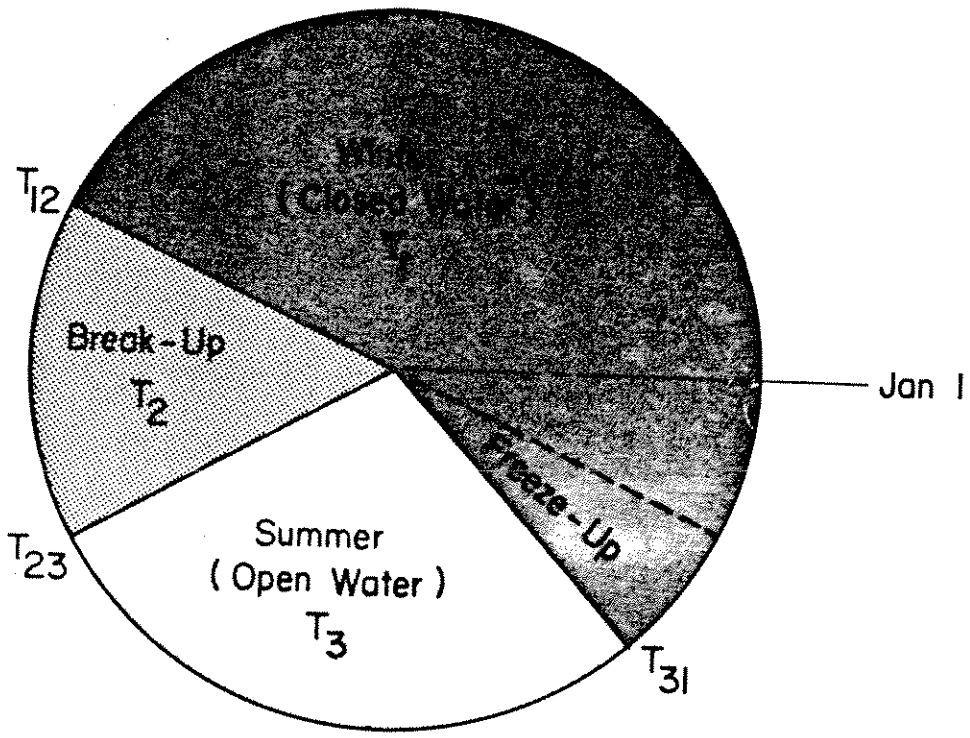

$T_1 = T_{12} - T_{31}$

$T_2 = T_{23} - T_{12}$

$T_3 = T_{31} - T_{23}$

Figure 6.1

Illustration of the derivation of season lengths from season boundaries

If the season lengths after applying this truncation are denoted T', the probability distribution of T' is given by:

$$
\begin{aligned}
p_{T'}(T' = t_{min}) &= \int_{0}^{t_{min}} N(\mu_T, \sigma_T)\, dt = p_1 \\
f_{T'}(T') &= N(\mu_T, \sigma_T), \qquad t_{min} < t < t_{max}, \\
p_{T'}(T' = t_{max}) &= 1 - \int_{t_{max}}^{\infty} N(\mu_T, \sigma_T)\, dt = p_2
\end{aligned}
\tag{6.7}
$$

where p denotes probability, and t_{min} and t_{max} are the minimum and maximum values of t, and $N(\mu, \sigma)$ is the normal density function for a random quantity, with mean μ and standard deviation σ.

As discussed in Section 3.4, the average interaction rate for ice features is calculated in terms of the average season length. This is the mean value of the probability distribution defined by Eq.(6.7), and is given by:

$$
\mu_{T'} = t_{min} p_1 + \frac{\sigma_T \left(\exp\left\{ -\frac{1}{2} \left(\frac{t_{min} - \mu_T}{\sigma_T} \right)^2 \right\} - \exp\left\{ -\frac{1}{2} \left(\frac{t_{max} - \mu_T}{\sigma_T} \right) \right\} \right)}{2\pi (1 - p_1 - p_2)}
$$

$$
+ \mu_T (1 - p_1 - p_2) + t_{max} p_2 \tag{6.8}
$$

Equation (6.8) can be used with the appropriate parameters to calculate the average length of each season. The application of this analysis to the season boundary dates for Prudhoe Bay (default values as given in Chapte 4), gives average season lengths of 257, 92, and 20 days for the winter, summer and break-up seasons, respectively. These add up to 369 days within 1% of the total number of 365 days per year. This confirms the validity of the approach and its underlying assumptions.

6.3 Discrete Ice Features (Discrete Processes)

Interactions with all discrete ice features (i.e. multi-year floes, ice islands and first-year ridges) in all seasons are modelled as discrete processes. The derivation of the extremal load distribution during a given period of time $f_Y(y)$ from the average rate of interactions $\bar{\lambda}$ and the probability distribution of the peak load during each interacton $f_X(x)$, was dealt with in Section 3.7. In this section, the calculation of $f_X(x)$ and the average rate of the process $\bar{\lambda}$ will be discussed.

6.3.1 The probability density function of the load per event

The derivation of the pdf of the maximum load from the probabilistic descriptions of the input parameters to a given ice-structure interaction model is a problem of functions of random quantities. Let X be a random quantity (load) defined as:

$$X = g\ \{Z_1,\ Z_2,\ \ldots,\ Z_m\} \tag{6.9}$$

where $Z_1, Z_2, \ldots, Z_m$ are also random quantities(ice parameters). In principle, the probability density function of X can be calculated from the pdf's of Z_i, i = 1, m, and the function g. The application of this principle was illustrated in Section 6.2, where the pdf of the season length was calculated in closed form from the pdf's of the season boundaries. In practice, closed-form solutions are available only for limited cases, with special types of pdf's and special functional forms (g in Eq.(6.9)).

In the present analysis, g in Eq. (6.9) represents the ice-structure interaction model and $Z_1, Z_2, \ldots, Z_m$ represent the input parameters. With the level of complexity of ice-structure interaction models used, closed form solutions are not available. The problem can be solved numerically using Monte Carlo simulation. The basic principle behind this method is to simulate a number of combinations of the parameters $Z_1, Z_2, \ldots, Z_m$ from their respective probability distributions. Each combination can be used to calculate a vlaue of the parameter X until a sufficient number of data points to define $f_X(x)$ is obtained. The number of simulations is

determined by limiting the variation in the mean value of X due to an additional data point to a user-defined tolerance. A smaller tolerance will lead to a larger number of simulated data points. It is noted that Monte Carlo simulation is resorted to here as a numerical solution for a problem which cannot be solved in closed form . Due to the computer costs involved, the use of Monte Carlo simulation has been avoided wherever possible. Closed-form solutions have been used in modelling the stochastic process of the occurrence of interaction, calculating the average rate of the process, and evaluating the extremal load pdf (Chapter 3). Monte Carlo simulation is only used for calculating the pdf of the load for one interaction from the probabilistic descriptions of the input parameters to the ice-structure interaction model.

The set of parameters required for each load scenario are listed in Table 2.2. The probability distributions of these parameters can be defined by the user from a set of distributions available in the model. Besides most of the standard mathematical distributions, a data set which cannot be fitted to a mathematical model can be used directly by defining the cumulative density function numerically. Any parameter or set of parameters can be assigned deterministic values if desired. A set of default probability distributions (see Chapter 4) are offered to the user, but these should be replaced by site specific data for a given problem.

The probability distributions for some of the parameters related to multi-year floe and ice island collisions are not defined on the basis of data, but on the basis of nature of the parameter. These parameters, for which the probability distributions are built into the model, are as follows:

(i) The eccentricity of the collision.

(ii) The ice feature approach angle.

(iii) The orientation of a multi-year ridge on a multi-year floe at the instant of interaction between the ridge and the structure.

(iv) The thickness of first-year ice behind a multi-year floe during a winter interaction.

(v) The percentage of the width of a multi-year floe subject to first-year ice pressure during an interaction in the break-up season. This is to account for the fact that in the break-up season, the first-year ice will cover only part of the opening between multi-year floes, and consequently only part of the multi-year floe will be subjected to first-year ice pressure.

For all of the above parameters, there is no reason to believe that any value of the parameter is more likely to occur than other values. These parameters are therefore assigned uniform probability density functions of the form:

$$f_Z(z) = \frac{1}{Z_{max} - Z_{min}} \qquad (6.10)$$

where Z_{max} and Z_{min} are the maximum and minimum values of the parameter.

It is also interesting to note that the characteristics of the extremal distribution are mostly dependent on the characteristics of the tail of the original distribution, especially for high rates of occurrence of the event. It is, therefore, of great importance to obtain enough data points on the tail of the probability distribution of the force in one interaction event. This can be effeciently achieved by setting lower bounds on some of the interaction parameters under which the parameter values are not to be considered. This will result in a large number of data points in the high force range and a better definition of the extremal distribution. The model is structured in such a manner as to allow the user to define lower bound values for any number of parametres.

6.3.2 The average rate of interaction

The principles and methodology used to calculate the average rate of interaction with discrete features was discussed in Section 3.3. Equation 3.6 is used to calculate the average rate of interaction with ice islands in the summer and multi-year floes in all seasons. First-year ridge average interaction rates are calculated using Eq. (3.10)

for the winter season, where a full ice cover is present. For the break-up season, first-year ice coverage varies between 3/10ths and 8/10ths (as defined in Section 2.2). The average rate for the break-up season can, therefore, be calculated by multiplying the results of Eq.(3.10) by the average break-up ice concentration of 5.5/10ths.

If lower bounds are used, the interaction rate is adjusted to obtain the rate of interactions with features which have parameter values larger than the defined lower bounds. This is done by multiplying the rate of all interactions by the probability that the interacting feature will have parameter values in the specified range. The average rate of interactions with multi-year floes larger than 500 m in diameter, for example ($\bar{\lambda}_{500}$) can be obtained from:

$$\bar{\lambda}_{500} = \bar{\lambda} \int_{500}^{\infty} f_D(d)\, d\, d \qquad (6.11)$$

where $f_D(d)$ is the pdf of the diameter of colliding floes and $\bar{\lambda}$ is the average rate of interaction for all floes.

The submerged thickness of an ice island which interacts with the structure is limited by the water depth. Since 90% of the island thickness is submerged, its total thickness cannot exceed about 1.1 times the water depth. This upper bound truncation is accounted for by adjusting the average rate of interaction in a similar manner to that discussed earlier for parameter lower bounds.

6.4 Level Ice in the Winter Season (Continuous Process)

Ice loads from a full first-year level ice cover can be modelled by a continuous process, as shown in Figure 6.2. The variability in the ice force in this process results from two sources:

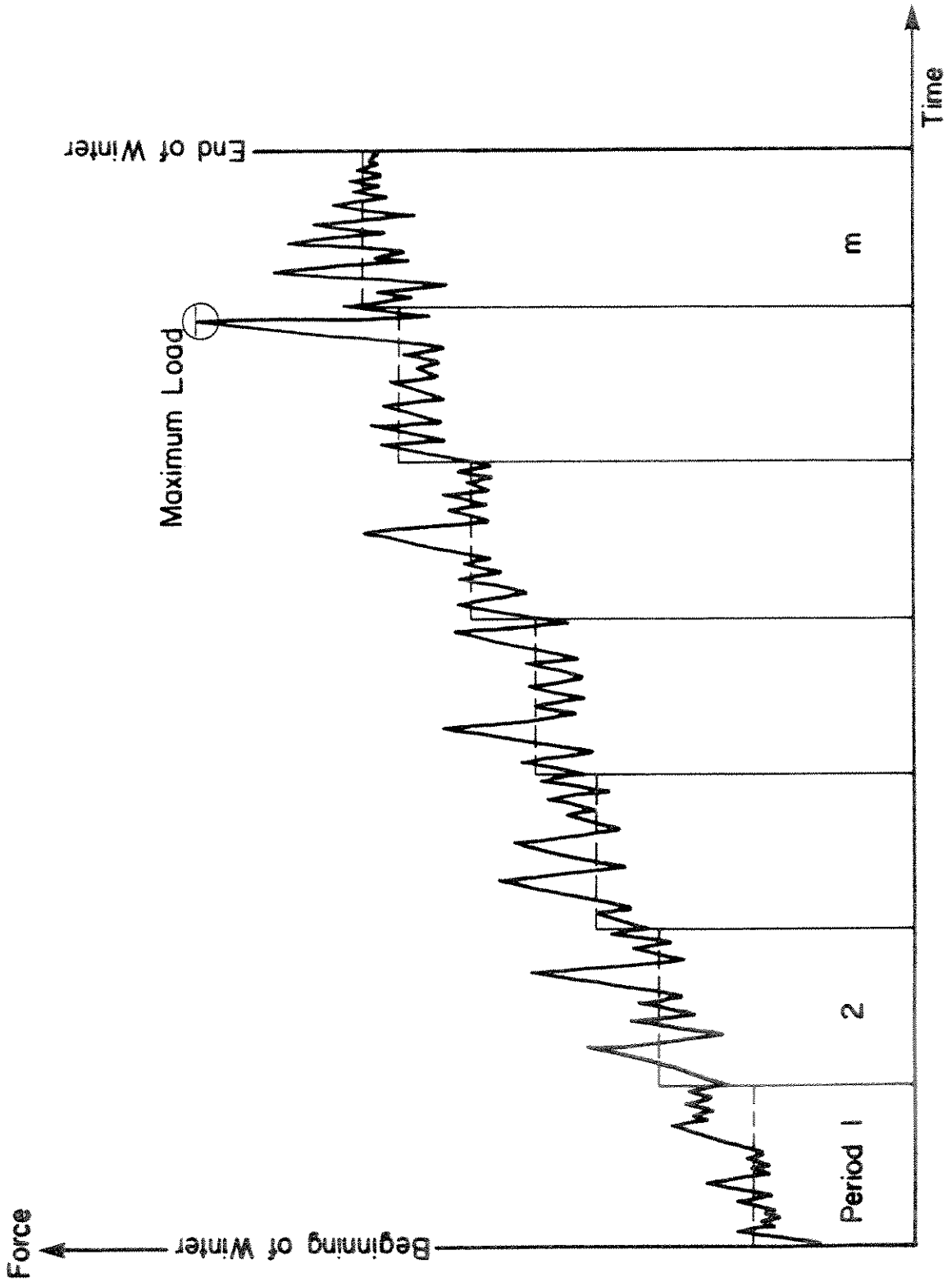

Figure 6.2. Schematic Representation of the Variation of Ice Load with Time

(i) A systematic variation: This is due to the monotonic increase in ice thickness with time during the winter season. The process is therefore non-stationary (i.e. has a variable mean). The variation in the mean value of the ice thickness at any point in time is very small, as has been discussed in Section 4.2.3.1. Moreover, this variation is mostly due to season-to-season variations and not due to fluctuations within the same season. This is illustrated in Figure 6.3, where ice growth curves for three years at Cape Perry are plotted. Each season displays regular growth with very little variation around the mean value. It is concluded, therefore, that only the systematic variation in ice thickness need be considered.

(ii) Random variations: Because the force on the structure is only dependent on the ice thickness and the stress in ice (see Section 5.5), this variation can only be attributed to fluctuations in the ice pressure.

The non-stationary random process discussed above is treated by discretizing it into a number of stationary random processes applicable at time intervals of suitable length, as shown in Figure 6.2. This amounts to modelling the ice thickness by the step function shown by the dashed line in Figure 6.2. The cumulative probability distribution of the final extremal load during the whole season can be calculated using:

$$F_Y(y) = \prod_{i=1}^{m} F_{Y_i|t_i}(y_i) \tag{6.12}$$

where $F_{Y_i|t_i}(y_i)$ are the cumulative distribution functions of the extreme load during each time interval, which are conditional on the ice thickness for that interval. Equatoin (6.12) implies that given the ice thickness, extrem load during each time interval is independent of the extreme loads during other time intervals. The time interval t_i is taken as one month in this study.

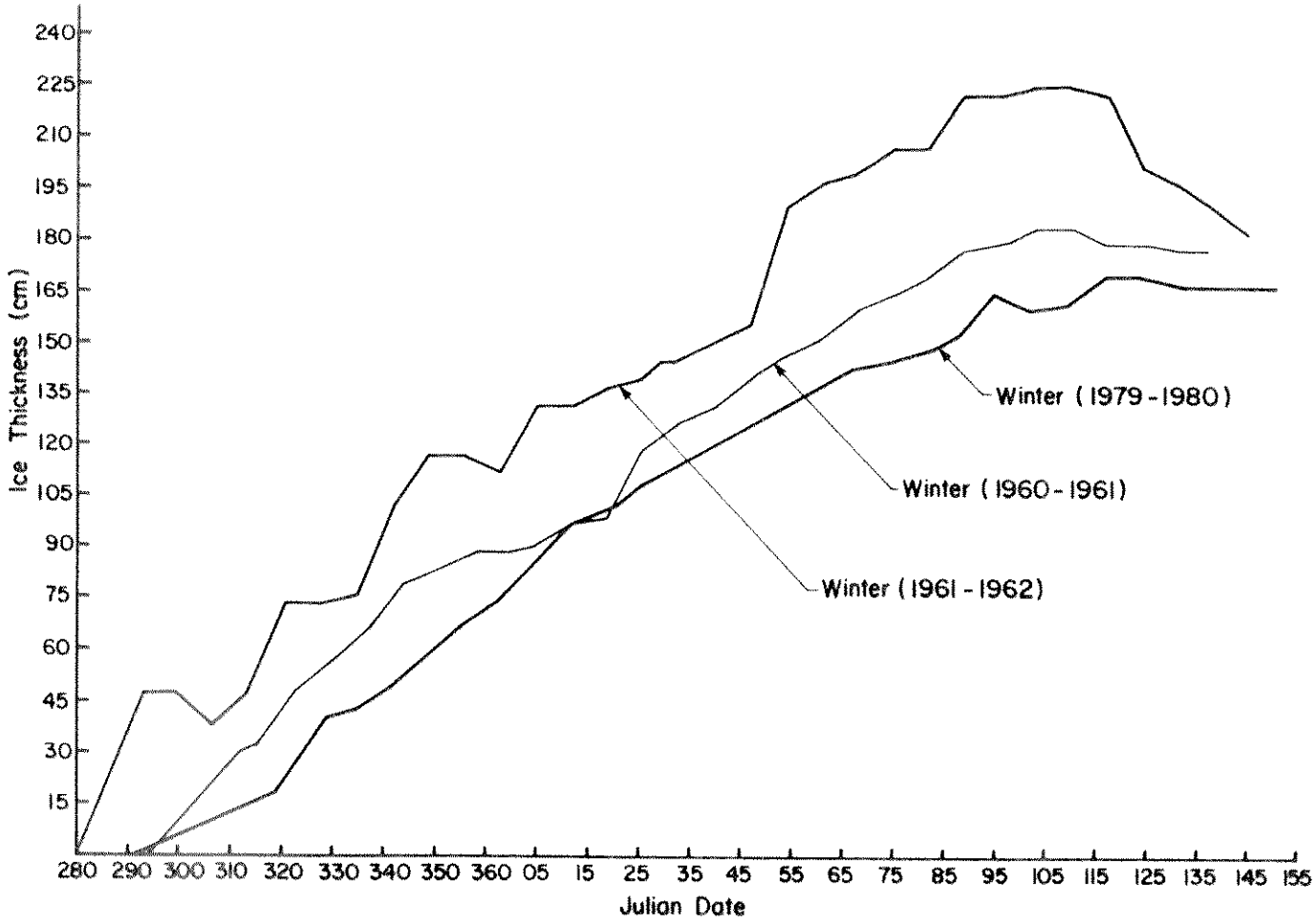

Figure 6.3. Ice Growth Curves at Cape Perry for Three Winter Seasons

The final extremal load distribution $F_Y(y)$ is more influenced by $F_{Y_i|t_i}(y_i)$ corresponding to higher values of t_i. This effect is more pronounced as the number of force peaks during each time interval increases. This is a reflection of the expected trend that the maximum force will tend to occur when the ice thickness is high, especially if the number of occurrences of a peak force during the corresponding time interval is large.

The evaluation of $F_{Y_i|t_i}(y_i)$ is dependent on the ice-structure interaction model used in the ice zone under consideration. The landfast and the active ice zones will be discussed separately in the following sub-sections.

6.4.1 The landfast ice zone

Only vertical-sided structures are considered in the landfast ice zone. The maximum ice movement ratio in the landfast zone in the data set analyzed in the study was about 10 m/hr. For a 100m wide structure, this corresponds to a nominal strain rate of 5.6×10^{-5}. Average speeds are in the order of 0.4-0.5 m/hr, which would lead to nominal strain rates well below the creep-crushing transition. Therefore, the stresses in the ice at normal landfast movement rates are determined from a creep model which is dependent on the velocity of the ice (see Sec. 5.4.1.3). In the creep mode, the force is monotonically increasing with the velocity as can be seen from Eq.(5.23). The peak forces will, therefore, occur at the peak speeds for a given ice thickness, t_i. A sample time trace of the ice movement rate in the landfast zone is given in Figure 6.4 (Spedding, 1977). This is obtained from hourly interrogations of the ice movement, which means that these speeds are averages over a one-hour interval. This is appropriate for the creep model, since the ice speed must be sustained for a reasonable interval of time before the steady state maximum creep load is reached. The load fluctuations can be expected to follow a similar pattern to the velocity fluctuations in Figure 6.4. The probability density function of the load at a velocity peak can be obtained by using the velocity peak density function in Eq.(5.25). The latter is obtained by measuring velocity peaks from velocity data in the format given in Figure 6.4. The final extremal distributoin of the creep force during each month can be obtained by modelling the number of peaks with a Poisson distribution. The

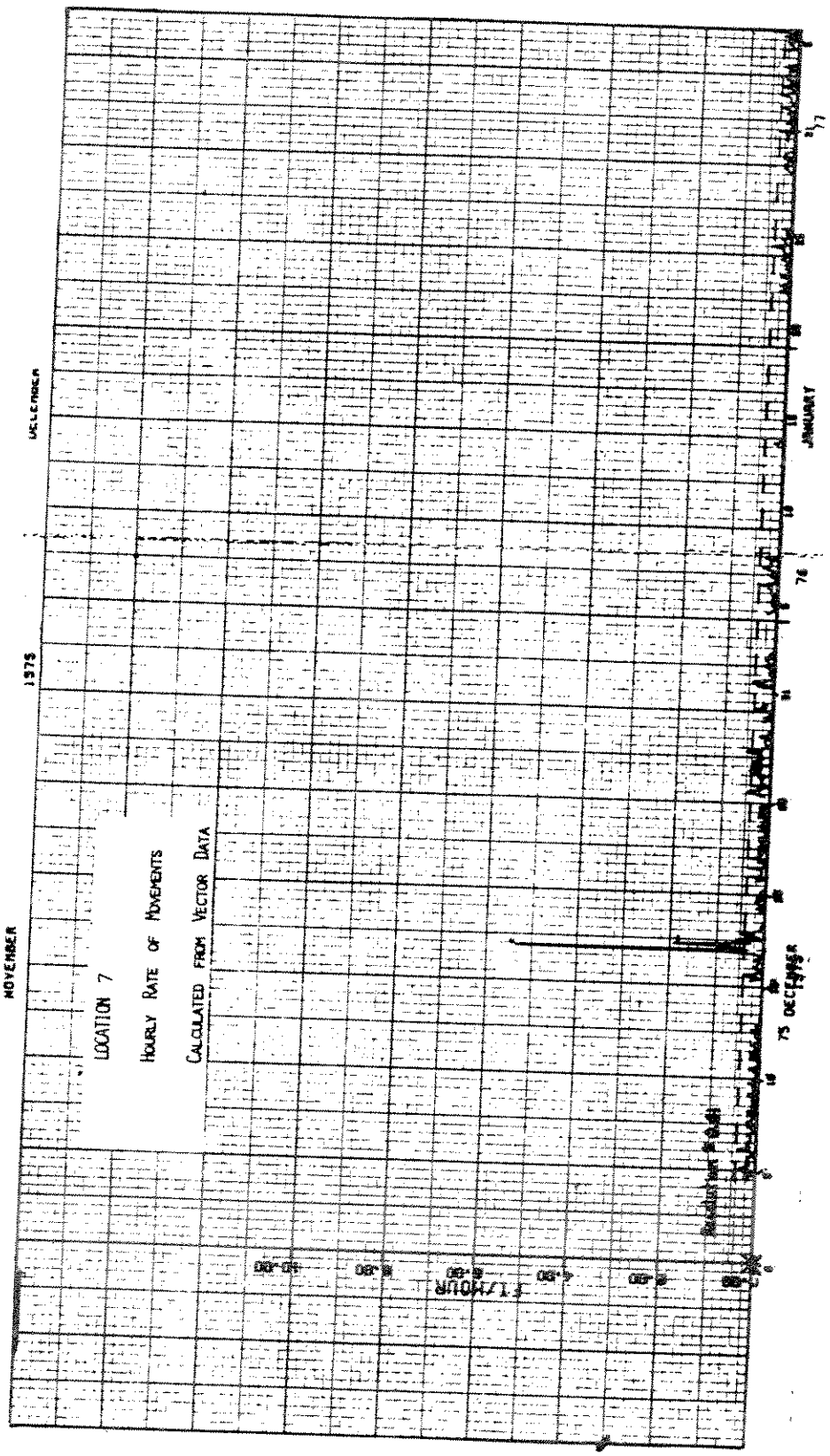

Figure 6.4. Sample Trace of Landfast Ice Movement Rate

rate of this distribution can be obtained as the product of the time interval during which creep dominates and the rate of occurrence of velocity peaks, which can be counted from the velocity trace.

The above-mentioned extremal load distribution is conditional on normal landfast ice movement rates. During "break-off" (see Section 5.4.1.2), higher speeds occur and crushing is expected to dominate. The method for calculating the extremal force distribution during such an event is the same as for the active ice zones, and this will be explained in detail in Section 6.4.2. Based on the rate of occurrence of break-off events and the average duration of each event, the average length of time during each month for which ice crushing is dominant can be estimated. This time span can then be used with the appropriate ice distribution (see Section 6.4.2) to calculate the monthly extremal force distribution during break-off events (i.e. crushing dominated events). The overall monthly extremal $F_{Y_i|t_i}(y_i)$ can then be obtained by combining the creep monthly extremal and the crushing monthly extremal using Eq. (3.46).

6.4.2 The active ice zone

In the active ice zones, the ice is constantly in motion. For vertical structures, there is a cut-off speed which separates creep dominated movements and crushing dominated movements (creep in the low range, and crushing in the high range). The monthly extremal force distribution is calculated by combining two separate components, one for creep and one for crushing, as discussed in Section 6.4. The time period during which each process is dominant is calculated from the velocity density function by apportioning each month according to the probability of the velocity being in the appropriate range.

During crushing, fluctuations in ice pressure are due to variations in the ice properties and response, as it crushes along the structure. The time variation of the average ice pressure on the structure can be quantified on the basis of experimental results. This is a continuous stochastic process for which the pressure at any local peak can be expressed as (see Figure 6.5):

$$\sigma = \sigma_m + \sigma_r \qquad (6.12)$$

where σ_m is the mean pressure component, and σ_r is a random pressure component. The pdf of σ_r in a given time period can be assigned on the basis of a pressure time trace such as the one shown Figure 6.5. This can be modelled by a double exponential distribution (see Section 3.8) with parameters depending on the length of time during which the maximum load is sought. In the model, the mean pressure σ_m and the mean and standard deviation for the extremal component of the peak pressure σ_r are used in the ice-structure interaction model of Eq.(5.21), to calculate the probability distribution of the monthly peak load during crushing.

The creep case is treated in a similar manner to that described in Sectoin 6.4.1. The main difference is that average velocities in adjacent time intervals are used instead of velocity peaks. The length of these adjacent intervals is equal to the length of time over which velocities are averaged in the measurement used in defining the velocity distribution. It is felt that hourly measurements are most appropriate, but 24 hours are used as model default, since reliable hourly velocities were not available.

For conical structures, the same approach is used as for the crushing case discussed above, with the ice flexural strength and the appropriate ice-structure interaction model (Section 5.4.2).

6.5 Level Ice in the Break-Up Season (Interrupted Process)

The stochastic model for ice pressure in the break-up season is illustrated in Figure 6.6. This is similar to the winter season with the following two differences:

(i) There are open-water patches within the ice cover, and the load is therefore not applied throughout the season as shown in Figure 6.5. This introduces a reduction to the time priod during which the load is applied. The reduction factor is equal to the average ice concentration during the season (5.5 tenths).

(ii) Due to the small, average length of the break-up season (approximately 3 weeks), the systematic change in ice thickness due to melting is small. Therefore, the season is modelled as a stationary process with a constant mean.

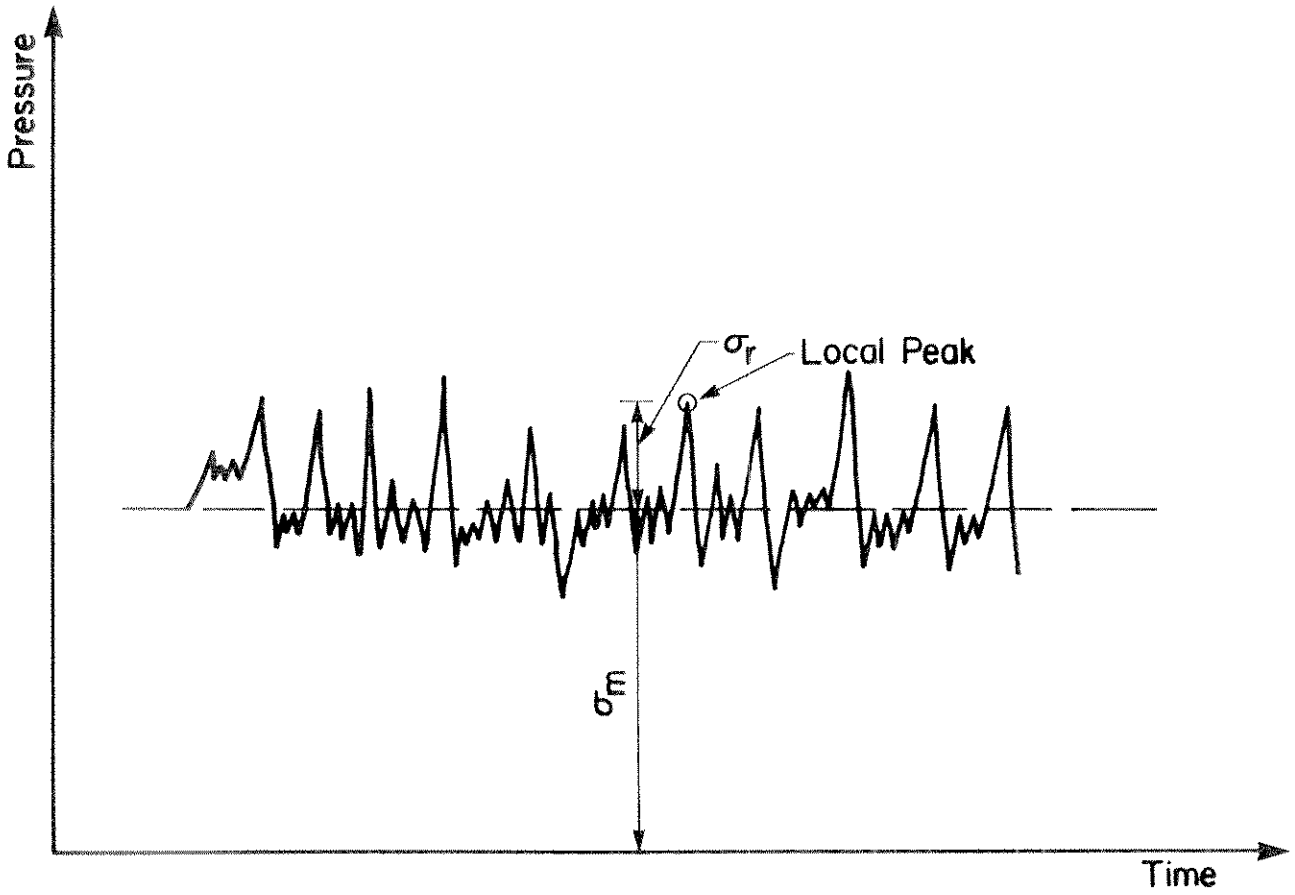

Figure 6.5. Modelling of the Peak Ice Pressure
as the Sum of Mean and Random Components

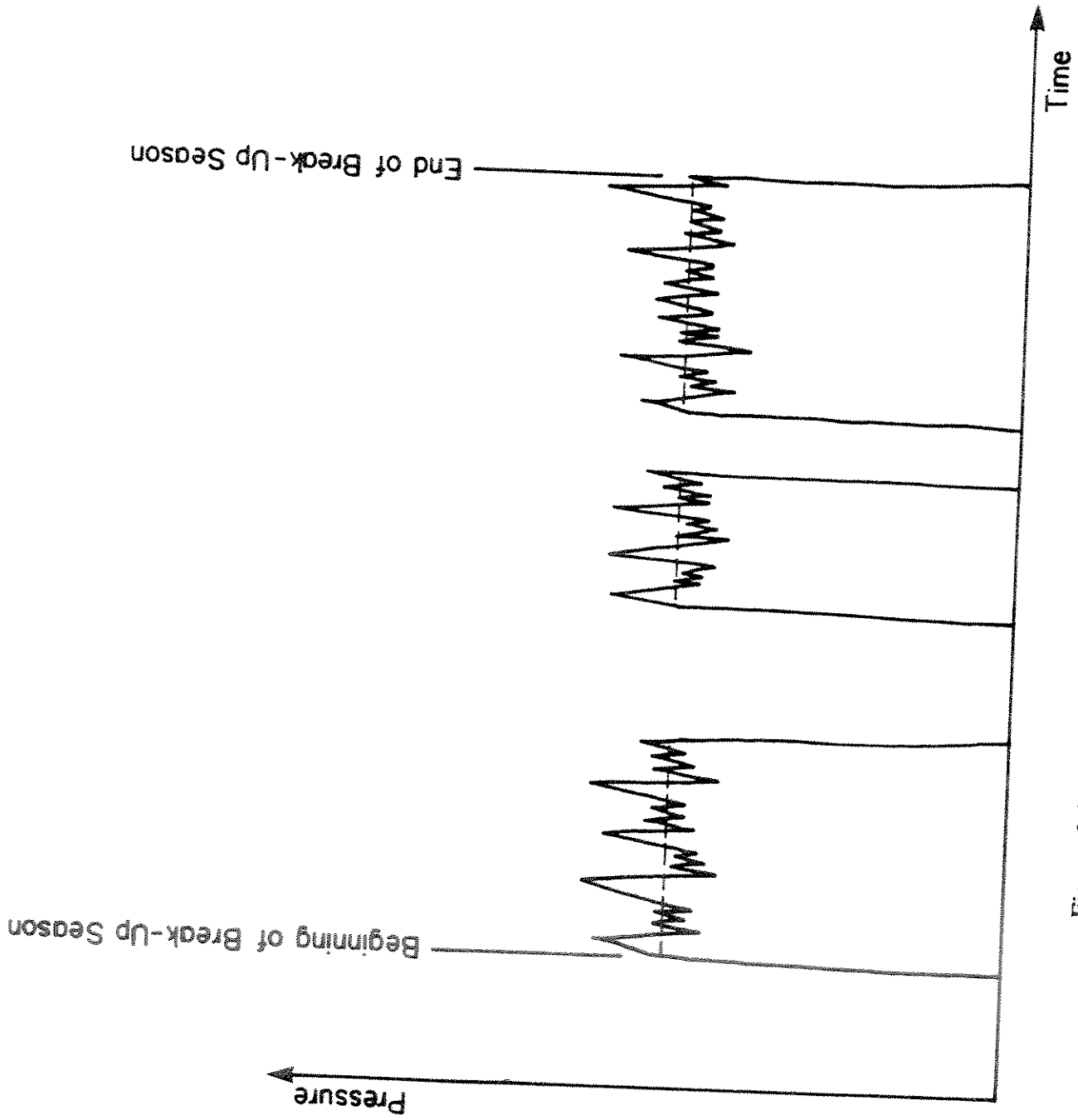

Figure 6.6. Interrupted Process for Level Ice in the Break-up Season

The procedure for calculating the cumulative probability distribution of the extreme load $F_Y(y)$ is the same as for the crushing load in one month during the winter season. The only modification required is to adjust the mean and standard deviation of the monthly extremal pressure (which are given as input), according to the actual average season length using Eqs. (3.48).

6.5 Sample Results

Results of an example run of BOREAS for a circular vertical structure 100 m in diameter are given in Figures 6.7 to 6.14. In the figures, CDF denotes cumulative density function whereas POE denotes the probability of exceedance. The structure was assumed to be located in the shear zone of the Canadian Beaufort Sea at water depth of 30 m. The results were produced using version 1 of the program for a tolerance of 5×10^{-3} on the mean force value as a criterion for determining the number of simulations in each case. The default values were used for all parameters. The curves could be made smoother by reducing the tolerance, but this was not done here since these results are only for illustration. The following points are noted:

(i) In Figure 6.7, the extremal force cumulative density function does not start at zero. This is because the rate of occurrence of multi-year floe collisions during the break-up season is smaller than 1, and therefore there is a finite probability (0.21 in this case) of not having any collisions (i.e. zero force).

(ii) For level ice in the break-up season (Figure 6.8), there is only one result representing the season extreme.

(iii) The extremal force distribution for first-year ridges in the winter season (Figure 6.10) has very little associated uncertainty, and is approximately equal to the maximum force simulated in one interaction. This is a reflection of a very high rate of interactions with first-year ridges, which causes the extremal force to be almost certainly equal to the maximum possible load.

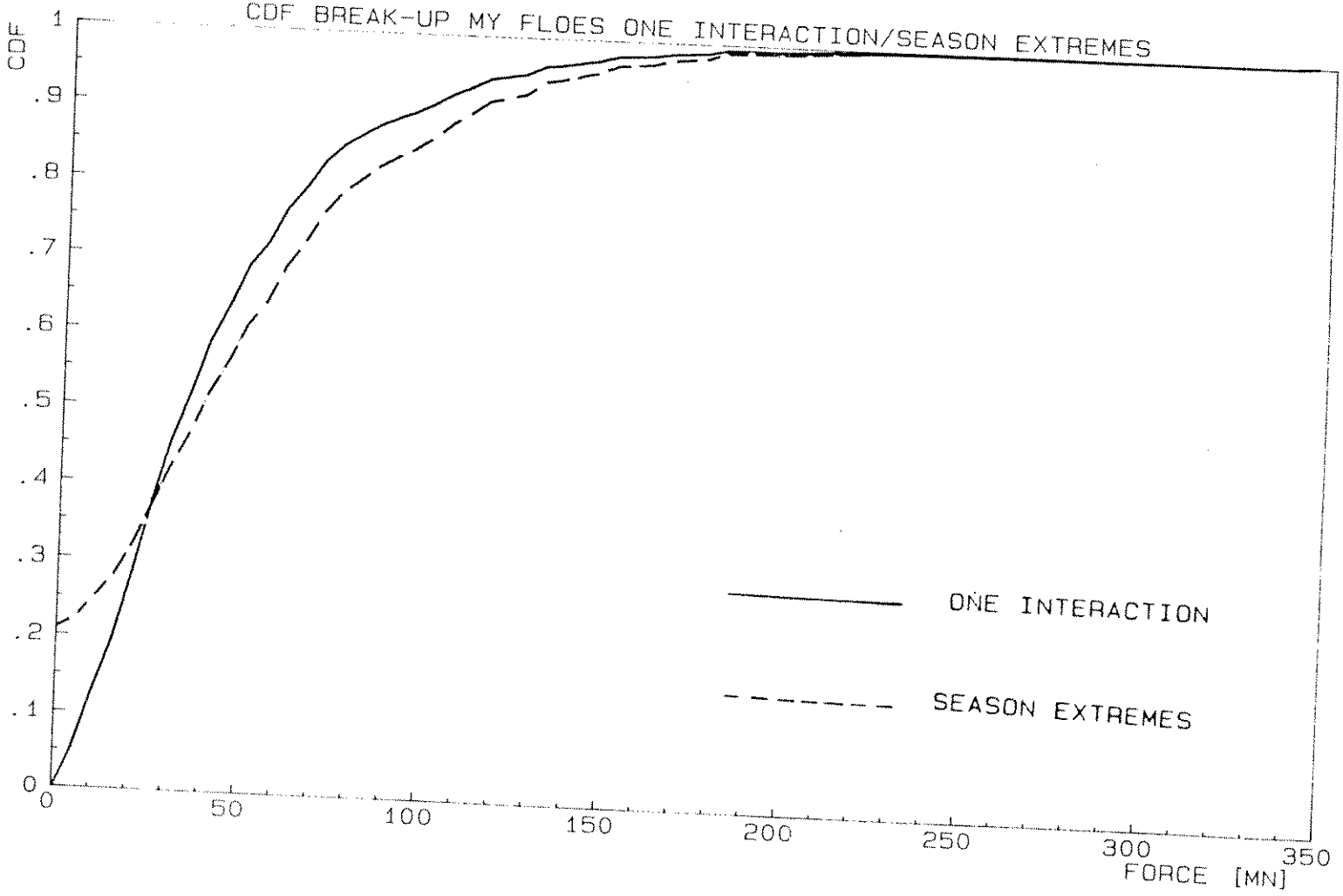

Figure 6.7. Sample results for a circular vertical structure

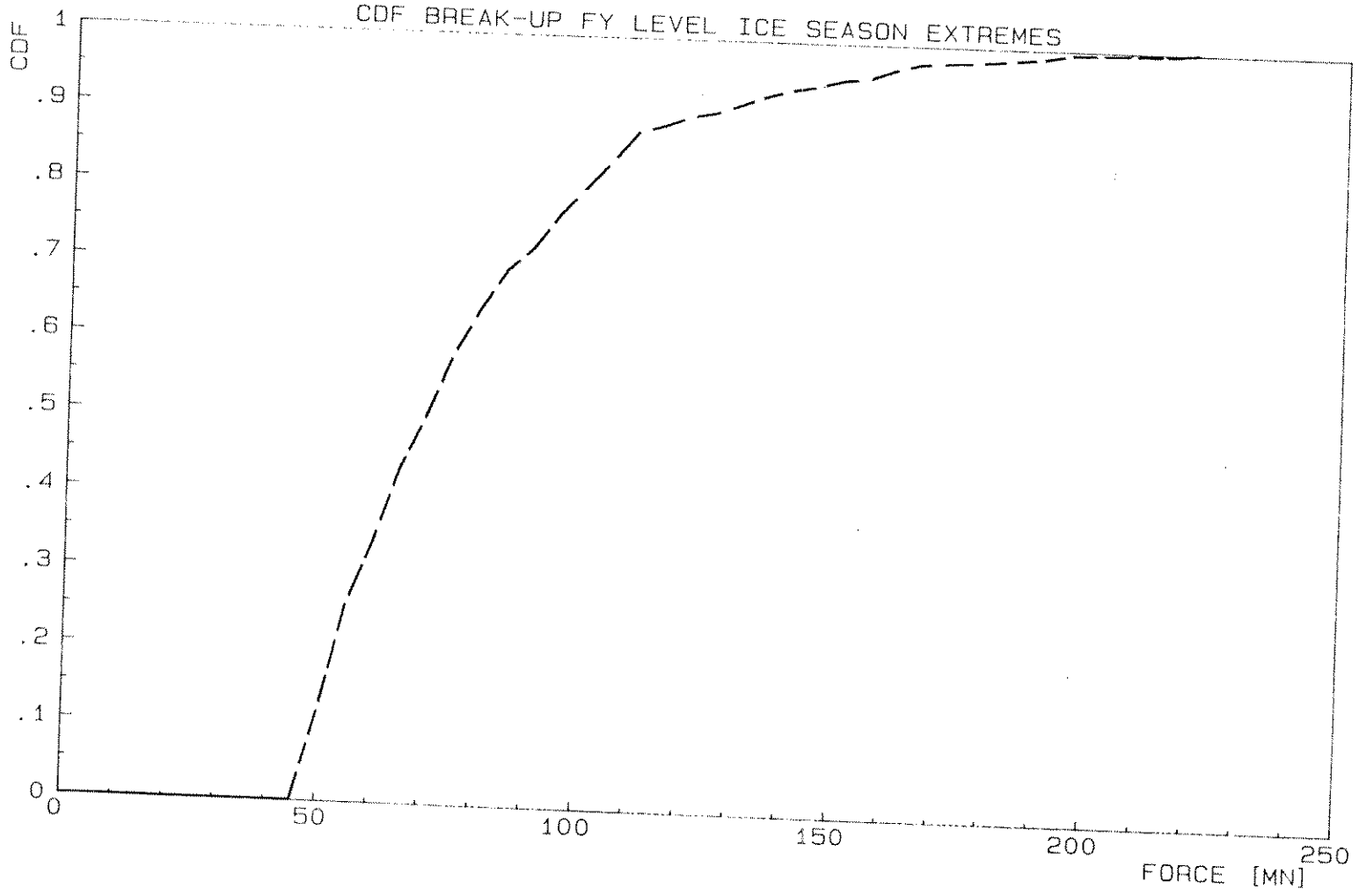

Figure 6.8. Sample results for a circular vertical structure (continued)

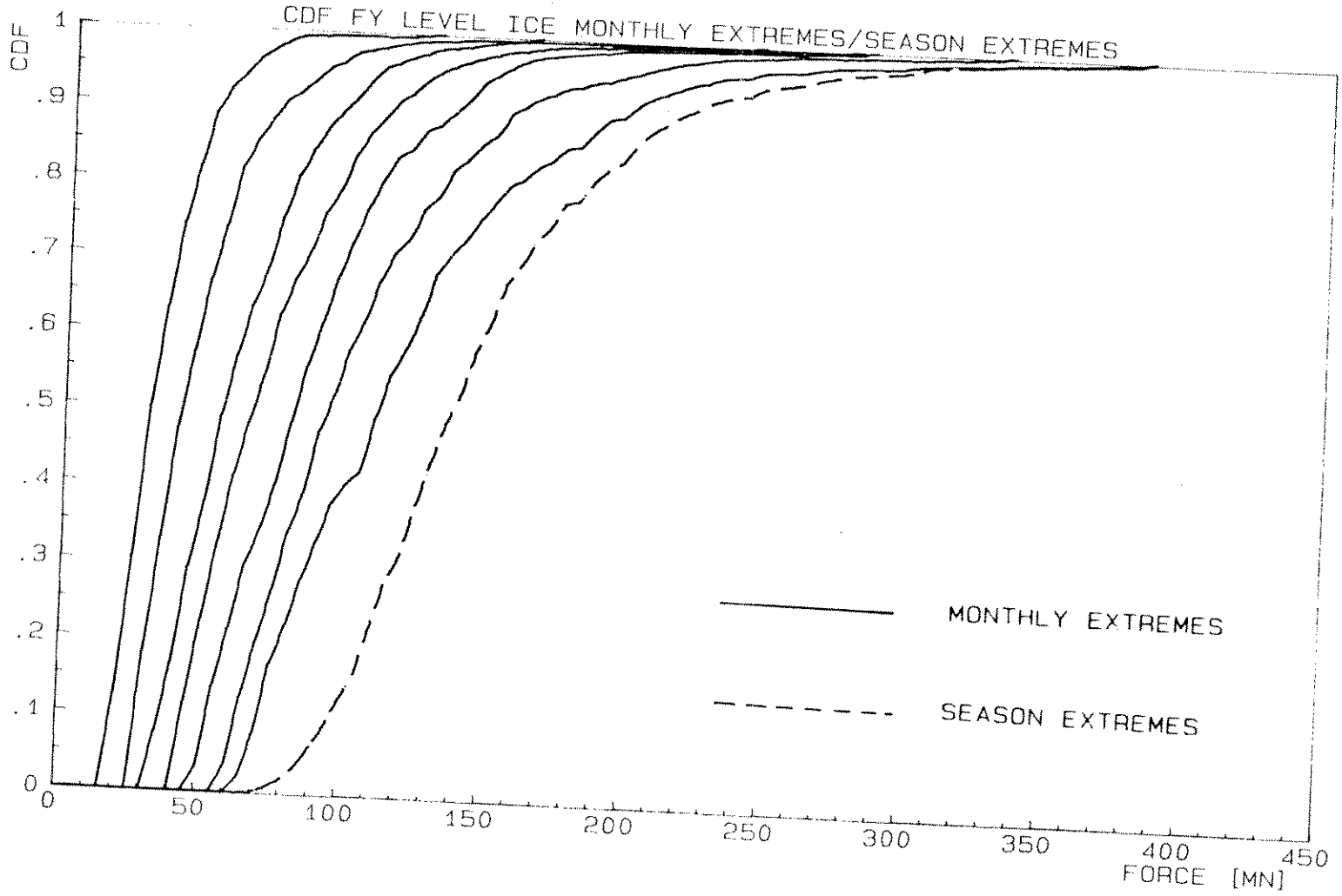

Figure 6.9. Sample results for a circular vertical structure (continued)

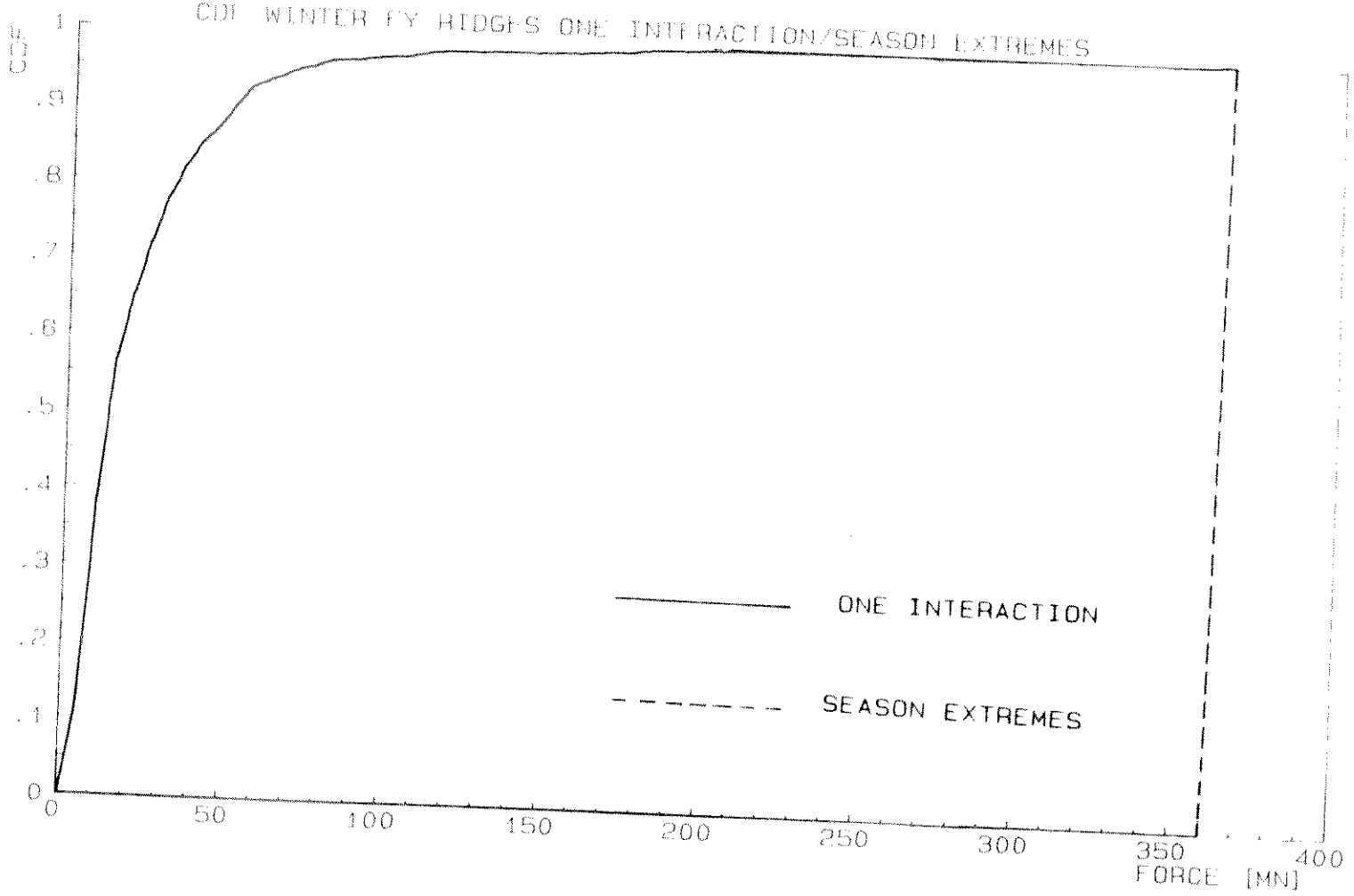

Figure 6.10. Sample results for a circular vertical structure (continued)

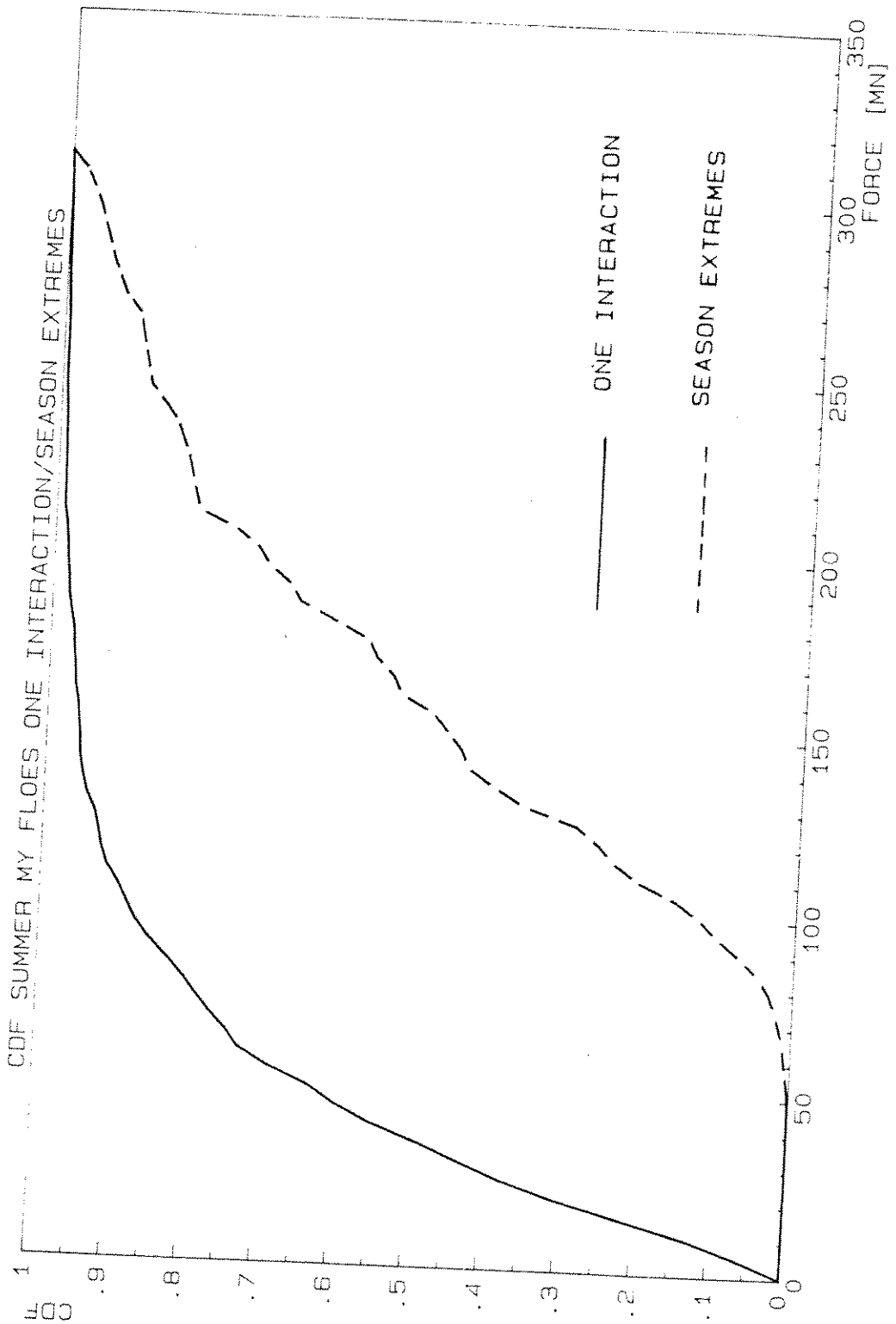

Figure 6.11. Sample results for a circular vertical structure (continued)

Figure 6.12. Sample results for a circular vertical structure (continued)

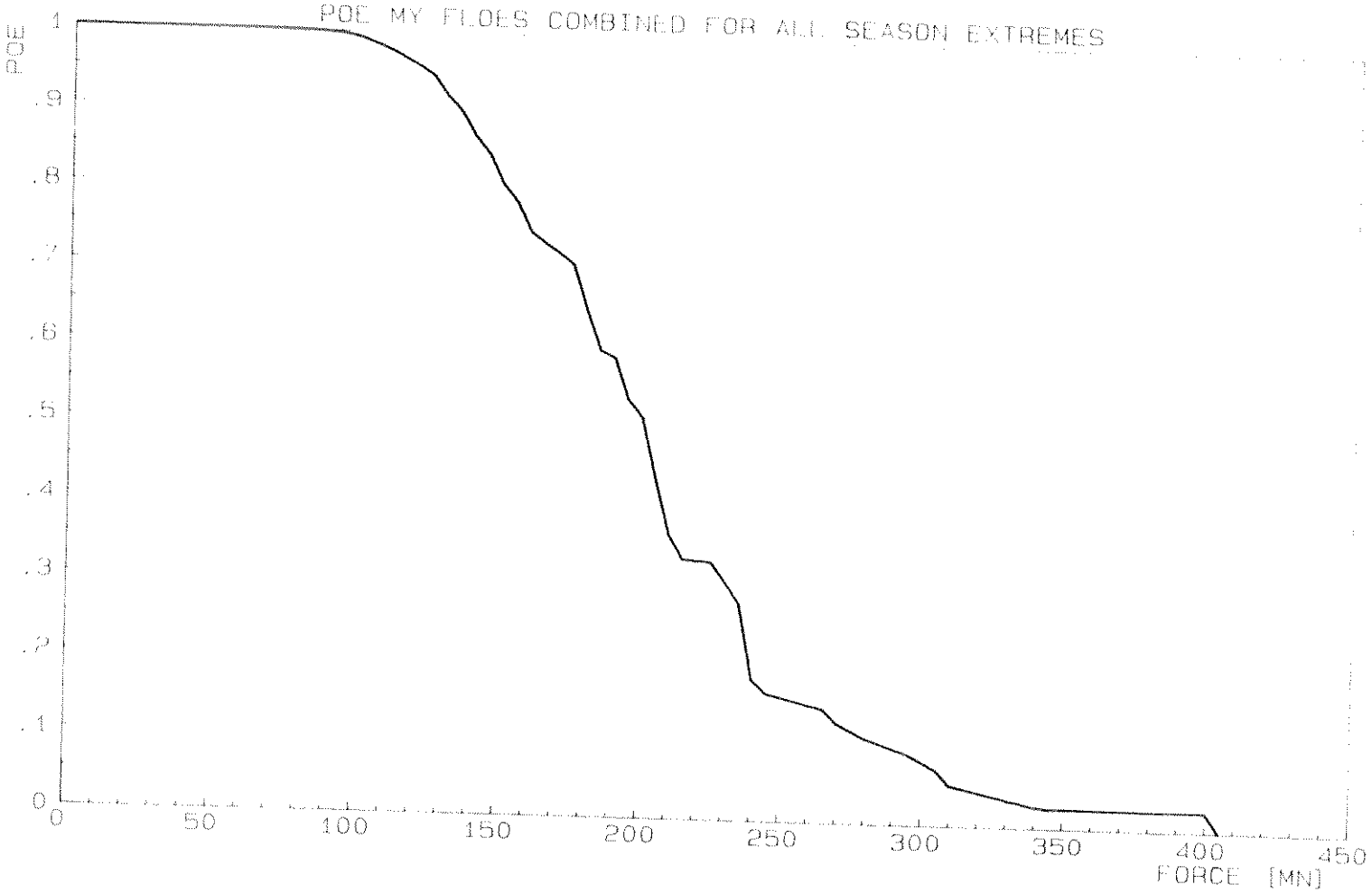

Figure 6.13. Sample results for a circular vertical structure (continued)

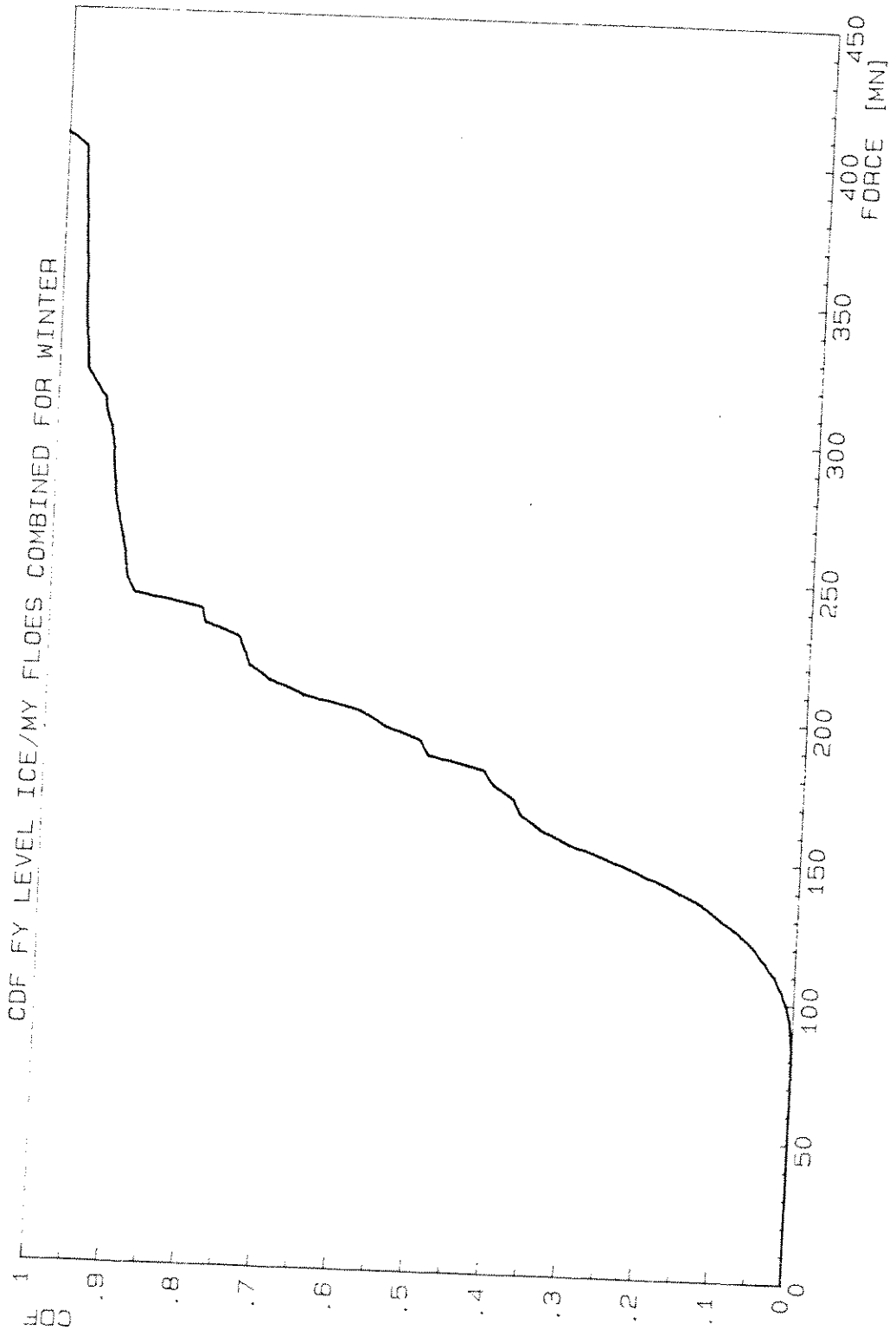

Figure 6.14. Sample results for a circular vertical structure (continued)

Examples of the extremal force probabilistic descriptions for different scenario combinations are given in Figures 6.12 to 6.14.

Results for an upward breaking 45^{o} conical structure with a water line diameter of 75 m, a freeboard of 15 m, with a coefficient of friction of 0.15 with the ice are given in Figures 6.15 and 6.16. Version 1 of BOREAS was also used for this example, with the same tolerance as for the vertical structure discussed above. The program default values were used. Only the cumulative density functions for winter multi-year floes for different scenario combinations are given in Figures 6.15 and 6.16 for illustration. Other scenarios and scenario combinations produce similar results to those given for vertical structures, except that the force is represented by its horizontal and vertical components in each case.

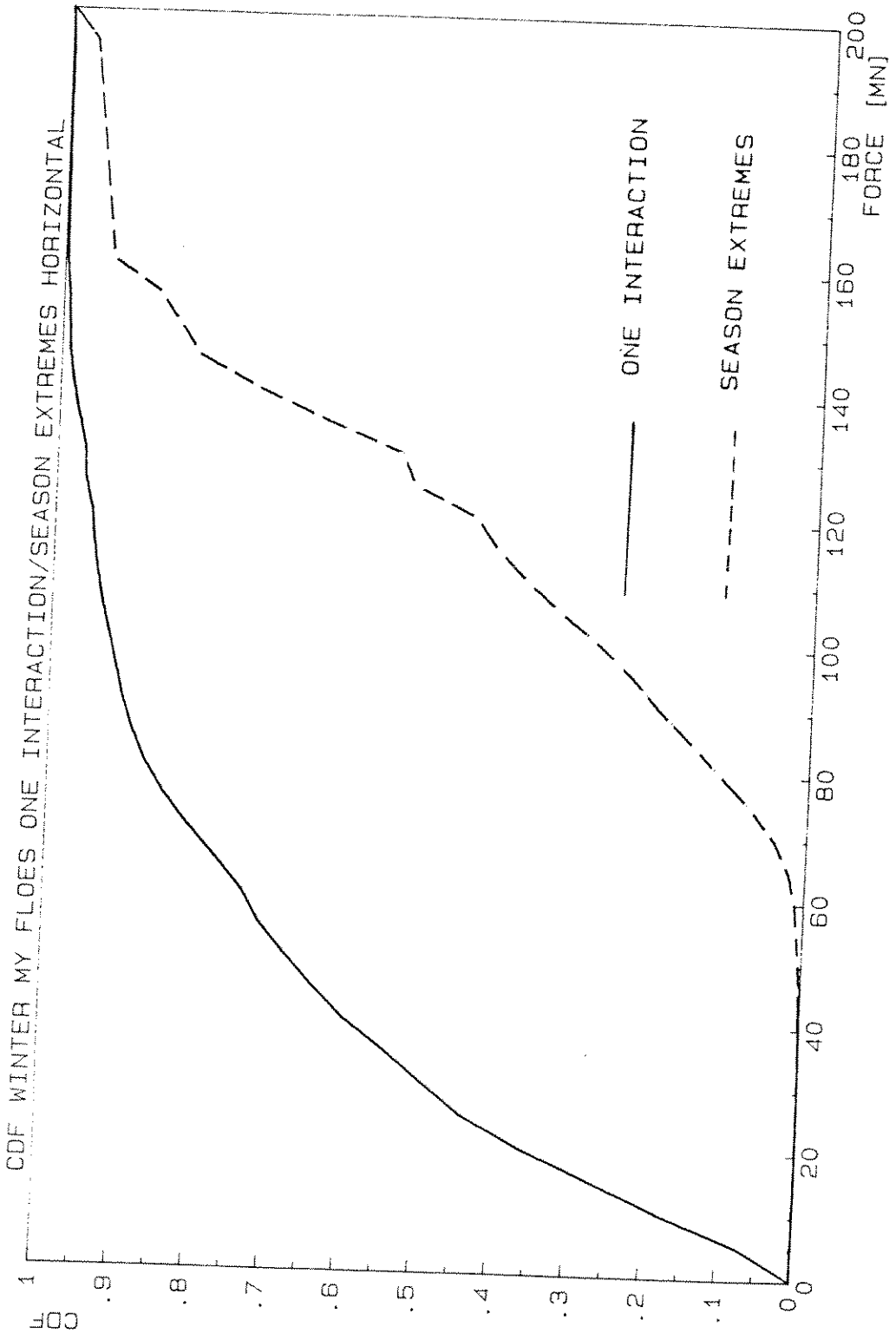

Figure 6.15. Sample results for upward breaking conical structure

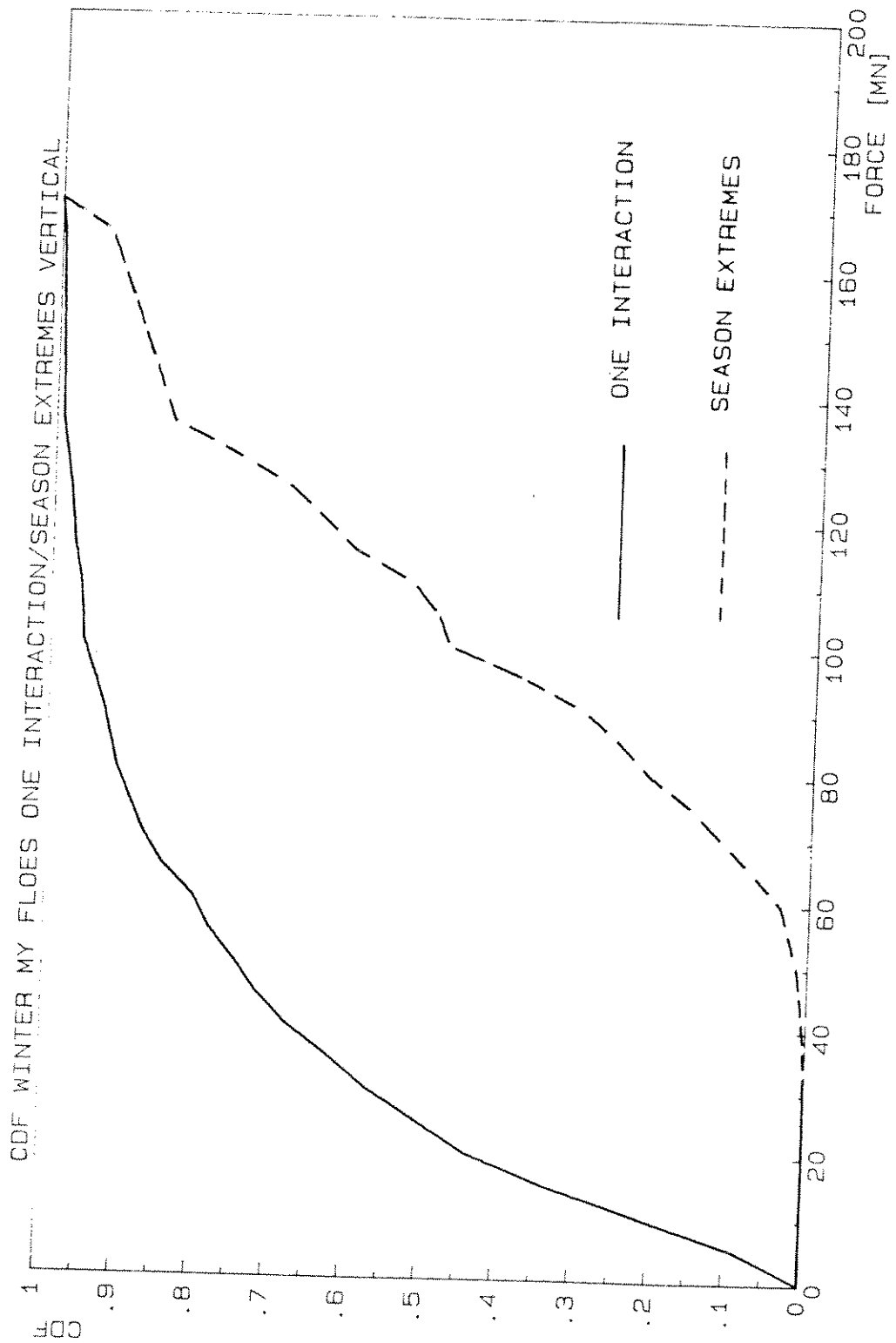

Figure 6.16. Sample results for upward breaking conical structure (continued)

7. CONCLUDING REMARKS

A comprehensive model for estimating year-round ice loads in the Beaufort Sea has been developed. The structural geometries considered in the study are vertical-sided, structures with circular or polygonal cross sections, as well as upward and downward breaking cones. Ice load scenarios are defined on the basis of the ice conditions in the Beaufort Sea. The developed models can, however, be used for other geographic areas which experience one or more of the loading scenarios addressed in the study. Statistical models have been developed for season boundaries and season lengths, and for the environmental and mechanical ice parameters needed for the calculation of ice loads. These are combined with appropriate ice structure interaction models in order to calculate probabilistic descriptions of ice loads which are later combined in an overall model of extremal analysis to calculate the probability distribution of the maximum annual load resulting from any scenario or combination of scenarios.

The original intent was to use existing state-of-the-art ice structure interaction models, and concentrate on the environmental and statistical aspects of the problem. It was found, however, that in order to account for some of the statistical aspects, novel work in the area of ice structure interaction was needed. This included the development of an integrated multi-year floe model for open and closed water interactions, which accounts for the energy dissipation in the presence of the pack ice forces. Much of the work needed for this model was related to the calculation of the local forces for the different structural geometries at different penetration values. Finite element work was also carried out as background for the application of the reference stress method to the problem of ice creep in the landfast zone.

A computer package BOREAS was developed to carry out the analysis. The package is divided into an input program, a main program, and an output program. The input and output programs are fully interactive, and all three programs have back-up and data retrieval facilities. The program is developed in a modular form to allow for replacements and future modifications of certain parts of the model with minimum effort.

The emphasis in the study is on model and computer program development. The user should choose and input the appropriate statistical descriptions for the specific location being considered. Default values are given in the model, but these should not be construed as recommended values for the development of design loads.

In the course of the study, it became evident that ice mechanics and ice-structure interaction are important areas which greatly affect the calculated loads. Some aspects of ice mechanics such as the effect of global fracture and the behaviour of ice during crushing appear to be important, and need to be adequately modelled. The statistical and extremal aspects of the problem have been comprehensively addressed, and appropriate models have been used. This results in a well-defined set of input parameters, which are useful as a guide for the collection of information. Some of the required parameters need better definition than is presently available in the literature. These include ridge coverage, ridge geometric properties (e.g. length and width). Also, some statistical data analysis of actual ice pressure histories would be useful in defining the appropriate extremal pressure distributions.

References

AIDJEX, 1976. Ice Thickness. AIDJEX Bulletin No. 32, pp. 65-68.

Atmospheric Environment Service, 1953-1984. Ice Charts. Environment Canada.

Barton, R., et. al., 1972. Ice-Island Count, South Beaufort Sea, APOA PROJECT 053-01.

Bathe, R.J., and Wilson, E.L., 1976. Numerical Methods in Finite Element Analysis. Prentice Hall, New Jersey.

Cochran, W.G., 1952. The χ^2 Test of Goodness of Fit. Annals of Mathematical Statistics, 23, pp. 315-345.

Cornell, C.A., 1969. Structural Safety Specifications Based on Second-Moment Reliability Analysis. IABSE Final Report on Concepts of Structures and Methods of Design, London, pp. 235-245.

Cornett, S. and B.W. Danielewicz, 1982. Ground Ridge Frequency and the Stability of Landfast Ice in the Beaufort Sea. Dome Petroleum Ltd.

Croasdale, K.R., 1980. Ice Forces on Fixed Rigid Structures.In Working Group on Ice Forces on Structures. A State-of-the-Art Report, CRREL Special Report 8-26.

Croasdale, K.R. and L.G. Spedding, 1972. Landfast Ice Movement - Mackenzie Delta 1972. APOA Project 33. Esso Resources Canada Limited, Internal Report IPRT-5ME-72.

Danielewicz and Pilkington, 1980. Selected Environmental Characteristics of Beaufort Sea Ice. Beaufort Sea EIS Study.

De Paoli, S., Morrison, T.B, and Marcellus, R.W., 1982. Analysis of Interaction Probabilities Between Large Ice Features and Offshore Structures in the Canadian Beaufort Sea, Beaufort EIS.

Dickins, D.F., A. Dickinson and B. Humphrey, 1985. Statistical Description of Pack Ice in the Beaufort Sea, Lancaster Sound, and the Labrador Sea. for Environmental Protection Service, Environment Canada.

Dunwoody, A.B., 1983. The Design Ice Island for Impact Against an Offshore Structure, OTC '83.

Fidjestoel, P., 1983 b. VOSIL - Vertical Offshore Structures Ice Loading, Simulation Program Documentation, Veritas Report 83-8513 (Proprietary).

Frederking, R., 1978. The Flexural Behaviour of Ice From In-Situ Cantilever Beam Tests. Presented at IAHR Symposium on Ice Problems, Lutea, Sweden.

Gladwell, R.W., 1976. Statistical Analysis of Ice Pressure Ridge Distribution in the Southern Beaufort Sea. APOA Project 54. Esso Resources Canada Limited, Internal Report IPRT-13ME-76.

Gregory, P., and Tschebotarioff, 1973. Foundations, Retaining and Earth Structures, McGraw Hill, New York.

Hetenyi, M., 1946. Beams on Elastic Foundations. The University of Michigan Press.

Hibler III, W.d., S. Ackley, W.F. Weeks and A. Kovacs, 1972. Top and Bottom Roughness of a Multiyear Ice Floe. AIDJEX Bulleting No.13, pp. 77-92.

Hoare, R.D. et al., 1980. Seasonal Pack Ice Characteristics in the Shear Zone of the Beaufort Sea Based on Data from an Upward Looking Sonic Profiler (1978-1979). APOA Project 147. Canadian Marine Drilling Ltd.

Hutter, K., 1975. Floating Sea Ice Plates and the Significance of Dependence of the Poisson Ratio on Brine Content. Proceedings of the Royal Society of London, Ser. A, Vol.343, No.1632, pp. 85-108.

Jordaan, I.J., Lantos, S., and Nessim, M., 1985. A Probabilistic Approach to the Estimation of Environmental Driving Forces Acting Upon Arctic Offshore Structures, presented at Arctic '85.

Korzhavin, K.N., 1962. Action of Ice on Engineering Structures. USSR Academy of Science, Draft Translation 260, CRREL, 1971.

Kovacs, A., 1983. Characteristics of Multiyear Pressure Ridges. POAC '83, Vol.3, pp. 173-182.

Kry, P.R., 1977. Ice Rubble Fields in the Vicinity of Artificial Islands. Proceedings of POAC, St. John's, Newfoundland, Vol.I, pp. 200-211.

Kurdymov, V.A. and Kheisin, D.E., 1976. Hydrodynamic Model of the Impact of a Solid on Ice. Prikladnaya Mechanika, Vol.12, No.10, pp. 103-109.

Lainey, L., and Tinawi, R., 1984. Mechanical Properties of Sea Ice - A Compilation of Available Data. Can. J. Civ. Eng., 11, pp. 884-923.

Lind, N.C., and Davenport, A.G., 1972. Towards Practical Application of Structural Reliability Theory, ACI Special Publication, SP-31.

Maes, M., 1985. Extremal Analysis of Environmental Loads on Engineering Structures, Ph.D. Thesis, University of Calgary.

Marcellus, R.W. and Morrison, T.V. (1982). Ice Design Statistics for the Canadian Beaufort Sea. Beaufort Sea EIS Study.

Marcellus, R.W. (1985). Private communication.

McGonigal, D. and B.D. Wright, 1977. Beaufort Sea Ice Movement from Rams Buoy Data Analysis 1975-1977. Volumes I, II. Gulf Canada Resources Inc.

McGonigal, D., 1978. Beaufort Sea Ice Movement from Rams Buoy Data Analysis, 1977-1978. Gulf Canada Resources Inc.

Michel, B. and Toussaint, N., 1977. Mechanisms and Theory of Indentation of Ice Plates. Journal of Glaciology, Vol.19, No. 81, pp. 285-300.

Murphy, D.L., I.M. Lissauer and J.C. Myers, 1983. Movement of Satellite-Tracked Buoys in the Beaufort Sea (1979-1981). U.S.C.G. Office of Research and Development, Washington, D.C.

Nessim, M.A., et al., 1984. State-of-the-Art Description of Methods for Computation of Global and Local Loades in Ice-Structure Interaction. DnV report no. 84-CGY-018.

Oceanographic Services, Inc., 1980. Beaufort Sea Ice Movement Study. Three Year Summary. Volume I.

Ponter, A.R.S., Palmer, A.C., Goodman, D.J., Ashby, M.F., Evans, A.G., and Hutchinson, J.W., 1983. The Force Exerted by a Moving Ice Sheet on an Offshore Structure, Cold Regions Science and Technology, s, pp. 109-118.

Prodanovic, A., 1981. Upper Bounds of Ridge Pressure on Structures, Proceedings POAC, Quebec, Canada, Vol.3, pp. 1288-1302.

Richardson, F.A. and B.M. Burns, 1975. Ice Thickness Climatology for Canadian Stations. Atmospheric Environment Service, Environment Canada.

Sanderson, T.J.O., 1984. Theoretical and Measured Ice Forces on Wide Structures, Prepared for IAHR State-of-the-Art Report on Ice Forces.

Schwab, D.L., 1978. Beaufort Sea Ice Movement from Landsat Imagery Analysis. Gulf Canada Resources Inc.

Schwarz, J. and Weeks, W.F., 1977. Engineering Properties of Sea Ice, Journal of Glaciology, Vol.19, No.81, 1977.

Sinha, N.K., 1981. Deformation Behaviour of Ice-Like Materials in Engineering Applications, DBR Paper No. 992, Division of Building Research, NRCC.

Snyder, D.L., 1975. Random Point Processes, Wiley & Sons.

Spedding, L.G., 1973. Landfast Ice Movement - Mackenzie Delta 1972-72. APOA Project 51, Esso Resources Canada, IPRT-23ME-73.

Spedding, L.G., 1974. Ice Island Count - Southern Beaufort Sea, 1973. IPRT - 21ME - 74, Esso Resources Canada Ltd.

Spedding, L.G., 1975. Ice Island Count - Southern Beaufort Sea, 1974. Esso Resources Canada Ltd., IPRT-18ME-75.

Spedding, L.G., 1975. Landfast Ice Movement - Mackenzie Delta 1973-74. APOA Project 67, Esso Resources Canada, IPRT-23ME-75.

Spedding, L.G., 1975. Landfast Ice Movement - Mackenzie Delta 1974-75. APOA Project 83, Esso Resources Canada, IPRT-26ME-75.

Spedding, L.G., 1977. Landfast Ice Movement - Mackenzie Delta 1975-76. APOA Project 105(b), Esso Resources Canada, IPRT-1ME-77.

Spedding, L.G., 1978. Statistics on Beaufort Sea Summer Ice Cover for Ice/Structure Collision Assessment. Esso Resources Canada Limited, Internal Report IPRT-2ME-78.

Spedding, L.G., 1978. Summer Ice Floe Size Distribution in the Southern Beaufort Sea, Esso Resources Canada Ltd.

Spedding, L.G., 1979. Landfast and Shear Zone Ice Conditions in the Southern Beaufort Sea - Winter 1977/78. Esso Resources Canada Limited, Internal Report IPRT-16ME-79.

Spedding, L.G., 1981. Landfast Ice Motion Observed in the Mackenzie Delta Region of the Southern Beaufort Sea in the 1972/1973 Winter. Coastal Engineering, Vol.5, pp. 193-209.

Spedding, L.G., 1983. A Large Landfast Ice Movement. POAC '83, Vol.1, pp. 203-213.

Spedding, L.G. and B.W. Danielowicz, 1983. Artificial Islands and Their Effects on Regional Landfast Ice Conditions in the Beaufort Sea. Esso Resources Canada.

Stringer, W.J., S.A. Barrett and L.K. Schreurs, 1978. Morphology of Beaufort, Chukchi, and Bering Seas: Nearshore Ice Conditions by Means of Satellite and Aerial Remote Sensing. Geophysical Institute, University of Alaska for NOAA-OCS.

Stringer, W.J., S.A. Barrett and L.K. Schreurs, 1980. Nearshore Ice Conditions and Hazards in the Beaufort, Chukchi and Bering Seas. Geophysical Institute, University of Alaska, for NOAA-OCS.

Takekuma, K., et al., 1983. Field Study on Mechanical Strength of Sea Ice at East Coast of Hokkaids. Technical Review, June.

Timco, G.W., 1986. Indentation and Penetration in Freshwater Ice. Prepared for 5th Symposium on Offshore Mech. and Arctic Engineering, OMAE, Japan, April 13-17.

Tomin, M.J., Cheung, M., Jordaan, I.J., and Cormeau, A., 1986. Analysis of Failure Models and Damage Processes of Freshwater Ice in Indentation Tests, Prepared for 5th Symposium on Offshore Mech. and Arctic Engineering, OMAE, Japan, April 13-17.

Tredt, L., 1983. PROBAN Technical Manual, Veritas Rep. No. 83-0880, Clients: Conoco, U.S. Coast Guard.

Tucker III, W.B. and J.W. Govani, 1981. Morphological Investigations of First-Year Sea Ice Pressure Ridge Sails. Cold Regions Science and Tedhnology, Vol.5, pp. 1-12.

Wang, Y.S., 1979. Crystallographic Studies and Strength Tests of Field Ice in the Alaskan Beaufort Sea. Proceedings, POAC, Trondheim, Norway, pp. 651-665.

Weeks, W.F., Tucker III, W.B., Frank, M., and Fungcharoen, S., 1977. Characterization of Surface Roughness and Floe Geometry of Sea Ice Over the Continental Shelves of the Beaufort and Chukchi Seas.

Wright, B.D., Hnatiuk, J., and Kovacs, A., 1978. Sea Ice Pressure Ridges in the Beaufort Sea, Proceedings IAHR, Lulea, Sweden, Part I, pp. 249-271.

Wright, B.D.and D.L. Schwab, 1979. Beaufort Sea Ice Stereo Photo Analysis: 1973-76. Gulf Canada Resources Inc.

Wright, B.D.and D.L. Schwab, 1979. Beaufort Sea Ice Stereo Photo Analysis: 1977-78. Gulf Canada Resources Inc.

Wright, B.D., P. Gupta and Y. Lussenburg, 1982. Beaufort Sea Ice Stereo Photo Analysis: 1979-1981. Gulf Canada Resources Inc.

APPENDIX A

PROBABILITY OF ENCOUNTERING A DISCRETE FEATURE IN THE LANDFAST ZONE

Landfast Ice Displacement

To investigate the probability of interaction between ice features embedded in the landfast ice, and a structure, data from Spedding (1975) was analyzed.

From the data, a sample of which is provided in Table A.1, it was observed that the net movements were very small (typically < 10 m). This fact, combined with the randomness of the direction of motion (see Figure A.1), suggested that features embedded in the ice would have a very low probability of interacting with a structure, and even if such an interaction would take place, the penetrations would be negligible.

A sample calculation of the interaction probability, corresponding to the data in Table A.1, is shown below. Note that Table A.1 is only a portion of the data set used to generate Figure A.1, and the interaction probability.

EXAMPLE: Water Depth = 20 - 30 m

Total Movement = 49.5 m

Distance covered = 5.7 m

Multi-year ice concentration = $\frac{0.5}{10}$ ($\bar{c}$ 1974-1975 130°W - 137°W)

Structure width = 100 m

Probability of interaction = 0.0023

TABLE A.1

SUMMARY OF MOVEMENT AND DIRECTION OF MOVEMENT - STATION 6

DATES MOVEMENT OCCURRED BETWEEN

DAY	INITIAL DATE (START OF MOVEMENT) MONTH	YEAR	DAY NO.	HOUR	FINAL DATE END MOVEMENT DAY NO.	HOUR	(1)	(2)	SPEED	WIND DIRECTION
10	02	75	041	1814	042	2108	2.0	165		165 - 280
11	02	75	042	2108	044	0709	2.75	0		270 - 205
13	02	75	044	0709	045	0709	3.0	109		210 - 280
14	02	75	045	0709	046	0009	2.0	340		250-290-95
15	02	75	046	0009	048	0311	1.0	175		95-0-265
17	02	75	048	0311	048	1903	3.0	135		265 - 240
17	02	75	048	1903	052	1211	2.5	330		240-290-175-0-242
21	02	75	052	1211	052	2211	1.25	170		260 - 195
21	02	75	052	2211	053	1811	1.0	350		210 - 100
22	02	75	053	1811	054	1911	3.0	170	6 - 16	110-35-110
23	02	75	054	1911	055	1530	2.0	0	15 - 10	110 - 300
24	02	75	055	1530	057	1709	4.5	175	13-9-19	280-0-95
26	02	75	057	1709	058	2009	2.25	5	12-20-0	50 - 130
27	02	75	058	2009	059	0609	1.75	190	5 - 17	200 - 290
28	02	75	059	0609	060	1009	2.25	110	14 - 4	280 - 225

(1) Amount of Movement (in feet)

(2) Direction of Movement (^{0}T)

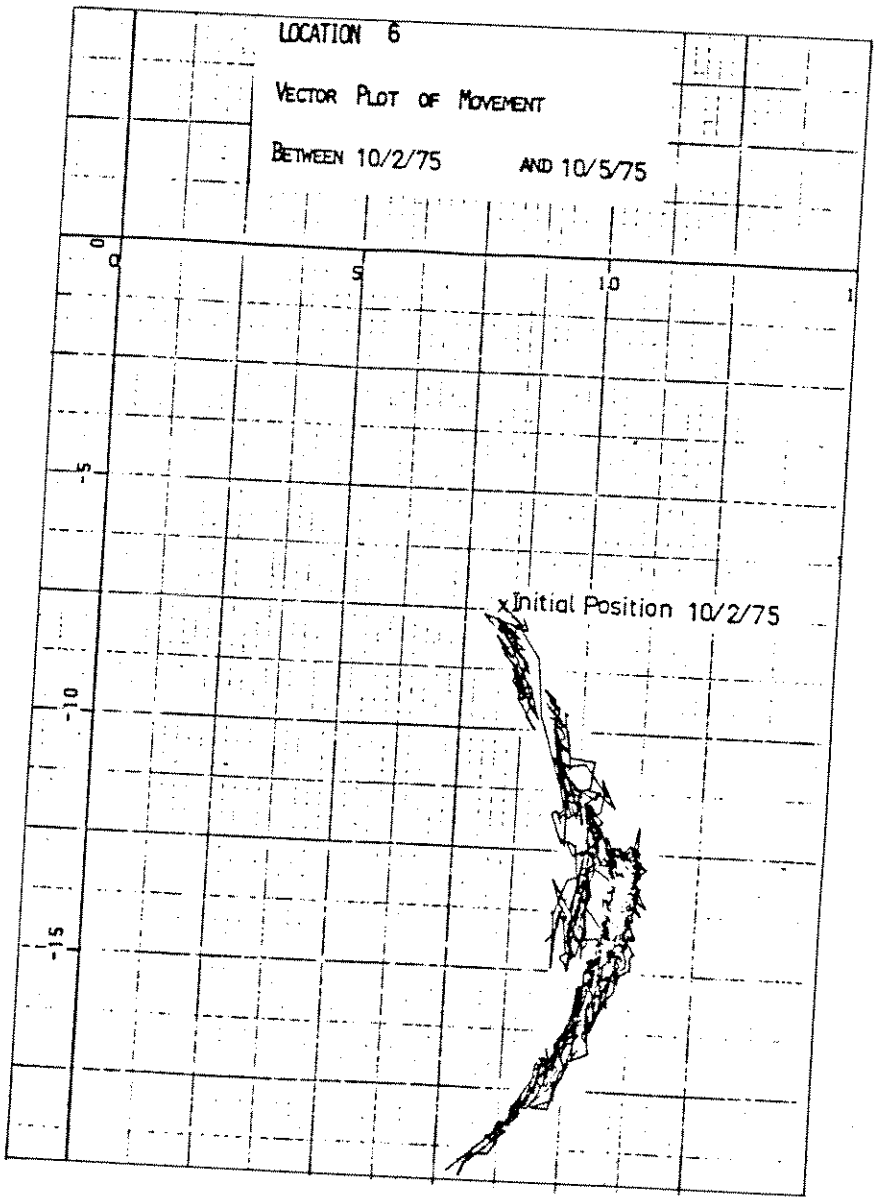
LOCATION 6
VECTOR PLOT OF MOVEMENT
BETWEEN 10/2/75 AND 10/5/75
0
.5
1.0
-5
-10
-15
x Initial Position 10/2/75

Figure A.1

APPENDIX B

RANDOM MULTI-YEAR FLOE MODEL

The motivation for this analysis is to develop a realistic model to estimate the probability of interaction between a structure and a multi-year ridge, and to examine the characteristics of the interaction if it occurs. The important aspects which are taken into account in the model are as follows:

(i) A multi-year ridge is a thickened part of a multi-year floe, and therefore multi-year ridges should be modelled in this context. This is an important aspect, because the interaction will only occur if the structure penetrates a sufficient distance into the floe to contact the ridge. This will depend on the impact characteristics, such as the floe size, speed eccentricty, etc.

(ii) The probability of encountering a multi-year ridge depends on the number of multi-year ridges on the floe, and the average size of these features.

(iii) The orientation of the ridge during an interaction is a random quantity. This also leads to uncertainty regarding the position of the point of contact along the ridge.

(iv) The geometric properties of a multi-year ridge (i.e. height, width, length) are random.

Taking the above factors into account, the floe can be modelled as depicted in Figure B.1. The ridges on the floe have random heights and lengths.

The number of ridges for a given ridge coverage is obtained from:

$$\text{No. of Ridges} = \frac{\text{Floe area X \% area covered by ridges}}{\text{Average ridge area}} \qquad \text{(B.1)}$$

to the nearest integer. The location and geometric properties of each ridge are randomly generated on the basis of the assumptions shown in Figure B.2. The location is defined by the polar coordinates of the ridge centre (r,), and the orientation by the ridge angle from an arbitrary datum ( ). All three parameters, r, and are uniformly distributed. The ridge height and length were simulated from the

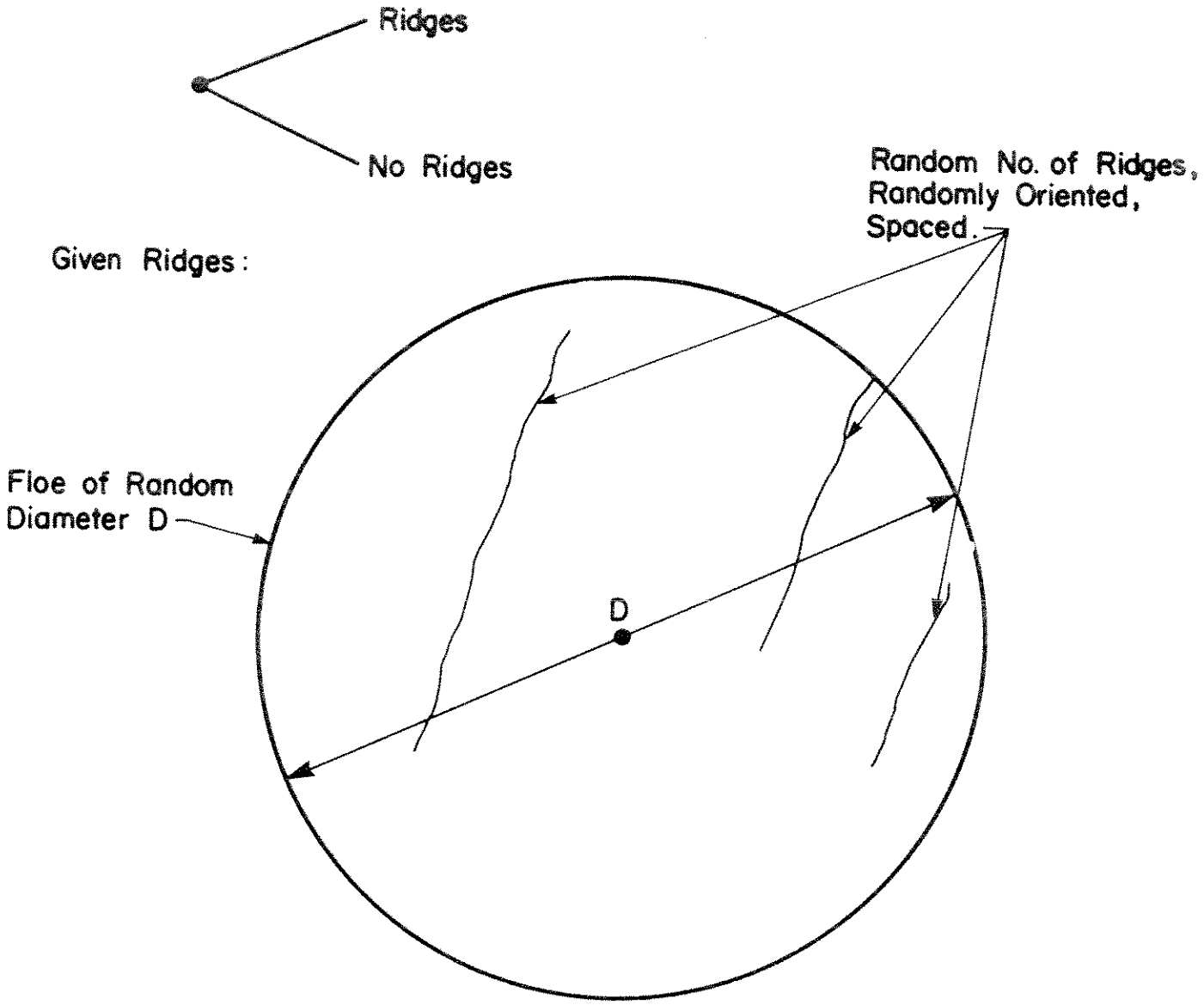

— Impact With Structure , Giving :

Pr (Ridge Impact)

Pr (Impact With Ice Between Ridges)

Figure B.1

Illustration of the random floe model

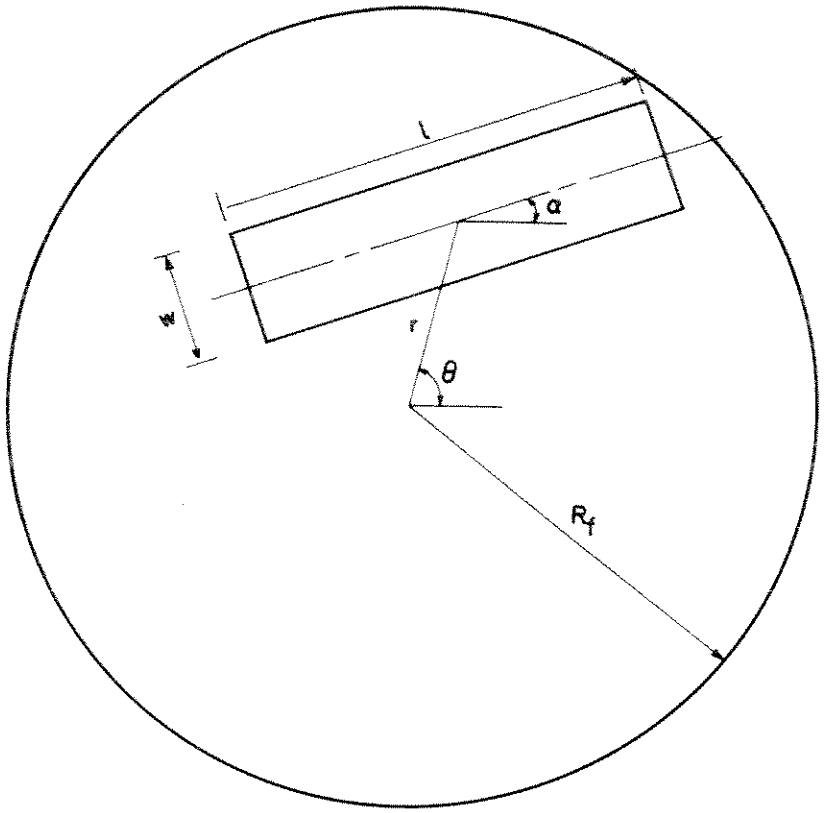

r uniformly distributed in $0 — R_f$

θ uniformly distributed in $0 — \pi$

α uniformly distributed in $0 — \pi$

w = 17h

RANDOM FLOE MODEL

Figure B.2

Ridge geometric parameters and main probability distributions

appropriate distributions (see Sections 4.2.3.13 and 4.2.3.14), and the ridge width was estimated from its height based on the Kovacs ridge model (see Section 5.3.2.1). Any part of the ridge which lies outside the floe boundary was eliminated.

The probability of ridge encounter for a given penetration can be calculated as the probability that the contact point on the ridge perimeter is such that the structure would contact the ridge. This is illustrated in Figure B.3, where the hatched areas represent the areas of ridge with which the structure can interact for the given penetration. Angles θ_1 and θ_2 limit the points on the floe perimeter, which would lead to ridge interaction. Note that θ_1 and θ_2 enclose the ridge extreme points in the penetrated zone, as well as an angle on each side corresponding to half the contact width of the structure with the floe on the outside perimeter. Based on the assumption that each point on the floe perimeter is an equally likely point of contact, the probability of ridge encounter can be expressed as:

$$\text{Probability of ridge encounter} = \frac{\theta_1 + \theta_2}{2\pi} \tag{B.2}$$

For a given penetration and ridge coverage, the above procedure is repeated to generate different configurations of the ridge positions and geometric properties. The final probability of encountering a ridge is calculated as the average of the probability values for all configurations.

Results of this analysis are illustrated in Figures B.4 and B.5, for a circular structure with 60 m diameter, and a floe with 1000 m diameter. The following observations were made:

(i) As expected, the probability of ridge encounter increases as the ridge coverage and/or the penetration increase. This means that this probability is dependent on the specific parameters of each interaction, and therefore, multi-year ridges are best treated within the multi-year floe interaction model.

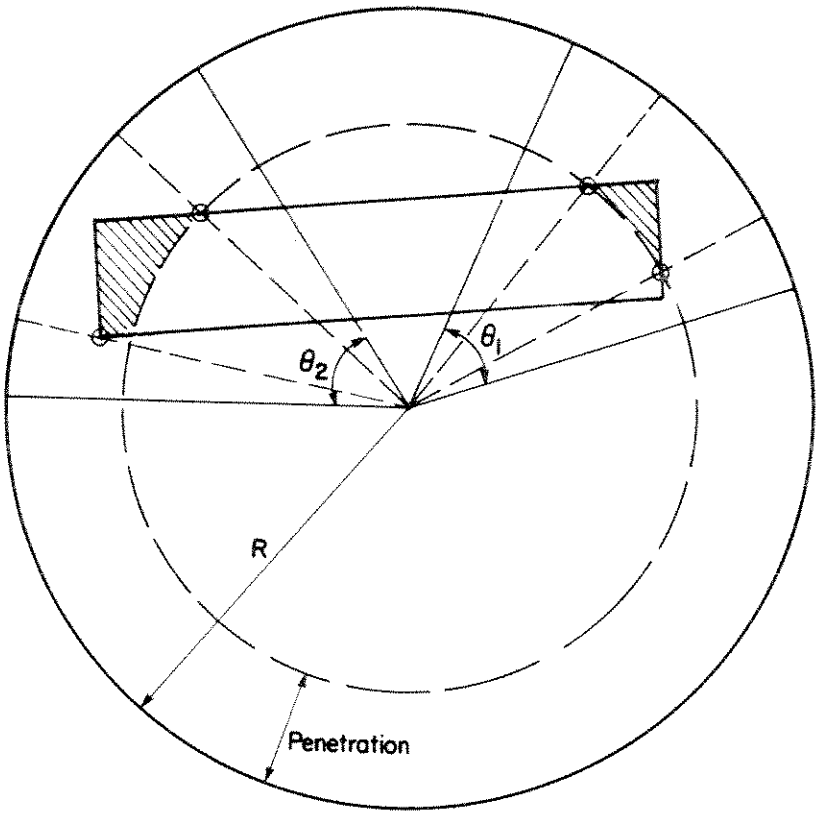

$$\text{Probability of ridge encounter} = \frac{\theta_1 + \theta_2}{2\pi}$$

RANDOM FLOE MODEL.

Figure B.3

Probability of ridge encounter given the penetration

VARIATION OF RIDGE ENCOUNTER PROBABILITY WITH % AREA OF RIDGED ICE.

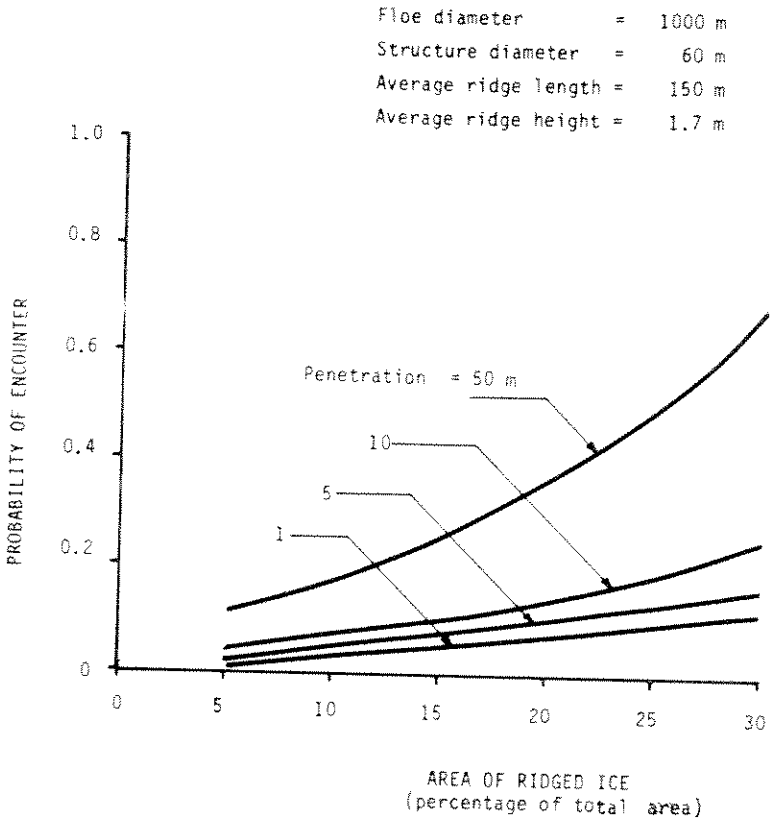

Figure B.4

Probability of ridge encounter versus % area of ridged ice for different penetrations

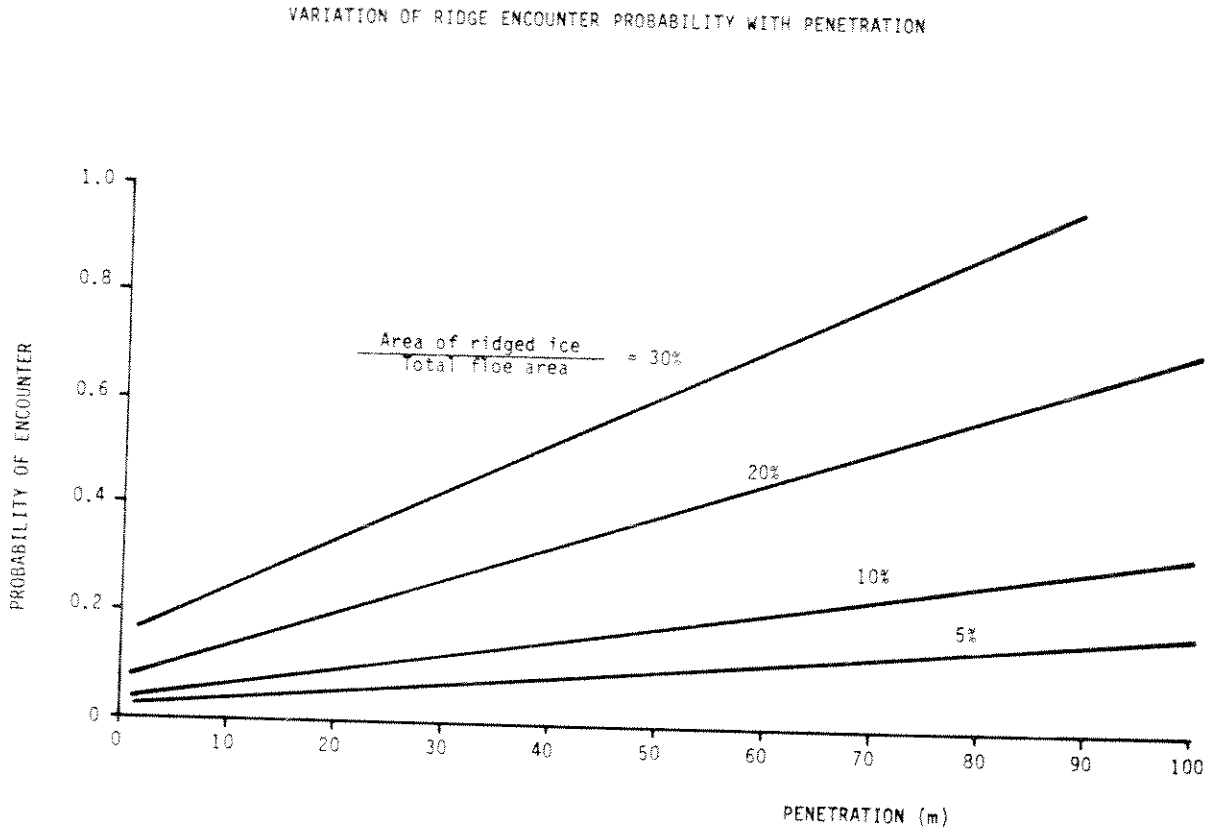

Figure B.5

Probability of ridge encounter versus penetration for different % areas of ridged ice

(ii) Most of the interactions will occur with ridge corners and ridge ends. This indicates that a ridge-crushing model is more appropriate than one based on ridge bending.

(iii) Typical penetration values for average multi-year floe sizes and velocities are in the low range of those considered in Figures B.4 and B.5. The probability of encountering a ridge is therefore generally small.

APPENDIX C

ORIGINAL DATA SETS

TABLE C.1

Frequency of start of break-up occurring on a given date
North Point, Canadian Beaufort Sea, 1963-1984

Date		SECTION (km)				
		20-40	60-80	80-100	100-120	120-140
April	30	0	1	0	0	0
May	11-17	0	0	0	0	0
	18-24	0	2	1	1	2
	25-31	0	2	1	1	1
June	01-07	3	2	3	3	1
	08-14	1	3	0	1	2
	15-21	5	7	7	6	6
	22-28	5	1	3	2	2
July	29-05	3	1	2	2	2
	06-12	2	1	2	2	2
	13-19	1	2	3	2	2
	20-26	1	0	0	0	0
	27-02	0	0	0	1	1
August	03-09	1	0	0	1	1
	10-16	0	0	0	0	0
	17-23	0	0	0	0	0
	24-30	0	0	0	0	0

TABLE C.2

Frequency of end of break-up occurring on a given date
North Point, Canadian Beaufort Sea, 1963-1984

Date		SECTION (km)				
		20-40	60-80	80-100	100-120	120-140
May	18-24	0	1	0	0	0
	25-31	0	2	1	1	1
June	01-07	2	3	1	1	0
	08-14	0	1	1	0	0
	15-21	2	4	2	1	2
	22-28	4	1	3	3	2
July	29-05	4	1	5	5	4
	06-12	3	3	3	2	2
	13-19	1	1	1	1	3
	20-26	1	1	1	2	0
	27-02	1	1	1	2	3
August	03-09	2	1	1	1	1
	10-16	1	0	0	1	1
	17-23	0	0	0	0	0
	24-30	0	0	1	0	0
Sept.	31-06	0	1	0	0	1
	07-13	0	0	0	1	0
Final break-up did not occur		1	1	1	1	2

TABLE C.3

Frequency of freeze-up occuring on a given date
North Point, Canadian Beaufort Sea, 1963-1984

Date		SECTION (km)				
		20-40	60-80	80-100	100-120	120-140
Sept.	07-13	0	1	0	0	0
	14-20	0	0	0	0	0
	21-27	0	0	0	0	1
Oct.	28-04	0	1	1	2	1
	05-11	1	0	1	1	1
	12-18	0	0	0	0	0
	19-25	0	0	1	1	1
	26-01	0	1	1	1	1
Nov.	02-08	1	0	0	0	1
	09-15	2	1	1	1	1
	16-22	0	1	1	1	1
	23-29	2	3	3	3	3
Dec.	30-05	0	0	0	0	0
	06-12	1	0	0	0	0
	13-19	0	0	0	0	0
After Oct. 01		1		1	1	1
After Oct. 19		13	13	11	10	9
After Nov. 04		1	1	1	1	1

TABLE C.4

Start of break-up
North of Prudhoe Bay, 1975–1984

Year	SECTION (km)			
	0–20	20–40	40–60	60–80
1975	July 11	July 11	July 25	July 25
1976	July 16	July 23	July 23	July 23
1977	July 22	Aug. 12	Aug. 12	Aug. 12
1978	July 06	July 27	Aug. 03	Aug. 10
1979	July 19	July 26	Aug. 09	Aug. 23
1980	July 17	July 17	June 12	July 17
1981	July 16	July 16	July 16	July 30
1982	July 01	Aug. 12	June 17	June 17
1983	July 05	Aug. 11	July 05	July 05
1984	June 28	May 15	May 15	June 28

TABLE C.5

End of Break-Up
North of Prudhoe Bay, 1975-1984

Year	SECTION (km)			
	0-20	20-40	40-60	60-80
1975	July 11	July 11	*	*
1976	July 23	July 30	Sept.24	Sept.24
1977	July 22	Aug. 26	Aug. 12	Aug. 12
1978	July 20	Aug. 03	Sept.21	Sept.21
1979	July 19	July 26	Aug. 09	Aug. 23
1980	July 17	July 17	July 31	July 31
1981	July 16	July 16	July 16	July 30
1982	July 15	Aug. 26	Aug. 26	Aug. 26
1983	Aug. 04	Aug. 25	*	*
1984	July 08	July 29	Sept.16	Sept.16

* Final break-up did not occur

TABLE C.6

Freeze-Up North of Prudhoe Bay
1975-1984

Year	SECTION (km)			
	0-20	20-40	40-60	60-80
1975	Oct.17	Oct.31	Aug.29	Aug.29
1976	>Oct.29	>Oct. 29	>Oct.29	>Oct.29
1977	>Nov.04	>Nov.04	>Nov.04	>Nov.04
1978	Oct.26	Nov.02	Nov.02	Nov.02
1979	Nov.08	Dec.13	Dec.13	Dec.13
1980	Nov.20	Oct.30	Oct.30	Oct.30
1981	Oct.29	Nov.26	Nov.19	Nov.19
1982	Oct.28	Nov.11	Nov.11	Nov.11
1983	Oct.28	Nov.11	Nov.11	Nov.11
1984	Oct.28	Nov.04	Nov.04	Nov.04

TABLE C.7

Summer Ice Floe Speed Data

Speed (cm/s)	Number of Data Points		
	1980 Data	1979 Data	Combined Data
0 - 5	1,290	1,155	2,445
5 - 10	1,185	1,045	2,230
10 - 15	1041	889	1,930
15 - 20	854	752	1,606
20 - 25	633	632	1,265
25 - 30	453	515	968
30 - 35	303	406	709
35 - 40	196	331	527
40 - 45	126	229	355
45 - 50	95	169	264
50 - 55	40	68	108
55 - 60	18	56	74
60 - 65	10	23	33
65 - 70	0	19	19
70 - 75	0	11	11
75 - 80	0	4	4
TOTAL	6,244	6,304	12,548

TABLE C.8

Multi-Year Floe Thickness Data

Thickness (m)	Number of Observations
0 - 1	0
1 - 2	1
2 - 3	4
3 - 4	11
4 - 5	19
5 - 6	13
6 - 7	6
7 - 8	2
8 - 9	1
9 - 10	2

TABLE C.9

Ice Concentration Data for the
Canadian Beaufort Sea (North Point)
Summer Season (July - October)

Concentration (Ratio)	Section North of North Point							
	0–20	20–40	40–60	60–80	80–100	100–120	120–140	140–160
0	154	147	142	132	136	128	123	112
0 - 0.5/10	8	7	8	9	8	10	11	11
0.5/10 - 1.5/10	4	9	9	13	9	12	13	14
1.5/10 - 2.5/10	5	4	5	7	3	1	5	7
2.5/10 - 3.5/10	2	4	4	3	4	4	6	7
3.5/10 - 4.5/10	3	3	4	7	9	6	2	4
4.5/10 - 5.5/10		1	1	-	2	3	3	2
5.5/10 - 6.5/10		-	1	1	1	5	5	8
6.5/10 - 7.5/10		-	1	1	1	2	2	2
7.5/10 - 8.5/10		1	-	1	1	3	2	2
8.5/10 - 9.5/10			1	2	3	2	4	6
9.5/10 - 10/10								1

TABLE C.10

Ice Concentration Data for
North of Prudhoe Bay
Summer Season (July - October)

Concentration (Ratio)	SECTION (km) north of North Point			
	0-20	20-40	40-60	60-80
0	134	81	62	64
0.5/10-1.5/10	13	32	40	43
1.5/10-2.5/10	12	25	23	18
2.5/10-3.5/10	5	6	9	3
3.5/10-4.5/10	0	3	3	3
4.5/10-5.5/10	0	3	1	2
5.5/10-6.5/10	0	4	6	4
6.5/10-7.5/10	0	1	4	3
7.5/10-8.5/10	0	2	1	7
8.5/10-9.5/10	0	4	8	11
9.5/10-10/10	1	1	1	1

TABLE C.11

Ice Island Fragment Diameter Data

Diameter (m)	No. of Observations
0 - 15	1
15 - 30	60
30 - 75	219
75 - 150	99
150-225	15
225-300	4
TOTAL	398

TABLE C.12

Ice Island Diameter Data

LOCATION	AREA (km^2)	EQUIVALENT DIAMETER (km)
Marham Bay	45	7.57
East Ward Hunt	500	25.23
West Ward Hunt	330	20.50
Ayleo Fiord Edge	50	7.98
Ayleo Fiord Interim	35	6.68
Milne Fiord (isolated by cracks)	35	6.68
Milne Fiod Interior	100	11.28
West Yelverton Bay	50	7.98
Alert Point	300	19.54
Cape Armstrong	20	5.05

TABLE C.13

Ice Island/Fragment Thickness Data

LOCATION	AREA (km^2)	THICKNESS (m)
Marham Bay	45	30
East Ward Hunt	500	45
West Ward Hunt	330	45
Ayleo Fiord Edge	50	45
Ayleo Fiord Interim	35	45
Milne Fiord (isolated by cracks)	35	85-90
Milne Fiord Interior	100	60
West Yelverton Bay	50	15-30
Alert Point	300	45
Cape Armstrong	20	45

TABLE C.14

Summer Multi-Year Floe Diameter Data

Cape Simpson

Diameter (m)	No. of Observations
100 - 450.5	3,084
450.5 - 801	222
801 - 1151.5	56
1151.5 - 1502	11
1502 - 1852.5	14
1852.5 - 2203	3
2203 - 2553.5	1
2553.5 -2904	0
2904 - 3254.5	0
>3254.5	2
TOTAL	3,393

Pt. Barrow

Diameter (m)	No. of Observations
100 - 300	3021
300 - 500	438
500 - 700	143
700 - 900	59
900 - 1100	16
1100 - 1300	21
1300 - 1500	15
1500 - 1700	7
1700 - 1900	4
1900 - 2100	1
2100 - 2300	0
2300 - 2500	2
2500 - 2700	1
2700 - 2900	0
2900 - 3100	1
TOTAL	3,729

TABLE C.15

Floe Diameter Data for the Months of August and September

Diameter (ft.)	0 - 250	250 - 500	500 - 1000	1000 - 2500	2500 - 5000	Total
Number	12205	3887	1609	657	206	18564

TABLE C.16

First-Year Ice Thickness Data

CAPE PARRY, N.W.T. GILLET BAY 70 10N 124 41W 1959 - 1972

PERIOD	ICE THICKNESS (inches) MEAN	S.D.	MAXIMUM	MINIMUM	# OF OBS	SNOW DEPTH MEAN	S.D.	# OF OBS
JAN01-JAN07	39.5	5.5	52.0	31.0	13	4.4	3.2	13
JAN08-JAN14	41.9	5.2	52.0	34.5	13	4.5	3.3	13
JAN15-JAN21	44.5	5.2	54.0	36.0	12	4.8	3.4	12
JAN22-JAN28	47.9	4.8	56.0	38.5	14	4.6	3.4	14
JAN29-FEB04	50.3	5.2	58.0	40.5	14	5.5	3.3	14
FEB05-FEB11	52.3	4.6	60.0	43.5	15	5.2	3.1	13
FEB12-FEB18	55.3	4.7	63.5	46.5	12	5.8	3.3	12
FEB19-FEB25	58.6	6.6	75.0	47.5	13	5.6	2.7	13
FEB26-MAR04	60.0	6.6	78.0	53.0	14	5.8	3.4	14
MAR05-MAR11	63.9	6.0	79.0	57.0	12	5.9	4.3	12
MAR12-MAR18	65.4	6.4	82.0	57.0	13	6.4	3.7	13
MAR19-MAR25	66.8	6.4	82.0	58.0	12	6.5	3.8	12
MAR26-APR01	69.5	7.5	88.0	58.5	11	6.7	4.4	11
APR02-APR08	69.9	7.2	88.0	59.0	13	6.2	3.3	13
APR09-APR15	71.8	7.2	89.0	61.0	12	6.2	2.8	12
APR16-APR22	73.1	7.3	89.0	62.0	12	6.0	3.1	12
APR23-APR29	74.8	6.7	88.0	62.0	12	6.3	3.1	12
APR30-MAY06	72.2	6.5	81.0	60.0	13	6.4	3.0	13
MAY07-MAY13	73.1	6.6	82.5	61.0	12	6.7	2.7	12
MAY14-MAY20	73.2	5.5	83.5	64.0	14	6.5	2.6	14
MAY21-MAY27	74.6	5.5	84.0	65.0	11	5.7	2.1	11
MAY28-JUN03	74.1	6.8	84.0	61.0	10	6.2	2.1	10
JUN04-JUN10	74.0	8.3	81.5	55.0	10	2.9	2.0	10
JUN11-JUN17	71.1	11.6	83.0	47.0	8	1.6	1.5	8
JUN18-JUN24	65.7	13.3	80.0	42.0	7	2.3	2.5	7
JUN25-JUL01	54.6	16.3	80.0	37.0	6	0.7	0.8	6
JUL02-JUL08	35.6	15.5	48.0	13.0	4	0.5	0.6	4
JUL09-JUL15	36.0	4.2	39.0	33.0	2	0.0	0.0	2
JUL16-JUL22	0.0	0.0	0.0	0.0	0	0.0	0.0	0
JUL23-JUL29	0.0	0.0	0.0	0.0	0	0.0	0.0	0
JUL30-AUG05	0.0	0.0	0.0	0.0	0	0.0	0.0	0
AUG06-AUG12	0.0	0.0	0.0	0.0	0	0.0	0.0	0
AUG13-AUG19	0.0	0.0	0.0	0.0	0	0.0	0.0	0
AUG20-AUG26	0.0	0.0	0.0	0.0	0	0.0	0.0	0
AUG27-SEP03	0.0	0.0	0.0	0.0	0	0.0	0.0	0
SEP04-SEP10	0.0	0.0	0.0	0.0	0	0.0	0.0	0
SEP11-SEP17	0.0	0.0	0.0	0.0	0	0.0	0.0	0
SEP18-SEP24	4.5	0.0	4.5	4.5	1	0.0	0.0	1
SEP25-OCT01	6.0	0.0	6.0	6.0	1	0.0	0.0	1
OCT02-OCT08	6.0	0.0	6.0	6.0	1	0.0	0.0	1
OCT09-OCT15	5.3	1.1	6.0	4.5	2	0.5	0.7	2
OCT16-OCT22	12.5	5.8	19.0	8.0	3	1.0	0.0	3
OCT23-OCT29	13.8	4.6	19.0	10.0	3	2.0	1.0	3
OCT30-NOV05	10.9	3.7	15.0	5.0	7	3.1	2.6	7
NOV06-NOV12	15.1	3.3	19.5	11.0	8	2.5	1.6	8
NOV13-NOV19	19.1	5.5	29.0	13.0	8	2.8	2.4	8
NOV20-NOV26	22.6	4.6	31.0	17.0	11	3.1	3.2	11
NOV27-DEC03	25.7	6.9	45.0	18.0	14	3.6	3.1	14
DEC04-DEC10	28.7	5.0	40.0	20.0	12	3.3	3.0	12
DEC11-DEC17	31.6	6.1	46.0	23.0	13	4.2	3.4	13
DEC18-DEC24	33.5	5.8	46.0	24.0	14	4.3	3.2	14
DEC25-DEC31	37.2	4.0	44.0	30.5	13	3.8	3.0	13

MAXIMUM ICE THICKNESS = 89.0 SNOW DEPTH = 12.0 DATE = APR 20 1962

TABLE C.17

First Year Level Ice Speed Data

WATER DEPTH 0-20 ft

Speed ft/hr	Number of Observations						
	Nov.	Dec.	Jan.	Feb.	Mar.	Apr.	May
0.5 - 1.0	43	68	29	82	33	33	10
1.0 - 1.5	7	8	10	18	1	4	0
1.5 - 2.0	0	4	3	7	-	-	0
2.0 - 2.5	2	4	-	1	-	-	0
2.5 - 3.0	0	3	-	2	-	-	0
3.5 - 4.0	0	1	-	0	-	-	1
4.0 - 4.5	0	1	-	1	-	-	-
4.5 - 4.0	1	1	-	-	-	-	-
5.0 - 5.5	-	2	-	-	-	-	-
TOTAL	53	92	42	11	34	37	11

TABLE C.17 (continued)

WATER DEPTH 20 - 40 ft

Speed ft/hr	Number of Observations					
	Dec.	Jan.	Feb.	Mar.	Apr.	May
0.5 - 1.0	23	8	48	85	44	10
1.0 - 1.5	3	1	9	14	5	0
1.5 - 2.0	3	0	2	4	1	0
2.0 - 2.5	2	0	0	2	3	1
2.5 - 3.0	0	0	1	-	-	0
3.0 - 3.5	0	0	0	-	-	1
3.5 - 4.0	1	0	0	-	-	-
4.0 - 4.5	0	0	0	-	-	-
4.5 - 5.0	0	0	1	-	-	-
5.0 - 5.5	1	0	0	-	-	-
5.5 - 6.0	0	0	0	-	-	-
6.0 - 6.5	0	0	0	-	-	-
6.5 - 7.0	1	0	0	-	-	-
TOTAL	34	9	61	105	53	12

TABLE C.17 (continued)

WATER DEPTH 40 - 60 ft.

Speed ft/hr	Number of Observations			
	Feb.	Mar.	Apr.	May
0.5 - 1.0	36	59	351	103
1.0 - 1.5	9	15	153	64
1.5 - 2.0	2	3	43	44
2.0 - 2.5	0	2	5	12
2.5 - 3.0	0	1	3	4
3.0 - 3.5	0	0	-	1
3.5 - 4.0	0	1	-	1
4.0 - 4.5	0	0	-	4
4.5 - 5.0	0	0	-	-
5.0 - 5.5	0	0	-	-
5.5 - 6.0	0	1	-	-
6.0 - 6.5	0	0	-	-
6.5 - 7.0	0	0	-	-
7.0 - 7.5	0	0	-	-

WATER DEPTH 40 - 60 ft. (continued)

Speed ft/hr	Number of Observations			
	Feb.	Mar.	Apr.	May
7.5 - 8.0	0	0	-	-
8.0 - 8.5	0	1	-	-
8.5 - 9.0	0	1	-	-
9.0 - 9.5	0	0	-	-
9.5 - 10.0	0	0	-	-
10.0 - 10.5	0	1	-	-
10.5 - 11.0	0	-	-	-
11.5 - 12.0	0	-	-	-
12.5 - 13.0	0	-	-	-
13.5 - 14.0	0	-	-	-
14.0 - 14.5	1	-	-	-
TOTAL	48	85	555	233

TABLE C.17 (continued)

WATER DEPTH >60 ft.

Speed ft/hr	Number of Observations			
	Feb.	Mar.	Apr.	May
0.5 - 1.0	5	24	17	65
1.0 - 1.5	2	13	3	3
1.5 - 2.0	1	2	0	0
2.0 - 2.5	0	0	1	0
2.5 - 3.0	1	1	1	1
3.0 - 3.5	0	0	1	0
3.5 - 4.0	1	0	0	0
4.0 - 4.5	0	0	0	0
4.5 - 5.0	0	0	0	0
5.0 - 5.5	0	0	1	1
5.5 - 6.0	0	0	1	1
6.0 - 6.5	0	0	0	1
6.5 - 7.0	0	1	0	-
7.0 - 7.5	0	1	0	-

WATER DEPTH >60 ft. (continued)

Speed ft/hr	Number of Observations			
	Feb.	Mar.	Apr.	May
7.5 - 8.0	1	0	0	-
8.0 - 8.5	0	0	0	-
8.5 - 9.0	0	0	0	-
9.0 - 9.5	0	0	0	-
9.5 - 10.0	0	0	0	-
10.5 - 11.0	1	1	0	-
11.0 - 11.5	-	0	0	-
11.5 - 12.0	-	1	1	-
12.0 - 12.5	-	0	-	-
12.5 - 13.0	-	0	-	-
13.0 - 13.5	-	0	-	-
13.5 - 14.0	-	0	-	-
14.0 - 14.5	-	1	-	-
14.5 - 15.0	-	2	-	-
TOTAL	12	47	26	72

TABLE C.18

Frequency of Landfast Ice Speed Peaks

MONTH	TOTAL HOURS OF OBS.	NUMBER OF PEAKS			WATER DEPTH
		TOTAL	AVERAGE PER HOUR	AVERAGE PER MONTH	
Nov.	3,072	53	1.725×10^{-2}	12.422	0 to 20 ft.
Dec.	5,256	93	1.769×10^{-2}	12.737	
Jan.	1,772	42	2.370×10^{-2}	17.065	
Feb.	4,914	110	2.239×10^{-2}	16.117	
Mar.	3,840	34	8.8542×10^{-3}	6.375	
Apr.	3,864	37	9.576×10^{-3}	6.894	
May	3,192	11	3.446×10^{-3}	2.481	
TOTAL	**25,910**	**380**	**1.467×10^{-2}**	**10.560**	
Dec.	2,256	34	1.507×10^{-2}	10.851	20 to 40 ft.
Jan.	936	10	1.068×10^{-2}	7.692	
Feb.	1,272	62	4.874×10^{-2}	35.094	
Mar.	1,776	105	5.912×10^{-2}	42.568	
Apr.	2,112	53	2.510×10^{-2}	18.068	
May	600	12	2.000×10^{-2}	14.400	
TOTAL	**8,952**	**276**	**3.083×10^{-2}**	**22.198**	

TABLE C.18 (continued)

MONTH	TOTAL HOURS OF OBS.	NUMBER OF PEAKS			WATER DEPTH
		TOTAL	AVERAGE PER HOUR	AVERAGE PER MONTH	
Feb.	480	48	1.0×10^{-1}	72.000	
Mar.	1,440	85	5.903×10^{-2}	42.500	40
Apr.	2,640	555	2.102×10^{-1}	151.36	to
May	1,392	233	1.674×10^{-1}	120.52	60 ft.
TOTAL	**5,952**	**921**	**1.547×10^{-1}**	**111.41**	
Feb.	312	12	3.846×10^{-2}	27.692	
Mar.	552	47	8.515×10^{-2}	61.304	60 ft.
Apr.	192	27	1.406×10^{-1}	101.25	
May	72	72	1.000	720.00	
TOTAL	**1,128**	**158**	**1.401×10^{-1}**	**100.85**	

TABLE C.18 (continued)

MONTH	TOTAL HOURS OF OBS.	NUMBER OF PEAKS			WATER DEPTH
		TOTAL	AVERAGE PER HOUR	AVERAGE PER MONTH	
Nov.	3,072	53	1.725×10^{-2}	12.422	ALL DEPTHS
Dec.	7,512	127	1.691×10^{-2}	12.173	
Jan.	2,708	52	1.920×10^{-2}	13.826	
Feb.	6,978	232	3.325×10^{-2}	23.938	
Mar.	5,748	271	4.715×10^{-2}	33.946	
Apr.	8,808	672	7.629×10^{-2}	54.932	
May	5,257	328	6.239×10^{-2}	44.923	
TOTAL	**40,083**	**1,735**	**4.329×10^{-2}**	**31.165**	

Table C.19

First Year Ridge Height

Height (feet)	ACTIVE ICE ZONE		LANDFAST ICE ZONE	
	NUMBER OF OBSERVATIONS (years 1980-1981)		Height (feet)	Number of Observations
	Shear Zone	Pack Zone		
2.5 - 3.5	61	242	2 - 3	157
3.5 - 4.5	45	158	3 - 4	104
4.5 - 5.5	22	74	4 - 5	51
5.5 - 6.5	11	49	5 - 6	46
6.5 - 7.5	11	48	6 - 7	38
7.5 - 8.5	6	29	7 - 8	36
8.5 - 9.5	5	24	8 - 9	20
9.5 - 10.5	7	7	9 - 10	11
10.5 - 11.5	3	4	10 - 11	12
11.5 - 12.5	5	4	11 - 12	6
12.5 - 13.5	0	2	12 - 13	12
13.5 - 14.5	5	1	13 - 14	9
14.5 - 15.5	2	1	14 - 15	5
15.5 - 16.5	0	2	15 - 16	1
16.5 - 17.5	1	0	16 - 17	2
17.5 - 18.5	0	1	17 - 18	1
18.5 - 19.5	0	0	18 - 19	1
19.5 - 20.5	1	0	19 - 20	0
TOTAL	185	646	TOTAL	512

TABLE C.20

First Year Ridge Orientation (From True North)

ANGLE	% FREQUENCY IN ICE ZONE		
	LANDFAST	SHEAR	PACK
0^{o} - 45^{o}	11.0 (6)*	17.8 (53)	18.6 (93)
45^{o} - 90^{o}	30.0 (15)	30.6 (92)	31.0 (155)
90^{o} - 135^{o}	48.0 (24)	34.6 (104)	27.2 (136)
135^{o} - 180^{o}	11.0 (5)	17.0 (51)	23.2 (116)
TOTAL	100.0 (50)	100.0 (300)	100.0 (500)

* ( ) are actual number of observations.

TABLE C.21

First Year Ridge Frequency Data

RIDGES PER MILE	NUMBER OF OBSERVATIONS		
	LANDFAST	SHEAR	PACK
0 - 5	0	6	8
5 - 10	0	9	9
10 - 15	1	8	12
15 - 20	3	8	13
20 - 25	6	1	19
25 - 30	4	11	12
30 - 35	2	8	12
35 - 40	3	7	10
40 - 45	1	5	8
45 - 50	0	2	3
50 - 55	0	0	1
55 - 60	0	0	1
TOTAL	20	65	108

TABLE C.23

Break-Up Speeds
Prudhoe Bay

Speed cm/s	NUMBER OF EVENTS (HOURLY MEASUREMENTS)			
	Station 1	Station 3	Station 4	TOTAL
0 - 0.833	10	9	7	26
0.833 - 1.667	5	6	8	19
1.667 - 2.50	5	10	3	18
2.50 - 3.333	3	4	4	11
3.333 - 4.167	5	2	5	12
4.167 - 6.250	2	9	1	12
6.250 - 8.333	2	5	3	10
8.333 - 12.50		4	3	7
12.50 - 16.67		1	1	2
16.67 - 20.83		0	0	0
20.83 - 25.00		1	2	3
25.00 - 29.17		2		2

Speed cm/s	NUMBER OF EVENTS (HOURLY MEASUREMENTS)			
	Station 1	Station 3	Station 4	TOTAL
0 - 1	19	59	12	90
1 - 2	29	61	7	97
2 - 3	46	99	5	150
3 - 4	40	70	41	151
4 - 5	23	68	13	104
5 - 7.5	41	113	29	183
7.5 - 10	17	58	21	96
10 - 15	6	58	58	122
15 - 20	0	16	30	46
20 - 25	0	22	25	47
25 - 30	1	40	11	52
30 - 35		8	10	18
35 - 40		0	3	3
40 - 45		2	2	4
45 - 50			0	0
50 - 60			2	2

TABLE C.22

Winter Ice Speed Data
Canadian and U.S. Beaufort Sea

Daily Drift Speed	CANADIAN BEAUFORT				U.S. BEAUFORT			Combined Total
	Jan	Feb	Mar	Total	Mar	April	Total	
0-.05	13	20	6	39	18	24	42	81
.06-.1	12	4	1	17	1	0	1	18
.11-.15	2	1		3	0	5	5	8
.16-.20	2	3		5	1	1	2	7
.21-.25	2	0		2	1	0	1	3
.26-.30	0	0		0	0	0	0	0
.31-.35	0	0		0	0	0	0	0
.36-.40	0	0		0	2	0	2	2
.41-.45	0	0		0	1	0	1	1
TOTAL	31	28	7	66	24	30	54	120